Utilization of Organic Glass Scintillators in a Dual-Particle Imager for Source Localization and Characterization

by

Ricardo Lopez

A dissertation submitted in partial fulfillment
of the requirements for the degree of
Doctor of Philosophy
(Nuclear Engineering and Radiological Sciences)
in the University of Michigan
2026

Doctoral Committee:

Professor Sara A. Pozzi, Chair
Professor Zhong He
Dr. Peter Marleau, Sandia National Laboratories
Professor Michael Nebeling

Ricardo Lopez
rlopezle@umich.edu
ORCID iD: 0000-0002-6945-5121

© Ricardo Lopez 2026

For my parents, Ricardo and Imelda Lopez.

ACKNOWLEDGMENTS

To begin, thank you Professor Pozzi for letting me part of the Detection for Nuclear Nonproliferation Group (DNNG). I've had the pleasure of experiencing many great opportunities while being a part of DNNG and am excited for what comes next. Thank you Dr. Clarke for your mentorship throughout my time with DNNG. I am grateful for the support during ideation and paper review editing. I'd also like to thank the rest of DNNG throughout all the years that I've been here at Michigan. I've received a great amount of support, both academic and mental, from many. I would like to thank my other committee members: Professor He, Professor Nebeling, and Dr. Marleau. Thank you all for being part of my committee and helping focus and refine my research. Lastly, I'd like to thank my family and friends for their support these past five years.

Locations where experiments performed for this dissertation include the National Criticality Experiments Research Center and Lawrence Livermore National Laboratory. I would like to give my sincerest thanks to the staff and scientists who helped arrange the logistics and provided their lab expertise to make the measurements a reality.

Finally, I would like to thank the sponsors for making my work possible. This work was funded by the Consortium for Monitoring, Technology, and Verification under Department of Energy National Nuclear Security Administration award number DE-NA0003920. The Consortium was further responsible for funding my time in the PhD program through the MTV-COE Excellence Fellowship. I am grateful fro the support. Any opinions, findings, conclusions or recommendations expressed in this material are those of the author(s) and do not necessarily reflect the views of any funding organization.

TABLE OF CONTENTS

DEDICATION ii

ACKNOWLEDGMENTS iii

LIST OF FIGURES vii

LIST OF TABLES xi

ABSTRACT xii

CHAPTER

1 Introduction 1

1.1 Motivation 1
1.1.1 A Historical Overview 1
1.1.2 Modern Status and Needs of Nuclear Safeguards and Nonproliferation . . 2
1.2 Role of Dual-Particle Imaging in Nuclear Safeguards and Nonproliferation 3
1.3 Contributions of this Work 4
1.4 Thesis Overview 5

2 Organic Glass Scintillators 6

2.1 Inorganic and Organic Glasses 6
2.2 History of Organic Glass Scintillators (OGS) 7
2.3 Scintillation Process 8
2.4 OGS Properties from Literature 10
2.5 Use of OGS in this Work 12

3 A Handheld Dual Particle Imaging System 15

3.1 The OGS Handheld Dual-Particle Imager (H2DPI) 15
3.1.1 System Calibration 16
3.1.2 System Energy Resolution 20
3.1.3 Z-Position Reconstruction 21
3.1.4 Pulse Shape Discrimination 25
3.1.5 Neutron Light Output Response 27
3.1.6 Digitizer Board Timing Synchronization 30
3.2 Fast-Neutron Imaging Methodology 31
3.3 Gamma-Ray Imaging Methodology 34

3.4 Simple Backprojection Imaging . . . 34
3.5 List-Mode Maximum Likelihood Expectation Maximization . . . 37

4 Imaging and Spectroscopy Using the OGS H2DPI . . . 40

4.1 Single Source Neutron Imaging . . . 40
4.1.1 Bare ^{252}Cf . . . 40
4.1.2 Shielded ^{252}Cf . . . 42
4.1.3 ^{244}Cm . . . 48
4.2 Single Source Gamma-Ray Imaging . . . 50
4.2.1 ^{137}Cs . . . 50
4.2.2 ^{252}Cf . . . 52
4.2.3 ^{244}Cm . . . 54
4.2.4 ^{237}Np . . . 55
4.3 Multisource Imaging and Spectroscopy Capabilities . . . 59
4.3.1 Multisource Neutron Imaging and Spectroscopy . . . 59
4.3.2 Multisource Gamma-Ray Imaging and Spectroscopy . . . 63
4.4 Localization and Spectrometry of SNM Using OGS . . . 72
4.4.1 Highly Enriched Uranium (HEU) . . . 72
4.4.2 Plutonium . . . 85
4.5 Implications and Conclusions . . . 98
4.5.1 General Capabilities . . . 98
4.5.2 SNM Detection Performance . . . 98
4.5.3 Broader Implications . . . 99

5 Development of a Neutron Simulation Pipeline for Scatter-Based Imaging and Spectroscopy . . . 100

5.1 Motivation . . . 100
5.2 Simulation Pipeline Structure . . . 101
5.2.1 MCNPX-PoliMi . . . 101
5.2.2 MPPost . . . 102
5.2.3 Python Post-Processing Code . . . 104
5.3 Neutron Pipeline Validation . . . 109
5.3.1 Neutron Singles Response . . . 109
5.3.2 Neutron Spectroscopy Results . . . 111
5.3.3 Neutron Imaging Results . . . 115
5.4 Characterization of Coincidence Time Resolution (CTR) as a Function of Light Output . . . 120
5.4.1 CTR Experimental Setup . . . 121
5.4.2 Results of CTR Dependence on Light Output . . . 122
5.5 Implications . . . 124

6 Using Mixed Reality for the Real-Time Visualization of Imaging Data . . . 125

6.1 Motivation . . . 125
6.2 Mixed Reality Implementation . . . 126
6.2.1 Overview of Pipeline . . . 126

6.2.2 Real-Time Imaging in Mixed Reality . . . 128
6.2.3 Prototype Neural Network for Fast Source Searching . . . 131
6.3 Mock Inspection Scenario . . . 134
6.4 Implications . . . 137

7 Conclusions and Future Work . . . 138

7.1 Conclusions . . . 138
7.2 Future Work . . . 140
7.2.1 OGS Material Science . . . 140
7.2.2 H2DPI System Design . . . 141
7.2.3 H2DPI Simulation Pipeline . . . 141
7.2.4 Mixed Reality Visualization . . . 142

BIBLIOGRAPHY . . . 143

LIST OF FIGURES

FIGURE

2.1 Photograph of OGS compound. 8
2.2 Diagram showing energy levels of an organic molecule with π-electron structure. . . . 9
2.3 Photographs showing steps involved in the OGS casting process. 13
2.4 Example of a melt-cast sample of OGS in the shape of a bar. 13
2.5 Set of 12 OGS bars cast for the imaging system. 14

3.1 Top-down view schematic of the H2DPI layout. 16
3.2 Photographs of the active volume of the OGS H2DPI, illustrating support structures, spacers, and PCBs. 17
3.3 Calibrated $CeBr_3$ spectrum for ^{137}Cs and comparison of the polynomial calibration. . . 18
3.4 ^{137}Cs calibration point analysis for an OGS bar. 19
3.5 Demonstration of Compton edge calibration and resulting calibrated ^{137}Cs spectrum. . 20
3.6 Calibrated ^{137}Cs spectrum from $CeBr_3$ showing extraction of energy resolution at the 662 keV photopeak. 21
3.7 Coincidence ^{137}Cs spectrum from an OGS bar showing extraction of energy resolution using the 478 keVee Compton edge peak. 22
3.8 Photo of experimental setup for Z-position reconstruction characterization. 23
3.9 Z-position reconstruction function obtained for the twelve OGS bars in the H2DPI. . . 24
3.10 Average uncertainty in the position reconstruction as a function of interaction location along length of bars for the twelve OGS detectors in the H2DPI. Error bars are one standard deviation of the average values. 24
3.11 Average uncertainty in the position reconstruction for events at the center of the OGS bars as a function of light output. Error bars are one standard deviation of the average values from all twelve bars in the system. 25
3.12 Example PSD ratio plot with corresponding unique discrimination line shown for an OGS bar in the H2DPI. 27
3.13 Plot of proton stopping power in OGS from 1 eV and 25 MeV. 28
3.14 Measured light output vs recoil proton energy for an OGS bar with Birks' function. . . 30
3.15 Schematic diagram and photograph of the experimental setup used to evaluate inherent timing offsets in the H2DPI digitizer channels. 31
3.16 Histograms of time differences between channel 0 and other channels demonstrating the different degrees of timing offsets identified. 32
3.17 Simplified schematic of a neutron double scatter event in the OGS bars and the relevant metrics obtained. 33

3.18 Simplified schematic of a gamma-ray imageable event in the OGS bars and $CeBr_3$ cylinders, along with the relevant metrics obtained. 35
3.19 Schematic showing the H2DPI angular field of view, where azimuth (θ) and altitude (ϕ) directions are defined relative to the detector center (star marker) and $(0,\ 0)$ is indicated by the yellow arrow. 36
3.20 Example gamma-ray SBP image obtained with the OGS H2DPI of a ^{137}Cs source located at $(-26.6,\ 0)$. 37
3.21 Plots of MSSI and (1 - MSSI) metrics used to determine stopping criterion for LM-MLEM. 39
3.22 Example gamma-ray LM-MLEM image obtained with the OGS H2DPI of a ^{137}Cs source located at $(-26.6,\ 0)$. 39

4.1 Neutron SBP and Lm-MLEM images of bare ^{252}Cf. 41
4.2 Neutron SBP image of bare ^{252}Cf from 5 minutes of data acquisition. 42
4.3 Photograph of the experimental setup for the variable HDPE thickness series of measurements. 43
4.4 Neutron SBP image of ^{252}Cf shielded with 10.16 cm of HDPE. 44
4.5 Azimuth (θ) and Altitude (ϕ) angle distributions from neutron SBP images for various HDPE thicknesses. 45
4.6 Photograph of the experimental setup for the ^{252}Cf stored-source measurements. . . . 47
4.7 Neutron SBP image of ^{252}Cf in the TOP configuration. 47
4.8 Reconstructed SBP and LM-MLEM neutron images of ^{244}Cm. 49
4.9 Reconstructed SBP and LM-MLEM gamma-ray images of ^{137}Cs with 662 ± 37 keV energy gate. 51
4.10 Gamma-ray SBP and LM-MLEM images of ^{252}Cf. 53
4.11 Gamma-ray SBP image of ^{252}Cf reconstructed using 2210 events from 5 minutes of data collection. 54
4.12 Gamma ray coincidence spectrum from ^{244}Cm with a 140-160 keV energy gate and corresponding SBP and LM-MLEM images. 55
4.13 Gamma ray coincidence spectrum from ^{244}Cm with no applied energy gate and corresponding SBP and LM-MLEM images. 56
4.14 Photograph of the experimental setup for the ^{237}Np sphere measurement at the National Criticality Experiments Research Center. 57
4.15 Gamma-ray singles and coincidence spectra from ^{237}Np. 57
4.16 ^{237}Np LM-MLEM gamma-ray images produced using energy gates of 275 – 325 keV and 380 – 440 keV. 58
4.17 SBP and LM-MLEM gamma-ray images of ^{237}Np with no applied energy gates. . . . 59
4.18 Photograph of the experimental setup for the multisource neutron measurement. 60
4.19 Neutron SBP and LM-MLEM images of multisource neutron measurment. 61
4.20 Extracted neutron spectra from PuBe and ^{252}Cf sources. 62
4.21 Photograph of the experimental setup for the multisource gamma-ray measurement. . . 63
4.22 Gamma coincidence spectrum for the multisource gamma-ray measurement. 64
4.23 LM-MLEM gamma-ray images from the multisource gamma-ray measurement with various energy gates used. 65
4.24 Experimental setup for the ^{232}Th hemishell measurement. 66

4.25 Images and spread analysis for the ^{232}Th hemishell measurement with no energy gate applied. . . . 68
4.26 $CeBr_3$ gamma-ray energy spectra for the ^{232}Th and coincident spectra for the with various energy gates applied. . . . 69
4.27 Reconstructed SBP and LM-MLEM gamma-ray images of ^{232}Th with various energy gates applied. . . . 70
4.28 Reconstructed SBP and LM-MLEM gamma-ray images of the multisource neutron measurement with a 662 ± 37 keV energy gate applied. . . . 71
4.29 Photograph of the experimental setup for the HEU oxide measurement. . . . 73
4.30 Extracted gamma ray spectrum obtained from single events across all eight $CeBr_3$ and gamma coincidence spectrum between OGS and $CeBr_3$ for HEU oxide measurement . 74
4.31 SBP gamma-ray images of the HEU oxide measurement at 26 cones (4 minutes), 96 cones (15 minutes), 386 cones (1 hour), and 8777 cones (23 hours) . . . 75
4.32 Photograph of the experimental setup for the HEU metal measurement. . . . 75
4.33 Extracted gamma ray spectrum obtained from single events across all eight $CeBr_3$ and gamma coincidence spectrum between OGS and $CeBr_3$. . . . 76
4.34 Gamma-ray SBP and LM-MLEM images of HEU metal. . . . 77
4.35 Photographs of the experimental setup for the HEU interrogation measurements with AmLi at the National Criticality Experiments Research Center. . . . 78
4.36 Neutron singles response of the two HEU interrogation configurations. . . . 79
4.37 Neutron SBP and LM-MLEM of 14-kg HEU configuration. . . . 81
4.38 Neutron SBP and LM-MLEM of 10-kg HEU configuration. . . . 82
4.39 Reconstructed neutron energy spectra of the two HEU interrogation configurations. . . 83
4.40 Neutron SBP and LM-MLEM of 14-kg HEU configuration with increased imageable energy thresholds. . . . 84
4.41 Photographs of the experimental setups of the BeRP Ball and Thor core at the National Criticality Experiments Research Center. . . . 85
4.42 BeRP Ball gamma-ray spectroscopy spectra. . . . 86
4.43 Thor core gamma-ray spectroscopy spectra. . . . 86
4.44 Neutron and gamma-ray LM-MLEM images of the BeRP Ball. . . . 87
4.45 Neutron and gamma-ray LM-MLEM images of the Thor core. . . . 89
4.46 Measured neutron light output spectra for the plutonium metal and plutonium oxide samples. . . . 90
4.47 Comparison of simulated and measured neutron light output spectra for plutonium metal and plutonium oxide sources. . . . 91
4.48 Measured light output spectra for plutonium metal, plutonium oxide, and plutonium–beryllium sources. . . . 92
4.49 Photograph of the experimental setup for the plutonium oxide discrimination measurement at Lawrence Livermore National Laboratory. . . . 93
4.50 Extracted gamma ray spectrum from plutonium oxide discrimination measurement obtained from single events across all eight $CeBr_3$. . . . 94
4.51 Gamma coincidence spectrum between OGS and $CeBr_3$ from the plutonium oxide discrimination measurement. . . . 94
4.52 Gamma-ray SBP and LM-MLEM images of plutonium oxide discrimination measurement with energy gate of 300-475 keV applied to isolate plutonium in the FOV. . . . 96

4.53 Gamma-ray SBP and LM-MLEM images of plutonium oxide discrimination measurement with energy gate of 500-600 keV applied to isolate thorium in the FOV. 97

5.1 Geometry of the active volume and housing of the H2DPI shown using Gxsview. . . . 102
5.2 PSD ratio distribution for the light output range of 175–200 keVee. 106
5.3 Neutron removal percentages due to PSD in the twelve OGS bars in the H2DPI as a function of light output. 107
5.4 Photos of experimental setup used for validation of neutron simulation pipeline 110
5.5 Configuration-A neutron singles pulse integral distributions of ^{252}Cf from simulated (both ideal and processed) and measured data across all bars of the H2DPI. 111
5.6 Configuration-A reconstructed neutron energy spectra comparison for various simulated data sets and the measured response. 112
5.7 SBP neutron images from the simulated ideal, simulated processed, and measured data sets for configuration A. 117
5.8 SBP neutron images from the simulated ideal, simulated processed, and measured data sets for configuration B. 118
5.9 Configuration A angular distributions from SBP images for azimuth and altitude directions. 119
5.10 Configuration B angular distributions from SBP images for azimuth and altitude directions. 120
5.11 Photo and schematic of the experimental setup for CTR measurement. 122
5.12 ^{60}Co CTR results for OGS bars 3 and 4 as a function of light output. 123

6.1 Overview of the data processing from particle interactions to MR display. 127
6.2 Screenshot taken on the HoloLens 2 demonstrating the native spatial mesh. 128
6.3 Examples of the mixed reality visuals as seen by the user wearing the HoloLens 2. . . 130
6.4 Screenshot taken on the HoloLens 2 demonstrating application of energy gate on the coincidence gamma-ray spectrum in real-time. 131
6.5 Overview of the training data generation for the source direction prediction using a neural net. 133
6.6 Diagnostic plots of neural network training. 134
6.7 Examples of the MR visuals as seen by the user wearing the HoloLens 2 for the fast source direction estimate using a neural net. 134
6.8 Experimental setup for the mock inspection scenario demonstration. 135
6.9 Screenshot taken on the HoloLens 2 demonstrating the final converged source locations for both imaging modes. 136
6.10 Screenshot taken on the HoloLens 2 demonstrating the agreement between the MR visuals and true source locations in physical space. 136
6.11 Screenshots taken on the HoloLens 2 demonstrating gamma-ray and neutron live-time spectroscopy visuals. 136

LIST OF TABLES

TABLE

2.1 Summary of scintillator properties comparing different geometries of OGS, EJ-309, EJ-276, and stilbene samples. 11

3.1 Summary of characterized channel timing offsets for the OGS H2DPI 33

4.1 Summary of spread in neutron SBP images with increasing HDPE. Measurement times used to achieve equal number of imageable events are also noted. 44
4.2 Summary of emissions of interest for gamma-ray imaging of ^{232}Th 64

5.1 Summary of agreement with measured spectrometry response of configuration A for the various components of the simulation analysis. 114
5.2 Expected angles using weighted mean of results from configuration A. Uncertainties represent the standard deviation (σ) derived from a Gaussian fit of the angular distribution. 119
5.3 Expected angles using weighted mean of results from configuration B. Uncertainties represent the standard deviation (σ) derived from a Gaussian fit of the angular distribution. 120
5.4 Summary of Equation 5.3 model parameters for CTR experiment. 124

ABSTRACT

The ability to precisely detect, localize, and characterize special nuclear material (SNM) is crucial in the verification of nuclear treaties and emergency response operations. SNM emits distinctive neutron and gamma-ray signatures, serving as key indicators of nuclear weapons or other nuclear materials. Yet, standard inspection or emergency environments often preclude the use of large, stationary instrumentation, underscoring the need for compact, human-portable imaging systems that deliver accurate localization and high-quality spectroscopy, even in complex and dynamic scenarios.

To address these challenges, this work leverages the unique properties of organic glass scintillators (OGS) for dual-particle imaging applications. Historically, trans-stilbene was considered the gold standard for compact neutron imagers due to its exceptional pulse shape discrimination capabilities. However, its mechanical instability, especially its tendency to crack with temperature variation, along with manufacturing complexity, high cost, and discontinuation from mass production, have necessitated the development of alternative solutions. OGS offers a distinct advantage, combining the high light output, good timing properties, and pulse shape discrimination comparable with that found in stilbene with the melt-castability and scalability of plastic scintillators. Furthermore, by replacing bulky and fragile photomultiplier tubes with silicon photomultipliers, the form factor of scintillator-based systems can be kept compact while maintaining robust timing and gain characteristics.

In this thesis, the development and characterization of the OGS Handheld Dual-Particle Imager is presented. The system utilizes an array of OGS bars and $CeBr_3$ cylinders to enable neutron and gamma-ray imaging through double-elastic scatter reconstruction and Compton scatter/photoelectric absorption sequencing, respectively. Imaging and spectroscopy results presented

in this thesis are based on experiments using a diverse array of sources, including ^{252}Cf, ^{244}Cm, ^{137}Cs, ^{22}Na, ^{232}Th, and ^{237}Np. Crucially, measurements on highly enriched uranium and weapons-grade plutonium were conducted to demonstrate the capability to localize and spectroscopically characterize SNM within the field of view. A custom simulation pipeline utilizing MCNPX-PoliMi is developed and validated against experimental results, providing accurate modeling of the neutron imaging and spectroscopy responses of the imager. Finally, a novel mixed reality framework is introduced, using the Microsoft HoloLens 2 headset to visualize 2D angular imaging data into intuitive holographic overlays in 3D space, thereby significantly enhancing the operator's real-time interpretation of radiation source locations and spectra.

CHAPTER 1

Introduction

1.1 Motivation

1.1.1 A Historical Overview

The use of nuclear weapons in the late 1940s firmly ushered in the atomic age and underscored the urgent need to safeguard the world from the misuse of nuclear technology. This concern was evident early on, as demonstrated by President Eisenhower's 1953 Atoms for Peace speech [1], which marked an initiative to foster international cooperation in peaceful nuclear uses. Soon after, the International Atomic Energy Agency (IAEA) was established in 1957 by the United Nations to encourage peaceful applications of nuclear technology while preventing proliferation, with an explicit mandate to implement safeguards [2]. A major milestone in nuclear security was reached in 1970 with the creation of the Treaty on the Non-Proliferation of Nuclear Weapons, which has become the cornerstone of international efforts to prevent the spread of nuclear weapons [3]. Under one component of the treaty, non-nuclear-weapon states commit not to pursue nuclear weapons and to accept IAEA safeguards on their nuclear activities, while nuclear-weapon states pledge to pursue disarmament. Finally, the Comprehensive Nuclear-Test-Ban Treaty was adopted in 1996 by the United Nations General Assembly [4] to prohibit any nuclear weapon test explosion or any other nuclear explosion. Although the treaty has not entered into force to this day, it has significantly contributed to limiting nuclear weapons testing globally and enabled the establishment of the International Monitoring System [5] for worldwide verification.

1.1.2 Modern Status and Needs of Nuclear Safeguards and Nonproliferation

Despite the extensive history of nuclear safeguards and nonproliferation, ongoing efforts remain essential to curtail the spread of nuclear weapons in the modern era. For instance, the New Strategic Arms Reduction Treaty [6], signed in 2010 by the United States and Russia, established limits on deployed strategic nuclear warheads and delivery systems. With this treaty set to expire in February 2026, the absence of an agreed-upon replacement or extension could put contemporary nonproliferation norms at risk. The negotiation and success of future treaties and agreements will be contingent upon the development and deployment of robust technology and effective detection systems. The U.S. administration has also been advised to consider that non-deployed and non-strategic weapons also be included in future nuclear arms control treaties [7]. As new requirements emerge, the challenges in nuclear nonproliferation increase in scope and become more critical, meaning that radiation detection systems likewise need to adapt. This evolution demands greater reliability and sophistication to meet updating objectives of global security.

For the purposes of this work, special nuclear material (SNM) is defined in accordance with the U.S. Nuclear Regulatory Commission as plutonium, ^{233}U, and uranium enriched in the isotope ^{235}U [8]. Enriched uranium includes anything above the 0.72% natural abundance of ^{235}U but common conventions define material enriched to less than 20% ^{235}U as low-enriched uranium and highly enriched uranium for 20% or greater. However, SNM is not the only material of interest for contemporary detection efforts. For example, ^{237}Np is notable due to its role as a signature of nuclear reactor irradiation [9], where its presence may indicate clandestine operations. ^{232}Th is a fertile isotope that has historically been considered a potential nuclear fuel [10], offering an alternative fuel cycle to traditional uranium-based approaches that would have new safeguard considerations. From an academic standpoint, ^{244}Cm has attracted interest for potential use in thermoelectric generators [11] and as a replacement for ^{252}Cf in characterization and calibration work [12]; however, this isotope is produced in nuclear power reactors and must be extracted from spent fuel.

1.2 Role of Dual-Particle Imaging in Nuclear Safeguards and Nonproliferation

Generally, radioactive materials will release energy during their radioactive decay processes in the form of beta particles, alpha particles, photons, and neutrons. Of these detectable emissions, neutrons and photons are the most useful in measurement applications due to their relatively long ranges in matter and ability to serve as unique signatures of source materials. An important property of SNM is its emission of both neutrons and gamma rays, either passively or in response to interrogation, with the specific emission profile depending on isotopic composition. Some of the previously deployed systems for SNM detection include ^{3}He-based systems [13], high-resolution gamma spectrometers [14], and active interrogation technologies [15, 16]. More recently, gamma-ray and neutron imaging systems have been developed and deployed for a variety of safeguard and nonproliferation efforts [17, 18], often in conjunction with non-radiation detection methods [19].

Imaging systems play a critical role in radiation detection by delivering both precise source localization and detailed spectroscopic information, making them essential for tasks such as nuclear material identification, threat assessment, and environmental monitoring. An application where imaging is especially advantageous is in search scenarios because traditional counting-based systems are subject to systematic uncertainty due to background fluctuations and variability since imagers are not subject to the background in the same way since different metrics are used. Most existing technologies are designed for the singular detection and imaging of either gamma rays [20] or fast neutrons [21]. However, it is important to note that the characteristic gamma rays emitted for identification of SNM and other materials can be effectively shielded with relatively small amounts of high atomic-number material. Conversely, neutrons require substantial amounts of hydrogen-rich material, such as high-density polyethylene, to achieve similar attenuation [22]. This fact implies that a deployed imaging system may be rendered ineffective if a party chooses to deliberately shield the relevant particle type. The significance and potential of dual-particle imaging systems has been identified in the literature, with examples ranging from large-scale [23, 24, 25] to

compact system designs [26, 27]. Systems capable of simultaneously detecting both gamma rays and fast neutrons possess significant value, because obscuring radioactive materials that emit both signatures, such as SNM, becomes markedly more challenging without conspicuous, multilayered shielding, which itself could raise suspicion under certain circumstances.

1.3 Contributions of this Work

The primary objective of this dissertation was to demonstrate the effectiveness of organic glass scintillators in dual-particle imaging applications, thereby expanding the range of potential options of deployable detection systems for safeguard and nonproliferation applications. In order to meet this objective, a compact imaging system composed of an array of organic glass and inorganic scintillators coupled to silicon photomultipliers was developed [28]. Experiments established successful imaging of single gamma-ray and neutron sources, as well as simultaneous multisource imaging within the instrument's field of view. Further experimental work demonstrated accurate localization and spectroscopy of SNM, including highly enriched uranium [29, 30] and weapons-grade plutonium [31, 32].

Simulation validation of the organic glass imager was also conducted to evaluate system performance and capabilities. A dedicated simulation pipeline was developed to accurately model neutron imaging and spectroscopy responses [33]. Comprehensive system characterization allowed simulation results to demonstrate close agreement between simulated and experimentally measured results for both spectroscopy and imaging. Notably, coincident timing resolution was investigated to determine the timing uncertainty of the imager as a function of scintillation light output, revealing a strong correlation between these parameters. The full-width-at-half-maximum for coincident timing resolution was found to vary significantly, ranging from approximately 650 ps at low scintillation light yields to an improved 120 ps at high light yields [34].

To further demonstrate the effectiveness of organic glass in imaging applications, the first field-deployable mixed reality visualization approach for dual-particle imaging was developed with the

Microsoft HoloLens 2 headset [35]. A custom Unity-based application was designed to integrate recorded data from the imaging system with the native spatial mapping capabilities of the HoloLens, enabling real-time source localization and spectroscopy. Unlike conventional 2D methods, this approach allows users to intuitively interpret and interact with spatial radiation source locations and spectra directly within their physical environment, dramatically enhancing situational awareness and decision-making during radiation measurements. As a proof of concept, a mock inspection scenario experiment was conducted to showcase the ability of the system to identify both the presence and absence of radioactive sources, distinguish between neutron and gamma sources, and perform concurrent spectroscopy [36].

1.4 Thesis Overview

This dissertation presents the development and characterization of a handheld organic glass imaging system that can help address the motivations described in Chapter 1. Chapter 2 introduces organic glass scintillators by detailing their recent advancements, discussing how these materials were utilized in this work, and summarizing important detector properties as reported in the literature. Chapter 3 details the development of the imaging system, while also outlining the concepts of fast-neutron and gamma-ray imaging used for the work. Chapter 4 evaluates the imaging capabilities of the system using standard radiation sources and further demonstrates system performance with a range of special nuclear material experiments. Chapter 5 details the creation of a simulation pipeline that models the neutron response of the imager in both spectroscopy and imaging. Chapter 6 proposes a new mixed-reality approach for visualizing imaging data, allowing for a wider array of potential users. Finally, Chapter 7 concludes the dissertation with recommendations for future research and a discussion of the broader implications of this work.

CHAPTER 2

Organic Glass Scintillators

2.1 Inorganic and Organic Glasses

Generally, glasses are amorphous solids and can be found in both inorganic and organic forms. Inorganic glasses are essential for numerous modern applications, including glass fiber cables used in communications, metallic glasses in medical technologies, and soda-lime glasses used for windows and bottles. Organic glasses, by contrast, show promise for radiation detection applications. The most common form of organic glass is thermoplastic polymer, which features covalently bonded, physically entangled chains composed of high-molecular-weight materials [37]. While these glasses are quite stable, their high molecular weight variability leads to compromised scintillation performance [38]. Fortunately, organic glasses can also be manufactured as molecular (monomeric) organic glasses. These materials are composed of individual, small-sized molecules with well-defined chemical structures, enabling precise control over their properties. As a result, molecular organic glasses can be tuned for specific applications ranging from enhancing charge transport properties [39] to scintillators [40].

One of the main challenges associated with molecular organic glasses is designing compositions that maintain long-term stability [41]. This challenge arises because small organic molecules reach thermodynamic equilibrium more rapidly, often resulting in a transition from the amorphous state to more ordered crystalline phases within the sample. This phenomenon is particularly critical for molecular glasses intended for scintillation applications in radiation detection, as the bulk

sample must retain high transparency across the expected optical path lengths. Ongoing research is addressing these stability issues by employing strategies such as incorporating bulky substituents, reducing molecular symmetry, restricting planarity, increasing molecular size, and creating physical blends of different molecules [37, 42, 43, 40].

2.2 History of Organic Glass Scintillators (OGS)

The first reported case of OGS in the literature was by Downs and Smith in 1958 [44], where triphenyl-p-biphenylyl-silane was converted into a glass by heating it to $120\,^{\circ}\mathrm{C}$ and poured into a nickel mold. The resulting OGS exhibited a gamma-ray light output of 60–75% compared to an anthracene reference crystal and a primary scintillation decay time of approximately 20 ns. While these properties appear promising with no context, several contemporary factors limited the practicality of OGS at the time [37]. Widespread materials such as polyvinyl toluene were already available, some plastic scintillators exhibited superior scintillation properties compared to the OGS sample, and plastics offered substantially greater stability. As a result, it is unsurprising that OGS development saw little to no progress in the literature over the following 58 years.

In 2016, Carlson and Feng from Sandia National Laboratories advanced the field of organic glass scintillators by reporting on compounds based on alkyl- and arylsilane structures functionalized with 9,9'-alkylfluorene chromophores [40]. One of the compounds in the study, bis(9,9-dimethylfluoren-2-yl)diphenylsilane, became a representative case study for subsequent OGS characterization in ongoing research. Figure 2.1 shows a photograph of the synthesized material alongside a schematic of the molecule's structure. Today, OGS materials are commercially available in a variety of compositions, ranging from pure forms [45] closely related to Carlson and Feng's original work, to tin-loaded variants designed to enhance gamma-ray spectroscopy performance [46]. Additionally, Sandia National Laboratories is exploring OGS formulations that incorporate mechanically blended pre-polymerized plastics to improve mechanical robustness [47].

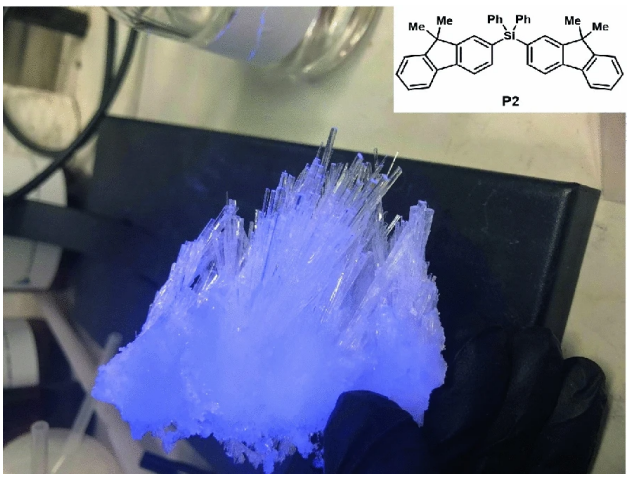

Figure 2.1: Photograph of the bis(9,9-dimethylfluoren-2-yl)diphenylsilane OGS compound synthesized at Sandia National Laboratories [37].

2.3 Scintillation Process

All organic scintillators undergo similar primary processes of excitation and ionization prior to the generation of scintillation light. According to the seminal work by Birks, these processes are: excitation into excited π-electron singlet states, ionization of π-electrons, direct excitation of σ-electron and carbon 1s electron excited states, and ionization of electrons other than π-electrons [48]. The first two processes predominantly determine scintillation yield, with excitation into π-electron singlet states accounting for the majority of light production. In contrast, the latter two pathways result in nonradiative de-excitation, which does not contribute to scintillation emission, but instead leads to energy loss through mechanisms such as heat. These radiationless de-excitation pathways are collectively referred to as quenching.

Figure 2.2 presents a schematic diagram illustrating π-electrons energy levels, intended to facilitate discussion of singlet and triplet states. When radiation interacts with an organic scintillator, energy may be absorbed, exciting the electron configurations of detector molecules into a variety of excited states. In Figure 2.2, singlet states are denoted S_0, S_1, S_2, ..., while triplet states are indicated as T_1, T_2, T_3, ... The principal scintillation light, termed prompt fluorescence, is produced during transitions from the S_{10} state to one of the vibrational states within the ground electronic

state S_{0X}. It is important to note that in organic molecular glasses, excitation into singlet states still occurs, but is accompanied by additional energy transfer steps, most notably Förster Resonance Energy Transfer (FRET) [49]. FRET encompasses the transfer of excited state electronic energy from a donor molecule to an acceptor molecule via a dipole–dipole coupling mechanism [50]. Consequently, efficient FRET is critical for optimizing OGS compositions.

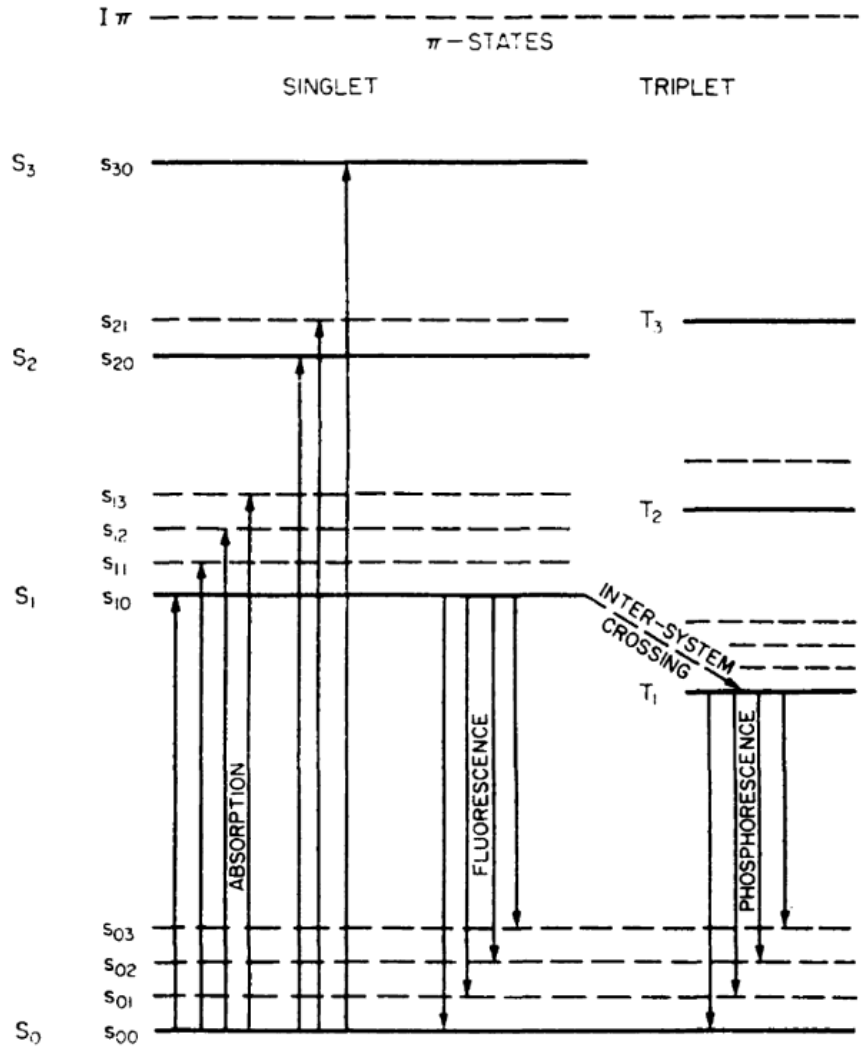

Figure 2.2: Diagram showing energy levels of an organic molecule with π-electron structure [48].

Following the ionization of π-electrons, ion recombination results in the population of both singlet and triplet excited states. Excited singlets produced through π-electron ionization contribute to fluorescence, thereby augmenting the prompt scintillation response initially generated

from direct excitation into π-electron singlet states. Excited singlet states may then undergo a transition in which singlet states are converted into triplet states called intersystem crossing [22]. This mechanism is particularly prevalent in organic scintillators, although direct excitation by energetic charged particles can also produce triplet states. The lifetime of the first triplet state T_1 is typically much longer than that of the singlet state S_1, and triplet excited states formally cannot decay to the ground state due to spin-parity rules. While in the T_1 state, some molecules may thermalize back to the S_1 state, and subsequently decay through the normal fluorescence pathway. This process is referred to as delayed fluorescence.

If triplet states do not undergo thermalization, they may interact with each other and annihilate, provided the triplet excitation density is sufficiently high. This process, called Triplet-Triplet Annihilation (TTA), occurs by Dexter energy transfer [51], which requires triplet wavefunction overlap. TTA contributes to the delayed component of the scintillation response and is fundamental to enabling pulse-shape discrimination techniques, which will be discussed in Chapter 3. The efficiency of TTA is influenced by the mobility and lifetime of the triplet excited states, both of which are strongly dependent on the molecular structure and electronic properties of the scintillator. For completeness, it should be noted that de-excitation from T_1 to S_0 produces a significantly delayed light emission known as phosphorescence. In organic scintillators, phosphorescence is typically suppressed or negligible, and is generally undesirable due to its long emission timescale.

2.4 OGS Properties from Literature

Because OGS materials from Sandia National Laboratories are novel within the field of radiation measurements, a range of published studies have explored their properties and performance. The original work by Carlson and Feng demonstrated that a 2.54 cm diameter sample made from 2 g of bis(9,9-dimethylfluoren-2-yl)diphenylsilane achieved a ^{137}Cs relative light yield 62% of a trans-stilbene scintillator of comparable dimensions [40]. Furthermore, when doped with the wavelength shifter bis-MSB at a concentration of 0.07 wt%, the light yield increased to 14% more relative to

trans-stilbene.

Subsequent collaborative studies validated OGS performance through direct comparisons of 5.08 cm × 5.08 cm cylinders made from EJ-309, a widely used liquid scintillator, EJ-276, a commercially available pulse shape discrimination-capable plastic scintillator, and Sandia OGS. As summarized in Table 2.1, OGS exhibited higher light yield than both EJ-309 and EJ-276 when irradiated with ^{137}Cs. Additional research compared 2.54 cm × 2.54 cm cylinders of trans-stilbene, EJ-276, and Sandia OGS, focusing on several key scintillator properties: 10–90 rise times (time it takes for a waveform to transition from 10% of its peak to 90% of that level), coincidence time resolutions at 325 keV, and luminosity, the results of which are also presented in Table 2.1. OGS outperformed its counterparts in all categories except for rise time, where its timing was comparable to the fastest response observed from EJ-276. In terms of neutron detection, studies with 5.08 cm × 5.08 cm cylinders found that OGS provided higher scintillation light output relative to trans-stilbene across the neutron energy range of 0.79–4.57 MeV. The neutron light output response of OGS resulted in an 11.92% greater intrinsic neutron detection efficiency than trans-stilbene over the light output range of 0.06–2.40 MeVee [52]. The initial characterization of OGS suggested that the material was well suited as a substitute for state-of-the-art detector systems involving neutron and gamma-ray detection.

Table 2.1: Summary of scintillator properties comparing different geometries of OGS, EJ-309, EJ-276, and stilbene samples in literature [53, 54].

Scintillator	**Geometry (cm)**	**Relative Light Yield (vs. OGS, %)***	**10–90 Rise Time (ns)**	**Coincidence Time Resolution at 325 keV (ps)**	**Luminosity (photons/MeV)**
OGS	5.08×5.08	100	-	-	-
EJ-309	5.08×5.08	70	-	-	-
EJ-276	5.08×5.08	50	-	-	-
OGS	2.54×2.54	-	0.82	200	15821
EJ-276	2.54×2.54	-	0.81	325	5522
Stilbene	2.54×2.54	-	1.01	325	13054

* Relative light yield under ^{137}Cs irradiation.

2.5 Use of OGS in this Work

The work presented in this dissertation utilized OGS synthesized by the team at Sandia National Laboratories. The composition was a 90:10 mixture of bis(9,9-dimethyl-9H-fluoren -2-yl)diphenylsilane ($C_{42}H_{36}Si$) and phenyltris(9,9-dimethyl-9H-fluorene-2-yl)silane ($C_{51}H_{44}Si$). To better align with photodetector sensitivity, an additional 0.2 wt% of the wavelength shifter 1,4-bis(2-methylstyryl)benzene (bis-MSB, $C_{24}H_{22}$) was incorporated into the mixture. All OGS samples were cast at the University of Michigan. Figure 2.3 illustrates the steps involved in the OGS casting process. First, the OGS material received from Sandia is heated with a hotplate and heat gun to $200\,^{\circ}\mathrm{C}$, transitioning from a solid to a liquid with a viscosity similar to water. Next, the vial is connected to a vacuum system for degassing at pressures below 10 torr. This degassing step is crucial to remove trapped air, preventing the formation of microscopic voids in the final OGS sample. Finally, OGS is poured into a silicon mold of the desired shape and placed in a temperature-controlled oven to cool gradually over a 14-hour period. The slow cool-down period helps reduce the development of internal stresses in a sample. The OGS detectors can then be removed from the mold and utilized as shown in Figure 2.4.

The imaging system developed for this dissertation utilized 12 OGS bars cast according to the described process. Figure 2.5 shows the completed set of bars, each wrapped in Teflon to enhance light collection. It is important to note that the OGS bars used in this work were kept bare, with no surface coating or film applied. At the time of system development, best practices for OGS surface stabilization were not yet widely recognized. Contemporary OGS samples now typically include a thin coating of polyvinyl alcohol and/or optical-grade epoxy, which helps stabilize surface molecules and inhibit crystallization at the glass surface, thereby extending the long-term performance of the amorphous solid [55]. Chapter 3 will continue with a discussion of the imaging system design and the basic performance characteristics of the OGS bars.

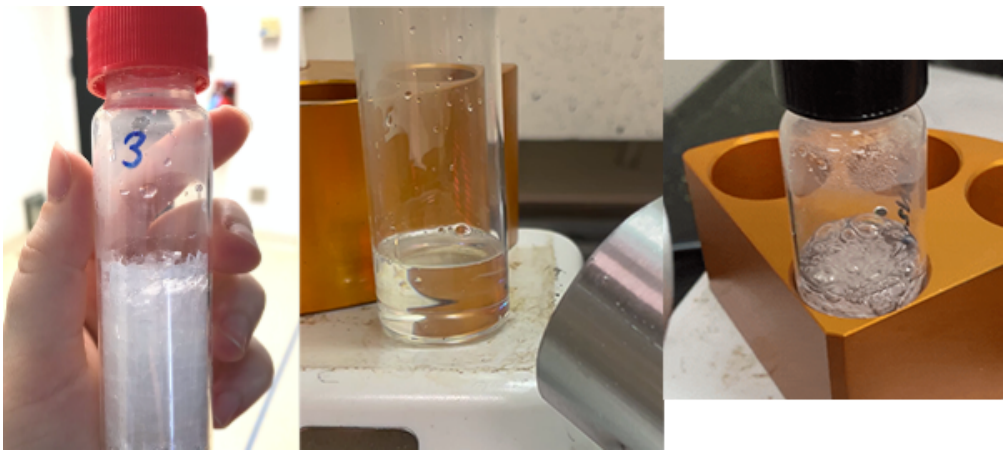

Figure 2.3: Photographs showing steps involved in the OGS casting process. Notably, OGS material is melted down and degassed under vacuum.

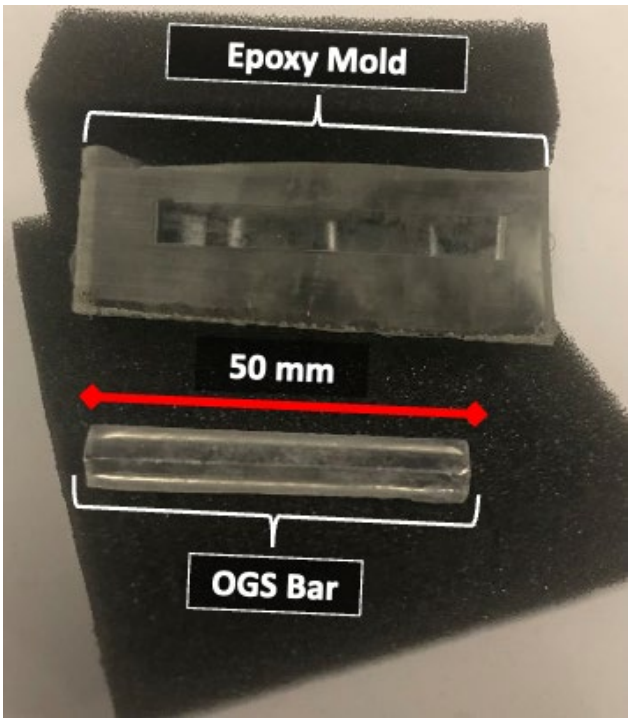

Figure 2.4: Example of a melt-cast sample of OGS in the shape of a bar. The epoxy mold used is also shown for reference.



Figure 2.5: Set of 12 OGS bars cast at the University of Michigan. Bars were covered in a Teflon wrapping to improve the light collection efficiency and only open at the top and bottom ends.

CHAPTER 3

A Handheld Dual Particle Imaging System

3.1 The OGS Handheld Dual-Particle Imager (H2DPI)

The imaging system presented in this dissertation, hereafter referred to as the H2DPI, was developed at the University of Michigan and consists of an array of organic glass and $CeBr_3$ scintillators. Its design is based on a previous iteration of a compact imaging system that utilized trans-stilbene detectors [26]. Detector placement was primarily optimized to enable gamma-ray imaging capabilities while maintaining maximum neutron imaging efficiency. Through simulation studies in previous work, the array configuration shown in Figure 3.1 was identified as optimal, achieving intrinsic neutron and gamma-ray efficiencies of approximately 0.1% and 0.013%, respectively [56]. The rationale for transitioning from stilbene to OGS detectors for the H2DPI will be demonstrated throughout the system characterization presented in this chapter.

The glass-based H2DPI consists of twelve OGS bars (6 mm × 6 mm × 50 mm) wrapped in white polytetrafluoroethylene (Teflon) tape, serving as a diffuse reflector to enhance light collection. The 6×6 mm^2 cross-sectional area of the bars was determined by the pixel dimensions of the silicon photomultiplier arrays employed. To further improve gamma-ray imaging efficiency, the system incorporates eight encapsulated cylindrical $CeBr_3$ crystals. The $CeBr_3$ crystals are hermetically sealed in aluminum, feature a single glass window, and measure 6 mm in both diameter and height. The bars and cylinders are optically coupled between two 64-pixel ArrayJ-60035-64P-PCB Onsemi silicon photomultiplier (SiPM) arrays [57], using 0.5 mm thick silicone rubber EJ-560 op-

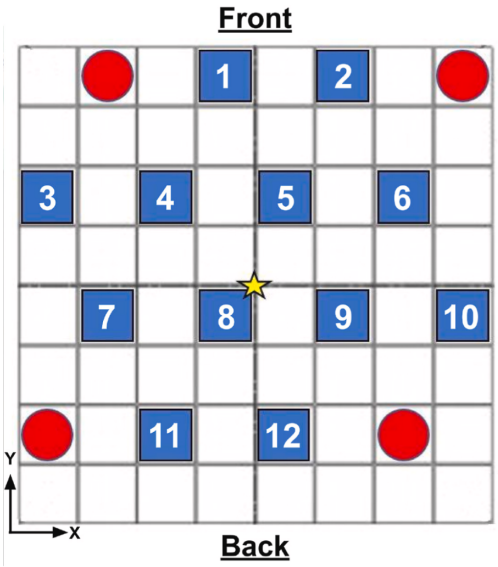

Figure 3.1: Top-down view schematic of the H2DPI layout. Numbered squares represent organic detectors while the red circles represent inorganic detectors. Note that each circle represents two detectors as they are stacked on top of one another in the z-axis. The star marker represents the center of the system.

tical interface pads cut to 6 mm squares. The $CeBr_3$ detectors are held firmly against the coupling surface by small compression springs within the inorganic detector housings. Custom-built printed circuit boards (PCBs) are used to apply voltage bias and to facilitate signal readout from the SiPM arrays [58]. The output signals are routed to a pair of v1730 CAEN digitizers [59], which offer 14-bit resolution, a 500 MHz digitization rate, and a 2 V dynamic range. The SiPMs are powered with an applied voltage of 29.6 V using a Keysight E3649A low voltage dual-output power supply [60] to ensure stability during operation. Figure 3.2 provides images of the active volume of the H2DPI. In total, the system comprises 32 output channels: 24 assigned to the OGS bars and 8 to the $CeBr_3$ detectors. Data acquisition is achieved using the CAEN multi-parameter spectroscopy (CoMPASS) software [61].

3.1.1 System Calibration

The OGS and $CeBr_3$ detectors in the H2DPI are primarily calibrated using a ^{137}Cs source. Calibration of the $CeBr_3$ detectors is particularly straightforward due to their photoelectric absorption ca-

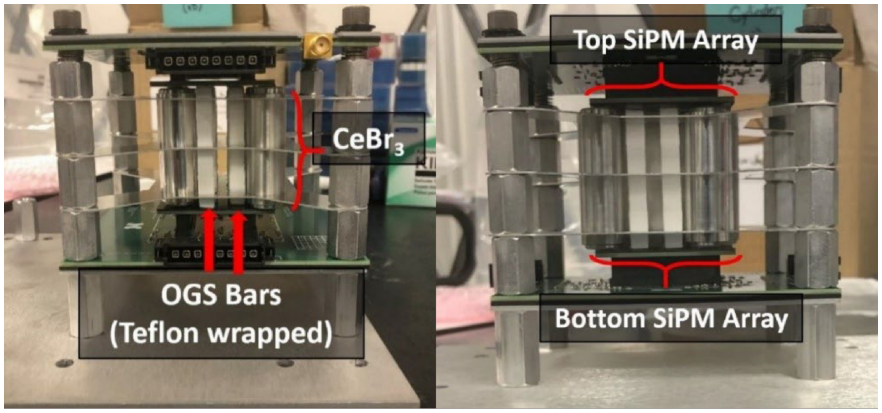

Figure 3.2: Photographs of the active volume of the OGS H2DPI, illustrating support structures, spacers, and PCBs.

pabilities, which result in photopeaks in the measured spectra. For ^{137}Cs calibration, three spectral features are of interest: the photopeak at 662 keV, the Compton edge at 478 keV, and a backscatter peak at 184 keV. Figure 3.3 presents an example of a calibrated $CeBr_3$ spectrum from one of the detectors within the H2DPI, with the relevant features highlighted. For $CeBr_3$ calibration, this work employs a second-order polynomial fit of the form,

$$Ax^2 + Bx + C. \tag{3.1}$$

Figure 3.3 also compares the results of this polynomial fit with those from a linear fit using only the photopeak, illustrating differences in calibration values at lower and higher energies. It is important to note that the current iteration of the H2DPI system lacks any methods of temperature control. The inability to keep the SiPMs at a constant temperature is significant, as SiPMs exhibit a temperature dependence in their gain, stemming from changes in breakdown voltage due to temperature variations [57]. To mitigate this effect, calibrations are performed both at the beginning and end of each measurement sequence. Linear interpolation is then applied to correct calibration factors across the dataset, compensating for any drift arising from temperature changes, which typically manifest as increases due to the operation of the SiPMs and associated electronics within the box housing the H2DPI.

Calibration of the OGS bars is straightforward, as the Compton edge is typically the sole dis-

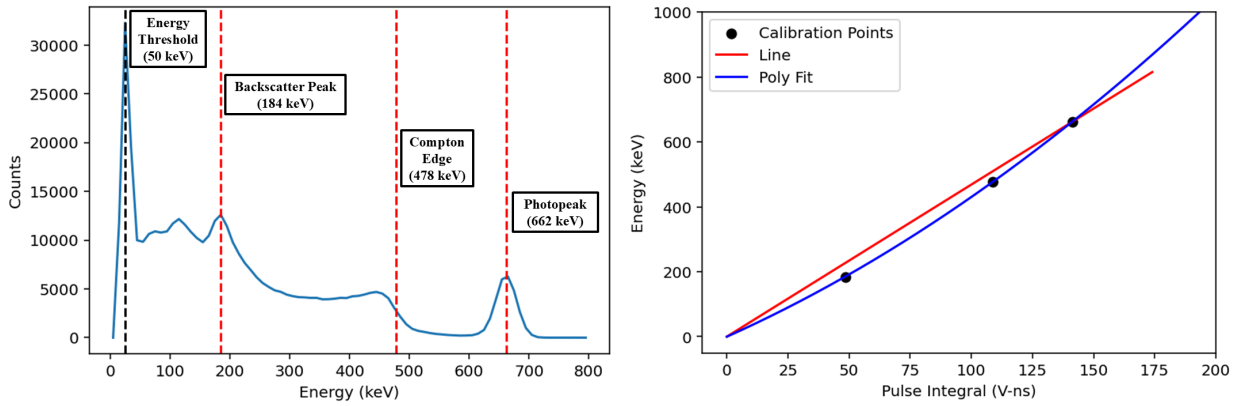

Figure 3.3: Calibrated $CeBr_3$ spectrum for ^{137}Cs with the features of interest noted with red dashed lines (left). Comparison of a polynomial calibration used for the ^{137}Cs measurement with a linear fit using just the photopeak (right).

cernible feature within the measured spectra. A critical aspect of this characterization, however, involves determining the precise location of the true Compton edge along the falling edge of the measured spectrum. To accomplish this, a calibration methodology adapted from previous work [62] was applied to establish suitable calibration points for OGS bars in the H2DPI. The process begins with an unbroadened simulation of a ^{137}Cs source to generate the gamma-ray response data for a given OGS bar. Next, a light output-broadened simulation is performed to best match the measured detector response. The following light output broadening function [63] is utilized in this analysis:

$$\Delta L = L\sqrt{\alpha^2 + \frac{\beta^2}{L} + \frac{\gamma^2}{L^2}}, \tag{3.2}$$

where ΔL is the light output full width at half maximum (FWHM), L is the light output for an event in MeVee, and α, β, and γ are fitting coefficients that account for the effects of light transport efficiencies, counting statistics, and electronic noise, respectively, on the detector resolution. A brute-force approach is employed to determine the optimal set of fitting coefficients. The intersection point between the unbroadened and broadened simulated spectra is then identified, and the calibration point for the measurement data is defined as the fraction of the Compton edge height corresponding to this intersection. Figure 3.4 presents this analysis for one of the OGS bars in

the H2DPI, where a calibration point of 63.1% was obtained. These fractional edge calibration points for OGS are consistent with those observed for trans-stilbene bars of identical form factor and readout configuration from the previous H2DPI [64], suggesting comparable energy resolution performance. Figure 3.5 presents a diagnostic plot illustrating the process of identifying the calibration point corresponding to the Compton edge from a measured spectrum. Fitting procedures are employed to accurately determine the pulse integral value at the specified fractional edge position. In addition, Figure 3.5 displays an example of a calibrated OGS ^{137}Cs light output spectrum from one of the bars within the H2DPI.

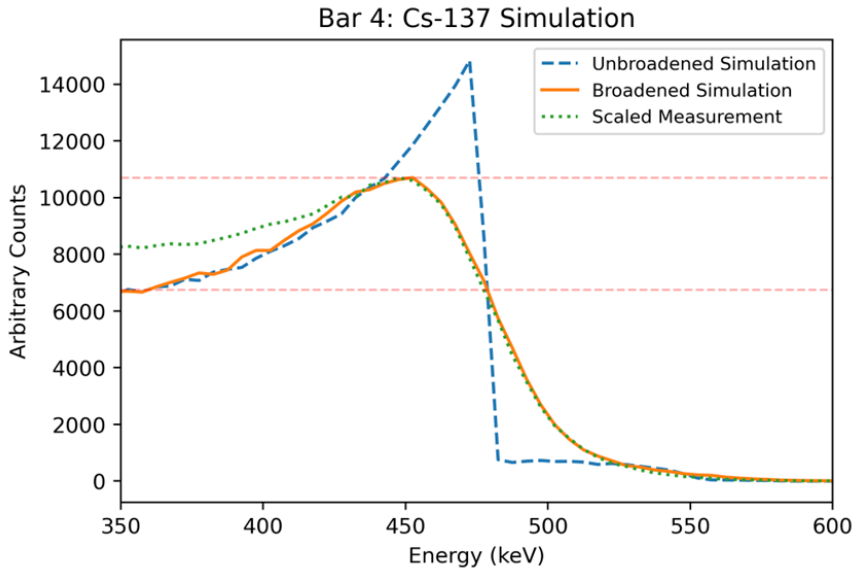

Figure 3.4: ^{137}Cs calibration point analysis for an OGS bar. The blue dashed line shows the simulated pulse integral distribution without broadening. The solid orange and dotted green lines show the broadened simulation and measured distributions.

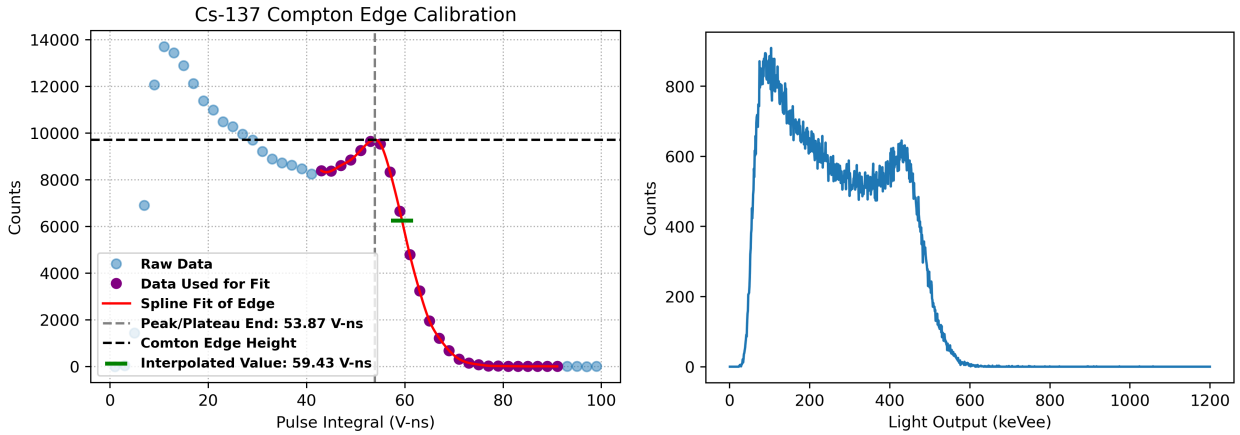

Figure 3.5: Diagnostic plot illustrating the identification of the calibration point corresponding to the Compton edge from a measured OGS gamma spectrum (left). Example of a calibrated OGS ^{137}Cs light output spectrum from one of the bars within the H2DPI (right).

3.1.2 System Energy Resolution

Energy resolution is defined as:

$$\text{Resolution } (\%) = \frac{\text{FWHM}}{E_0} \times 100, \tag{3.3}$$

where FWHM represents the full width at half maximum of a given photopeak at energy E_0. Equation 3.3 is therefore used to calculate the energy resolution of a $CeBr_3$ cylinder. Figure 3.6 shows a calibrated ^{137}Cs spectrum from a H2DPI $CeBr_3$, in which the energy resolution at 662 keV was determined to be $6.0 \pm 0.1\%$.

Determining the energy resolution of OGS is somewhat more complex, owing to the low probability of gamma rays below 1 MeV undergoing photoelectric absorption, which would produce a distinct photopeak. Instead, the dominant interaction, Compton scattering, must be leveraged. Historically, coincident Compton scatter measurements have been employed to obtain suitable peaks for energy resolution analysis [65]. In this work, a simple measurement was performed using a ^{137}Cs source and two OGS bars in the H2DPI, with the source aligned along a collinear set of bars (e.g., bars 3 and 4 in Figure 3.1). By applying a coincidence timing window of 2 ns, a spectrum

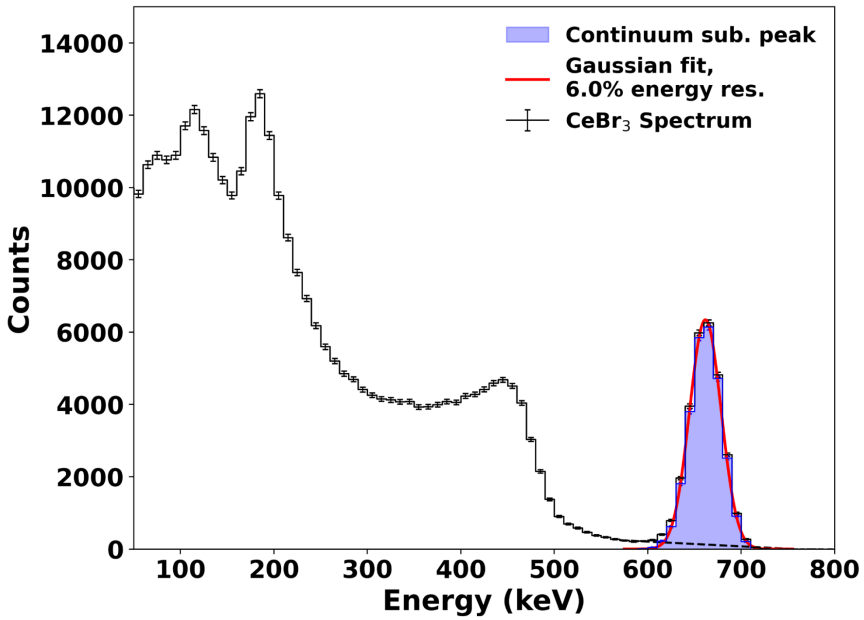

Figure 3.6: Calibrated ^{137}Cs spectrum from $CeBr_3$ showing extraction of energy resolution at the 662 keV photopeak.

was recorded from the furthest bar, yielding a distribution such as that shown in Figure 3.7. This configuration enables the isolation of gamma rays that undergo a 180° backscatter in the furthest bar before returning and interacting with the first bar, thereby producing a prominent peak in the spectrum around the 478-keVee Compton edge. The peak resulting from this backscatter measurement was fitted to a Gaussian distribution following subtraction of the underlying continuum. The FWHM of the peak was estimated using the sigma value of the fitted Gaussian to calculate the energy resultion using Equation 3.3. The energy resolution for OGS bars in the H2DPI at 478 keVee was determined to be $9.2 \pm 0.2\%$. Notably, this represents an improvement compared to previous trans-stilbene bars, which exhibited an energy resolution of $11.2 \pm 0.5\%$ at the same energy [64].

3.1.3 Z-Position Reconstruction

A significant advantage of the dual-ended readout configuration for the OGS bars in the H2DPI is the ability to reconstruct the event interaction position along the height (Z-axis) of each bar. This reconstruction is achieved by comparing the relative light output collected by the SiPM channels

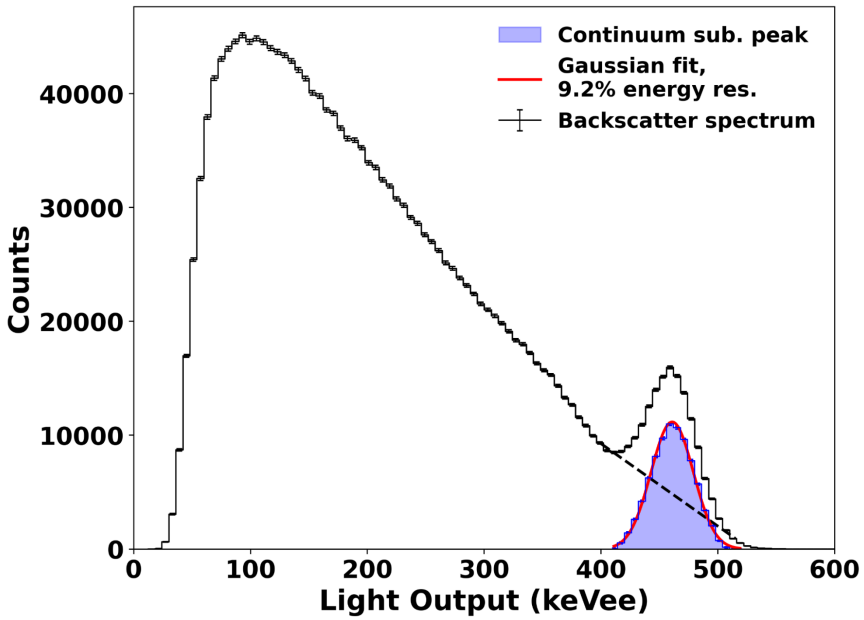

Figure 3.7: Coincidence ^{137}Cs spectrum from an OGS bar showing extraction of energy resolution using the 478 keVee Compton edge peak.

at the top and bottom of a bar, as described by:

$$\text{Ratio} = \frac{\text{PI}_{\text{Bottom}}}{\text{PI}_{\text{Top}} + \text{PI}_{\text{Bottom}}}, \tag{3.4}$$

where PI is the pulse integral of the SiPM waveform for the respective channel. In this scheme, a ratio of 0.5 indicates equal light collection at both ends, denoting an interaction at the midpoint of the bar. Ratios approaching 0 or 1 correspond to interactions occurring closer to the top or bottom ends, respectively.

To characterize the Z-position reconstruction capabilities of the twelve OGS bars in the H2DPI, a series of calibration measurements were performed. Figure 3.8 shows the experimental setup: a stack of ^{137}Cs, ^{60}Co, and ^{22}Na sources was collimated using lead bricks to produce a 1-mm fan beam. The beam's height was controlled with a precision jack, enabling measurements at 5 mm intervals along the 50 mm length of the OGS bars. A ruler and laser pointer were used to accurately track the true beam position relative to the H2DPI.

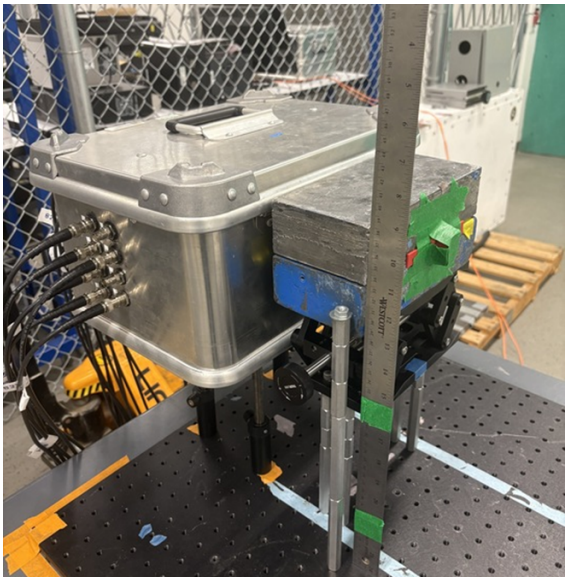

Figure 3.8: Photo of experimental setup for Z-position reconstruction characterization.

Figure 3.9 shows the reconstruction ratio trend for all twelve OGS bars as a function of calibration position along detector length. While all bars exhibited the expected dependence, some, such as upper halves of bars 1 and 8, deviated from the group trend. The most plausible explanation for these variations is nonuniform optical coupling, likely resulting from the manual alignment process that relies on hand and eye coordination and can introduce inconsistencies. The Z-position reconstruction characterization results allow for the creation of reconstruction functions, third order polynomials, unique to each OGS bar in the H2DPI. These functions can be used to associate any given ratio from Equation 3.4 with a corresponding Z position along a bar.

It was found that the uncertainty in position reconstruction depends on both the interaction location and the light output. Figure 3.10 shows the average uncertainty in the position reconstruction for the twelve OGS bars in the H2DPI. Events toward the center of the bars have less reconstruction uncertainty compared to those near either end of the bar. Position reconstruction uncertainties for each bar were obtained by propagating the uncertainty in the ratio metric through the corresponding reconstruction function. The error bars displayed represent one standard deviation of the average values for all twelve OGS bars in the system. Figure 3.11 shows the average uncertainty in position reconstruction for events at the center of the OGS bars as a function of light output

from 25-1100 keVee. The uncertainty in position reconstruction decreases as the light output of the event increases.

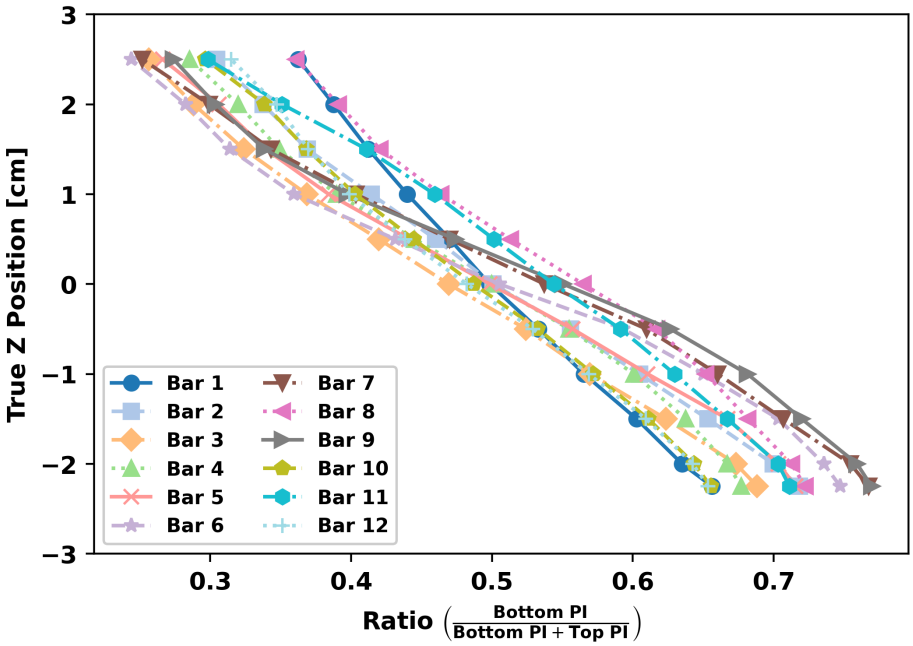

Figure 3.9: Z-position reconstruction function obtained for the twelve OGS bars in the H2DPI.

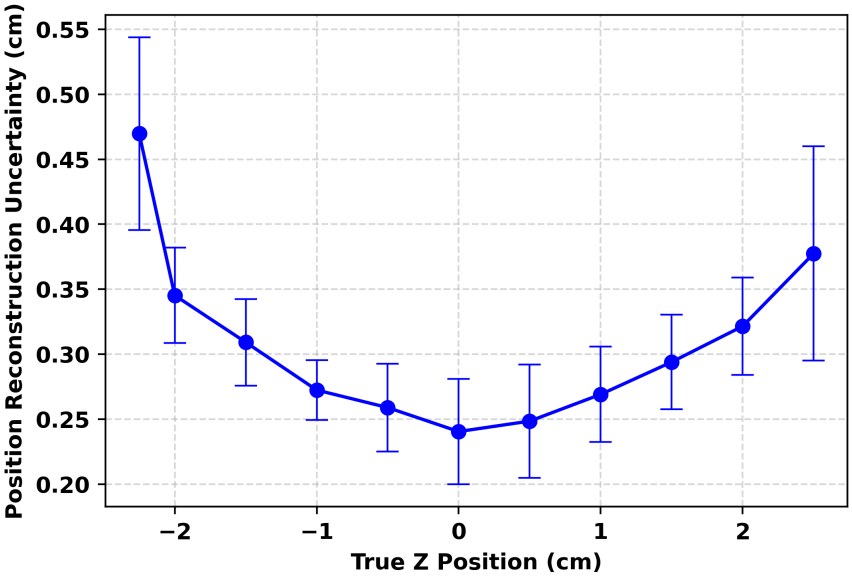

Figure 3.10: Average uncertainty in the position reconstruction as a function of interaction location along length of bars for the twelve OGS detectors in the H2DPI. Error bars are one standard deviation of the average values.

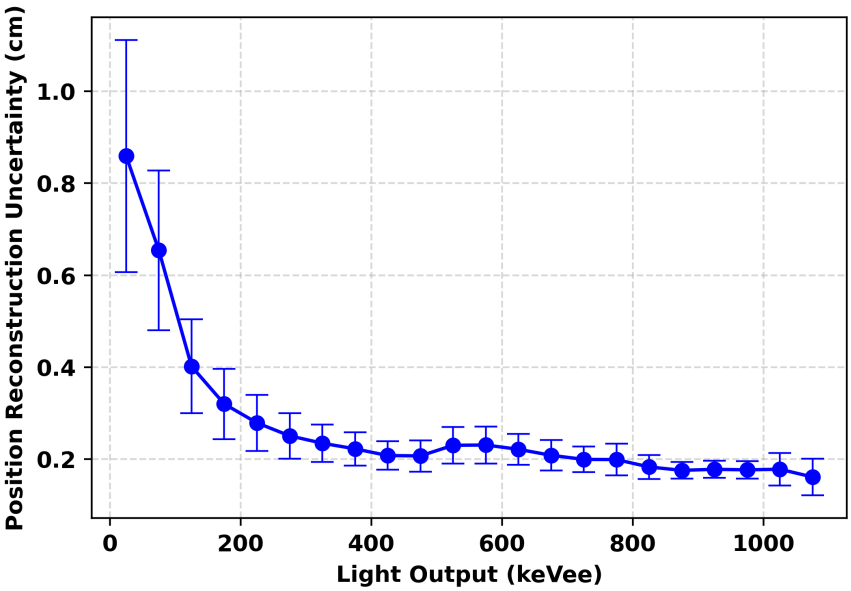

Figure 3.11: Average uncertainty in the position reconstruction for events at the center of the OGS bars as a function of light output. Error bars are one standard deviation of the average values from all twelve bars in the system.

3.1.4 Pulse Shape Discrimination

The classification of events as either neutron or gamma-ray interactions is an essential component of the H2DPI data analysis. Pulse shape discrimination (PSD) in this work refers to a charge integration technique that exploits differences in digitized waveforms resulting from differing scintillation processes when initiated by either neutrons and gamma rays, as detailed in Chapter 2. In particular, triplet-triplet annihilation results in a delayed component of the scintillation response, yielding longer tails in the waveforms for neutron scattering events in the OGS. While there are multiple ways of achieving PSD, the method utilized in this work involves calculating two integrals to derive a ratio metric for particle discrimination. The total integral window is defined as starting when the waveform reaches 5% of its peak value and ending when the falling edge drops to 1% of the peak value. The bounds were chosen such that the majority of the pulse would be integrated while minimizing noise contribution from the baseline. The tail integral window begins 60 ns after the start of the total integral window and also concludes at the point where the falling edge reaches 1% of the peak value. The tail integral start was optimized using the same figure of

merit methodology performed in other work [66]. The metric of interest, the PSD ratio, is defined as:

$$PSD_{\text{Ratio}} = \frac{Tail}{Total}, \tag{3.5}$$

where $Tail$ and $Total$ denote the tail and total integrals, respectively. It is important to note that, for the OGS bars, the dual-ended readout produces two waveforms for each event in a bar. Tail and total integrals are computed independently for both the top and bottom SiPM channels. However, to obtain the final PSD ratio for an event, the integrals from both channels are summed in quadrature prior to calculating the ratio [26], as shown below,

$$PSD_{\text{Ratio}} = \frac{\sqrt{Tail_T^2 + Tail_B^2}}{\sqrt{Total_T^2 + Total_B^2}}, \tag{3.6}$$

where the T and B subscripts denote top and bottom channels, respectively. As an aside, it should also be noted that due to the dual-readout nature of the bars, total light output and timing calculations are also processed slightly different. To obtain the total light output, energy, of an event in an OGS bar the two pulse integrals from the top and bottom SiPM channels are summed together. To obtain a time tag for an event in an OGS bar, the time tags from the bottom and top SiPM channels are averaged.

After calculating the PSD ratios for recorded events, a discrimination methodology adapted from previous work [67] is applied. Using a lower light output threshold of 50 keVee, the data are binned into 50 keVee slices to determine an appropriate PSD ratio discrimination threshold as a function of light output. The selection of this threshold is informed by considerations related to particle misclassification. The resulting set of PSD ratio discrimination points for a given OGS bar can then be fit to a function, yielding a unique PSD discrimination line for subsequent analysis. In this work, the function used to define the PSD discrimination line is given by:

$$f(x) = \sum_{i=1}^{n} a_i e^{-b_i x} + c, \tag{3.7}$$

where x is the light output in keVee, n is the number of exponential terms, a_i is the amplitude of the ith exponential, b_i is the decay rate of the ith exponential, and c is a constant offset. In this work, n = 6 exponential terms are used to construct the PSD discrimination lines. Figure 3.12 provides an example of a PSD ratio plot for an OGS bar in the H2DPI, along with its corresponding PSD discrimination line. Visually, two distinct bands are evident: an upper and a lower one. The upper band comprises neutron events, which exhibit proportionally larger waveform tails and thus greater PSD ratios. For particle classification, events located below the PSD discrimination line are assigned as gamma ray events, while those above are designated as neutrons.

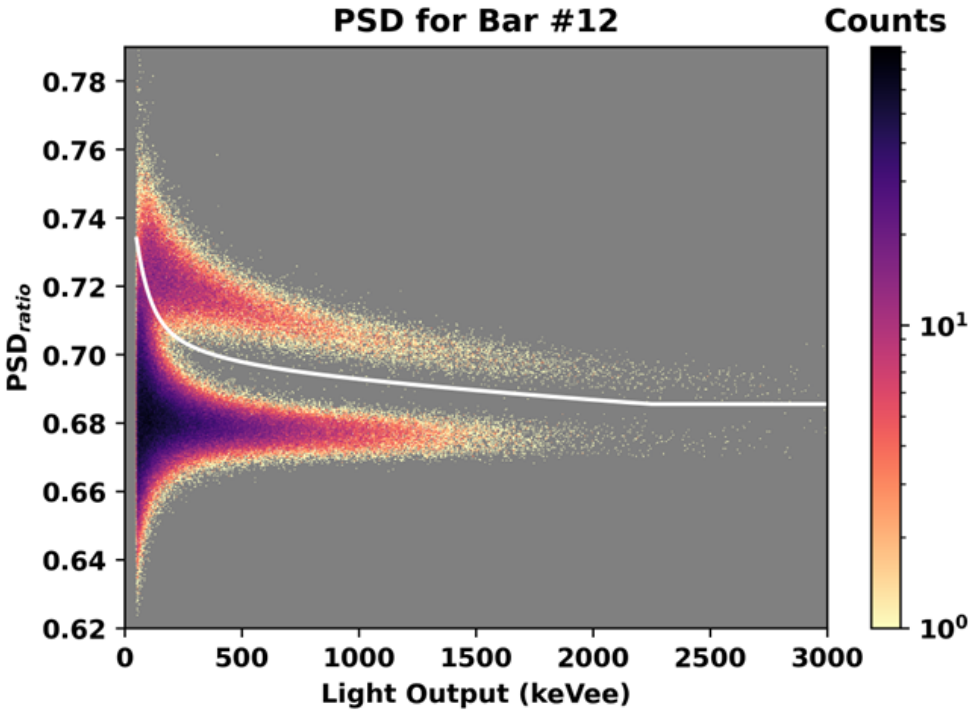

Figure 3.12: Example PSD ratio plot with corresponding unique discrimination line shown for an OGS bar in the H2DPI.

3.1.5 Neutron Light Output Response

An essential property of OGS that must be characterized is its neutron light output response as a function of deposited energy. During neutron elastic scattering within the OGS material, recoiling protons (hydrogen nuclei) generate the singlet and triplet states discussed previously in Section 2.3.

The high density of ionization along the particle track leads to quenching, resulting in a reduced scintillation light yield compared to the same energy deposition from electron recoils, such as those produced by gamma-ray Compton scattering. The degree of quenching varies according to the energy of the recoil proton, and is commonly estimated using Birks' law [48]:

$$\frac{dL}{dx} = S\frac{\frac{dE}{dx}}{1 + k_B\frac{dE}{dx}}, \tag{3.8}$$

where L is the amount of light produced, S is the scintillation efficiency, $\frac{dE}{dx}$ is the stopping power for protons in the scintillator, and k_B is a material dependent constant. A proton stopping power table for OGS was calculated using the Stopping and Range of Ions in Matter (SRIM, 2008) [68] software, with output in units of MeV/(mg/cm2). The calculations covered recoil proton energies ranging from 1 eV to 25 MeV. Figure 3.13 illustrates the calculated proton stopping power in OGS utilized in this work. The stopping power includes both a nuclear component, derived from target nuclei, and an electric component resulting from Coulombic interactions. For the energy ranges commonly encountered in measurements using OGS, the electric component dominates the stopping power.

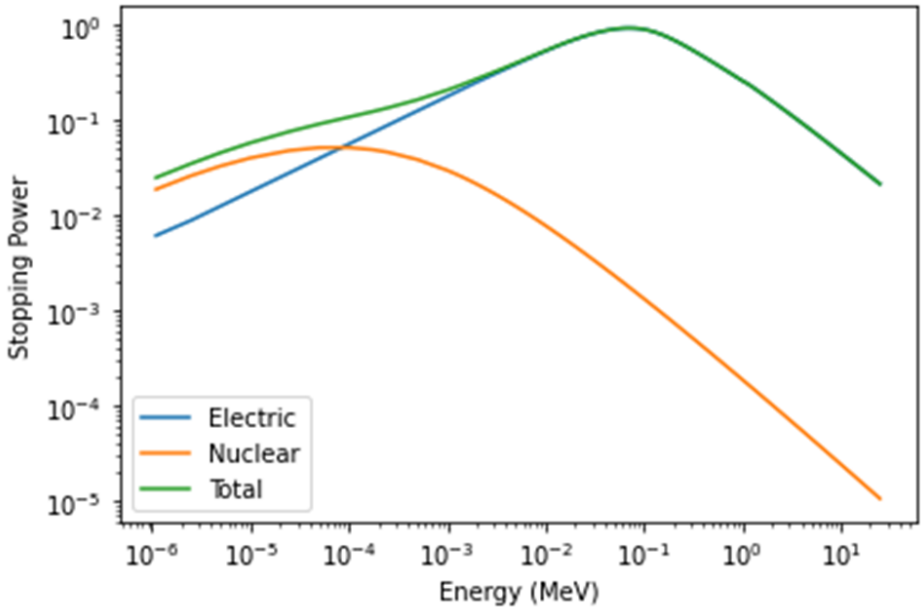

Figure 3.13: Plot of proton stopping power in OGS from 1 eV and 25 MeV.

Prior work performed neutron time-of-flight (TOF) experiments with OGS bars to measure the light output as a function of proton recoil energy [69]. In these experiments, a ^{252}Cf source was placed 50 cm from the front of the OGS bars, and a 2.54 cm × 2.54 cm stilbene tag detector coupled to a 2.54 cm PMT was positioned flush against the ^{252}Cf source. Spontaneous fissions of ^{252}Cf were identified by gamma-ray interactions in the tag detector, while the energies of coincident neutrons interacting in the OGS bars were reconstructed by measuring their TOF and applying the Newtonian equation for kinetic energy:

$$E_{TOF} = \frac{1}{2} m_n \left(\frac{\|\vec{x}_2 - \vec{x}_1\|}{\Delta t} \right)^2, \tag{3.9}$$

where m_n is the mass of a neutron, $\vec{x}_2$ and $\vec{x}_1$ are the interaction positions in a given OGS bar and the tag detector, respectively, and Δt is the time difference between the tagged event and the neutron scatter in the OGS. Neutron events in the OGS bars were sorted into TOF bins of equal width, with bin edges converted to neutron energy based on the known flight path length. The resulting light output distributions exhibit a defined upper edge corresponding to the kinetic energy of the incident neutron. The derivative of this edge was fitted with a Gaussian, following procedures from related work [64, 52]. The mean of the fitted Gaussian represents the light output for a neutron that elastically scatters on a proton and deposits its full energy. Consequently, the distribution of light output as a function of proton recoil energy can be determined for each individual OGS bar, as illustrated in Figure 3.14.

The experimental data of light output as a function of proton recoil energy for OGS bars is fitted using a semi-empirical function based on Birks' formula, where Equation 3.8 is integrated over energy [62]:

$$L(E) = \int_0^E dE' \frac{a}{1 + b\left(\frac{dE}{dx}(E')\right)}, \tag{3.10}$$

where a and b are fitting parameters. For the OGS H2DPI, a single combination of fitting parameters for Equation 3.10 is employed for all bars, which was obtained by averaging the parameters

derived from multiple OGS bars. The Birks' coefficients used in this work are a = 0.537 $\pm$ 0.018 MeVee/MeV and b = 2.678 $\pm$ 0.206 cm/MeV. Figure 3.14 displays the resulting Birks' fit using these coefficients alongside an example dataset of light output as a function of proton recoil energy for an OGS bar. Assuming that the Birks' equation remains true for all values, the neutron light output response can be converted to deposited energy. For example, 50 keVee light output from neutron events is equivalent to neutron energy deposition of 0.275 MeV using the characterized Birks' coefficients for OGS bars.

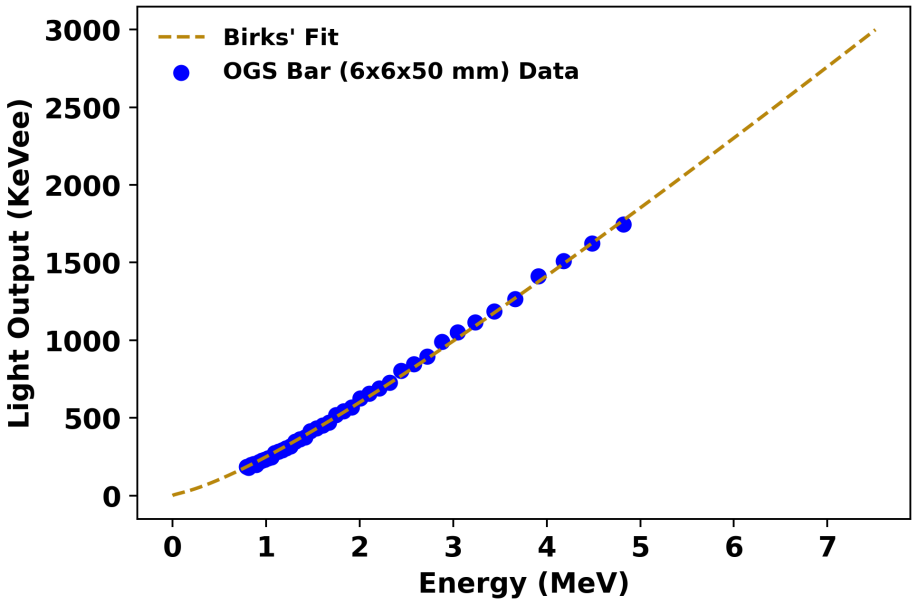

Figure 3.14: Measured light output vs recoil proton energy for an OGS bar with Birks' function.

3.1.6 Digitizer Board Timing Synchronization

The final aspect of the OGS H2DPI characterization discussed in this chapter is the evaluation of inherent timing offsets from the digitizer channels used in the system. As outlined in Section 3.1, two v1730 CAEN digitizers are employed to read out a total of 32 channels. These boards are synchronized using a clock cable and software configurations; however, inherent timing offsets still exist and must be characterized. To assess these offsets, an experiment was carried out using a Keysight 33210A waveform generator. Synchronized signals were generated and split into two

BNC cables. Figure 3.15 provides both a schematic and a photograph of the experimental setup. One BNC output was consistently connected to digitizer channel 0, serving as the reference clock for the H2DPI. The second BNC cable was sequentially attached to each of the remaining 31 channel inputs across a series of measurements. Time differences between channel 0 and each other channel were calculated and histogrammed to identify channel-specific offsets. Figure 3.16 shows the four distinct levels of offsets observed in the digitizers: 0.04 ± 0.05 ns, 7.96 ± 0.01 ns, 63.78 ± 0.02 ns, and 71.78 ± 0.01 ns. Table 3.1 summarizes the channel timing offsets applied on corresponding time tags during data processing for the OGS H2DPI.

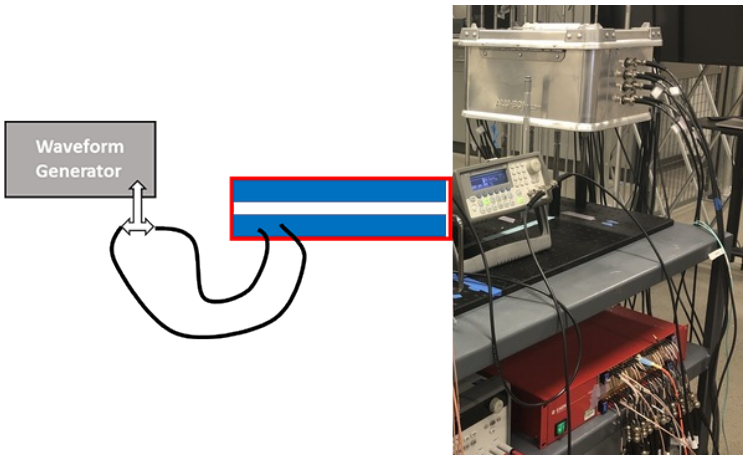

Figure 3.15: Schematic diagram and photograph of the experimental setup used to evaluate inherent timing offsets in the H2DPI digitizer channels.

3.2 Fast-Neutron Imaging Methodology

The OGS H2DPI operates as a conventional segmented neutron scatter camera, detecting a neutron's initial scatter interaction in one detector volume and its subsequent scatter in a separate detector volume. Figure 3.17 provides a schematic illustrating the neutron imaging process in the H2DPI based on these double scatter events. The cosine squared of θ, the angle at which the neutron is initially scattered during the first interaction, relative to the vector connecting the two interaction points, is defined as:

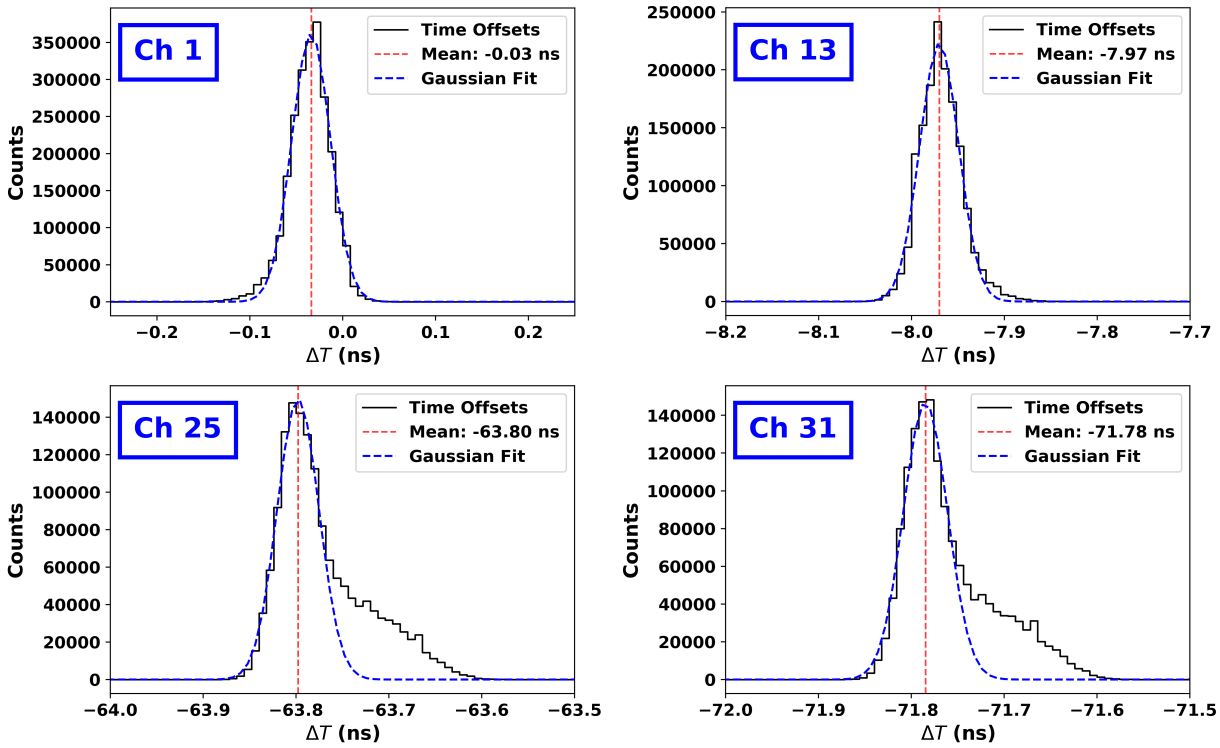

Figure 3.16: Histograms of time differences between channel 0 and other channels demonstrating the different degrees of timing offsets identified.

$$\alpha = \cos^2(\theta) = \frac{E_{\text{TOF}}}{E_{\text{TOF}} + E_1}, \tag{3.11}$$

where E_1 is the energy deposited in the first neutron scatter. E_{TOF} represents the energy of the neutron after the first scatter and can be calculated using Equation 3.9, utilizing the coordinates and time tags of the coincident scatters in the OGS bars. Detailed error propagation for Equation 3.11 is described in prior work [70] and was adopted for this dissertation work. This work uses a coincidence window of 0.138 to 10.4 ns for neutron imaging, corresponding to the TOF required for a 10 MeV neutron to traverse the shortest detector distance of 6 mm and a 0.25 MeV neutron to cover the longest distance of approximately 72 mm within the H2DPI.

Table 3.1: Summary of characterized channel timing offsets for the OGS H2DPI .

Channel Number	Offset (ns)	Channel Number	Offset (ns)
0	N/A	16	+63.78(3)
1	+0.03(2)	17	+63.78(3)
2	+0.02(2)	18	+63.80(2)
3	+0.02(2)	19	+63.80(2)
4	-0.06(2)	20	+63.74(2)
5	-0.06(2)	21	+63.74(2)
6	-0.08(2)	22	+63.77(2)
7	-0.08(2)	23	+63.77(2)
8	-0.09(2)	24	+63.79(2)
9	-0.09(2)	25	+63.80(2)
10	-0.02(2)	26	+63.77(2)
11	-0.02(2)	27	+63.76(2)
12	+7.97(2)	28	+71.78(2)
13	+7.97(2)	29	+71.78(2)
14	+7.95(2)	30	+71.77(2)
15	+7.95(2)	31	+71.78(2)

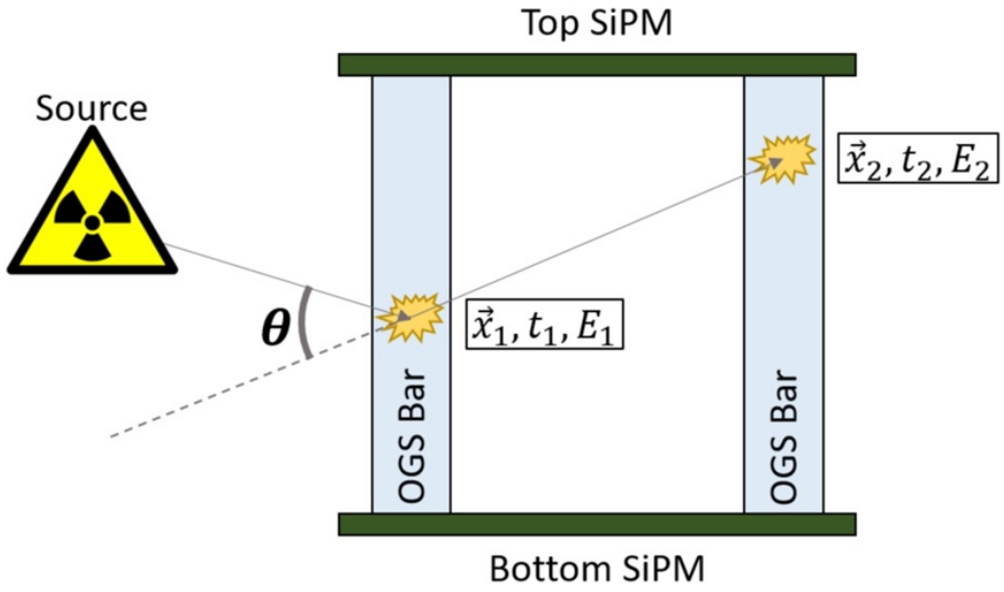

Figure 3.17: Simplified schematic of a neutron double scatter event in the OGS bars and the relevant metrics obtained.

3.3 Gamma-Ray Imaging Methodology

The OGS H2DPI can also operate as a conventional Compton camera by detecting a gamma-ray Compton scatter in one of the OGS bars followed by a subsequent photoelectric absorption in one of the $CeBr_3$ detectors. This specific event sequence is required to achieve full energy deposition, as the α metric is now defined as:

$$\alpha = \cos^2(\theta) = \left(1 + m_e c^2 \left[\frac{1}{E_1 + E_2} - \frac{1}{E_2}\right]\right)^2, \tag{3.12}$$

where m_e is the mass of an electron, E_1 is the energy deposited in the first interaction and E_2 is the energy deposited in the second interaction. Note that Equation 3.12 requires that the summation of E_1 and E_2 be equal to the total gamma-ray energy for correct localization. Since E_2 is not always guaranteed to result from photoelectric absorption in the $CeBr_3$, one approach to ensure correct sequencing of imageable gamma-ray events with the H2DPI is to apply energy gates to the data. For instance, when measuring ^{137}Cs, an energy gate of 662 $\pm$ 50 keV can be imposed on the summed coincidence spectrum to ensure selection of full-energy deposition events. By gating on the expected photopeaks, the analysis effectively filters for the correct event sequence, Compton scatter in the OGS followed by photoelectric absorption in the $CeBr_3$, thereby improving imaging accuracy by fulfilling the criteria for Equation 3.12. Figure 3.18 provides a schematic illustrating the gamma-ray imaging process in the H2DPI. This work uses a coincidence window of 0 to 5 ns for gamma-ray imaging.

3.4 Simple Backprojection Imaging

Once a scattering angle has been determined for an event, the event is projected onto the surface of a sphere of arbitrary fixed radius. This sphere is then pixelated so that each pixel, b, corresponds to a position relative to the center of the H2DPI. The value assigned to each pixel for a given cone, d, is determined by a Gaussian distribution described by [26]:

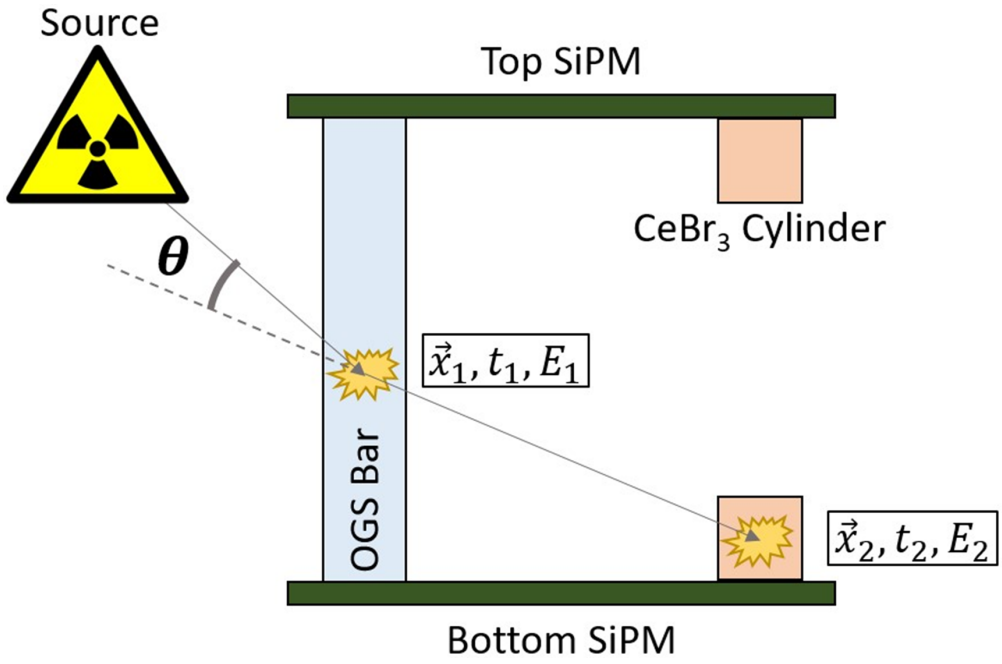

Figure 3.18: Simplified schematic of a gamma-ray imageable event in the OGS bars and $CeBr_3$ cylinders, along with the relevant metrics obtained.

$$C_{d,b} = e^{\frac{-(\beta_b - \alpha)^2}{2(\sigma_\beta^2 + \sigma_\alpha^2)}}, \tag{3.13}$$

where β_b is the cosine squared of the angle ψ, which is defined as the angle between the cone axis (the vector connecting the two interaction points, $\vec{X}_1 - \vec{X}_2$) and the ray extending from the first interaction point to the center of pixel b on the projection sphere, represented by the vector $\vec{X}_b - \vec{X}_1$. β_b can be calculated as follows:

$$\beta_b = \cos^2(\psi) = \frac{((\vec{x}_1 - \vec{x}_2) \cdot (\vec{x}_b - \vec{x}_1))^2}{|\vec{x}_1 - \vec{x}_2|^2 |\vec{x}_b - \vec{x}_1|^2}. \tag{3.14}$$

Extensive error propagation for the β_b term is discussed in prior work [70] and utilized in this work during data analysis. In the context of simple backprojection imaging with the H2DPI, the angular field of view is defined as follows: the centerline height of the H2DPI corresponds to an altitude angle (ϕ) of $0°$. Positive altitude values indicate directions toward the zenith, while negative values extend toward the nadir. The H2DPI forward direction is set at an azimuth angle

(θ) of $0°$, with positive azimuth values extending to the right and negative values to the left. It is important to note that when discussing angular directions throughout this work, coordinates are always presented in the order (θ,ϕ), i.e., (azimuth, altitude). Figure 3.19 provides a schematic depicting this frame of reference, where the star marker indicates the center of the H2DPI and the yellow arrow denotes an angular direction of ($0°$, $0°$), that is, directly ahead and centered relative to the H2DPI, for reference.

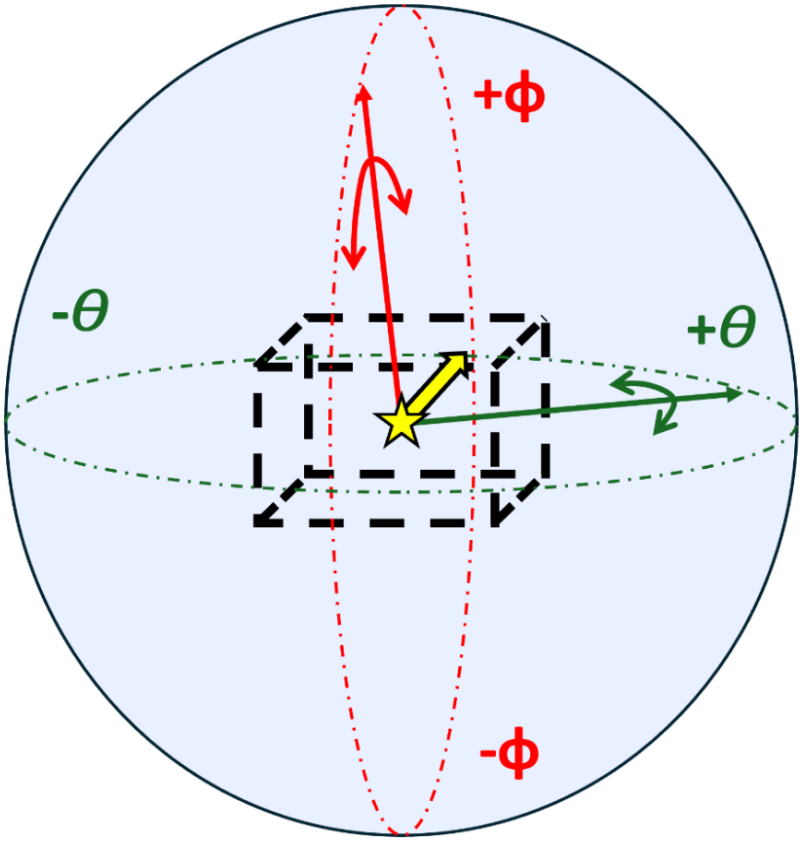

Figure 3.19: Schematic showing the H2DPI angular field of view, where azimuth (θ) and altitude (ϕ) directions are defined relative to the detector center (star marker) and ($0°$, $0°$) is indicated by the yellow arrow.

Figure 3.20 presents an example gamma-ray simple backprojection (SBP) image obtained with the OGS H2DPI, where a ^{137}Cs source was placed 11.36 cm away at an angular direction of ($-26.6°$, $0°$). The radius of the backprojection sphere was set to the measurement distance in this example. It should be noted that the radius should be set as close to the source-to-detector

distance as possible for the best accuracy. Using a poor estimate for the radius can lead to poor images if the source was placed very close to the imager (<15 cm) due to near-field effects. The SBP image consists of 285 cones collected over 1 minute, with a circular outline indicating the true source location in the H2DPI field of view. Cones are aggregated into a single image to arrive at a localized source location. Since a single cone only demonstrates that a source is likely to lie along it, multiple events are required to break the ambiguity and create a proper image of the source.

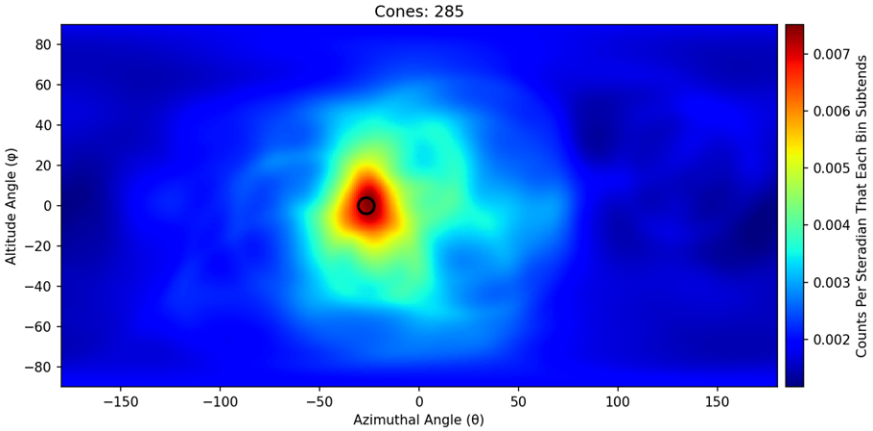

Figure 3.20: Example gamma-ray SBP image obtained with the OGS H2DPI of a ^{137}Cs source located at $(-26.6°, 0°)$, with the true source location indicated by the circular outline.

3.5 List-Mode Maximum Likelihood Expectation Maximization

List-mode maximum likelihood expectation maximization (LM-MLEM) can be applied to SBP images to aid in localizing sources using the imaging data acquired from measurements. In this work, the final SBP matrix is used as the likelihood distribution for each event in the list during the first iteration of LM-MLEM. Since LM-MLEM is an iterative process, the output of an iteration is used as the new likelihood distribution for the following one. The LM-MLEM method will converge on the most probable point source location(s) in a given image. LM-MLEM has previously been employed in a range of imaging systems, including neutron scatter cameras, to enhance source localization and image convergence [71, 72]. Mathematically, the LM-MLEM process is

defined as follows [73, 74]:

$$\lambda_b^{\text{New}} = \lambda_b^{\text{Old}} \sum_{d=1}^{D} \frac{n_d^* C_{d,b}}{\sum_{b'=1}^{B} \lambda_{b'}^{\text{old}} C_{d,b'}}, \tag{3.15}$$

where is λ_b^{New} the posterior source distribution, λ_b^{Old} is the prior source distribution and n_d^* is the observation vector. The observation vector indicates the number of times a particular event occurs in the data set, which for LM-MLEM is only once and results in a vector of ones [75]. The two different summations are over all d cones and over all b pixels.

The LM-MLEM algorithm can be iterated indefinitely, thus a stopping criterion must be chosen. The stopping criterion chosen for this work relied on using the structural similarity index (SSI) as defined by [76],

$$\text{SSI}(x, y) = \frac{(2\mu_x\mu_y + c_1)(2\sigma_{xy} + c_2)}{(\mu_x^2 + \mu_y^2 + c_1)(\sigma_x^2 + \sigma_y^2 + c_2)}, \tag{3.16}$$

where $\mu_{x,y}$ are the means of the image pixel values, used to evaluate luminance; $\sigma_{x,y}$ are the standard deviations of the image pixel values, which represent contrast; σ_{xy} is the correlation coefficient between the two images, utilized to assess structural similarity; and $c_{1,2}$ are constants introduced to prevent potential instabilities in the calculation.

The mean SSI (MSSI) value is used as a metric, with values closer to 1 indicating greater similarity between the two images being compared. In this context, images x and y represent sequential iterations of LM-MLEM applied to the same original SBP image. By plotting the MSSI value against increasing LM-MLEM iterations, it is evident that early iterations produce greater changes in MSSI, whereas later iterations yield source distributions (images) that differ only marginally from their predecessors. Figure 3.21 illustrates this behavior, along with the potential for establishing a stopping criterion: the algorithm can be terminated at the iteration where (1-MSSI) reaches X% of the value observed in the first iteration. In this work, a 10% stopping criterion is used for gamma-ray images, while a 1% criterion is employed for neutron images. The reason for different stopping criterions is due to neutron SBP typically requiring more iterations to better converge on a source location. This behavior is due to the generally lower number of imageable events obtained

for neutrons leading to poorer statistics and more image artifacting. Gamma-ray SBP images on the other hand will tend to converge much quicker due to commonly having more imageable events to use in the reconstruction. Figure 3.22 presents an example of a gamma-ray LM-MLEM image after 7 iterations were performed on the previously discussed SBP image in Figure 3.20.

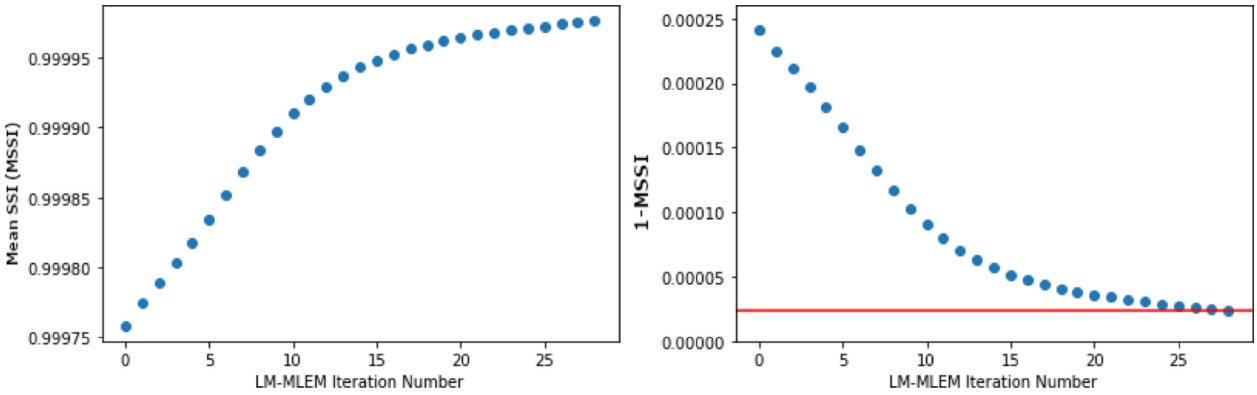

Figure 3.21: Plot of MSSI value versus LM-MLEM iteration number, illustrating convergence behavior (left). Plot of (1 – MSSI) against LM-MLEM iterations (right). The red horizontal line indicates the stopping criterion set at 10% of the initial value in this example.

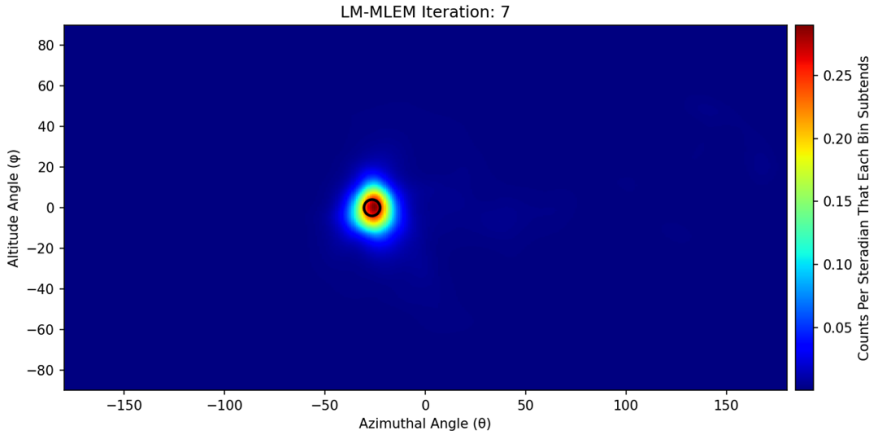

Figure 3.22: Example gamma-ray LM-MLEM image obtained with the OGS H2DPI of a ^{137}Cs source located at $(-26.6°, 0°)$, with the true source location indicated by the circular outline.

CHAPTER 4

Imaging and Spectroscopy Using the OGS H2DPI

This chapter demonstrates the potential of OGS for source localization and spectroscopy applications by showcasing the capabilities of the OGS-based dual-particle imaging system described in Chapter 3. Over the 4.5 years since its development, numerous measurements have been performed with the H2DPI; however, this chapter will not cover every effort in detail. Instead, it will begin by introducing the fundamental neutron and gamma-ray imaging capabilities in single-source experiments. The discussion will then progress to more complex scenarios involving multiple sources simultaneously present within the field of view (FOV). Finally, the chapter will present measurements conducted with a range of SNM sources relevant to nuclear safeguards and nonproliferation. Chapter 4 concludes with reflections on the broader implications of the work presented.

4.1 Single Source Neutron Imaging

4.1.1 Bare ^{252}Cf

The first result presented is neutron imaging of a bare ^{252}Cf source with an activity of 1021 μCi, corresponding to a neutron emission rate of 4.4×10^6 n/s. The source was positioned 58.42 cm from the imager, at an angular direction of $(20^\circ, 0^\circ)$. The total measurement time was 170 minutes. Figure 4.1 displays the neutron SBP image compiled from all collected data, which yielded 9759 imageable events, as well as the corresponding LM-MLEM image generated according to the stopping criterion defined in Section 3.5. Both images feature a circular outline centered at $(20^\circ, 0^\circ)$ to indicate the true source location within the FOV. The results demonstrate successful localization:

in both the SBP and LM-MLEM images, the converged source positions are in agreement with the actual location of the ^{252}Cf source. Additionally, Figure 4.2 presents the SBP neutron image generated from just 5 minutes of data acquisition (283 events), illustrating that the presence of the ^{252}Cf source can be confirmed, and reasonable localization accuracy achieved, even with a short measurement period. Naturally, extending the measurement time yields more imaging statistics and improved convergence of the source location.

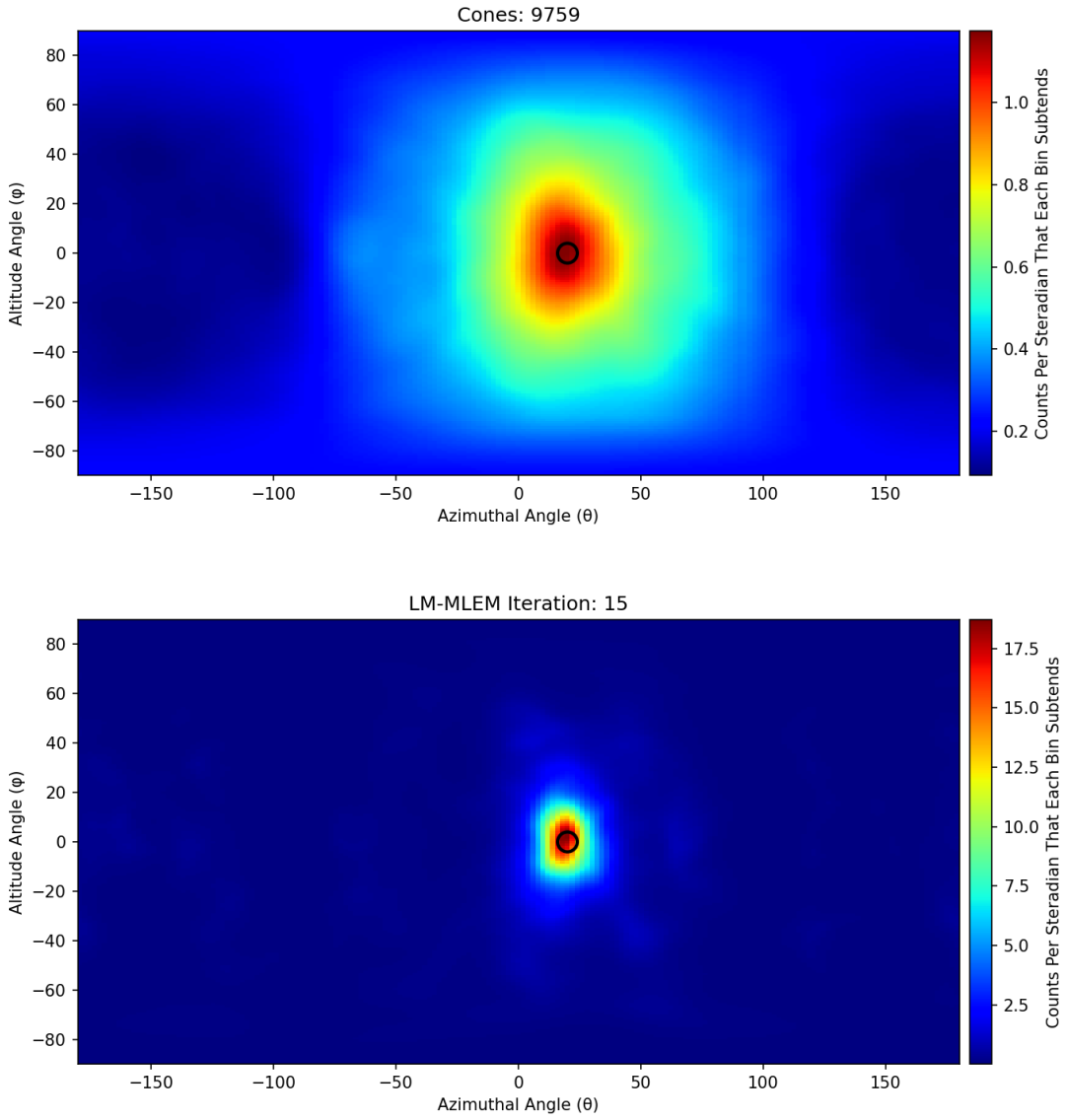

Figure 4.1: Neutron SBP image of bare ^{252}Cf reconstructed using 9759 events (top). Corresponding LM-MLEM image (bottom). True source location is marked with circular outlines centered at (20°, 0°).

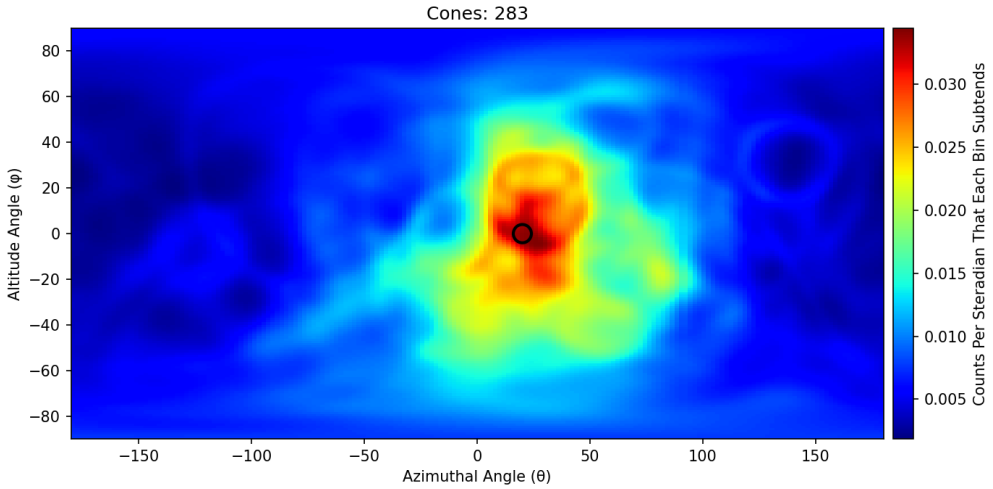

Figure 4.2: Neutron SBP image of bare ^{252}Cf reconstructed using 283 events from 5 minutes of data collection. True source location is marked with a circular outline centered at (20°, 0°).

4.1.2 Shielded ^{252}Cf

Shielded configurations are particularly relevant in nuclear verification work, as strong sources are frequently stored in containers designed to minimize radiation exposure, resulting in the inevitable presence of shielding material during measurements to ensure safety compliance. Additionally, in the context of nuclear safeguards, untrustworthy or malicious actors may deliberately attempt to conceal nuclear materials during inspections or transport. For these reasons, it is valuable to characterize the neutron imaging performance of the OGS H2DPI in the presence of shielding. In this subsection, results from two series of shielded ^{252}Cf measurements are presented. For a more complete analysis and additional details, refer to previous published work [77]. The ^{252}Cf source used in these experiments had an activity of 903 μCi, corresponding to a neutron emission rate of 3.88×10^6 n/s. Figure 4.3 illustrates the experimental setup for the first measurement series, in which slabs of high-density polyethylene (HDPE) were introduced as shielding between the H2DPI and the ^{252}Cf source, with thicknesses of 0 cm (bare source), 2.54 cm, 5.08 cm, 10.16 cm, and 20.32 cm. Measurement times increased with moderator thickness, ranging from 30 minutes for the bare source to several hours for the 20 cm HDPE configuration. In all cases, the neutron

source was placed 50 cm from the imager at an angular direction of (0°, 0°).

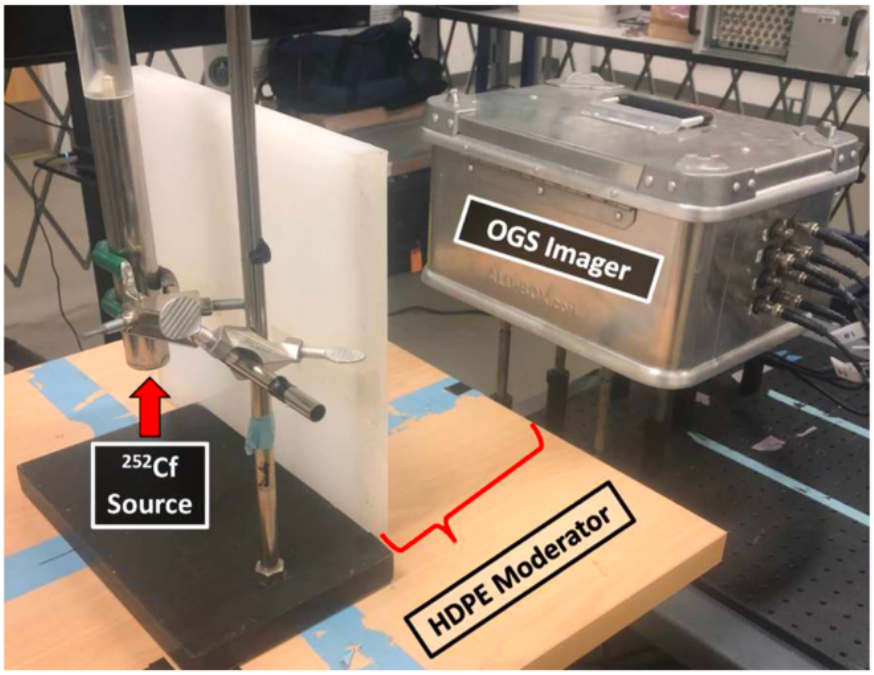

Figure 4.3: Photograph of the experimental setup for the variable HDPE thickness series of measurements.

Neutron SBP images were reconstructed using data from varying HDPE thicknesses. To facilitate fair comparisons between images, each was generated with identical imaging statistics. Reconstruction was performed using 782 events, corresponding to the maximum number of cones obtained from the 10.16 cm measurement, which was the data set with the smallest total number of imageable events available. Figure 4.4 provides a representative SBP neutron image for the 10.16 cm HDPE configuration. SBP images were sliced along the azimuth and altitude directions at the converged source location to obtain angular profile distributions, as shown in Figure 4.5. The key metric in this analysis was the σ value, determined from Gaussian fits to the angular profile distributions within range of [$-40°$,$40°$] for both azimuth and altitude. σ serves as an indicator of the spread of an image's converged source location and is therefore used to assess image quality. Table 4.1 summarizes the σ results for both azimuth and altitude directions. Results in Figure 4.4 and Table 4.1 reveal that the spread consistently increased with HDPE thickness for the altitude direction only. The σ for azimuth remained approximately constant at $19°$ across all SBP images,

indicating limited impact from shielding on image quality in this direction. It should be noted that there is an exception with the 20.32 cm HDPE configuration. While the σ for azimuth indicates little change, visually the angular distribution is wider across the entire angular space.

Meanwhile, the σ for altitude increased from 21° to 25° as HDPE thickness increased. Additionally, the angular profiles indicate an increased level of noise or background for the thickest HDPE configuration, signifying deteriorating source localization performance. Nevertheless, the SBP images for all HDPE configurations were able to localize the ^{252}Cf location in the FOV as evidenced by the locations of the peaks in the profile distributions for θ and ϕ.

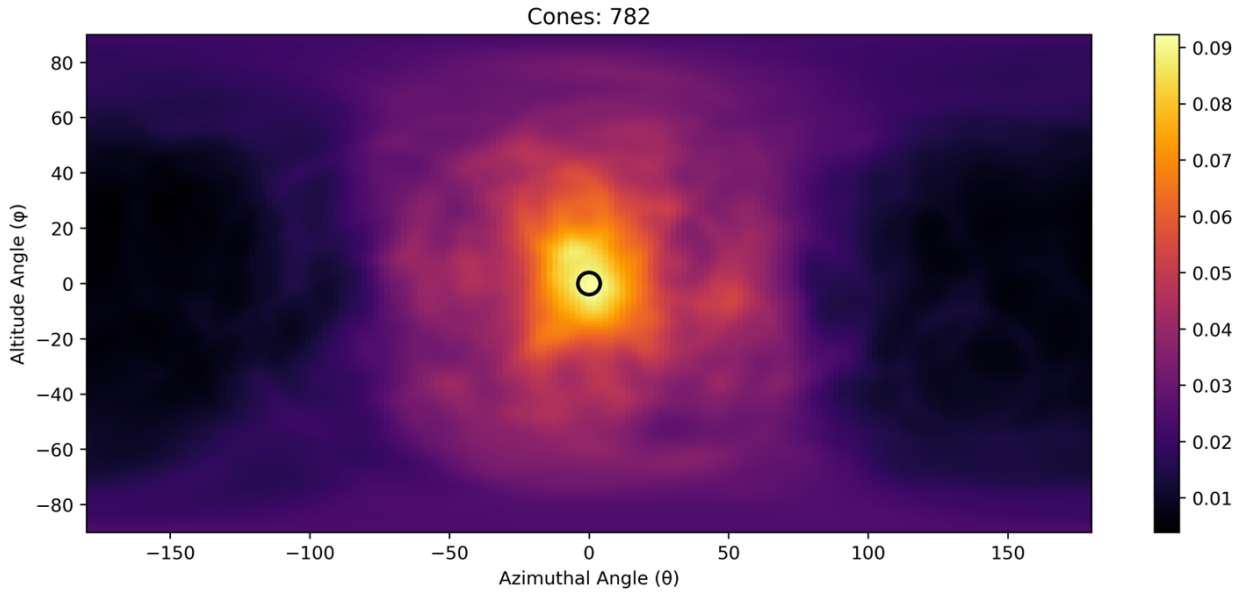

Figure 4.4: Neutron SBP image of ^{252}Cf shielded with 10.16 cm of HDPE using 782 events. True source location is marked with a circular outline centered at $(0^\circ, 0^\circ)$.

Table 4.1: Summary of spread in neutron SBP images with increasing HDPE. Measurement times used to achieve equal number of imageable events are also noted.

	0 cm (14 min)	**2.54 cm (23 min)**	**5.08 cm (35 min)**	**10.16 cm (90 min)**	**20.32 cm (352 min)**
$\boldsymbol{\sigma_\theta}$	19.10°	20.10°	19.63°	19.17°	19.37°
$\boldsymbol{\sigma_\phi}$	21.43°	22.34°	22.06°	22.62°	25.27°

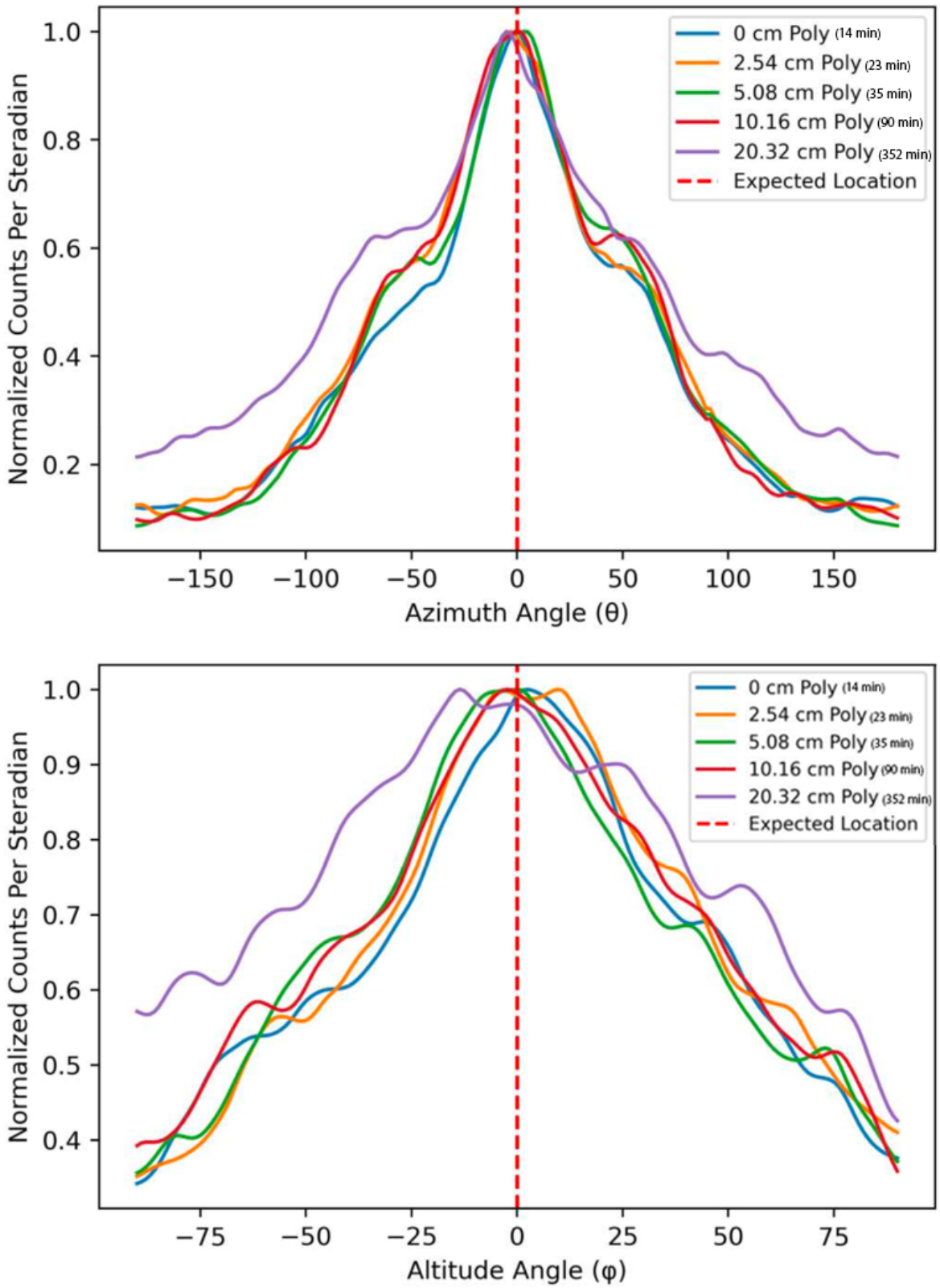

Figure 4.5: Azimuth (θ) and Altitude (ϕ) angle distributions from neutron SBP images for various HDPE thicknesses. Expected source location is represented by a red dashed line.

Figure 4.6 illustrates the experimental setup for the second shielded ^{252}Cf measurement. The source was positioned within a Nuclear-Chicago NH3 Neutron Howitzer [78], centered 1 m from the imager to imitate a typical stored-source configuration. The howitzer, which provides moderation using paraffin wax, has a radius of 30 cm and includes a hollow channel through which the source can be placed at specified heights. Three configurations, corresponding to different heights within the storage barrel, were evaluated. In the TOP configuration, the altitude angle of the source relative to the imager was $-8.1°$, with approximately 30 cm of paraffin between the source and the imager. In the MIDDLE configuration, $\phi = -20.5°$ with 40 cm of moderation, and in the BOTTOM configuration, $\phi = -33.0°$ with 60 cm of paraffin. Each configuration was measured for two hours. Due to the limited measurement time, only the TOP configuration produced sufficient statistics to generate a neutron SBP image; increased shielding in the MIDDLE and BOTTOM configurations attenuated the neutron signature beyond the capability of the imaging system. The resulting SBP neutron image in Figure 4.7 demonstrates that a neutron source stored in the upper region of the howitzer can be successfully localized.

Overall, the results from the shielding measurement series revealed several important implications for the OGS H2DPI. The angular profile distributions indicate that the spread of the source hotspot remains relatively unaffected by shielding up to 10 cm of HDPE; however, further increases in shielding lead to noticeable image quality degradation due to a reduced signal-to-noise ratio. The study also demonstrates that a relatively small number of events, approximately 800, is sufficient to accurately locate a shielded ^{252}Cf source within ang20 using SBP images alone. Ultimately, the thickness of shielding material between the source and H2DPI determines whether reasonable measurement times can be achieved. When neutron imaging is limited by excessive shielding, gamma-ray signatures can potentially be used as an alternative for source localization instead due to the dual nature of the H2DPI.

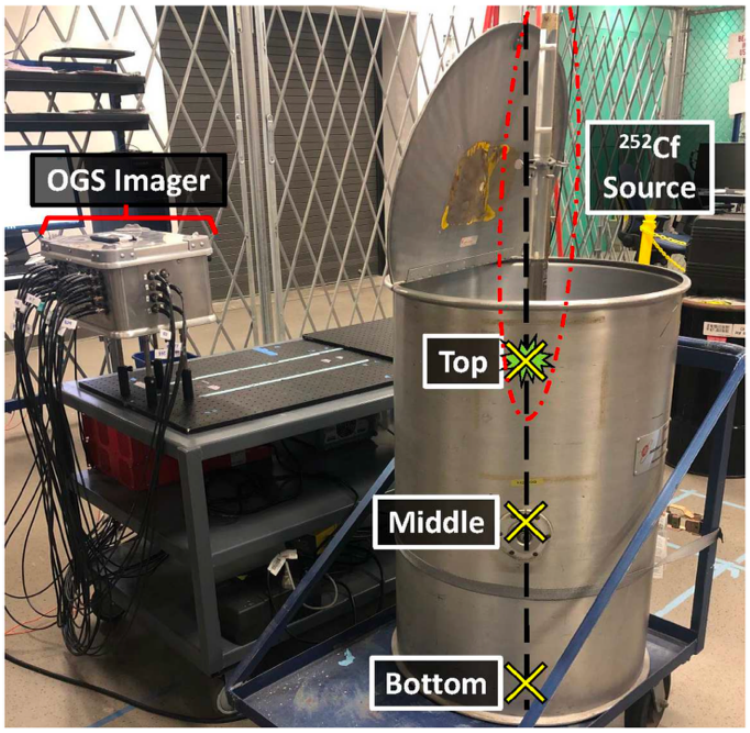

Figure 4.6: Photograph of the experimental setup for the ^{252}Cf stored-source measurements.

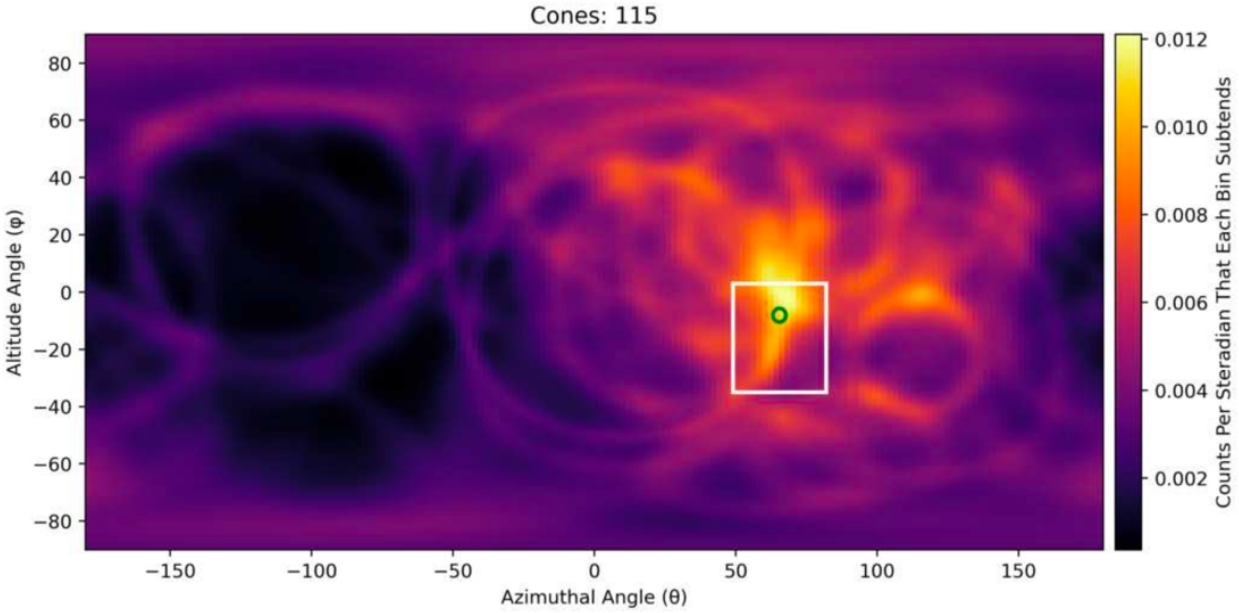

Figure 4.7: Neutron SBP image of ^{252}Cf in the TOP configuration using 115 events. Source location in the FOV indicated by circular outline. Container outline shown as a rectangle.

4.1.3 ^{244}Cm

^{244}Cm, another spontaneous fission source, was also measured in this work. The source consisted of curium oxide encapsulated within a stainless steel capsule of 7 mm diameter and 25 mm length. At the time of measurement, the neutron emission rate was approximately 1.85×10^5 n/s [12], which is substantially lower than the ^{252}Cf source discussed earlier in this chapter. The source was positioned 40 cm from the H2DPI, centered but slightly below the height centerline, resulting in an angular location of $(-3^\circ, -10^\circ)$. The measurement duration was 73 minutes. Figure 4.8 presents the SBP and LM-MLEM neutron images reconstructed from 210 imageable events, both accurately localizing the ^{244}Cm in the FOV. The LM-MLEM image contains fewer artifacts, making it preferable for interpretation.

^{244}Cm is a source of interest for potential future applications of the H2DPI in source inventory verification. As a spontaneous fission source, ^{244}Cm produces neutron spectra similar to the more commonly used ^{252}Cf, but its much longer half-life of 18.11 years makes it a promising substitute for ^{252}Cf in long-term calibration sources and other uses, despite its lower specific activity and neutron multiplicity [12]. An additional advantage of ^{244}Cm is its smaller prompt photon yield [79], which facilitates neutron discrimination and may result in higher neutron imaging rates. Furthermore, ^{244}Cm emits low-energy gamma rays that are valuable for assessing the lower detection limits of the H2DPI's gamma-ray imaging capabilities, as will be discussed in Section 4.2.3. The imaging results for ^{244}Cm demonstrate that the neutron imaging capabilities of the H2DPI extend to sources beyond ^{252}Cf and remain effective even for sources with lower activity at comparable standoff distances.

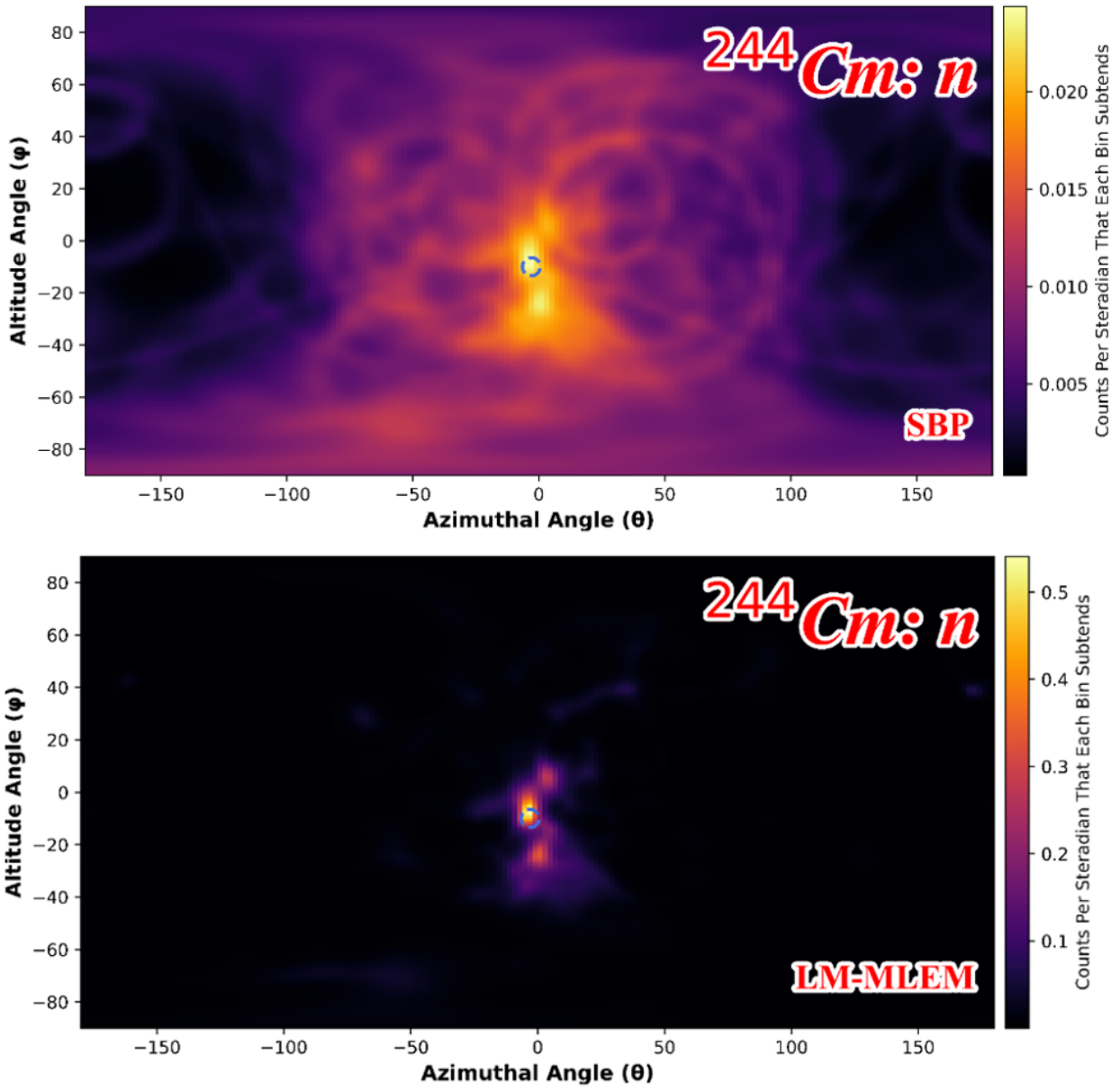

Figure 4.8: Reconstructed SBP and LM-MLEM neutron images of ^{244}Cm. True source location is marked with circular outlines centered at $(-3°, -10°)$.

4.2 Single Source Gamma-Ray Imaging

4.2.1 ^{137}Cs

The first result for gamma-ray imaging is presented for a ^{137}Cs source. The source had an activity of 87 μCi, was positioned 11.36 cm from the imager at an angular direction of $(-26.6^{\circ}, 0^{\circ})$, and was measured for 22 minutes. The gamma-ray coincidence spectrum for imageable events between the OGS and $CeBr_3$ detectors is shown at the top of Figure 4.9, with an energy gate of 662 ± 37 keV applied, as indicated in the spectrum. It should be noted that this window size was chosen based on the energy resolutions discussed in Section 3.1.2. The resulting SBP image comprises 6410 events and successfully localizes the source within the field of view. Application of LM-MLEM for 9 iterations, using the stopping criterion discussed in Section 3.5, yields a substantially more converged image with the image hotspot tightly constrained at the expected source location.

Considering the imaging results from Figure 4.9 alongside the spectral features observed in the coincidence spectrum, it is clear that a single ^{137}Cs source was present in the FOV. This straightforward scenario highlights the fundamental gamma-ray imaging and spectroscopy capabilities of the system under optimal measurement conditions. The data also show that several thousand imageable gamma-ray events can be readily obtained using the source's gamma-ray signatures, which enables shorter measurement times without compromising the quality of image convergence.

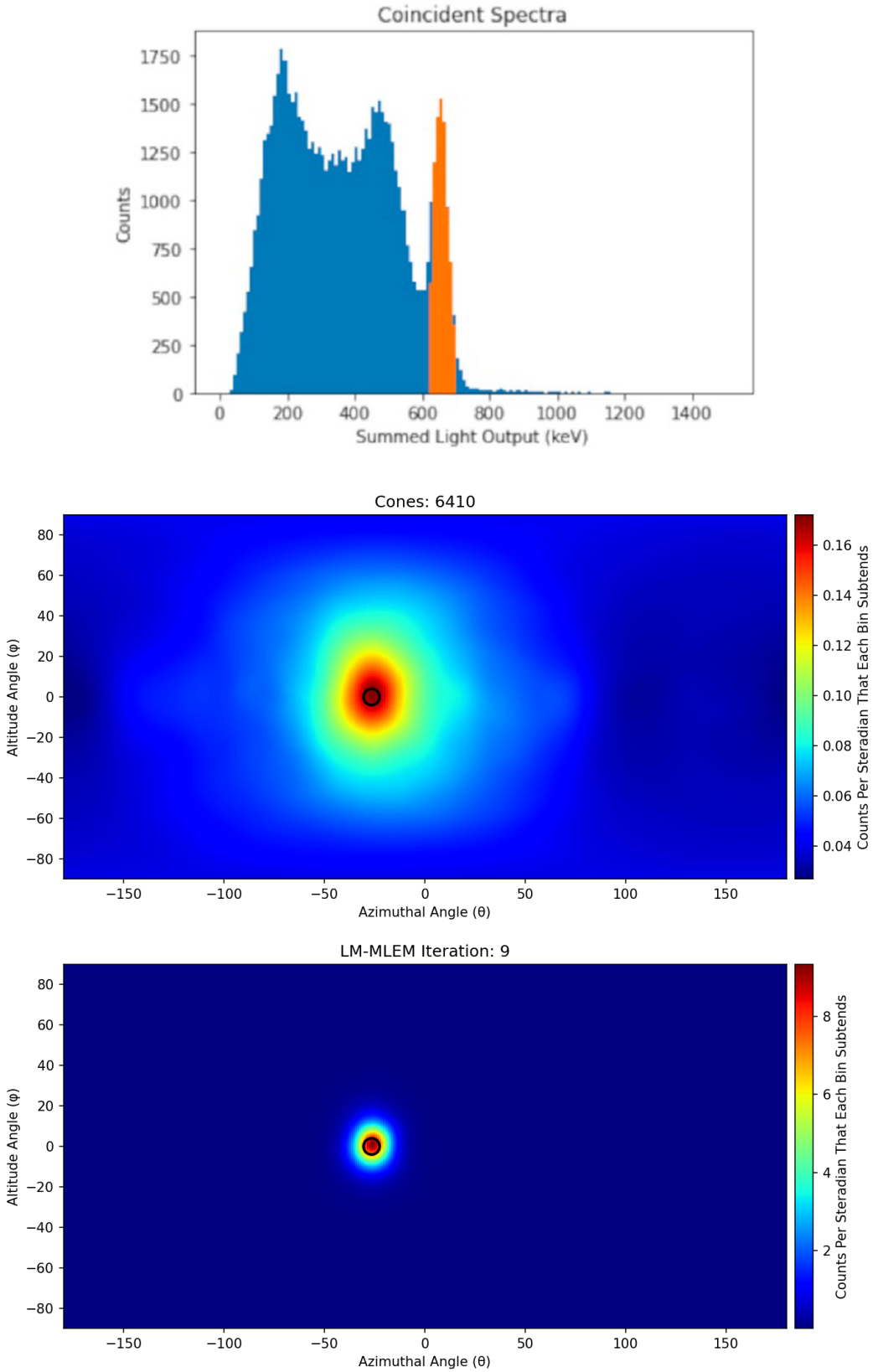

Figure 4.9: Reconstructed SBP and LM-MLEM gamma-ray images of ^{137}Cs with 662 $\pm$ 37 keV energy gate. True source location is marked with circular outlines centered at $(-26.6°, 0°)$.

4.2.2 ^{252}Cf

The same bare ^{252}Cf source discussed in Section 4.1.1 can also be imaged using gamma rays. In this case, no energy gate was applied, as ^{252}Cf emits a continuum of gamma-ray energies rather than discrete photopeaks. Although the full measurement time yielded 76210 events, Figure 4.10 displays the gamma-ray SBP image generated from a subset of 25000 events, along with the corresponding LM-MLEM image after four iterations. The number of cones was limited to reduce the required computation time for the LM-MLEM image reconstruction process. The subset of 25000 represents an equivalent measurement time of approximately 55 minutes. Despite using only a subset of the total data, the images exhibit strong convergence at (20°, 0°), demonstrating successful localization of the ^{252}Cf source using its gamma-ray signature.

A comparison of the neutron images from Section 4.1.1 demonstrates that the gamma-ray SBP image is more symmetric along both the altitude direction. This effect may be attributed to gamma-ray imaging using the $CeBr_3$, which do not require the same Z-coordinate reconstruction process. It is also evident that gamma-ray imaging yields significantly more imageable events compared to neutron imaging. For example, 9758 neutron events were collected over 170 minutes, whereas 25000 imageable gamma-ray events were obtained in just 55 minutes. As a result, gamma-ray imaging appears to be preferable for source localization, given its higher count rates and the shorter measurement times needed to produce SBP images suitable for localization. To further demonstrate this capability, Figure 4.11 presents the SBP gamma-ray image produced from only five minutes of data acquisition (2210 events), clearly showing that source presence and localization can be achieved within a brief measurement period.

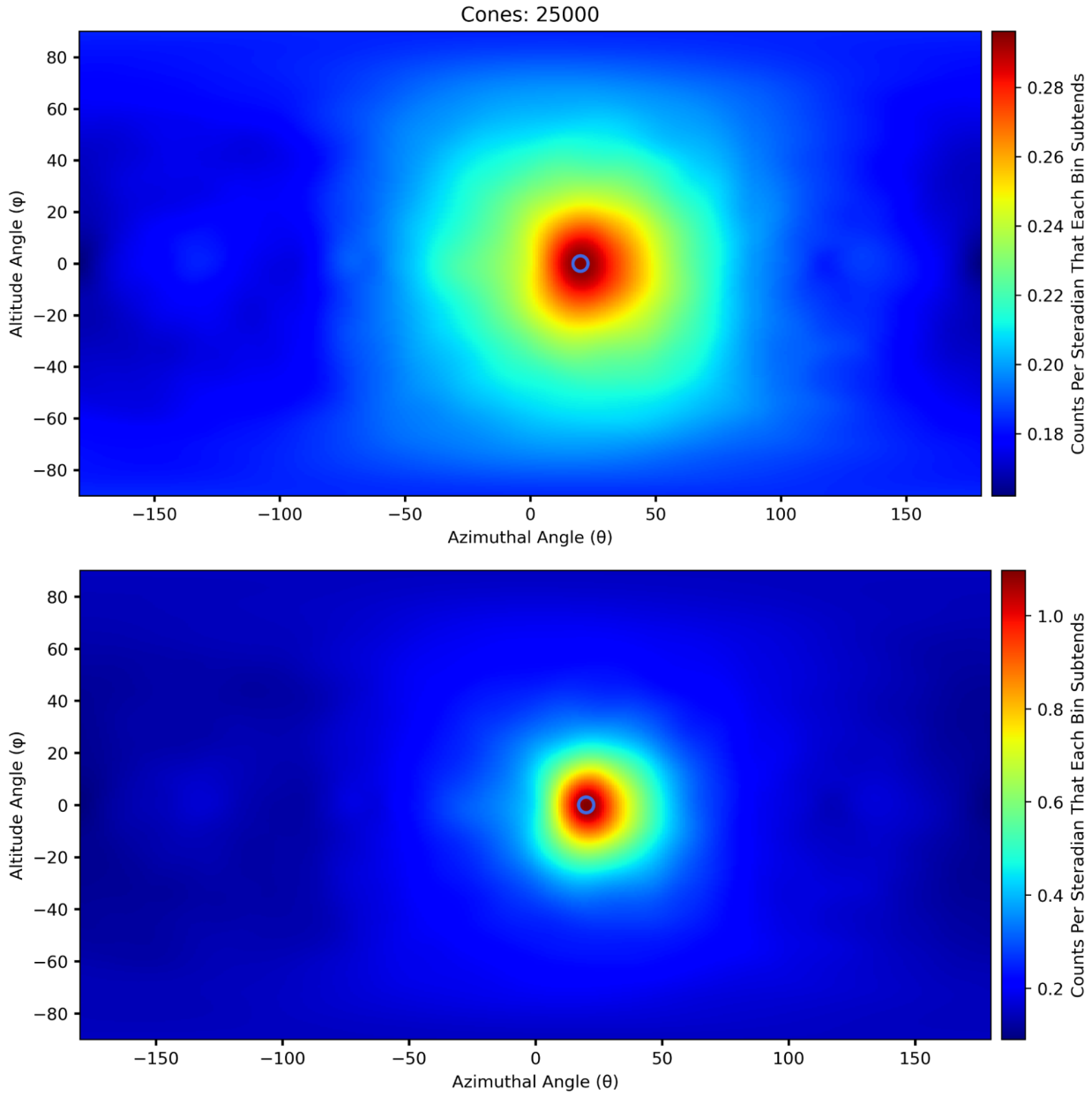

Figure 4.10: Gamma-ray SBP image of ^{252}Cf reconstructed using 25000 events (top). Corresponding LM-MLEM image (bottom). True source location is marked with circular outlines centered at (20°, 0°).

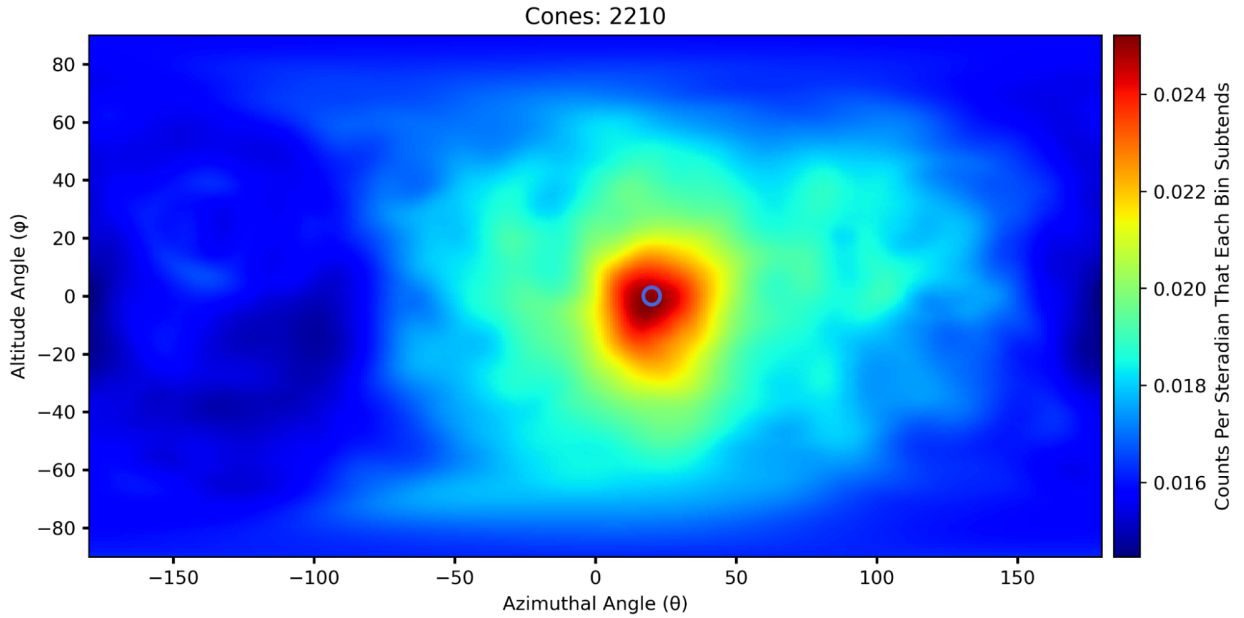

Figure 4.11: Gamma-ray SBP image of ^{252}Cf reconstructed using 2210 events from 5 minutes of data collection. True source location is marked with a circular outline centered at (20°, 0°).

4.2.3 ^{244}Cm

The same ^{244}Cm source described in Section 4.1.3 was also imaged using gamma rays. This source has an emission at 152.6 keV, which is of interest for imaging. Notably, this energy range is challenging for gamma Compton imagers, as most commercially available systems either have thresholds of 150 keV or are limited to higher energies [80, 81] making the imaging of these energies impossible for this system. An energy gate of 140–160 keV was applied to isolate this photopeak. The top panel of Figure 4.12 displays the gamma-ray coincidence spectrum obtained for the ^{244}Cm measurement, while the bottom panel shows the corresponding SBP and LM-MLEM gamma images constructed from 150 events. Circular outlines at $(-3°, -10°)$ mark the location of the ^{244}Cm source in the field of view. The SBP image shows a prominent hotspot in the FOV, while the LM-MLEM image converges to a small area near the anticipated source location. The observed spatial deviation is attributed to the limited number of imaging events and the worse energy resolution of the detectors at 150 keV, which causes smearing in the SBP image and consequently impacts

the LM-MLEM reconstruction. To emphasize the impact of energy gating, Figure 4.13 shows the resulting SBP and LM-MLEM images with no gate applied to the data set and using a subset of 2000 events. The reconstructed images clearly do not converge at any specific location in the FOV with high confidence, making source localization impossible unless appropriate energy gating is used when feasible.

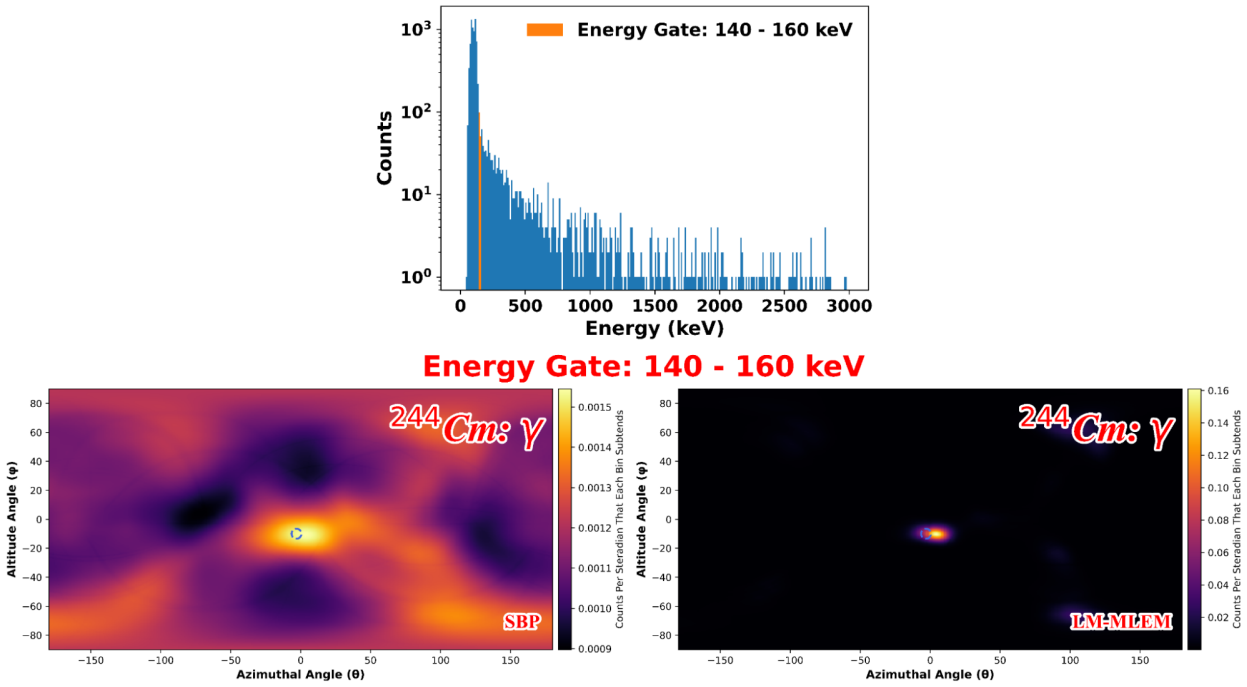

Figure 4.12: Gamma ray coincidence spectrum from ^{244}Cm with a 140-160 keV energy gate (top). Gamma-ray SBP and LM-MLEM reconstructed using 150 events (bottom). True source location is marked with circular outlines centered at $(-3°, -10°)$.

4.2.4 ^{237}Np

A noteworthy isotope that is not classified as SNM is ^{237}Np, as it can serve as an indicator of nuclear reactor irradiation [9]. ^{237}Np is produced through an (n, 2n) reaction on ^{238}U or by multiple neutron captures on ^{235}U [82]. Since these reactions occur in environments typical of nuclear reactors, ^{237}Np is among the actinides present in irradiated nuclear fuel. Accordingly, the detection of ^{237}Np is of interest for nuclear reactor safeguards and nonproliferation initiatives. In this work, two gamma-ray emissions that can be used to identify ^{237}Np originate from its daughter isotope ^{233}Pa:

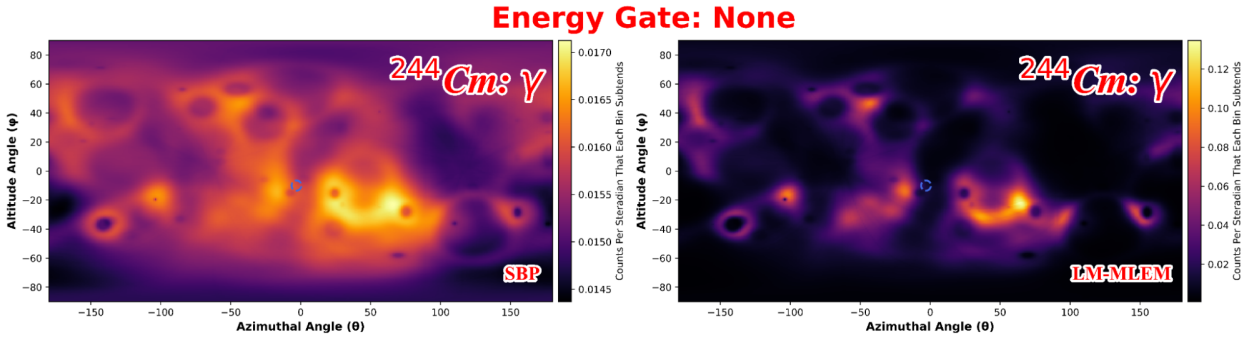

Figure 4.13: Gamma-ray SBP image of ^{244}Cm reconstructed using 2000 events with no energy gate applied. Corresponding LM-MLEM image. True source location is marked with circular outlines centered at $(-3°, -10°)$.

312 keV and 416 keV.

The source used in this measurement was a 6 kg ^{237}Np metal sphere (98.8 wt% Np), from the National Criticality Experiments Research Center operated by Los Alamos National Laboratory at the Nevada National Security Site [83]. The sphere has an outer diameter of 9.64 cm and an activity of approximately 4.2 Ci. Relative to the H2DPI, the ^{237}Np sphere was positioned 100 cm away at an angular position of $(-90°, -5°)$, as depicted in Figure 4.14. The total measurement time was 45 minutes.

The left plot in Figure 4.15 shows the detected gamma-ray energy spectrum compiled from all single events across the eight CeBr3 detectors in the H2DPI. The red dashed lines mark the 312 and 416 keV gamma-ray photopeaks, corresponding to prominent emissions from the daughter ^{233}Pa. The right plot in Figure 4.15 presents the measured gamma coincidence spectrum between the OGS and CeBr3 detectors, with red highlighted regions at 275–325 keV and 380–440 keV indicating the chosen energy gates for subsequent gamma-ray image reconstruction. Figure 4.16 presents the SBP gamma-ray images produced using the two previously described energy gates, following application of the LM-MLEM convergence algorithm. The true source location in angular space is indicated by a green outline, and both the lower and higher energy gamma images show good agreement with the actual position of the ^{237}Np sphere. This energy filtering capability can prove valuable in scenarios where multiple sources may be present in the field of view, enabling selective

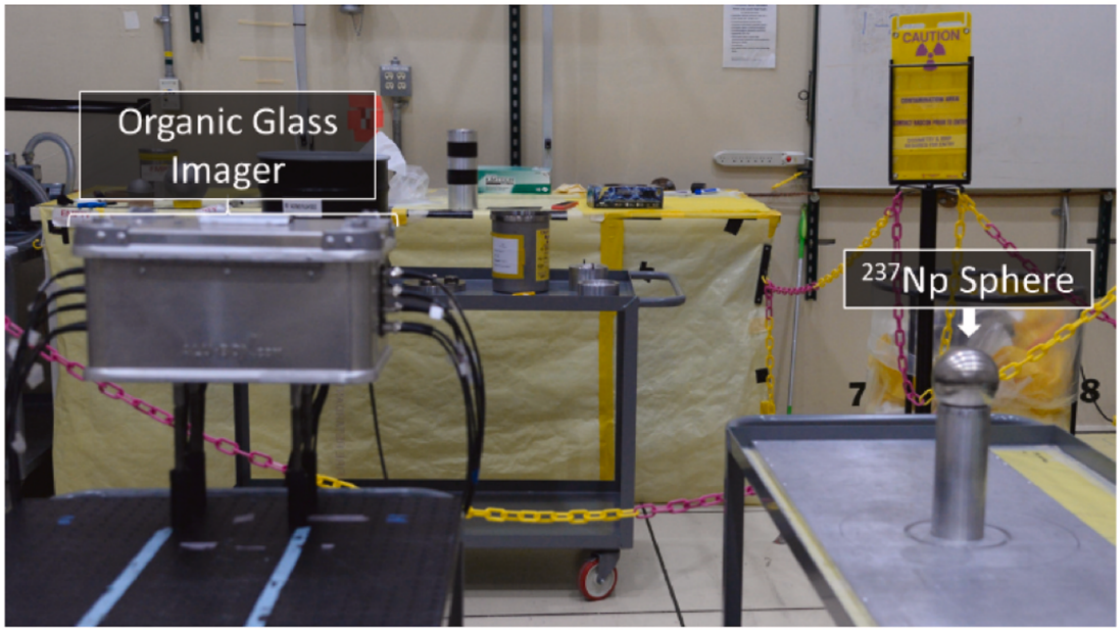

Figure 4.14: Photograph of the experimental setup for the ^{237}Np sphere measurement at the National Criticality Experiments Research Center.

imaging of ^{237}Np when it is the isotope of interest.

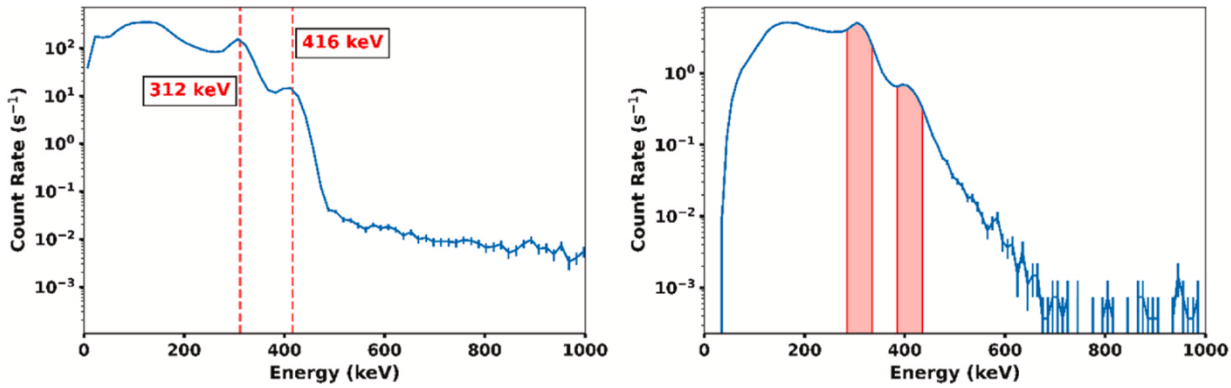

Figure 4.15: Extracted gamma ray spectrum obtained from single events across all eight $CeBr_3$ with 312 keV and 416 keV lines emphasized (left). Gamma coincidence spectrum between OGS and $CeBr_3$ with the two energy gated regions to be used for imaging highlighted in red (right).

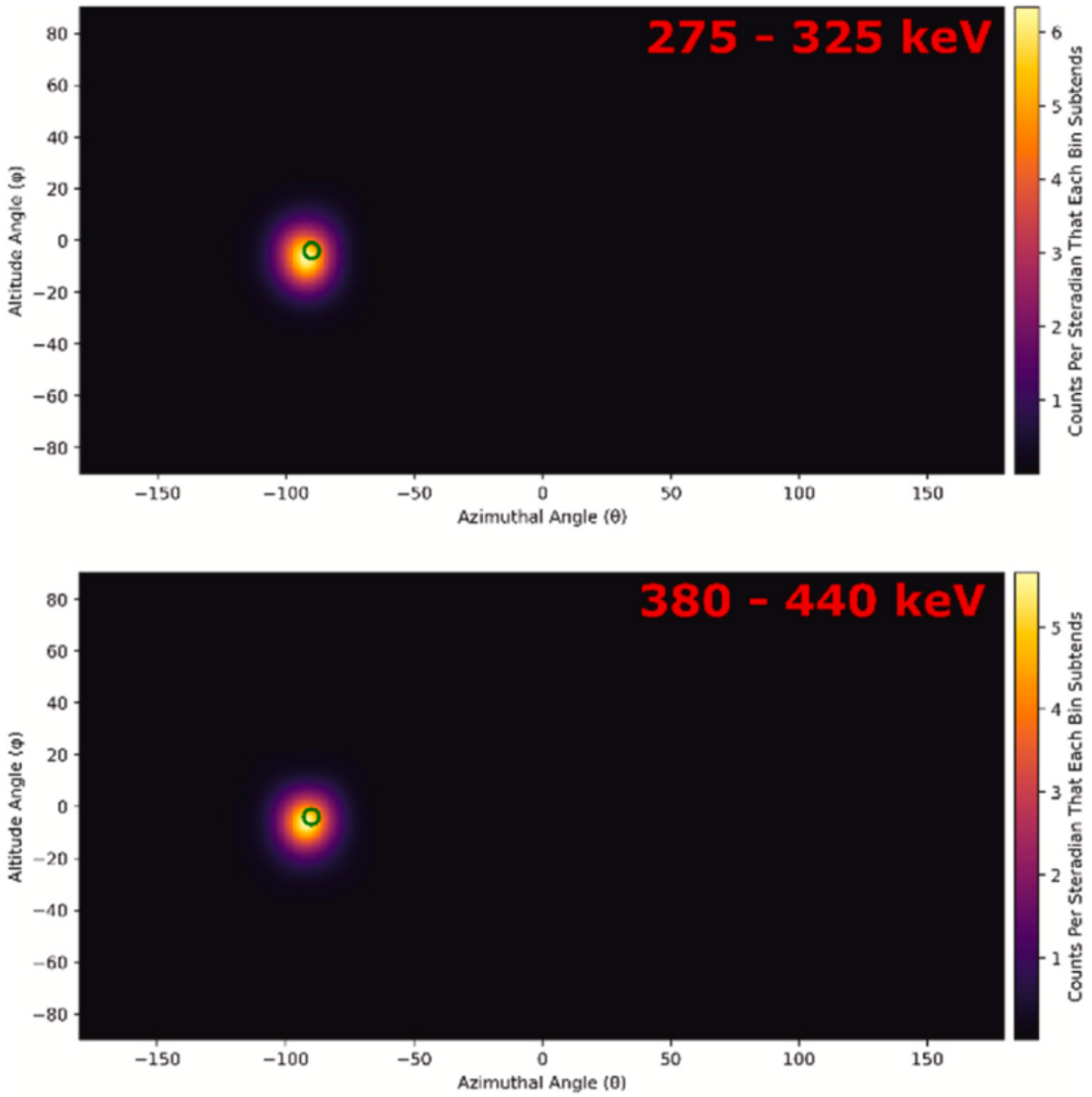

Figure 4.16: ^{237}Np LM-MLEM gamma-ray images produced using energy gates of 275 – 325 keV (top) and 380 – 440 keV (bottom). True source location is marked with circular outlines centered at $(-90°, -5°)$.

An additional analysis was conducted to evaluate the speed at which the imaging system could localize the ^{237}Np sphere without energy gating. Figure 4.17 illustrates the SBP and LM-MLEM images created using data collected over 1, 5, and 30 seconds of measurement time. The results indicate that with just 1 second of data, low statistics in both the SBP and LM-MLEM images

prevented reliable deduction of the source location. In contrast, acquisition times of 5 seconds or longer were sufficient to achieve source localization.

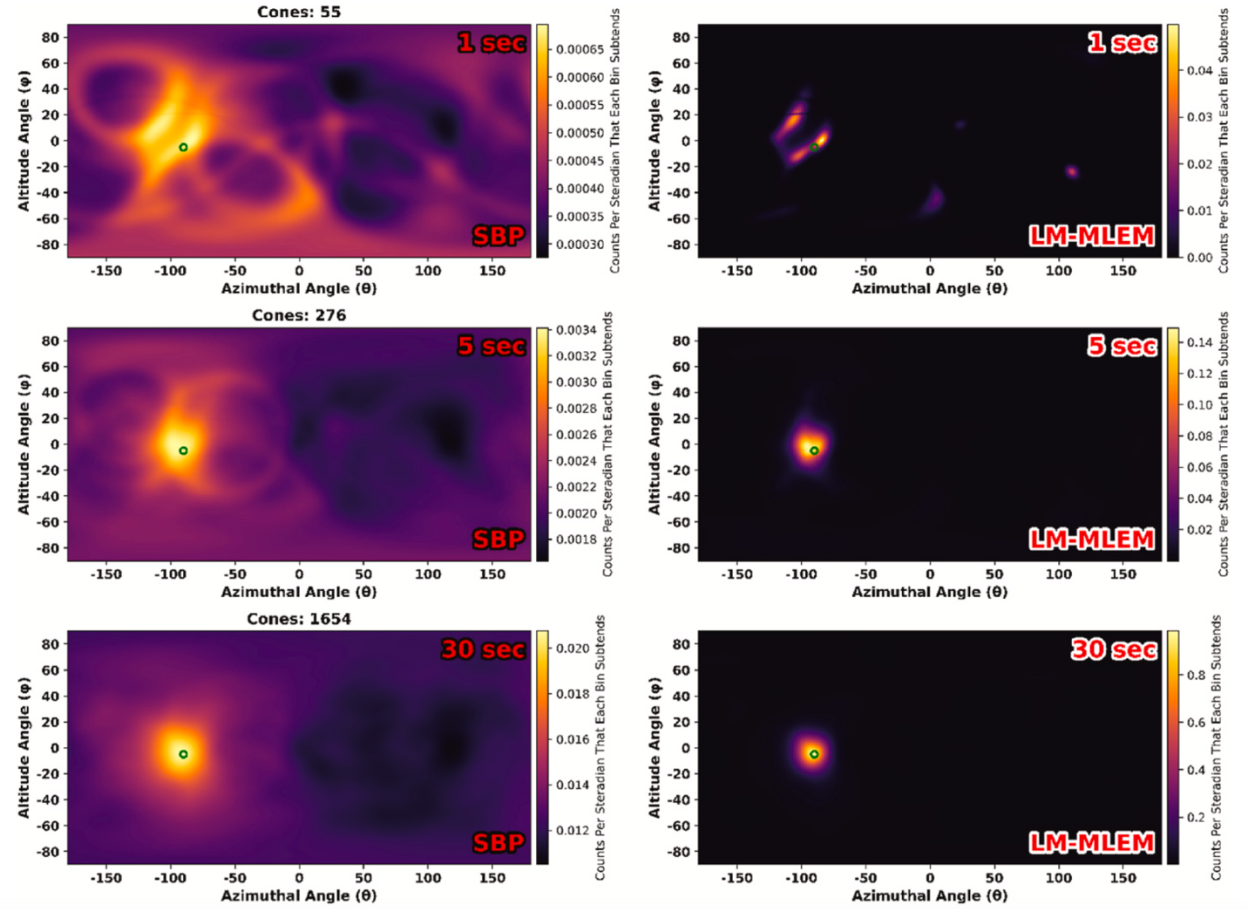

Figure 4.17: Comparison of gamma images of ^{237}Np generated using no applied energy gate on data from time allocations of 1, 5, and 30 s. The left column shows SBP images while the right column shows the same images after applying the LM-MLEM. True source location is marked with circular outlines centered at $(-90°, -5°)$.

4.3 Multisource Imaging and Spectroscopy Capabilities

4.3.1 Multisource Neutron Imaging and Spectroscopy

An experiment was performed to demonstrate the neutron source localization capabilities of the system when multiple sources were present within the FOV: two neutron sources and one gamma-

ray source. A PuBe source was positioned 36.37 cm from the system at $(-25°, 0°)$, a ^{252}Cf source was placed 58.42 cm away at $(25°, 0°)$, and a ^{137}Cs gamma-ray source was placed 20.32 cm from the imager at $(90°, 0°)$, as illustrated in Figure 4.18. The PuBe neutron source had a neutron emission rate of 1.7×10^6 neutrons per second (activity 1 Ci), while the ^{252}Cf neutron source had an emission rate of 4.4×10^6 neutrons per second (activity 1021 μCi). The activity of the ^{137}Cs gamma source was 86.7 μCi. The total measurement time was 2 hours. Figure 4.19 presents the neutron SBP image reconstructed from 17412 events. The image exhibits a two-lobed converged hotspot, suggesting the presence of either a disturbed neutron source or multiple sources. After 13 iterations of LM-MLEM, also shown in Figure 4.19, the image reveals two distinct source hotspots. The reconstructed positions for the PuBe and ^{252}Cf neutron sources based on the LM-MLEM data were $(-25.1°, 1.5°)$ and $(25.1°, 1.5°)$, respectively, which is in good agreement with the true positions.

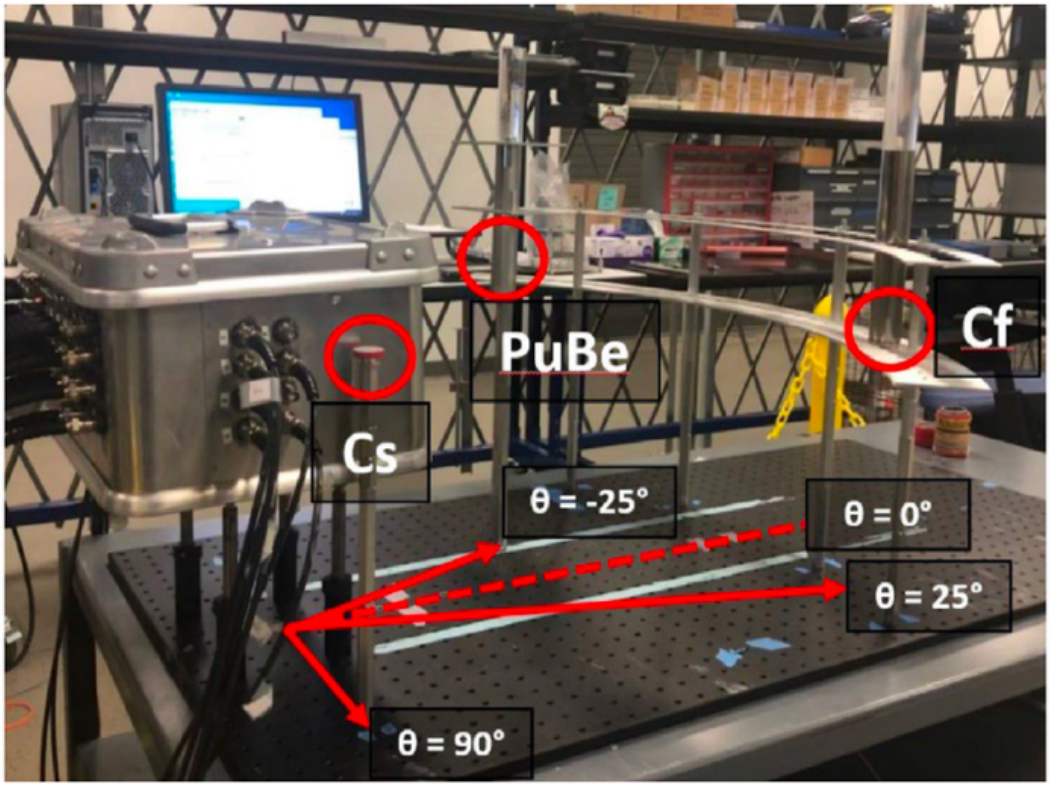

Figure 4.18: Photograph of the experimental setup for the multisource neutron measurement with azimuthal angular directions of the sources noted.

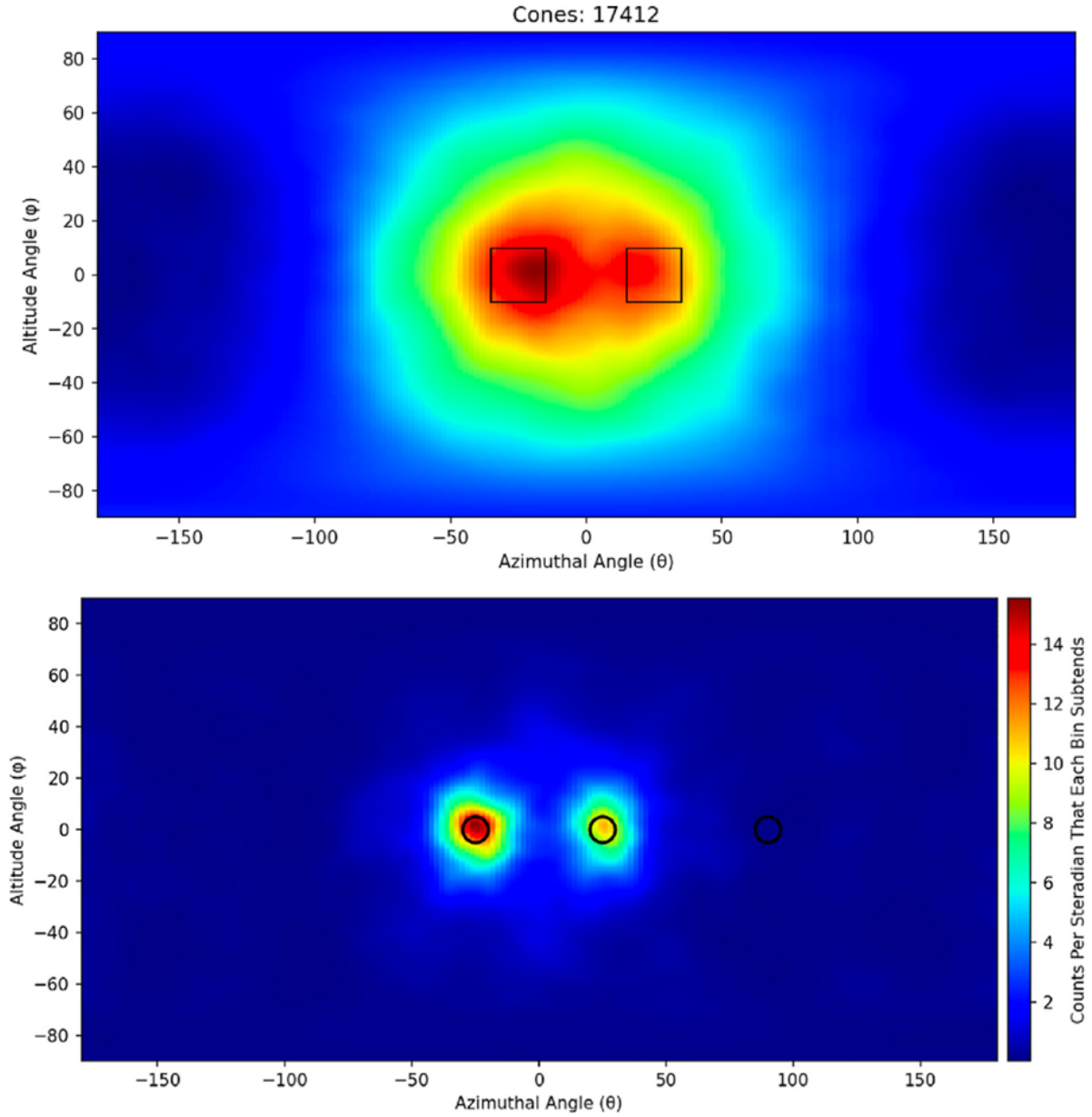

Figure 4.19: Neutron SBP image reconstructed using 17412 events (top). Corresponding LM-MLEM image (bottom). True source locations are marked in the LM-MLEM image with circular outlines centered at $(-25°, 0°)$, $(-5°, 0°)$, and $(90°, 0°)$ for the PuBe, ^{252}Cf, and ^{137}Cs, respectively. The SBP image shows boxed regions used in the neutron spectroscopy analysis.

The imaging data was subsequently used to perform coarse fast neutron spectrometry. Figure 4.20 displays the extracted neutron spectra for the PuBe and ^{252}Cf sources. Spectra were generated by selecting boxed regions centered at the converged locations of each source, extending

$\pm 10^{\circ}$ in both the azimuthal and altitude directions. The total neutron energies of cone projections that intersected these boxed regions were counted, with those intersecting more than one region excluded from analysis. The spectrometry results show that the shape of the ^{252}Cf neutron spectrum is consistent with expectations, while the extracted PuBe spectrum exhibits a harder profile, as indicated by the greater number of higher energy neutrons. This is consistent with the physics expectation that the average neutron energy of ^{252}Cf is lower than that of PuBe, and the measured results reflect this trend.

The multi-neutron source results presented in this section demonstrate that the OGS H2DPI is capable of imaging multiple sources simultaneously within the FOV and possesses neutron spectroscopy capabilities sufficient to differentiate between distinct neutron source types. These features significantly enhance the system's potential utility for applications such as IEEE verification, where several sources of varying types may be present and accurate characterization of each is required.

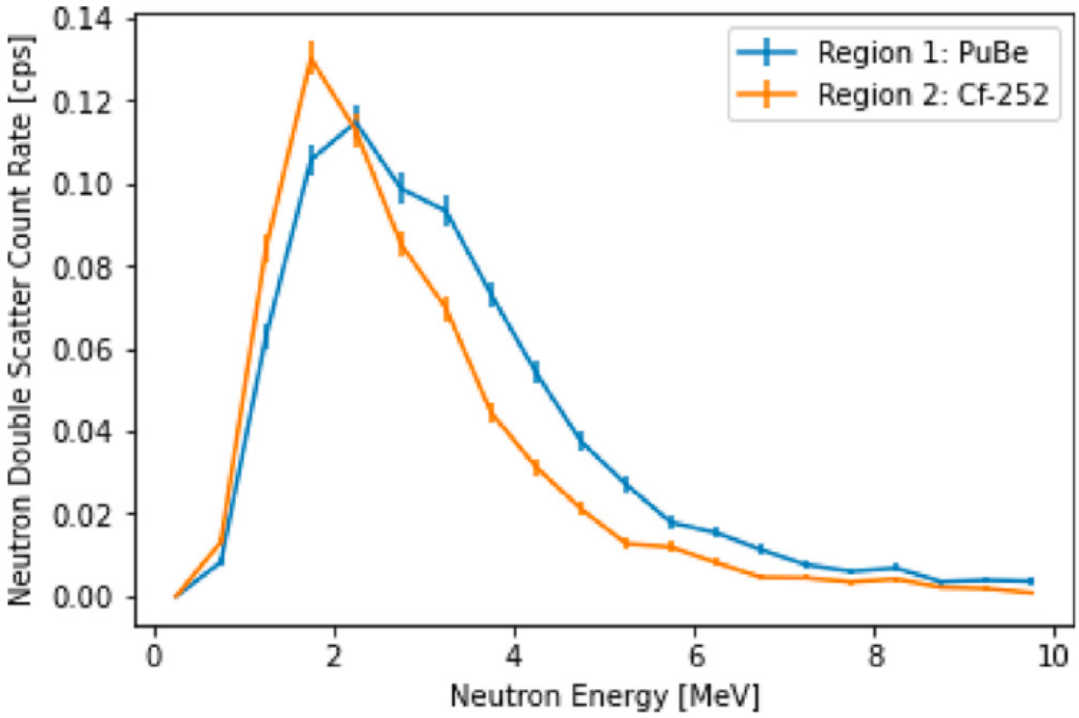

Figure 4.20: Extracted neutron spectra from PuBe and ^{252}Cf sources.

4.3.2 Multisource Gamma-Ray Imaging and Spectroscopy

This subsection demonstrates the capability of the system for gamma-ray source localization when multiple sources are present in the FOV simultaneously. A ^{22}Na source (20.3 μCi) was positioned 23.42 cm from the system at $(-50°, 0°)$, while a ^{137}Cs source (86.7 μCi) was placed equidistantly at $(50°, 0°)$. Figure 4.21 shows the experimental setup, with a total measurement time of 2 hours. Figure 4.22 presents the coincident gamma-ray spectrum collected during the measurement, with two highlighted energy gate regions for source localization: 511 ± 33 keV for ^{22}Na and 662 ± 37 keV for ^{137}Cs. The spectrum shows prominent peaks at 511 keV and 662 keV, providing valuable signatures if the sources had not been known. Using Equation 3.3 and Gaussian fits, the energy resolutions for the coincidence data at 511 keV and 662 keV were calculated to be $10.4 \pm 0.3\%$ and $8.2 \pm 0.2\%$, respectively. Given the energy resolutions discussed in Chapter 3, the resolutions from the coincidence spectrum, which is a convolution of OGS and $CeBr_3$, are reasonable.

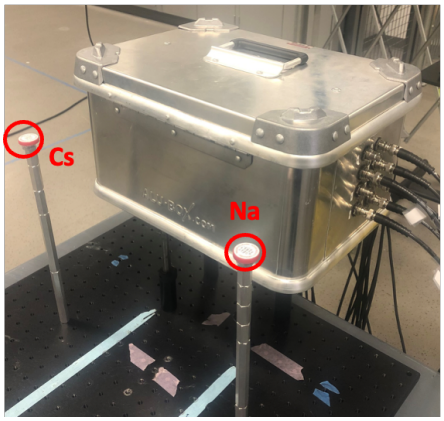

Figure 4.21: Photograph of the experimental setup for the multisource gamma-ray measurement.

Figure 4.23 shows a series of LM-MLEM gamma-ray images generated with different energy gate settings. The top image shows that when no energy gate is applied, both sources are clearly localized, with distributions consistent with their expected positions. Application of specific energy gates allows selective discrimination between individual sources, even in the presence of multiple emitters. The middle image illustrates the reconstructed position of the ^{22}Na source following energy gating and 14 iterations of LM-MLEM, while the bottom image shows the ^{137}Cs recon-

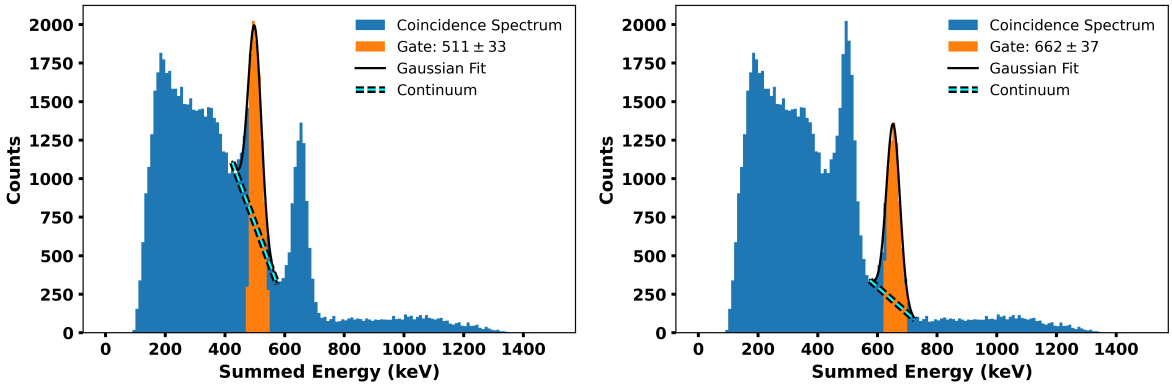

Figure 4.22: Gamma coincidence spectrum between OGS and $CeBr_3$ with the two energy gated regions to discriminate for ^{22}Na (left) and ^{137}Cs (right).

struction after energy gating and 8 LM-MLEM iterations. The reconstructed source positions were $(-48.6°, 0.3°)$ for ^{22}Na and $(48.6°, 0.3°)$ for ^{137}Cs.

It is important to note that when multiple sources are present in the FOV, the LM-MLEM algorithm tends to converge on the source with the greatest intensity. If two sources of similar intensity are present, LM-MLEM may oscillate between them, continuously attempting to converge on one or the other. Energy gating provides a powerful means to focus on specific sources of interest.

Gamma-ray source localization with multiple sources in the FOV also remains effective when the sources are of the same isotope, where energy gating is insufficient for discrimination. An experiment was conducted at Lawrence Livermore National Laboratory within a low-scatter building (approximately 12 m-high ceiling and a 3 m-deep void beneath the flooring) to measure ^{232}Th. ^{232}Th is a fertile isotope that has long been considered a candidate for nuclear fuel, with decades of research exploring the feasibility of its own fuel cycle, comparable to uranium [84]. Regarding gamma emissions relevant for imaging, ^{232}Th possesses several, and Table 4.2 summarizes the six gamma emissions utilized in this work.

Table 4.2: Summary of emissions of interest for gamma-ray imaging of ^{232}Th

	Energies (keV)		
^{232}Th	238.6	338.3	583.2
	911.2	964.8	969.0

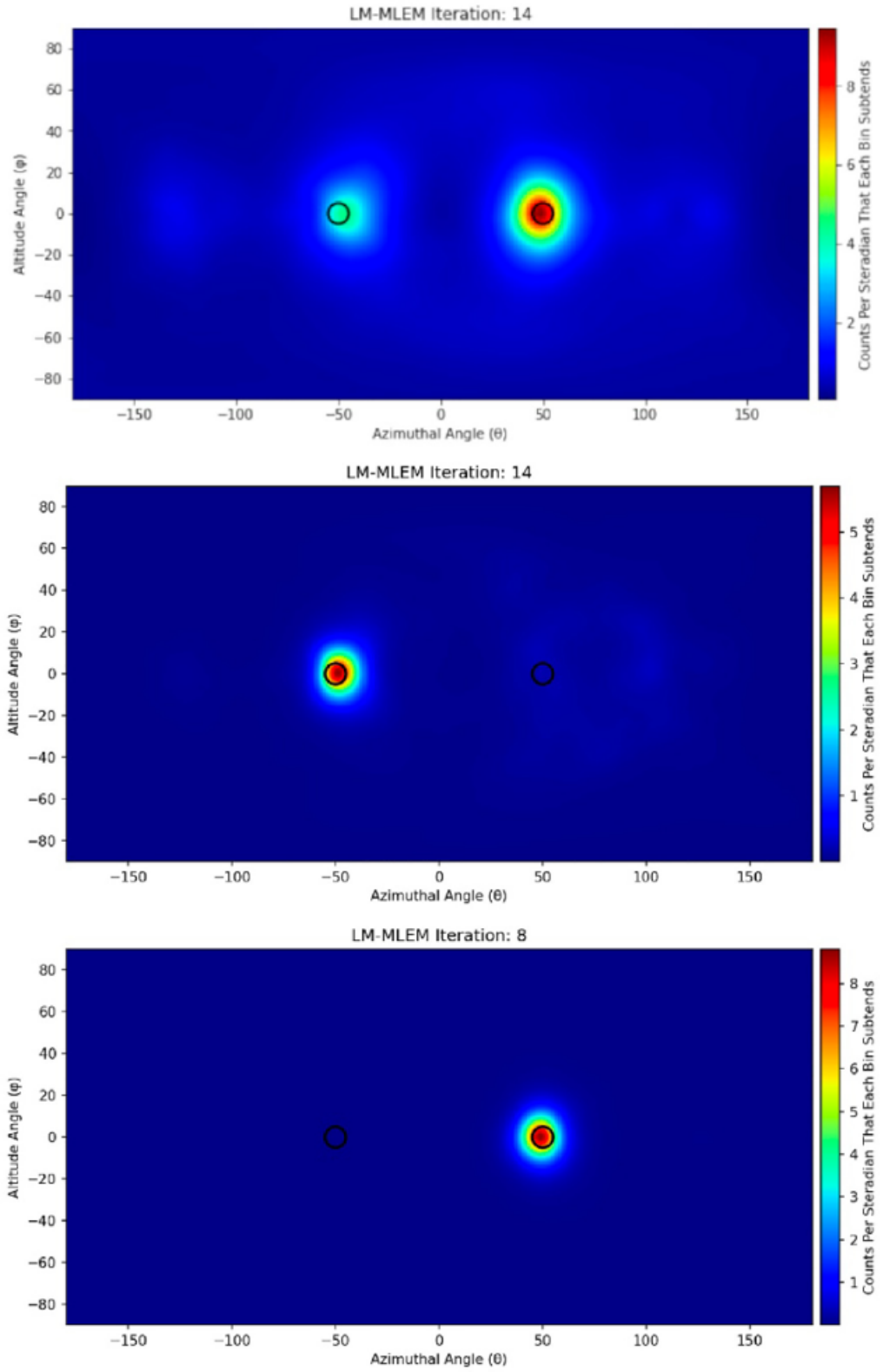

Figure 4.23: LM-MLEM gamma-ray images produced using no energy gate (top), 511 $\pm$ 33 keV (middle) and 662 $\pm$ 37 keV (bottom). True source locations are marked with circular outlines centered at $(-50^\circ, 0^\circ)$ and $(50^\circ, 0^\circ)$ corresponding to ^{22}Na and ^{137}Cs, respectively.

The sources used for the experiment consisted of two thin hemishells of ^{232}Th metal. Each hemishell had an outer diameter of 12.4 cm, a thickness of 0.1 cm, and a mass of approximately 590 g. The hemis were positioned side-by-side, 37 cm from the center of the H2DPI, as depicted in Figure 4.24. They were roughly aligned with the centerline height of the H2DPI and centered facing the front of the system. The centers of the two hemis were located at $(-12°, -5°)$ and $(12°, -5°)$. The measurement time was 87 minutes.

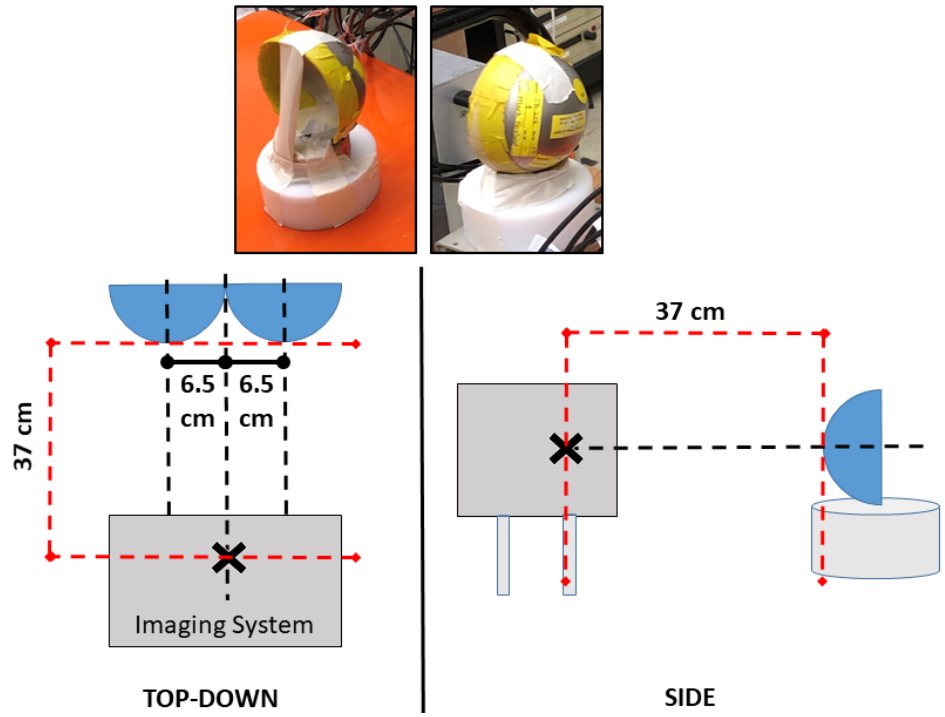

Figure 4.24: Photographs of the ^{232}Th hemishells used for the measurement (top). Schematics of the experimental setup shown from the top-down and side views (bottom).

SBP and LM-MLEM gamma-ray images of the ^{232}Th hemis were first generated without energy gating, as shown in Figure 4.25. Due to the large number of imageable events when no energy gate is applied, the analysis was limited to a subset of 4300 cones. Contrast profiles were calculated by making cuts in both the azimuth and altitude directions at the expected locations of the ^{232}Th hemi centers in the SBP and LM-MLEM images. Full Width at Half Maximum (FWHM) metrics were then determined by fitting Gaussian functions to the contrast profiles for each hemishell. In the SBP image, the FWHMs for the left hemi were $36°$ and $66°$ for the azimuth and altitude directions,

respectively, while the right hemi exhibited FWHMs of 31° and 57°. For reference, each hemishell occupied a 25°-wide footprint in both angular directions within the FOV. The resolution in the altitude direction is noticeably poorer, which can be attributed to the introduction of uncertainty during Z-coordinate reconstruction along the OGS bar and the limited number of $CeBr_3$ detectors in the system that restricts the possible imageable scattering events. Placing additional $CeBr_3$ detectors at varying Z positions would help to address this systematic issue and improve the altitude resolution. In the LM-MLEM image, the FWHMs for the left hemi were reduced to 22° and 33° for azimuth and altitude, respectively, and to 21° and 24° for the right hemi. As anticipated, the LM-MLEM process constrains the localized source hotspots, thereby facilitating easier and more accurate localization. It should be noted that the FWHMs provided were obtained using double gaussian fits on the angular profile distrubtions in Figure 4.25 within the range of $[-30^\circ,30^\circ]$.

The top panel of Figure 4.26 presents the gamma-ray spectroscopy results obtained by summing all single detection events across the eight CeBr3 detectors in the H2DPI. The ^{232}Th spectrum shows good agreement with the expected photopeaks from daughter isotopes ^{212}Pb, ^{208}Tl, and ^{228}Ac. The identified lines led to the selection of the following energy gates for imaging: 200–250 keV, 300–350 keV, 500–600 keV, and 850–975 keV. The subsequent plots in Figure 4.26 display the gamma-ray coincidence energy spectrum for the ^{232}Th measurement, with the four energy gates corresponding to emissions of interest.

Figure 4.27 presents the reconstructed SBP and LM-MLEM gamma-ray images generated by applying each energy gate. The number of imageable gamma-ray events in each energy gate were as follows: 7883 for 200–250 keV, 5007 for 300–350 keV, 3073 for 500–600 keV, and 1224 for 850–975 keV.A general observation from the four SBP images is that, as higher energy gates are applied, image artifacts diminish and background noise significantly decreases relative to the converged source location. This trend is primarily due to the removal of coincident Compton scatter events from the data sets. As the coincidence spectrum in Figure 4.26 indicates, a pronounced continuum is present at lower energy regions; this continuum diminishes with increasing total energy deposition. The continuum at lower energies includes a greater proportion of double Compton

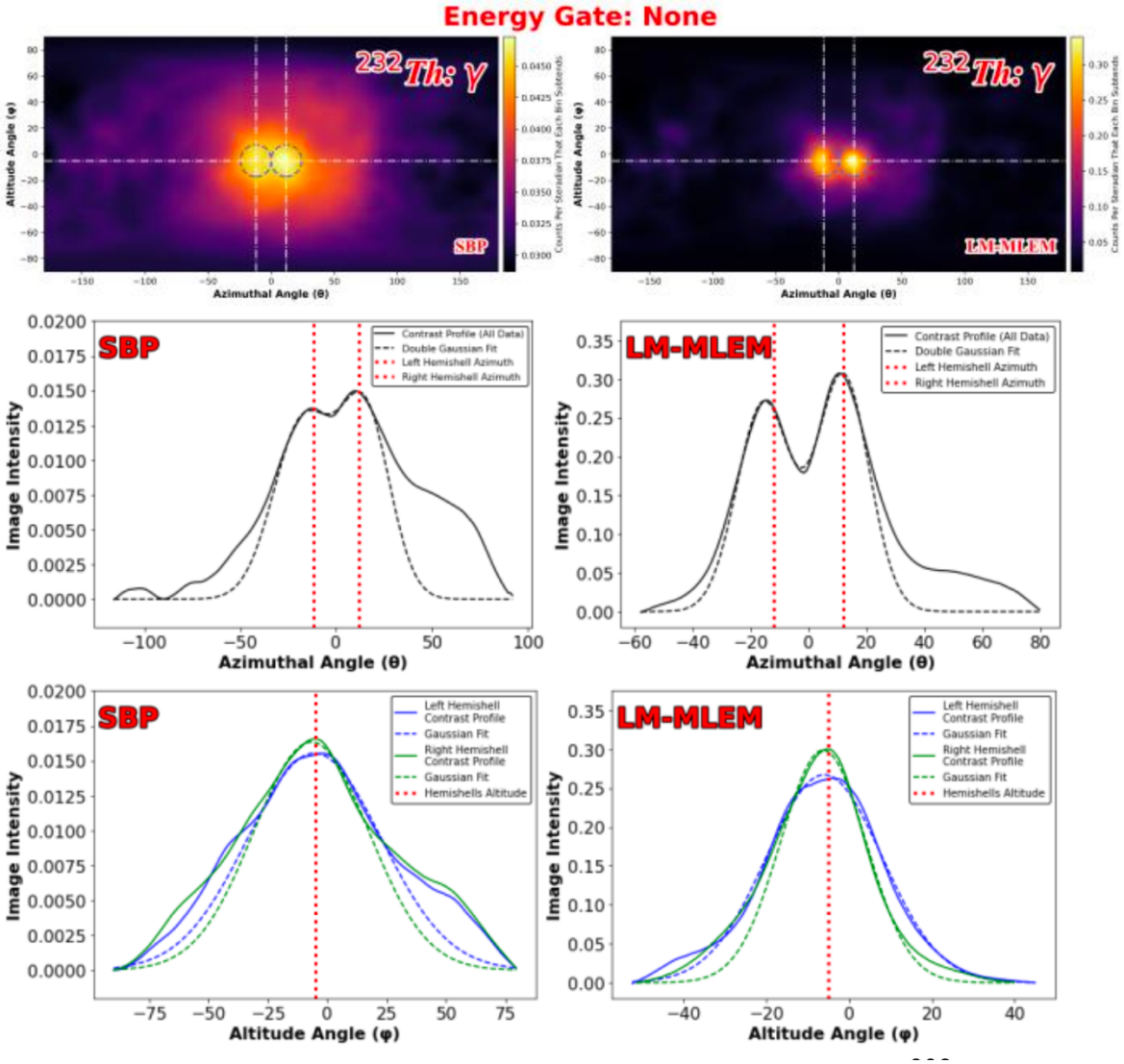

Figure 4.25: Reconstructed SBP and LM-MLEM gamma ray images of the ^{232}Th hemis with no energy gate applied and 4300 events (top). Circular outlines represent the locations of the hemis in the FOV. Contrast 2D profiles for the azimuth (middle) and altitude (bottom) directions of the SBP and LM-MLEM images according to the white dashed lines.

scatter coincidences, which derive from higher energy gamma rays. These double Compton scatter events degrade the quality of SBP images, as the assumptions of Equation 3.12 no longer hold, resulting in erroneous reconstruction. Figure 4.13 shown earlier in the chapter for the no energy gating case of ^{244}Cm emphasizes how source location attempts can be ruined by having too many double Compton scatters in the image.

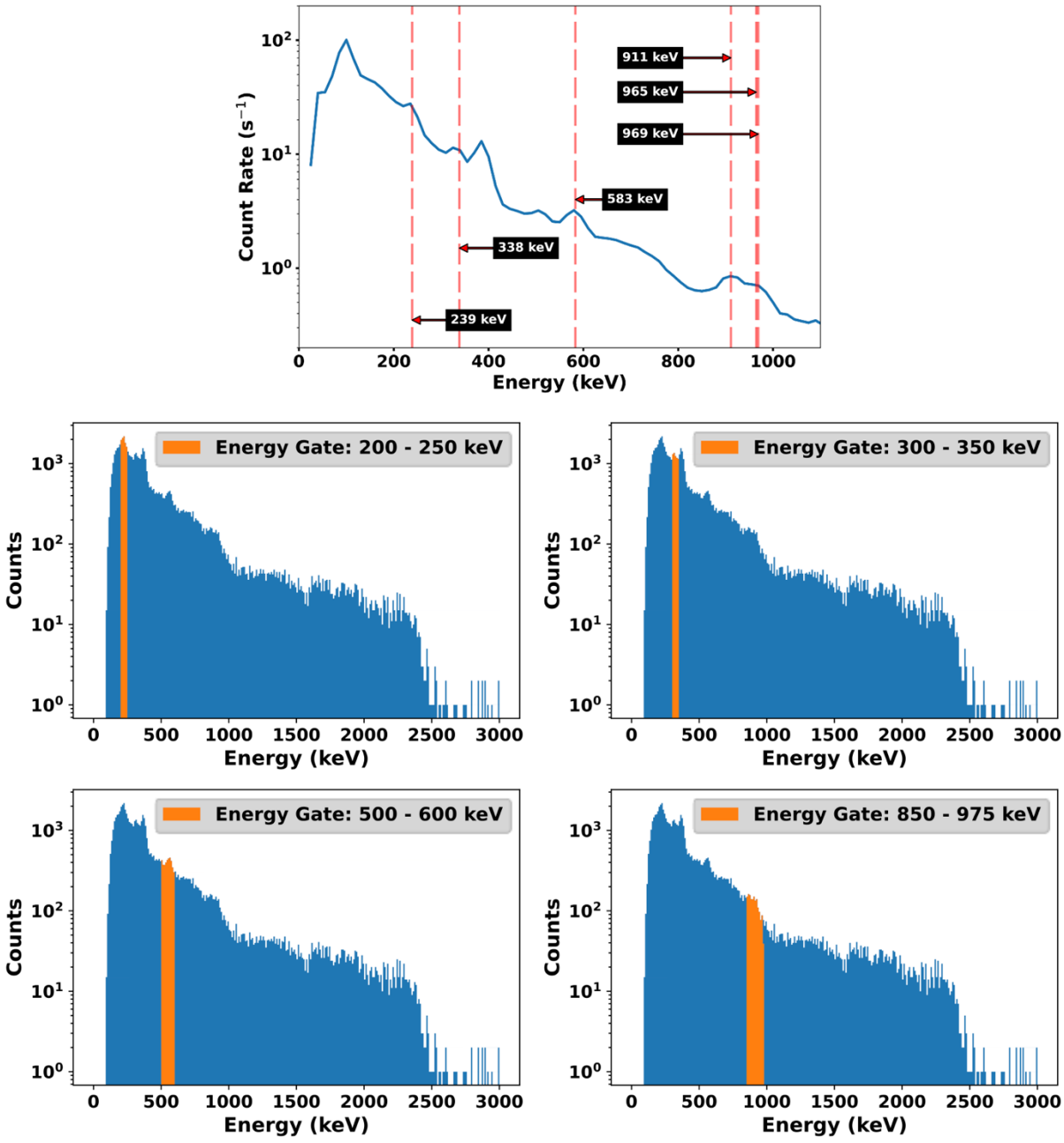

Figure 4.26: $CeBr_3$ gamma-ray energy spectra for the ^{232}Th (top). Coincident spectra for the with various energy gates applied: 200–250 keV, 300–350 keV, 500–600 keV, and 850–975 keV.

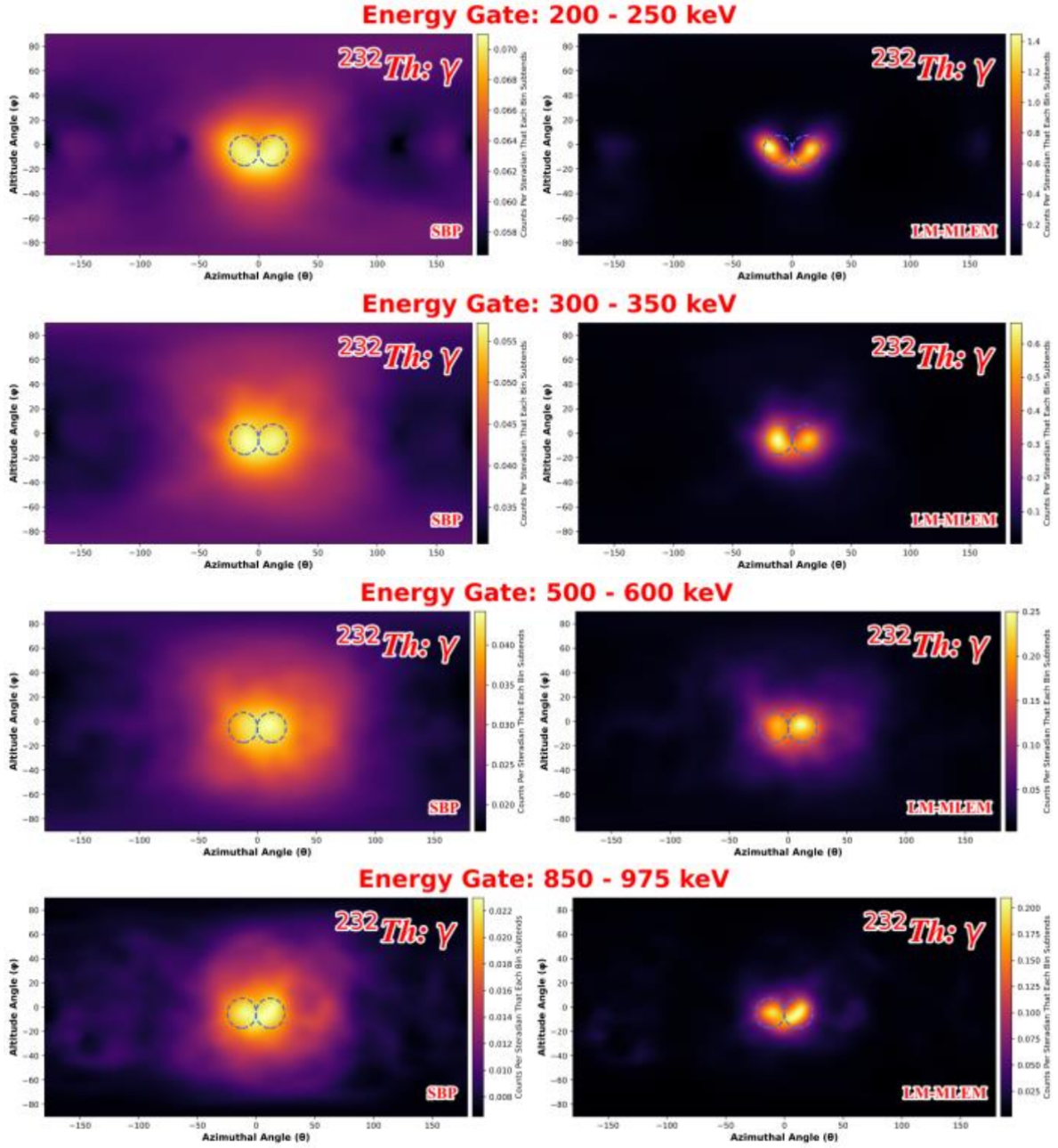

Figure 4.27: Reconstructed SBP and LM-MLEM gamma-ray images of ^{232}Th. Circular outlines represent the locations of the hemis in the FOV.

Finally, revisiting the experimental setup of the multisource neutron measurement from Section 4.3.1, an energy gate of 662 $\pm$ 37 keV was applied to the gamma-ray data set to isolate the ^{137}Cs source in the FOV. Figure 4.28 displays the resulting SBP image, composed of 11669 events, which successfully localizes the ^{137}Cs source. Application of LM-MLEM for nine iterations produces a substantially more converged image, with the hotspot tightly constrained at the expected location of ^{137}Cs at $(90°, 0°)$. These results highlight the effectiveness of source isolation using energy gating, demonstrating that accurate localization is achievable even when other sources in the FOV possess activities several orders of magnitude higher than that of the source of interest.

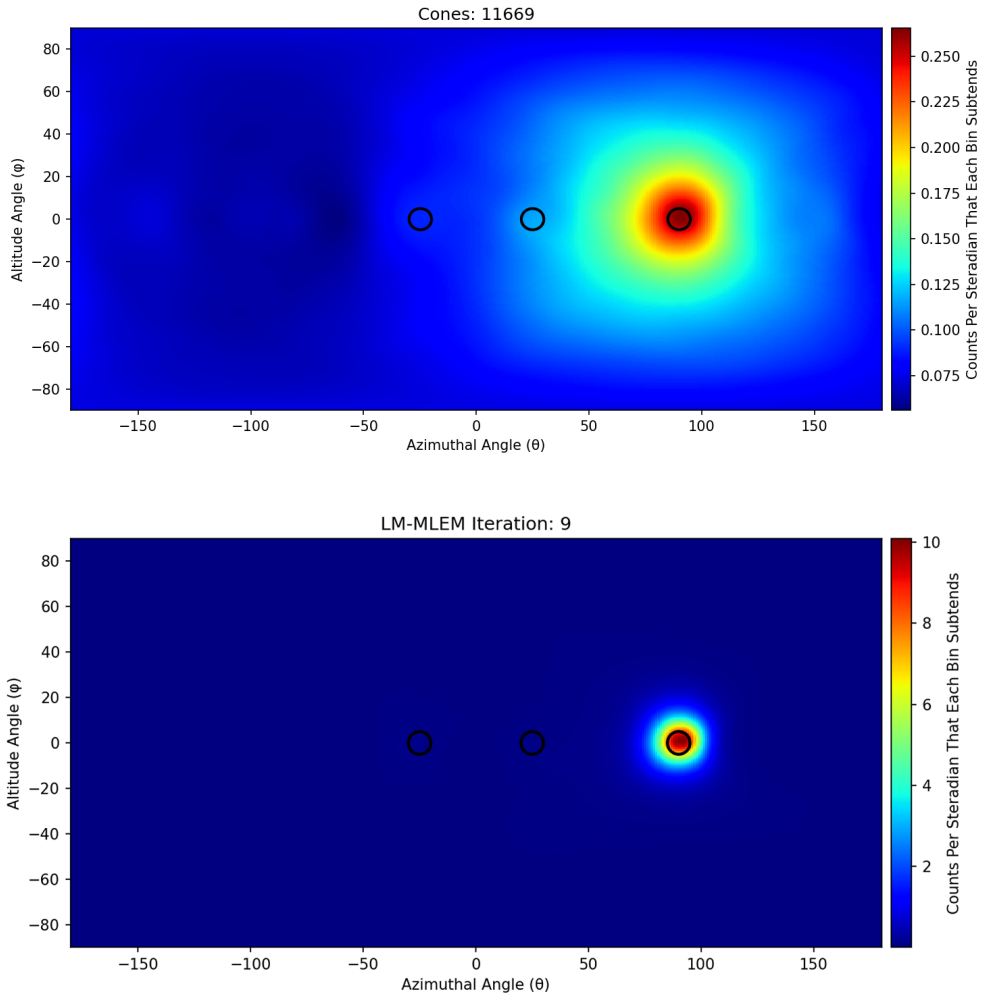

Figure 4.28: Reconstructed SBP and LM-MLEM gamma-ray images of the multisource neutron measurement with a 662 $\pm$ 37 keV energy gate applied. True source locations are marked with circular outlines centered at $(-25°, 0°)$, $(25°, 0°)$, and $(90°, 0°)$ for the PuBe, ^{252}Cf, and ^{137}Cs.

The results for multiple gamma-ray sources presented in this section show that the OGS H2DPI can image several sources at once within the FOV and provides gamma spectroscopy capabilities sufficient to distinguish between different isotopes. The energy gating method described further highlights its ability to discriminate between sources, making it a valuable tool for safeguards applications. For instance, during verification of a host facility's SNM inventory, undeclared or misplaced isotopes can be detected even if faux sources are present alongside actual SNM materials. The system's source discrimination capabilities enable inspectors to identify any anomalies or isotopes that are out of place.

4.4 Localization and Spectrometry of SNM Using OGS

The experimental results presented thus far in this chapter have demonstrated the general imaging and spectroscopy capabilities of the OGS H2DPI. The remainder of Chapter 4 will focus on system localization and spectrocpy of SNM as defined in Section 1.1.2, with particular attention to plutonium and highly enriched uranium sources. Gamma-ray and fast neutron imaging will be performed on a range of relevant SNM sources to assess system performance in nuclear safeguard and nonproliferation scenarios.

4.4.1 Highly Enriched Uranium (HEU)

4.4.1.1 HEU Oxide

Natural uranium is enriched through a complex chemical and mechanical process, most commonly involving the use of UF6 gas in centrifuges to increase the abundance of ^{235}U [85]. Once the desired enrichment level is achieved, the uranium is reconverted to its oxide form for transport and further processing as required for its intended application. HEU oxide is considered a potential precursor for weapons production; as such, its storage, transport, and handling are tightly regulated due to proliferation concerns. In this experiment, a 1-g sample of $>$99% enriched uranium oxide (U_3O_8) was measured using the H2DPI. The powder was contained within a glass vial, which was itself

enclosed in a cardboard tube holder. The HEU sample was positioned 16 cm from the imager at (18.4°, 0°), as indicated in Figure 4.29, and was measured over a period of approximately 23 hours.

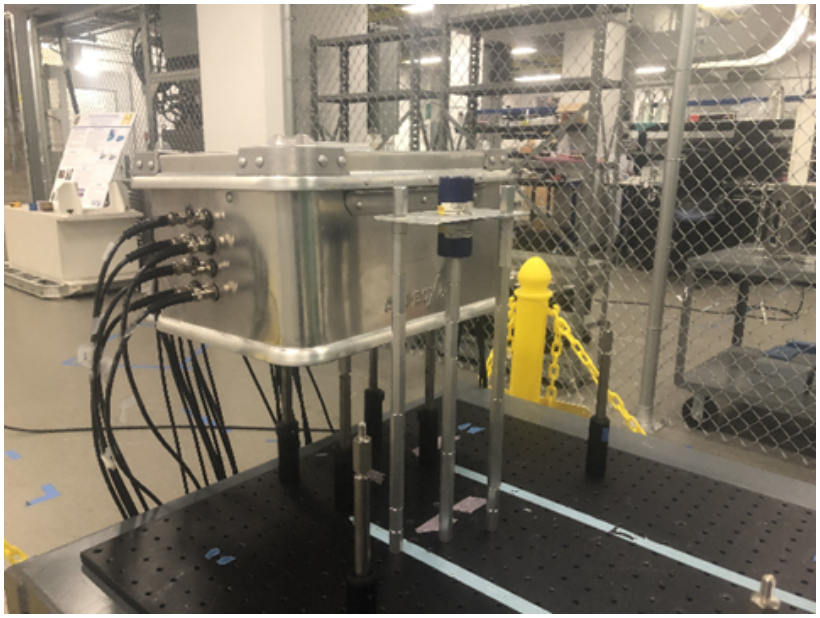

Figure 4.29: Photograph of the experimental setup for the HEU oxide measurement.

The gamma-ray spectrum obtained for the HEU oxide using the $CeBr_3$ scintillators is shown in the left plot of Figure 4.30. This spectrum has been corrected for background gamma-ray contributions by subtracting data collected during a prior background measurement. A prominent gamma-ray photopeak near 186 keV is clearly visible. The right plot in Figure 4.30 displays the resulting coincidence spectrum from the HEU oxide measurement, with the selected energy-gated region highlighted in red. This coincidence spectrum also features a distinct peak near 186 keV, consistent with expectations for a sample containing a high ^{235}U content.

Figure 4.31 presents SBP gamma-ray images from the HEU oxide sample, generated using increasing numbers of cones to illustrate the progression of image convergence over time. The images shown correspond to 4 minutes (26 cones), 15 minutes (96 cones), 1 hour (386 cones), and 23 hours (8777 cones) of data acquisition. The 4- and 15-minute images clearly indicate the presence of a source within the FOV, but are not fully converged at the expected source location; while the azimuth angle is accurate, the altitude is offset by approximately 15°. By contrast, the SBP image

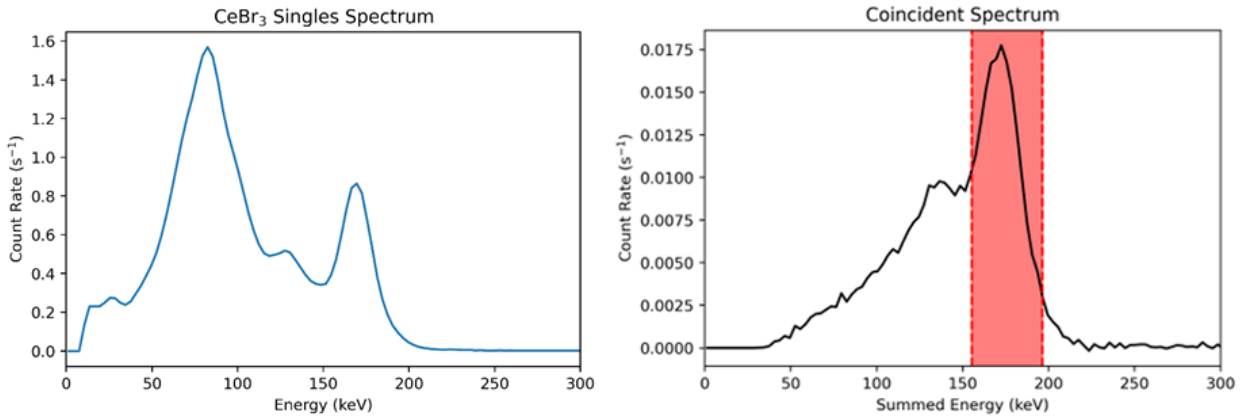

Figure 4.30: Extracted gamma ray spectrum obtained from single events across all eight $CeBr_3$. Gamma coincidence spectrum between OGS and $CeBr_3$ with the energy gated region, derived by the observed energy resolution in the spectrum, used for imaging highlighted in red.

after 1 hour of measurement converges at $(18.4°, 0°)$, closely matching the true location. Given the limited quantity of HEU material present, these results suggest that source convergence under the experimental conditions is likely achievable within approximately 30 minutes of measurement.

This subsection has demonstrated that localization and spectroscopy of HEU in its oxide form can be achieved using gamma-ray measurements with the OGS H2DPI. Detecting uranium oxide is important for applications related to the nuclear fuel cycle, as oxide is a common material in these processes and requires effective safeguarding. In this study, a small sample of HEU was used, which did not yield sufficient neutron statistics for further analysis. Future studies should investigate larger samples to enable neutron spectroscopy and characterize the ability to distinguish oxide from other forms based on measured neutron responses.

4.4.1.2 HEU Metal

The metallic form of HEU is of particular concern in nuclear nonproliferation due to its suitability for use as weapons-usable material. Experiments were conducted at the National Criticality Experiments Research Center at the Nevada National Security Site. The HEU metal used in this work is referred to as the Rocky Flats shells; each shell is hemispherical, and consecutive pairs (e.g., 1-2, 3-4) are combined to form full spherical shells, which can be nested and stacked to achieve

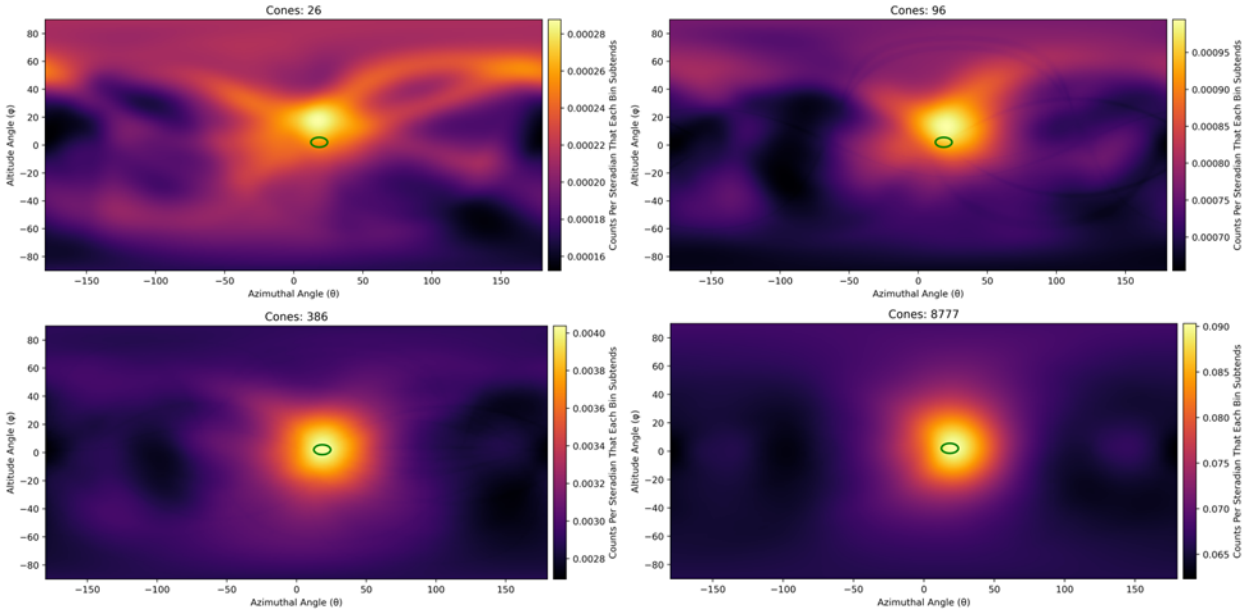

Figure 4.31: SBP gamma-ray images of the HEU oxide measurement at 26 cones (4 minutes), 96 cones (15 minutes), 386 cones (1 hour), and 8777 cones (23 hours). True source location is marked with circular outlines centered at $(18.4°, 0°)$.

greater total masses. The isotopic composition was approximately 93% ^{235}U and 5% ^{238}U [86].The experimental configuration involved shells 1–24, comprising a total mass of 13.74 kg and an outer radius of 5.7 cm. The assembled HEU source was placed 50 cm from the H2DPI at $(25.2°, -1°)$, as depicted in Figure 4.32, and was measured over a 30-minute period.

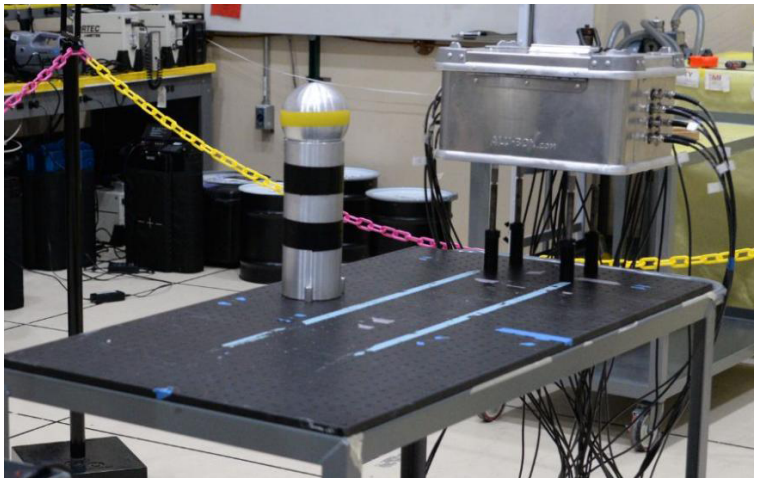

Figure 4.32: Photograph of the experimental setup for the HEU metal measurement.

The gamma-ray spectrum obtained for the HEU metal using the $CeBr_3$ scintillators is shown

in the left plot of Figure 4.33, revealing a prominent photopeak near 186 keV. The right plot in Figure 4.33 displays the corresponding coincidence spectrum, with the energy-gated region of 186 $\pm$ 21 keV highlighted in red. This coincidence spectrum also features the distinct peak near 186 keV, providing a strong signature for ^{235}U. Figure 4.34 shows the gamma-ray SBP image generated from the 2177 recorded events, along with the LM-MLEM image after 27 iterations. Both images demonstrate strong convergence at $(25.2°, -1°)$, demonstrating successful localization of the HEU metal source using its passive gamma-ray signature.

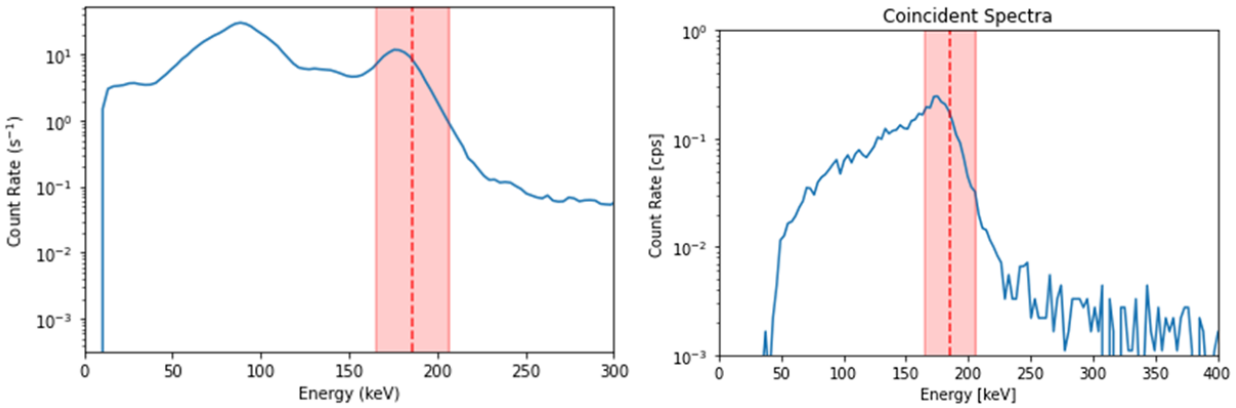

Figure 4.33: Extracted gamma ray spectrum obtained from single events across all eight $CeBr_3$ (left). Gamma coincidence spectrum between OGS and $CeBr_3$ with 186 $\pm$ 21 keV energy gated region used for imaging highlighted in red (right).

Detecting HEU can be challenging due to its relatively weak passive emissions; its characteristic 186 keV gamma rays are easily shielded, and its passive neutron emission rate is very low [87]. In this experiment, AmLi neutron sources were employed to interrogate two configurations of the Rocky Flats shells, enabling demonstration of neutron imaging of HEU metal. The first configuration used shells 1–24, previously described, while the second configuration comprised shells 13–24, yielding a mass of 10.04 kg, maintaining the same outer radius but with an internal void radius of 3.7 cm. Two AmLi sources, each with an activity of 1.22×10^3 mCi (as of 9/30/2020), were positioned on either side of the HEU assembly for interrogation. AmLi was chosen because its lower-energy neutron emission spectrum is more effective at inducing fission in HEU and enables easier discrimination during imaging through energy threshold selection. Figure 4.35 illus-

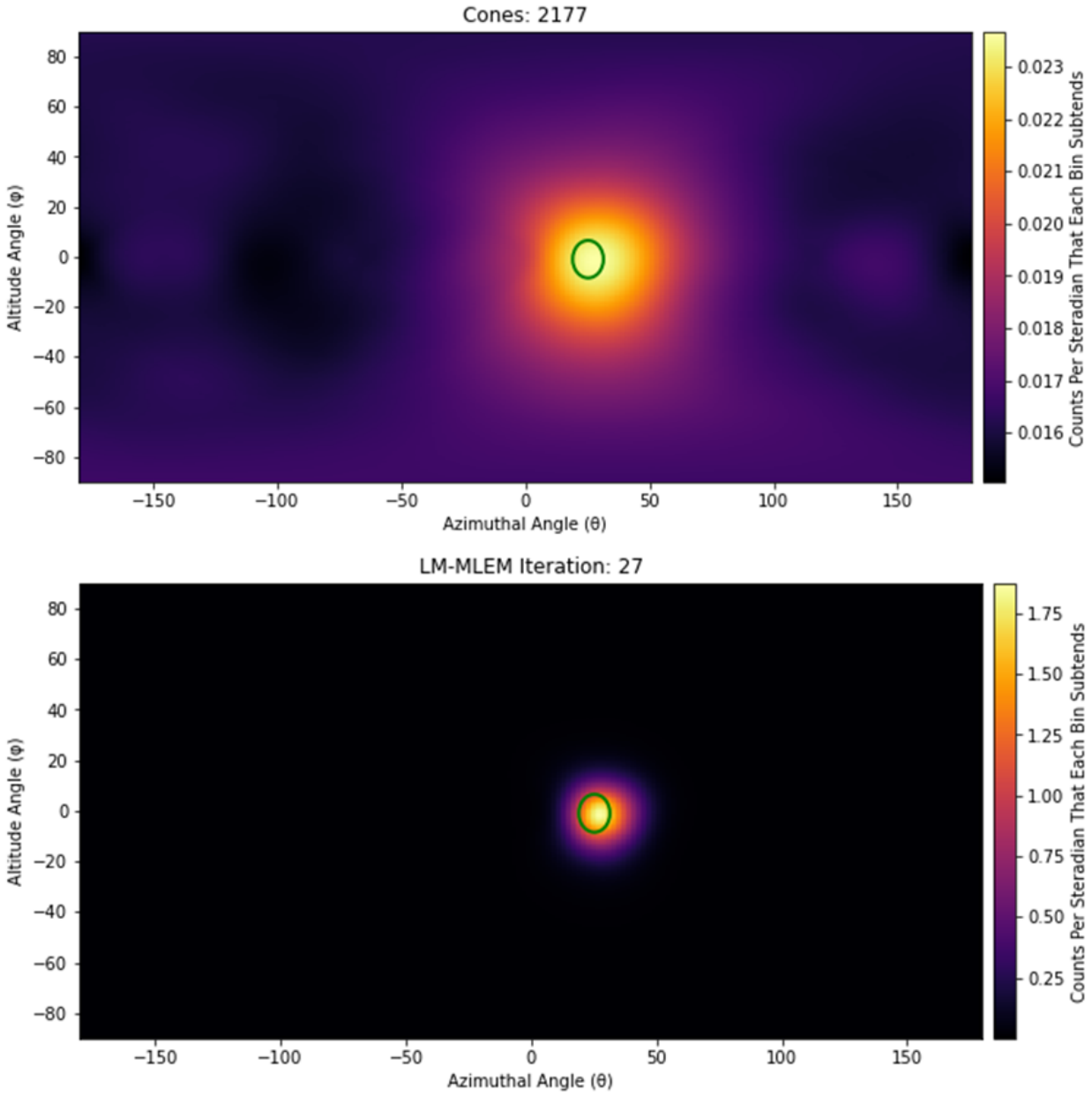

Figure 4.34: Gamma-ray SBP image of HEU metal reconstructed using 2177 events (top). Corresponding LM-MLEM image (bottom). True source location is marked with outlines centered at $(25.2°, -1°)$.

trates the experimental setup and the arrangement of the HEU relative to the H2DPI. To attenuate low-energy 60 keV gamma rays from the AmLi sources, copper, tin, and lead shielding was used. The copper and tin shielding used in this experiment, as well as in other measurements described in this dissertation, consisted of two tin plates, each with a thickness of 3.3 mm, and two copper

plates, each with a thickness of 2.5 mm. All four plates measured one foot in height and two feet in length. This graded copper and tin shield was selected based on previous research which used a genetic algorithm to optimize shielding for plutonium safeguards measurements [88]. Additional lead shielding was applied in the form of a one foot square plate with a thickness of one quarter inch to further reduce the gamma flux incident on the imager. The distance from the center of the H2DPI to the midpoint of the HEU mass was 42 cm for both measurements, with the HEU placed at the center of the FOV at (0°, 0°). Measurement durations were 16 hours for the 14-kg configuration and 4 hours for the 10-kg configuration.

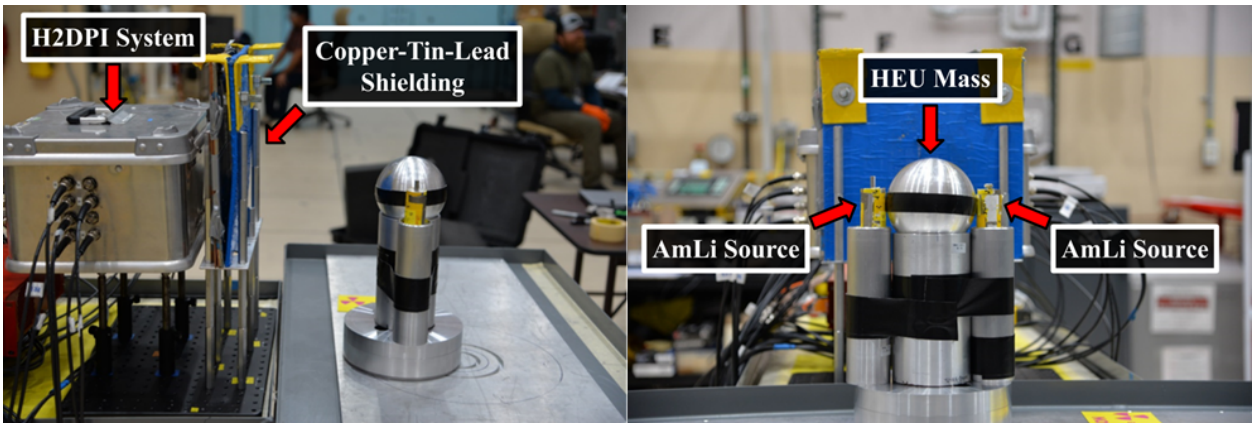

Figure 4.35: Photographs of the experimental setup for the HEU interrogation measurements with AmLi at the National Criticality Experiments Research Center.

A comparison of the neutron singles responses for the configurations is presented in Figure 4.36. This analysis applied a light output threshold of 50 keVee, which, for the OGS bars in the system corresponds to a deposited neutron energy of 0.275 MeV. As a result, the majority of neutrons emitted from the AmLi sources, with an average energy of 0.5 MeV and an effective maximum energy of 1.5 MeV, are included [89]. These neutrons account for the responses observed at low energies in both spectra resulting in a high slope. When applying an energy cutoff at 1.5 MeV, both HEU masses exhibited similar neutron singles responses. However, the 14-kg configuration produced a higher overall count rate compared to the 10-kg mass. Percent differences can be

calculated according to the following expression:

$$Percent\ Difference = \frac{(A - B)}{B} \times 100 \tag{4.1}$$

where A and B represent the integrals for the 14-kg and 10-kg interrogated HEU configurations, respectively. Integration of the portions of the neutron singles distributions above 1.5 MeV yields a 45.1 $\pm$ 2.1% increase in neutron counts for the 14-kg configuration relative to the 10-kg configuration. These results demonstrate that a simple singles analysis can provide preliminary mass characterization of HEU in terms of relative masses present.

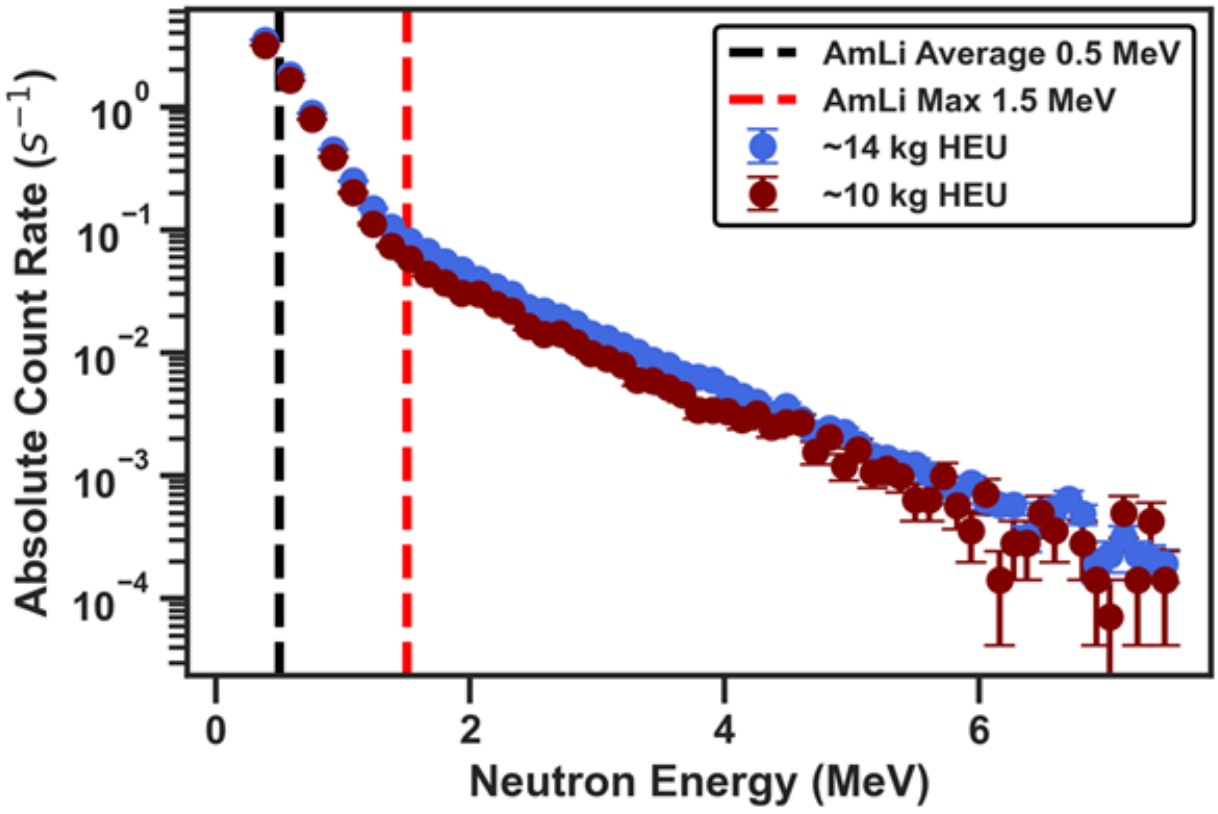

Figure 4.36: Neutron singles response of the two HEU interrogation configurations. Relevant AmLi neutron metrics are noted like average and max energies.

The reconstructed SBP neutron image and corresponding LM-MLEM image for the 14-kg configuration are presented in Figure 4.37. A 50 keVee light output threshold was applied to each neutron scatter event, setting a minimum imageable neutron energy of 0.54 MeV. A total of 749 imageable events were obtained for this measurement. SBP and LM-MLEM images for the 10-kg configuration are shown in Figure 4.38, with 149 imageable events acquired in that case. In both configurations, the images successfully localized the HEU mass within the FOV. For the 14-kg configuration, the images demonstrate good convergence at the center of the Rocky Flats assembly. Imaging results for the 10-kg configuration converge near one of the edges of the HEU mass, likely due to the limited statistics leading to artifacts in the image. LM-MLEM generally tends to converge to point-like distributions, which differs from the true extended source volume present in this study. These measurements represent the first neutron imaging of HEU using the OGS H2DPI system. The reconstructed neutron energy spectra derived from the imageable events are shown in Figure 4.39. Integration of the spectra above 1.5 MeV reveals a $42.2 \pm 17.6\%$ increase in neutron counts for the higher mass configuration compared to the lower mass configuration. Despite the large error bars associated with low statistics in the 10-kg measurement, the neutron spectroscopy analysis results are consistent with previous findings from the neutron singles analysis.

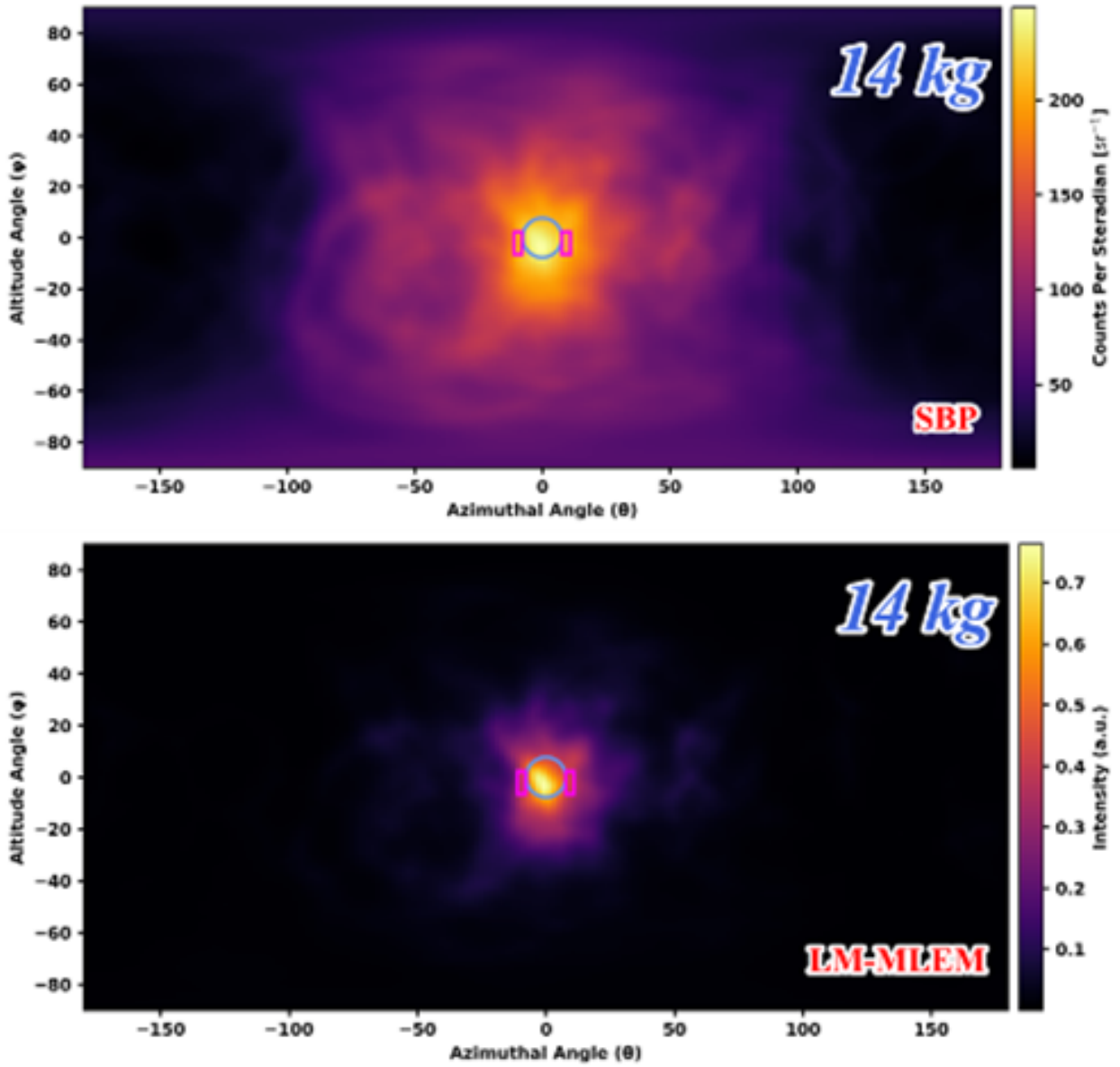

Figure 4.37: Neutron SBP image of 14-kg HEU configuration reconstructed using 749 events. Corresponding LM-MLEM image. True HEU location is marked with outlines centered at (0°, 0°). Encapsulated AmLi source locations are shown as rectangles for reference.

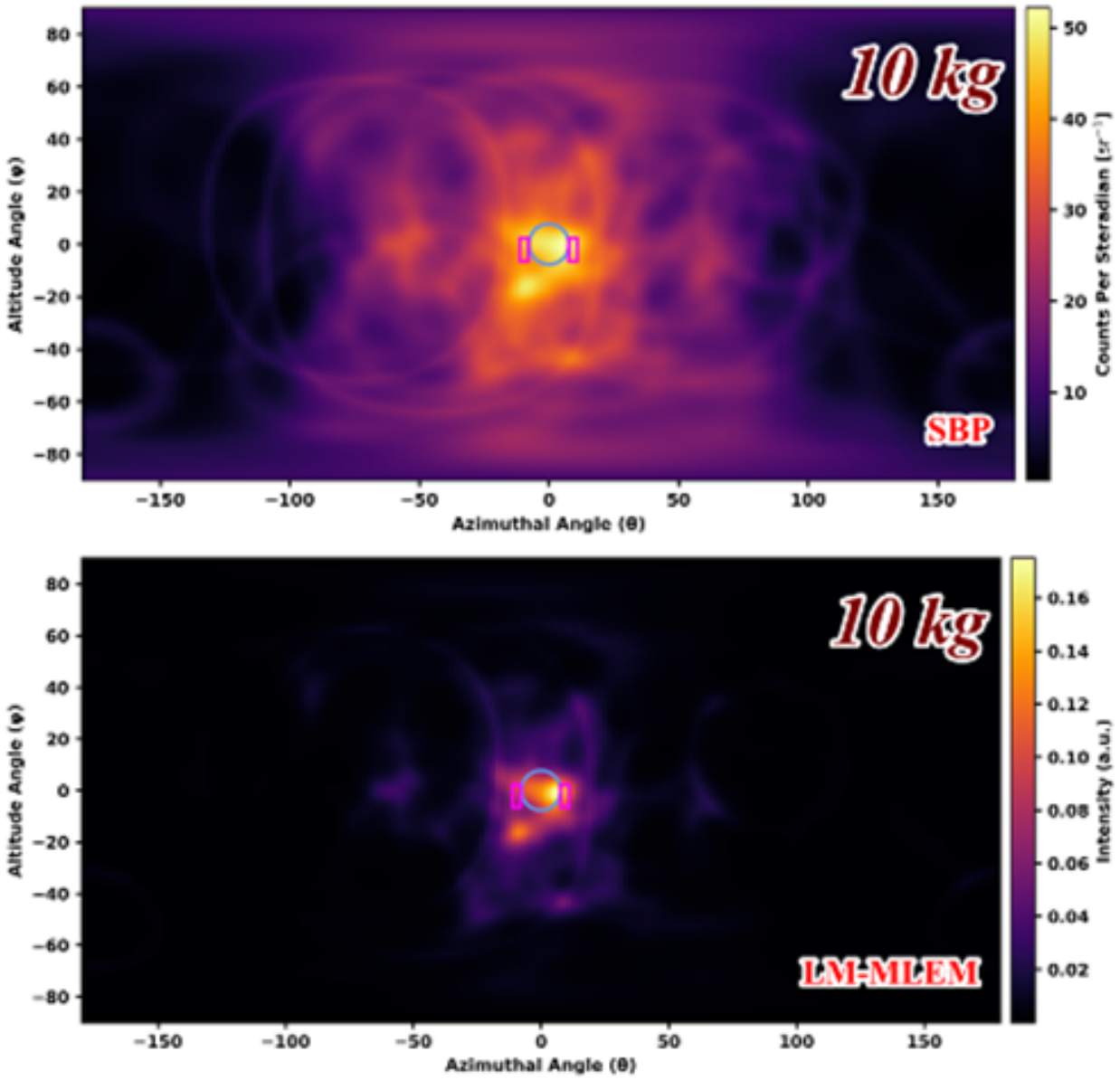

Figure 4.38: Neutron SBP image of 10-kg HEU configuration reconstructed using 149 events. Corresponding LM-MLEM image. True HEU location is marked with outlines centered at (0°, 0°). Encapsulated AmLi source locations are shown as rectangles for reference.

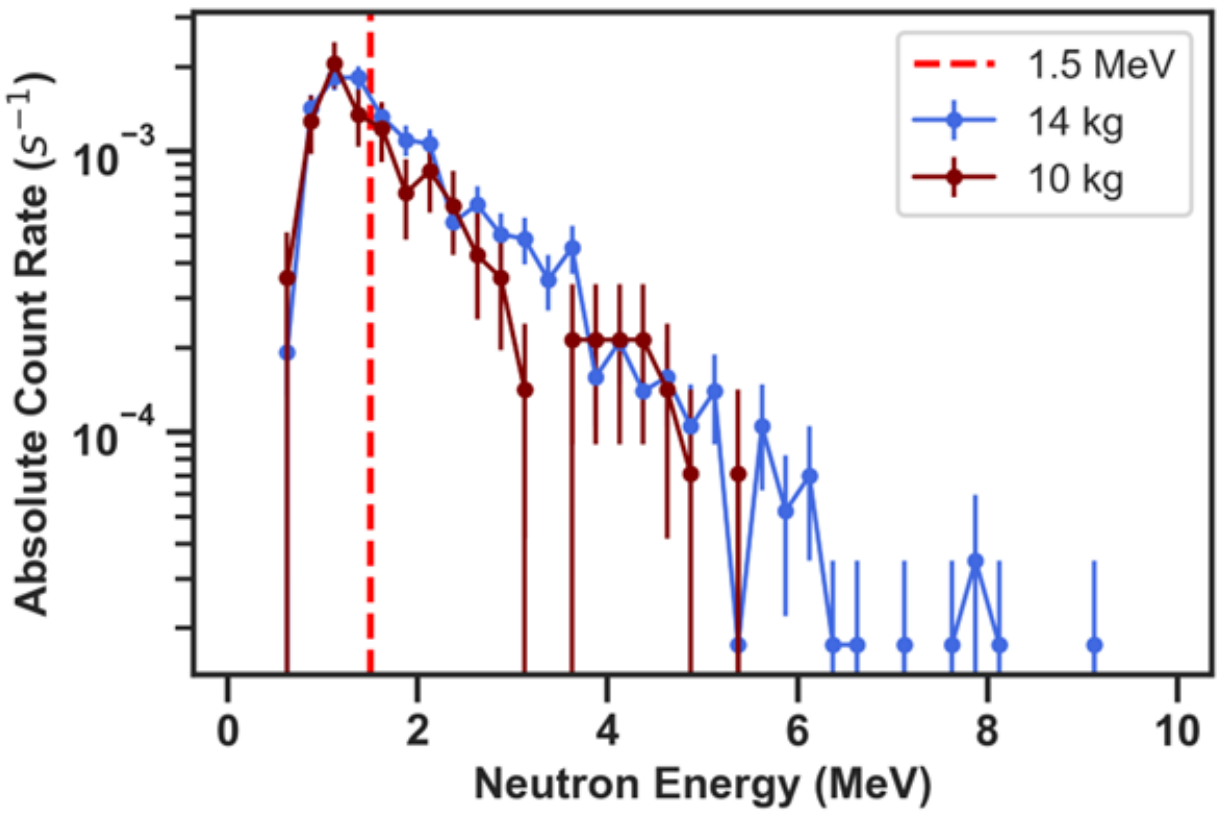

Figure 4.39: Reconstructed neutron energy spectra of the two HEU interrogation configurations. A vertical dashed line indicates the applied energy threshold for the integration comparison.

A final analysis using the 14-kg measurement was performed to confirm that the neutrons imaged in Figure 4.37 originated from HEU-induced fissions, rather than from the AmLi sources themselves. It should be noted that the 10-kg measurement did not undergo this analysis due to lack of imageable events obtained. For this analysis, the light output threshold was raised to 175 keVee, corresponding to an energy deposition of 0.76 MeV in the OGS bars for each neutron scatter event. This sets a minimum imageable neutron energy of 1.52 MeV, which is above the maximum neutron energy emitted by the AmLi sources. As a result, any recorded imageable events above this threshold can be attributed to fission originating in the Rocky Flats shells. Figure 4.40 presents the resulting SBP and LM-MLEM images from this high-threshold analysis. A total of 82 imageable events were obtained, with both neutron images clearly showing convergence at the expected location of the HEU within the FOV, consistent with earlier results.

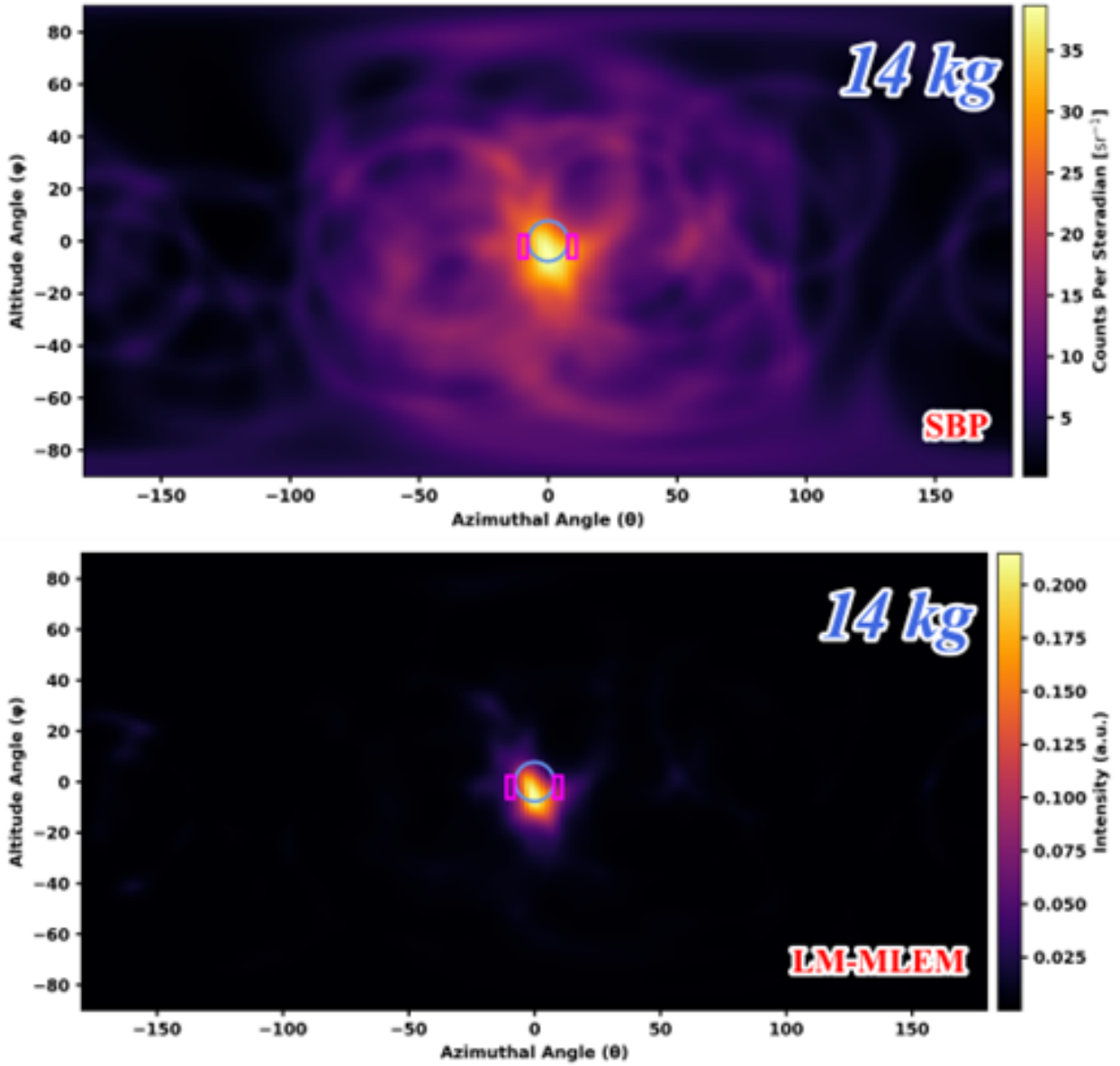

Figure 4.40: Neutron SBP image of 14-kg HEU configuration reconstructed using 149 events. Corresponding LM-MLEM image. True HEU location is marked with outlines centered at (0°, 0°). Encapsulated AmLi source locations are shown as rectangles for reference. The imageable neutron energy threshold was set to 1.5 MeV to remove neutrons from AmLi sources so only HEU fission neutrons are included in the imaging data set.

4.4.2 Plutonium

4.4.2.1 Plutonium Metals

As with HEU metal, plutonium is classified as SNM, necessitating even more stringent verification due to the relatively small quantity required for nuclear weapons development. This work reports on measurements conducted at the National Criticality Experiments Research Center. The first experimental setup utilized the BeRP Ball, a 4.5 kg sphere of α-phase plutonium metal composed of 93.3 wt% ^{239}Pu and 6 wt% ^{240}Pu. The BeRP Ball was positioned 90 cm from the imager at an angular direction of $(11°, -5.7°)$, as shown in the left photo of Figure 4.41, and measured for 60 minutes. The second setup employed the Thor core, a 4 kg δ-phase plutonium metal sample consisting of 94.9 wt% ^{239}Pu and 5.1 wt% ^{240}Pu. The Thor core was placed 100 cm from the H2DPI at an angular direction of $(11°, -0.6°)$, as depicted in the right photo of Figure 4.41, and measured for 40 minutes.

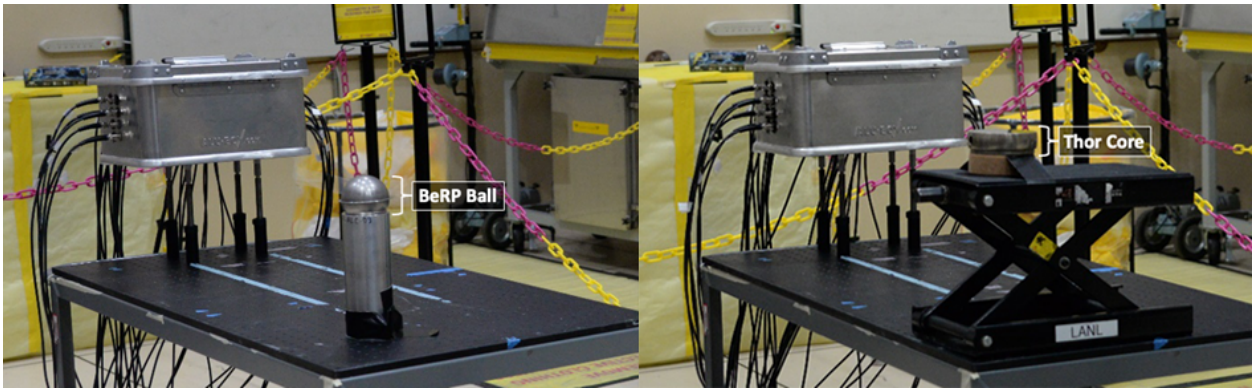

Figure 4.41: Photographs of the experimental setups of the BeRP Ball (left) and Thor core (right) at the National Criticality Experiments Research Center.

The gamma-ray singles spectrum obtained from the $CeBr_3$ in the BeRP Ball measurement is shown in the left panel of Figure 4.42. This spectrum features prominent peaks at 375 keV, 414 keV, and 646 keV, which are indicative of ^{239}Pu decay. The OGS-$CeBr_3$ gamma-ray coincidence spectrum is provided in the right panel of Figure 4.42. The peaks in the coincidence spectrum are less well resolved, which can be attributed to its energy resolution being the convolution of the OGS and $CeBr_3$ detectors, with the OGS contributing greater broadening. Figure 4.43 displays

equivalent plots for the Thor core data. As expected, both the singles and coincidence spectra are similar to those obtained from the BeRP Ball, reflecting their comparable isotopic compositions. In both coincidence spectra, different energy gates are highlighted to indicate the regions used for SBP imaging. For the BeRP Ball measurement, an energy gate of 646 $\pm$ 36 keV was applied, corresponding to the 646 keV emission, while the Thor core measurement used a gate of 350–425 keV, encompassing the 375 keV and 414 keV emissions.

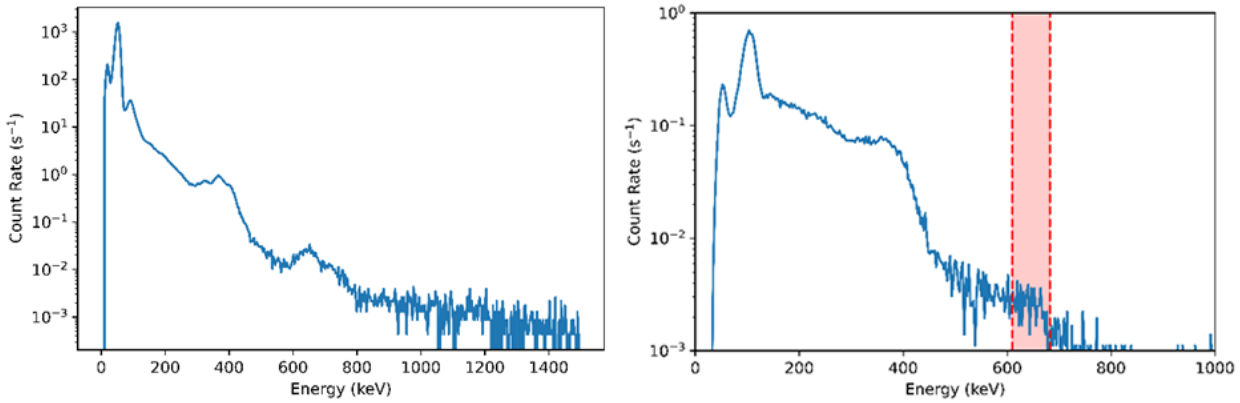

Figure 4.42: BeRP Ball measurement - Extracted gamma ray spectrum obtained from single events across all eight $CeBr_3$ (left). Gamma coincidence spectrum between OGS and $CeBr_3$ with 646 $\pm$ 36 keV energy gated region used for imaging highlighted in red (right).

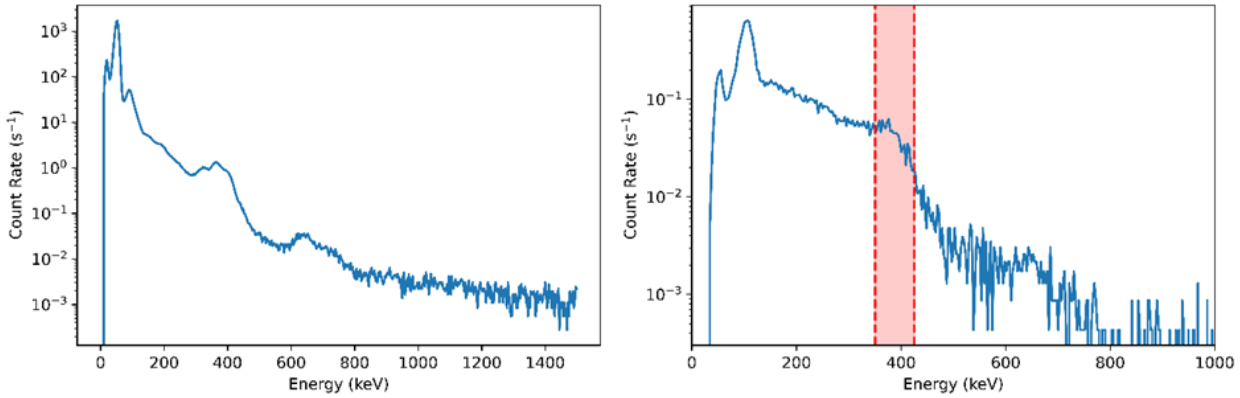

Figure 4.43: Thor core measurement - Extracted gamma ray spectrum obtained from single events across all eight $CeBr_3$ (left). Gamma coincidence spectrum between OGS and $CeBr_3$ with 350–425 keV energy gated region used for imaging highlighted in red (right).

Figure 4.44 presents the resulting LM-MLEM fast-neutron and energy-gated gamma-ray images from the BeRP Ball measurement, with the source location in angular space indicated by a

red outline. Neutron images were produced using a light output threshold of 75 keVee per scatter, corresponding to a minimum imageable neutron energy of 0.77 MeV. Gamma-ray images utilized a 25 keVee threshold, resulting in an effective minimum imageable gamma-ray energy of 50 keV. Both the neutron and gamma-ray images for the BeRP Ball are in good agreement with the true source location, $(11^\circ, -5.7^\circ)$.

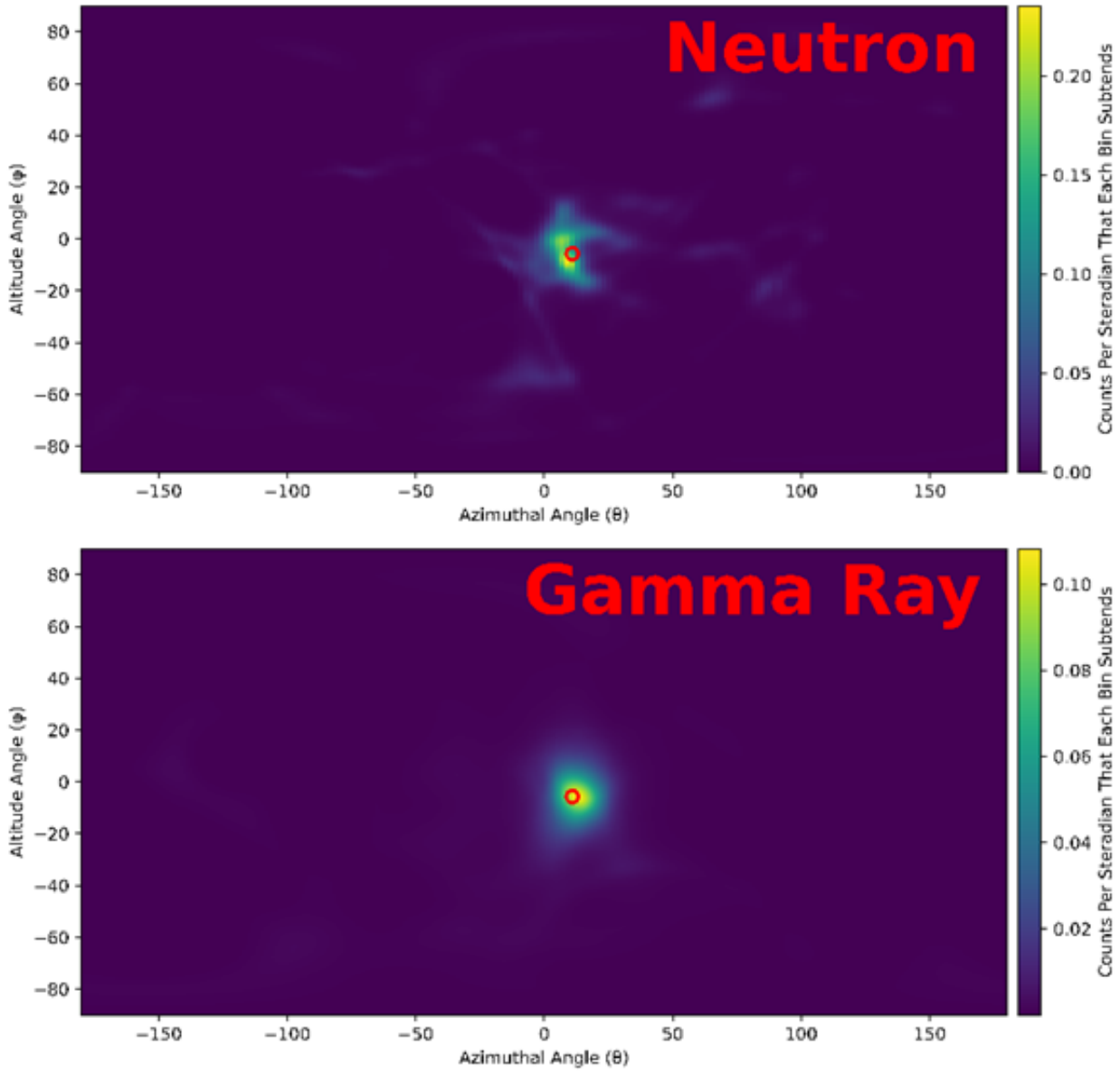

Figure 4.44: Neutron LM-MLEM image of BeRP Ball (top). Corresponding LM-MLEM gamma-ray image using 646 ± 36 keV energy gate (bottom). True BeRP Ball location is marked with red outlines centered at $(11^\circ, -5.7^\circ)$.

Figure 4.45 displays the LM-MLEM neutron and gamma-ray images obtained for the Thor core object. Although fewer imageable neutron double-scatter events were recorded, attributable to the greater distance and shorter measurement duration compared to the BeRP Ball experiment, accurate source localization was still achieved. Both images conformed to the experimental location of the Thor core at $(11^\circ, -0.6^\circ)$.

The results from the plutonium metal measurements in this subsection demonstrate that the OGS H2DPI is capable of using both neutron and gamma-ray signatures for reliable source localization. These experiments are part of previously published work by the group [31], which includes more detailed analysis and broader conclusions. Similar to the findings for metallic HEU, these results have important implications for the application of OGS in imaging systems. Since kg quantities of SNM represent an area of high priority, the flexibility of using either neutron or gamma-ray signatures for localization and spectroscopy greatly enhances the ability to confirm or verify SNM presence in field scenarios.

4.4.2.2 Plutonium Oxide

Plutonium oxides are also of significant interest for safeguarding and nonproliferation efforts. Unlike metallic forms, plutonium oxides are not directly used in weapons systems but serve as precursor material, notably in certain types of nuclear reactor fuels. From a detection standpoint, plutonium oxides exhibit distinct neutron signatures compared to plutonium metal. Oxide-based plutonium sources emit neutrons predominantly through (α, n) reactions with oxygen and are sensitive to the presence of different isotopes of Pu, resulting in energy spectra that differ from those of fission neutrons produced by plutonium metal. To illustrate the utility of the H2DPI for neutron spectroscopy and differentiation between plutonium source types, a comparison of the neutron singles response of the OGS bars in the H2DPI was conducted. Data were collected from both the BeRP Ball (metal) and 400-g of PuO_2. Due to differences in experimental setups and measurement durations, the spectra were compared using integral normalized counts, as depicted in Figure 4.46 The normalized spectral comparison reveals a greater prevalence of higher light output events from

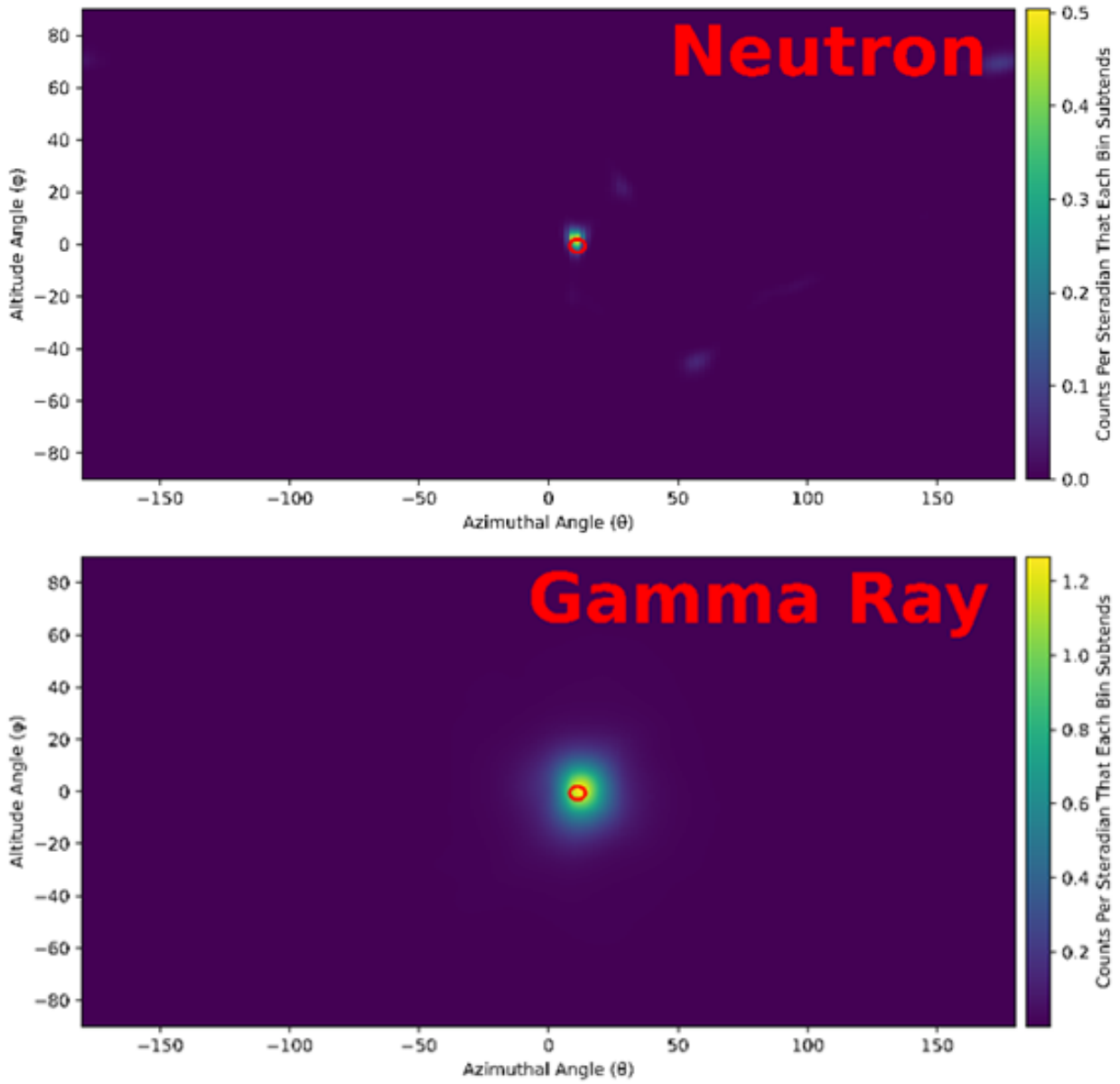

Figure 4.45: Neutron LM-MLEM image of Thor core (top). Corresponding LM-MLEM gamma-ray image using 350-452 keV energy gate (bottom). True Thor core location is marked with red outlines centered at $(11°, -0.6°)$.

the metal sample compared to the oxide. This observation is consistent with expectations, as plutonium metal emits higher energy neutrons due to the spontaneous fission of ^{240}Pu.

This part of the dissertation will go over neutron spectrum comparisons of plutonium using the OGS H2DPI along with simulation validation. A more detailed treatment of the topic is presented in this reference [90], but a summary is presented in this work. The light output spectra detected

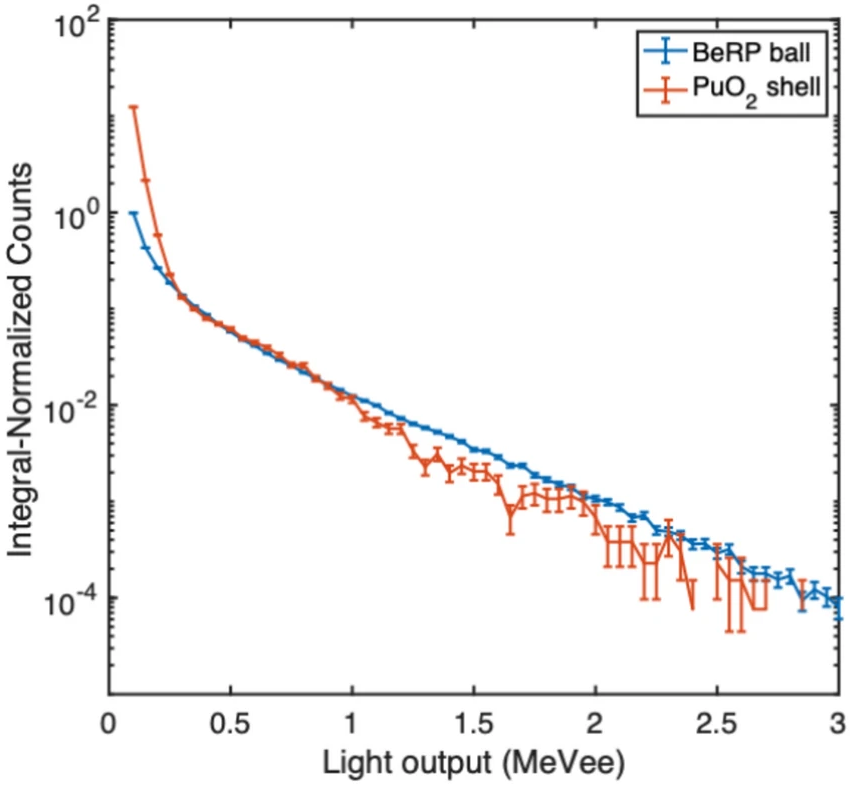

Figure 4.46: Measured neutron light output spectra for the plutonium metal and plutonium oxide samples plotted integral normalized [90].

with the H2DPI were simulated using the MCNPX-PoliMi code [91]. Figure 4.47 compares the simulated and experimental data for both the plutonium metal and oxide samples, with results scaled to absolute units of counts per second. The spectra are shown over a range with a lower threshold of 50 keVee (corresponding to 0.280 MeV neutron energy deposited on hydrogen) and an upper threshold of 3.0 MeVee (7.590 MeV neutron energy deposited). For the plutonium metal comparison, the measured and simulated spectra show good agreement across the entire range of light output values. For the PuO_2, some disagreement is observed at lower light output values, below 250 keVee (0.995 MeV neutron energy deposited). The increase in measured counts in this region can be attributed to PSD misclassification of gamma-ray pulses, due to the large gamma-ray background present in the PuO_2 measurement. At higher light outputs (greater than approximately 2.0 MeVee), the measured PuO_2 spectrum exhibits large statistical uncertainties, stemming from the low neutron counts in the data.

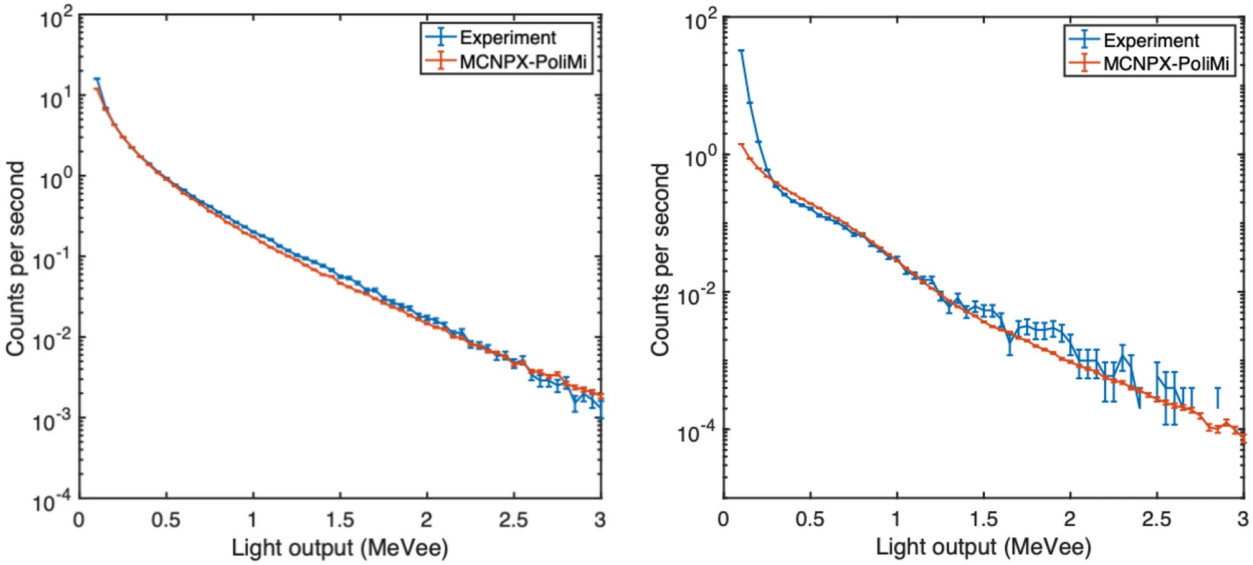

Figure 4.47: Comparison of simulated and measured neutron light output spectra for the plutonium metal (left) and plutonium oxide samples (right) [90].

Figure 4.48 presents the measured light output spectra for three plutonium forms: metal, oxide, and plutonium–beryllium (PuBe). The spectra for metal and oxide originate from the data described previously, while the spectrum for PuBe is included because these sources are widely used in industrial applications. PuBe emits neutrons via (α, n) reactions on beryllium, producing neutrons with much higher average energies than those resulting from the same reaction on oxygen, an effect that is readily apparent in the spectrum. Analysis of these neutron light output spectra enables discrimination between various forms of plutonium. To facilitate this, the spectra were integrated in two regions [90]:

$$I_1 : 0.250 < L < 1.0 \text{ MeVee } (0.995 < E < 3.014 \text{ MeV}),$$

$$I_2 : 1.0 < L < 3.0 \text{ MeVee } (3.014 < E < 7.590 \text{ MeV}).$$

These specific integration regions were informed by the energy spectra for neutrons emitted from spontaneous fission of ^{240}Pu and (α, n) reactions on ^{239}Pu and ^{240}Pu. The spectrum from the PuBe source exhibited the largest I_2/I_1 ratio (0.3998 ± 0.0025), which is consistent with its higher-energy neutron emission, while the PuO_2 spectrum had the smallest ratio (0.0598 ± 0.0067). The spectrum for plutonium metal showed an intermediate I_2/I_1 ratio (0.1029 ± 0.0023). These inte-

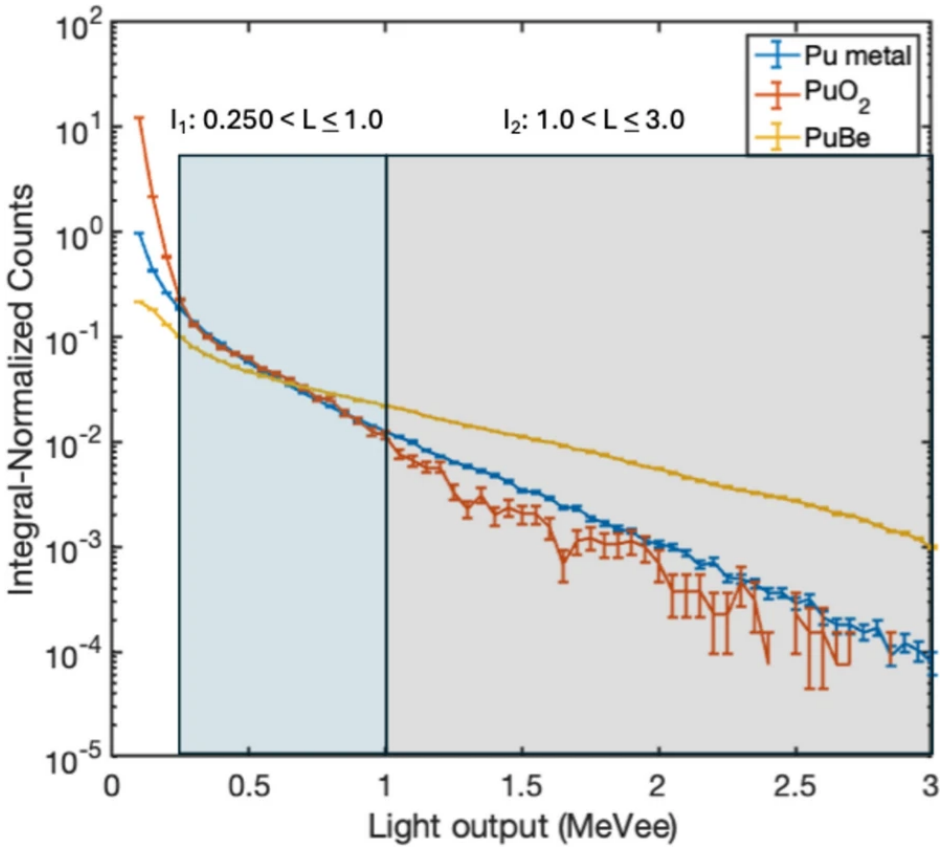

Figure 4.48: Measured light output spectra for plutonium metal, plutonium oxide, and plutonium–beryllium sources; shaded areas show regions of integration for low and high-light-output integrals, noted above [90].

grals were calculated using the full data set for each plutonium source: 144 minutes for PuBe, 219 minutes for metal, and 83 minutes for oxide. All three materials were distinguishable, with their ratios separated beyond three sigma error bars.

4.4.2.3 Plutonium Oxide Discrimination

The final results presented in this chapter demonstrate the SNM discrimination capabilities of the H2DPI when non-SNM sources are also present within its FOV. This work reports on a measurement conducted at Lawrence Livermore National Laboratory. Two stainless steel hemishells containing PuO_2, each with an outer diameter of 14.6 cm, were placed 0.9 m from the H2DPI. Each hemishell contained approximately 180 g of PuO_2, composed of 94.1 wt% ^{239}Pu and 6.9 wt% ^{240}Pu. The PuO_2 hemishells were positioned 180° apart, at $(132^\circ, 0^\circ)$ and $(-48^\circ, 0^\circ)$, re-

spectively. Additionally, a single thin hemishell of thorium metal served as the non-SNM material. The thorium hemishell weighed 590 g, consisted primarily of ^{232}Th, and had an outer diameter of 12.4 cm. It was placed 1 m from the H2DPI at a direction of (0°, 9.5°). Figure 4.49 presents a photograph of the experimental setup and the relative locations of the hemishells with respect to the H2DPI. Small square shielding was positioned in front of each plutonium hemishell to reduce the level of 60 keV gamma-ray emissions. The total measurement time was 40 minutes.

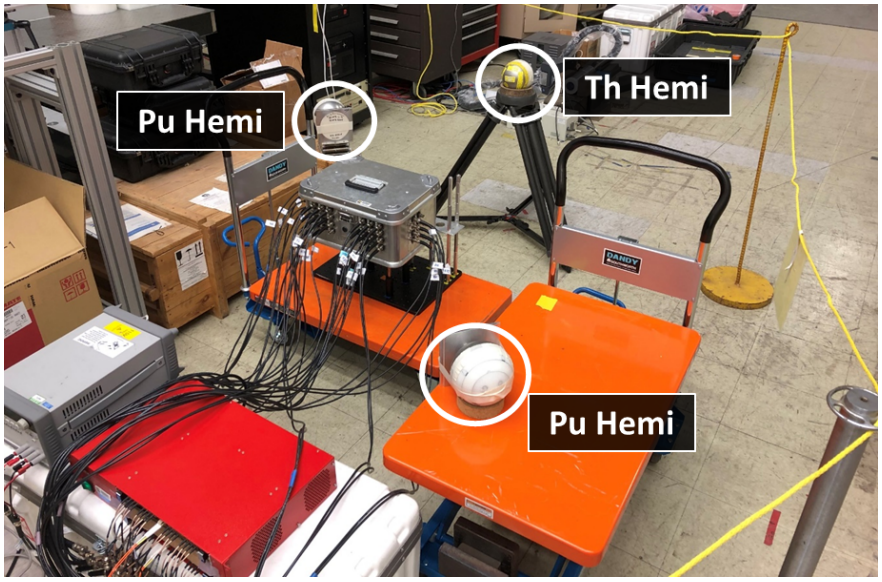

Figure 4.49: Photograph of the experimental setup for the plutonium oxide discrimination measurement at Lawrence Livermore National Laboratory.

The gamma-ray singles spectrum obtained from the $CeBr_3$ detectors during the plutonium oxide discrimination measurement is shown in Figure 4.50. This spectrum features prominent peaks at 332.8 keV, 345 keV, 375 keV, and 413.7 keV, which are indicative of ^{239}Pu decay. Additionally, the spectrum contains the 583.2 keV emission, highlighted in Table 4.2 as a signature of ^{232}Th, originating from its daughter ^{208}Tl.

Based on the gamma-ray singles spectroscopy results, energy gates were established to isolate the plutonium oxide and thorium metal. The left plot in Figure 4.51 displays the gamma-ray coincidence spectrum and the 300–475 keV energy gate chosen to isolate plutonium, as it encompasses the high-intensity emissions observed in the $CeBr_3$. The right plot in Figure 4.51 presents the

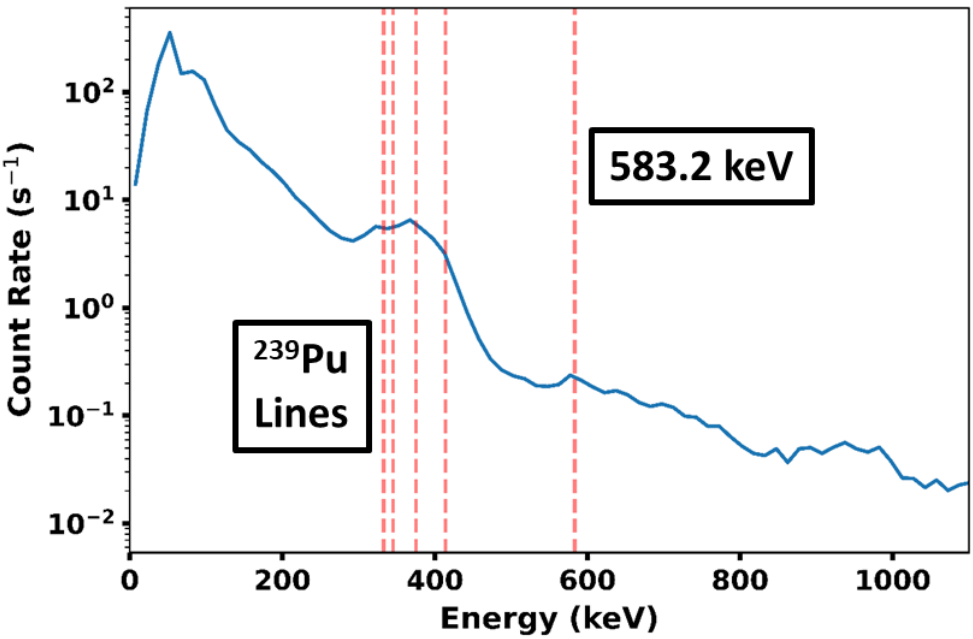

Figure 4.50: Extracted gamma ray spectrum from plutonium oxide discrimination measurement obtained from single events across all eight $CeBr_3$.

500–600 keV energy gate used to isolate thorium, which includes the 583.2 keV emission.

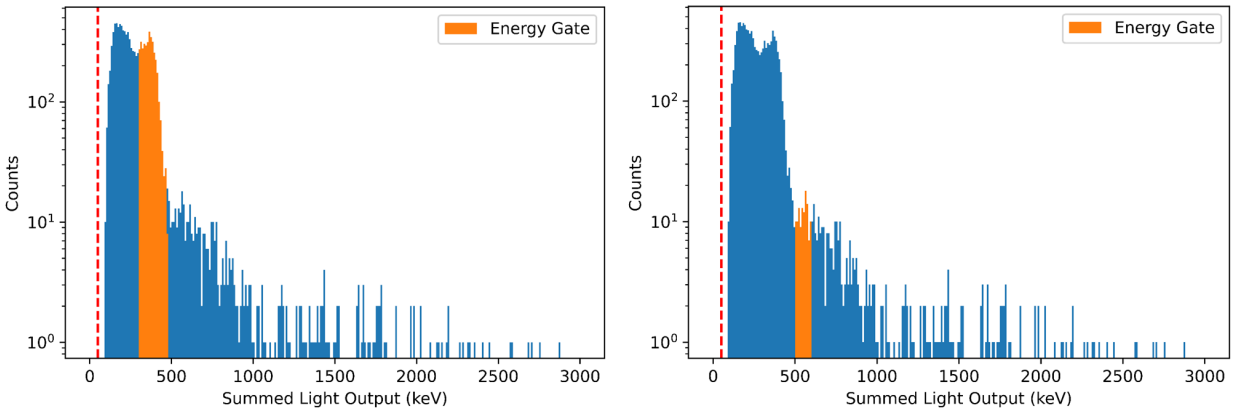

Figure 4.51: Gamma coincidence spectrum between OGS and $CeBr_3$ from the plutonium oxide discrimination measurement. The energy gate of 300-475 keV (left) isolates plutonium while the 500-600 keV energy gate (right) isolates thorium.

Figure 4.52 shows the SBP and LM-MLEM gamma-ray images generated from the 3740 imageable events within the 300–475 keV energy gate. The images show excellent agreement between the true locations of the plutonium oxide sources and the converged hotspots. Notably, the thorium

hemi location is also indicated in the FOV, with no features present at that position, confirming successful discrimination of SNM. Similarly, Figure 4.53 presents the SBP and LM-MLEM gamma-ray images generated from the 166 imageable events within the 500–600 keV energy gate. The SBP image demonstrates general agreement between the true location of the thorium hemi true location and the converged hotspot, while the LM-MLEM image converges closely around the $(0^\circ, 9.5^\circ)$ position. Importantly, the plutonium hemishells are not identified as strong potential source locations in this energy window, further demonstrating successful discrimination of different sources within the FOV. A use case where this demonstrated capability would be valuable is in situations where SNM is present, either intentionally or maliciously, alongside other radioactive sources such as at a boarder checkpoint or inventory room. In such scenarios, distinguishing SNM from other materials can be challenging using only an image or spectrum, but the ability to utilize discriminating techniques greatly improves source identification and separation.

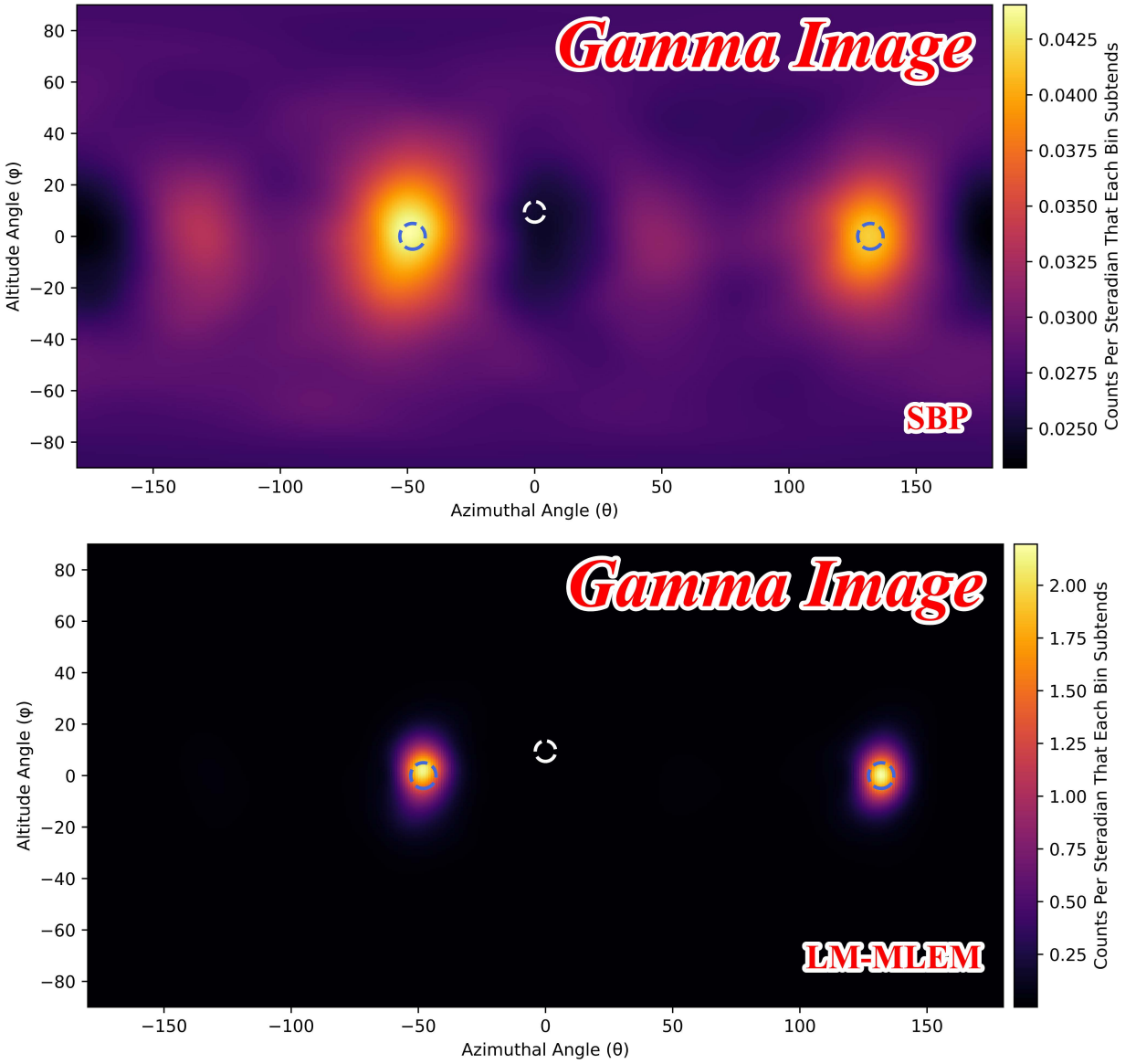

Figure 4.52: Gamma-ray SBP and LM-MLEM images of plutonium oxide discrimination measurement with energy gate of 300-475 keV applied to isolate plutonium in the FOV. Circular outlines centered at $(132°, 0°)$ and $(-48°, 0°)$ represent PuO_2 locations while the thorium source is at $(0°, 9.5°)$.

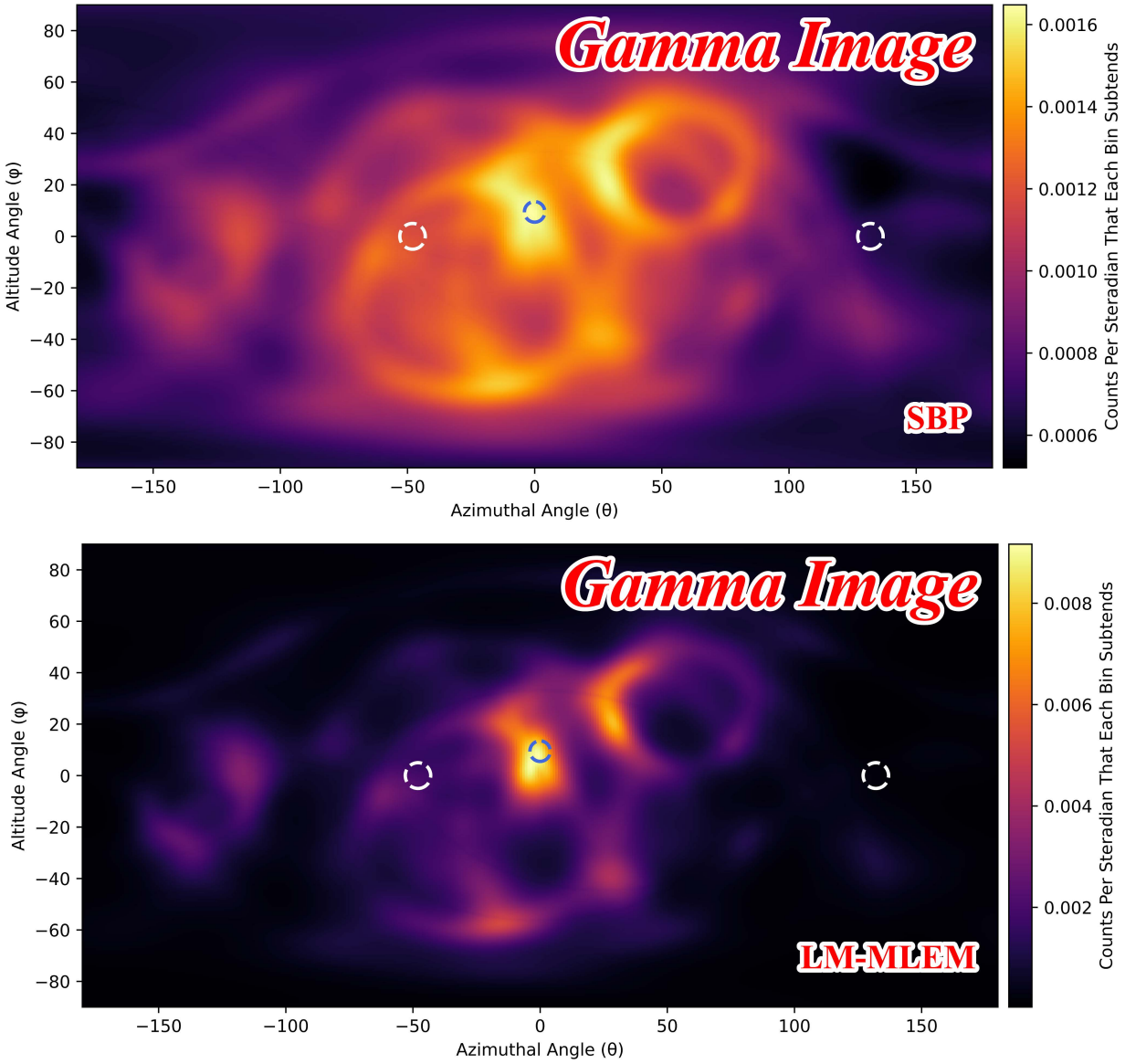

Figure 4.53: Gamma-ray SBP and LM-MLEM images of plutonium oxide discrimination measurement with energy gate of 500-600 keV applied to isolate thorium in the FOV. Circular outline centered at $(0°, 9.5°)$ represents the thorium location while the PuO_2 are at $(132°, 0°)$ and $(-48°, 0°)$.

4.5 Implications and Conclusions

This chapter has systematically demonstrated the capabilities of the OGS-based H2DPI for source localization and spectroscopy in nuclear safeguards and nonproliferation contexts. The experimental results provide compelling evidence that OGS exhibits considerable potential for particle imaging applications, with the H2DPI delivering robust performance in the imaging and discrimination of neutron and gamma-ray sources relevant to nuclear security, routine operations, and emergency scenarios.

4.5.1 General Capabilities

Across a range of single- and multisource experiments, the H2DPI system reliably localized radioactive sources within its 4π FOV. Neutron and gamma-ray SBP images, along with LM-MLEM reconstructions, consistently converged on true source positions, even under challenging conditions such as short measurement times, substantial shielding, and varying source strengths. The ability of the system to maintain localization accuracy, with only limited degradation in angular resolution or statistical confidence in more demanding scenarios, underscores its resilience in practical, real-world environments. The dual-particle imaging approach is particularly advantageous for discriminating between source types, and the use of energy gating and image processing techniques allowed for effective identification and isolation even in complex, multisource fields.

4.5.2 SNM Detection Performance

A central focus of this chapter was on the detection and characterization of SNM, specifically HEU and plutonium in metallic and oxide forms. The OGS H2DPI achieved successful passive gamma-ray imaging of HEU oxide and metal, utilizing the characteristic 186 keV emission. These results affirm the potential of the system for verification in regulatory or field settings where rapid assessment and discrimination are paramount. The interrogation of HEU metal with AmLi neutron sources enabled not only localization but also an assessment of relative HEU masses by threshold-

ing neutron singles and spectrometry responses, demonstrating coarse mass sensitivity for distinguishing between different configurations. The system design permitted the exclusion of neutrons from the interrogating AmLi sources, ensuring that detected signals arose exclusively from induced fission. Plutonium metal and oxide measurements further underscored the dual-particle imaging strengths; both neutron and gamma-ray channels supported localization and spectral discrimination. Crucially, neutron singles spectroscopy allowed for discrimination between metal, oxide, and PuBe sources, leveraging their unique emission spectra and underlying reaction channels. Experiments involving multiple sources, neighboring SNM and non-SNM materials, and complex backgrounds validated that the OGS H2DPI can perform in more realistic safeguard and verification scenarios. The system reliably localized and distinguished sources, supporting both rapid screening and spectral analysis.

4.5.3 Broader Implications

Collectively, this work highlights the OGS H2DPI as a powerful and versatile tool for nuclear safeguards and nonproliferation. Its ability to concurrently perform neutron and gamma-ray imaging position it as a next-generation solution for routine monitoring, treaty verification, and emergency response. The platform's sensitivity to SNM signatures, its energy-resolved discrimination abilities, and its capacity for mass characterization, make it well-suited to the evolving demands of nuclear security. The results presented form a foundation for the deployment and further development of OGS-based dual-particle imaging systems. Future work may address enhanced automation, real-time processing, and imaging in more complex operational environments, continuing the push toward reliable, field-ready radiation detection solutions. Of particular interest is the development of a H2DPI system with a greater number of OGS bars to fully utilize all available SiPM pixels. Increasing the active volume will improve the currently low absolute imaging efficiencies, helping to reduce measurement times and making the system more suitable for practical applications and field use.

CHAPTER 5

Development of a Neutron Simulation Pipeline for Scatter-Based Imaging and Spectroscopy

5.1 Motivation

Accurate modeling approaches for imaging systems are essential for the design and optimization of new technologies; however, current modeling capabilities fall short, particularly for neutron imaging and spectroscopy. Considerable effort has been dedicated to verifying and validating methods for modeling gamma-ray imaging systems. Various analytical models [92, 93] have been developed and investigated for applications such as radiation therapy, where gamma imaging provides crucial information for treatment planning. Overall, there exists a substantial body of literature describing models for Compton cameras and other gamma-ray imaging modalities. In contrast, neutron scatter-based imaging simulations are less explored in the literature. Published work on neutron simulations primarily addresses topics such as range calculations [94], neutron multiplicity [95], and enrichment verification [96].

In this work, a high-fidelity simulation pipeline specifically designed for scatter-based organic scintillator neutron imaging systems is developed. The pipeline incorporates critical detector attributes, such as particle discrimination rates and single detector time resolution, which have not been addressed in simulation studies for the previous iteration of the H2DPI [56]. To demonstrate the accuracy achieved by integrating detector-specific characteristics, the images and spectra generated by the simulation pipeline are validated against experimental data collected with the imager.

5.2 Simulation Pipeline Structure

The objective of the simulation pipeline is to provide users with the capability to simulate scatter-based imaging systems and obtain accurate representations of the system's neutron response. The code produces neutron singles distributions, reconstructed neutron energy spectra, and simple back-projection images. This section describes the structure of the pipeline, which is organized into three primary components: the main particle simulation code, pre-processing software, and post-processing Python routines. While all three components are essential, the discussion here will place particular emphasis on the post-processing stage, highlighting the specific considerations incorporated to closely align simulation outputs with experimental observations.

5.2.1 MCNPX-PoliMi

The MCNPX-PoliMi code was developed to provide accurate simulation of experiments involving the correlated detection of neutrons and gamma-rays [91, 97]. Unlike other versions of the MCNP code, where the characteristics of individual interactions, such as the number and energy of secondary particles, are determined using average quantities derived from nuclear data sets like ENDF/B-VII [98], MCNPX-PoliMi applies energy conservation to each interaction at the event level. This approach ensures a simulation methodology that is faithful to physical principles on an event-by-event basis. Additionally, MCNPX-PoliMi generates a data file containing detailed information about individual collisions within user-specified detector cells. The collision file output provides essential data for the simulation pipeline, including collision coordinates, time tags, particle types, and energy deposited. All simulations presented in this work utilized the ENDF70 (.70c) nuclear data library for neutrons.

The initial step of the pipeline involves executing MCNPX-PoliMi with the appropriate geometry input file to generate the collision file output, as illustrated in Figure 5.1. Key considerations for the MCNP input include specifying accurate material compositions and defining the radiation sources relevant to the scenario under investigation. In this study, two simulation configurations,

A and B as detailed in Section 5.3, were performed. Each configuration was simulated 15 times on a high-performance computing cluster at the University of Michigan to ensure robust statistical reliability. For each individual simulation, 109 fissions were modeled, and the results were subsequently scaled to absolute count rates by scaling with the emission rate of the measured neutron source.

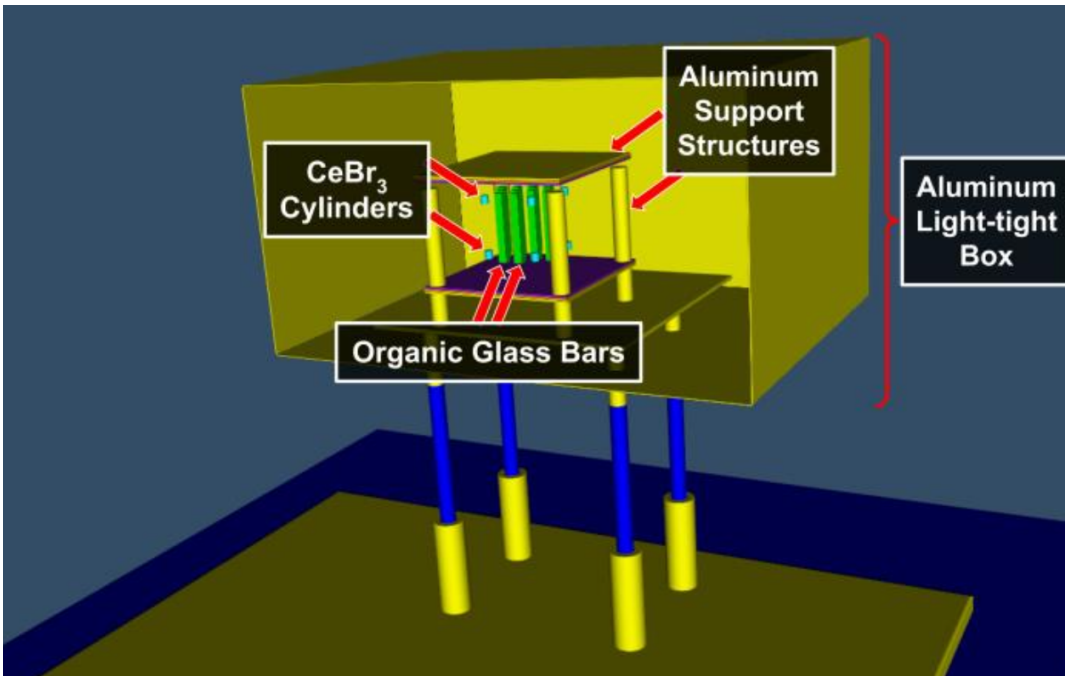

Figure 5.1: Geometry of the active volume and housing of the H2DPI shown using Gxsview [99].

5.2.2 MPPost

The next major component of the pipeline utilizes a software package called MPPost [100], which processes the collision output file from MCNPX-PoliMi to calculate the radiation detector response by generating pulse lists according to user-defined parameters. The pulse generation process involves several key steps: converting neutron energy deposition from the interactions into scintillation light output, incorporating single detector time resolution, and applying light output resolution effects to the simulated data. MPPost has been validated across various detector types, including stilbene organic scintillators, and has been employed in experimental studies involving neutron

time-of-flight and spectroscopy [52, 97].

During neutron elastic scattering in organic scintillators, neutrons transfer energy to recoil protons (hydrogen nuclei), which are responsible for the majority of scintillation light detected by the system. The relationship between energy deposition and light production in the detector material is nonlinear [101]. MPPost employs a semi-empirical function based on Birks' formula [48] to convert energy deposition (MeV), as recorded in the MCNPX-PoliMi collision file, into detector-observed light output (MeVee). This approach can also be applied in reverse, converting light output data back into energy deposition, assuming a single scatter on hydrogen. For this work, the Birks' coefficients used for the OGS in the H2DPI are a = 0.5366 MeVee/MeV and b = 2.6781 cm/MeV (sometimes referred to as S and kB, respectively, in the literature), as shown in Equation 3.10 of Chapter 3. While energy deposition from carbon scatter interactions also contributes to light output, the effect is much smaller than for proton recoils because quenching is significantly greater for carbon. This is due to the stopping power (dE/dx) depending on the particle's charge squared and mass, leading to much less scintillation light from carbon recoils. Accordingly, a linear conversion factor of 1.5% is applied to carbon scatters, reflecting typical organic scintillator responses to fast neutron scatters on carbon [102].

Additional properties of the OGS, such as time resolution and light output resolution, can be configured by the user during execution of MPPost. These detector attributes will be discussed in greater detail in subsequent sections. Currently, MPPost only allows for constant values for the time resolution parameter. MPPost generates an output file comprising a list of pulses detected by the system under the specified scenario and settings. The pulse output includes crucial information for the simulation pipeline, including the simulation history number, detector cell in which the pulse was recorded, particle type, interaction type, corresponding time tag, and expected light output observed by the detector.

5.2.3 Python Post-Processing Code

The final stage of the pipeline utilizes Python code to process the MPPost pulse output files. This stage follows the same methodology outlined in Chapter 3 to reconstruct neutron spectra and generate simple backprojection images. However, several steps used for experimental data are not required for simulated data: Z coordinate reconstruction is omitted because the true interaction locations are already known, and no PSD ratio calculation is performed because all events in the simulation are explicitly labeled with the correct particle type. This section provides a detailed discussion of the four primary additional considerations implemented to ensure the simulated data closely matches the measured detector responses of the H2DPI and other scatter-based imaging systems.

5.2.3.1 XYZ Coordinate Modification

As discussed in Section 5.2.1, MCNPX-PoliMi is capable of determining the exact X, Y, Z coordinates for each interaction, with a precision of up to 0.1 mm. In experimental data, however, the X and Y coordinates for each pulse are approximated using the center position of the OGS bar that recorded the pulse, as the true interaction locations are not available. The accuracy of the Cartesian coordinates for the two neutron scatter locations is critical for accurate neutron energy and time-of-flight calculations and projections. It is therefore essential that the simulation data employ the same coordinate approximation methodology as the experimental data when possible. Even small variations in path length can result in differences in neutron time-of-flight energy calculations, ultimately impacting the reconstructed neutron energies and scattering angles. For consistency, the coordinates in the simulated data are modified by assigning X and Y values based on the bar centers for which they occurred in. Z coordinate reconstruction via top and bottom signal comparisons as discussed in Section 3.1.3 is not feasible in simulation; therefore, the Z coordinate in the simulated data is adjusted by randomly sampling from a Gaussian distribution, where the mean is the exact Z coordinate according to the simulation and sigma is the expected Z reconstruction uncertainty for an event with the given light output.

5.2.3.2 PSD Particle Losses

One of the most significant differences between MPPost pulse output files and experimental data is the degree of certainty in particle classification. As discussed in Chapter 3, PSD is applied to measured data to classify events as either neutrons or gamma rays; however, this technique is subject to misclassification errors. Thus, the measured data may often remove a significant amount of neutron events due to strict particle classification metrics. In contrast, MCNPX-PoliMi assigns an explicit particle type number to each simulated collision, providing absolute certainty in particle identification and ensuring that all neutrons are retained in the data set. Because MCNP does not incorporate PSD as used in the experimental methodology, new post-processing code was developed to more accurately emulate detector response in the simulated data. To this end, a neutron PSD analysis was initially conducted to characterize the neutron removal rate in the OGS bars of the H2DPI as a function of light output.

To begin, light output slices are extracted from the PSD ratio plot of a characteristic neutron measurement. Figure 5.1 illustrates the PSD ratio distribution for the light output slice of 175–200 keVee, with gamma-ray and neutron data fit with separate Gaussian distributions, allowing for effective separation. The inset in Figure 5.1 compares the recorded neutron event distribution for this particular light output slice to its corresponding complete Gaussian fit. The raw neutron data distribution reflects events classified as neutrons based on PSD ratios exceeding the discrimination threshold, and has been truncated by the application of the PSD cut. Consequently, the full Gaussian fit represents the theoretical number of neutron events expected in the absence of this PSD cut. By comparing the number of counts classified as neutrons to the theoretical total, a neutron survival rate can be determined. This PSD analysis was systematically performed across the relevant light output range of 50–400 keVee in increments of 25 keVee. Neutron losses due to PSD are most pronounced at lower light output values, while the removal rate of neutron events above 300 keVee is negligible.

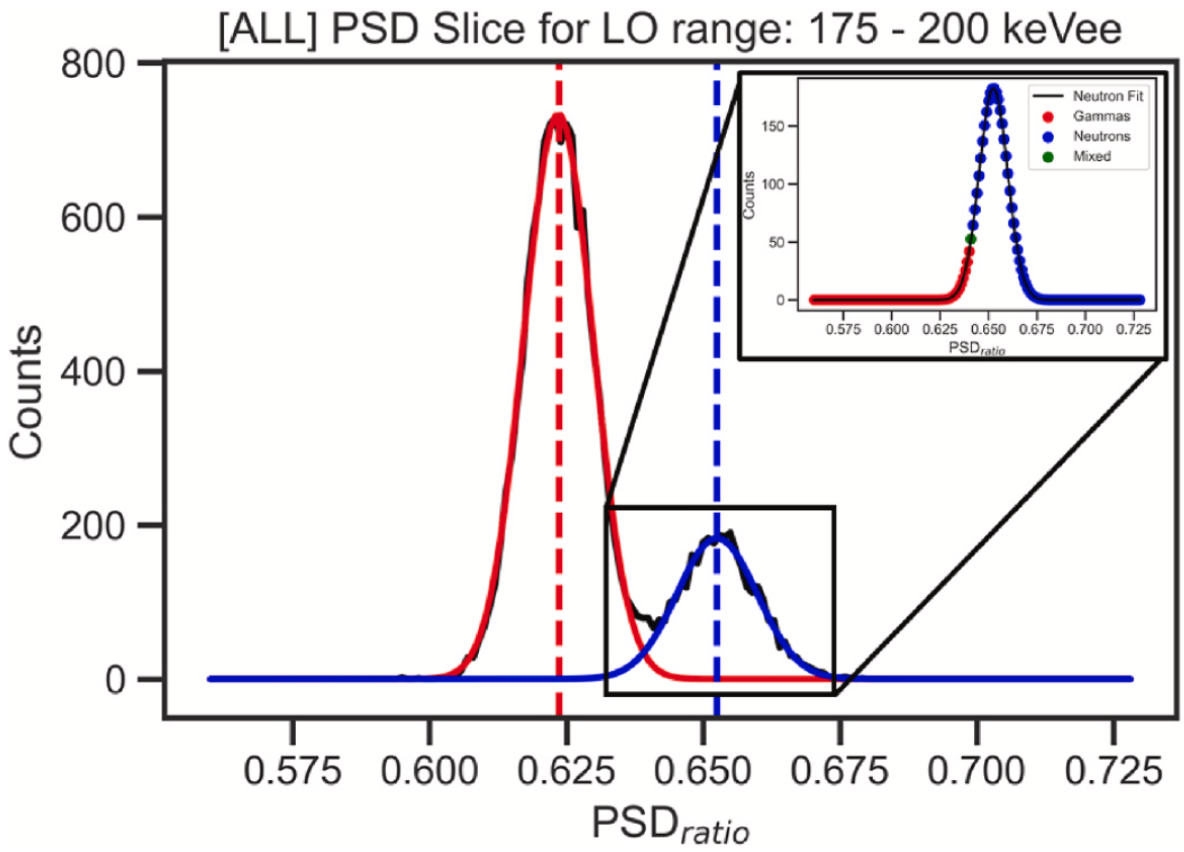

Figure 5.2: PSD ratio distribution for the light output range of 175–200 keVee. Gamma events are on the left distribution and neutrons on the right. The inset in the top right corner shows the particle classification breakdown for the neutron distribution, which is used to determine the neutron removal rate.

Figure 5.3 presents neutron removal percentages as a function of light output for each of the twelve OGS bars in the H2DPI, based on a representative ^{252}Cf measurement. While all bars exhibit the expected trend of decreasing removal rates with increasing light outputs, differences in the rate of change of these rates are observed on a bar-by-bar basis. This variability is attributed to differences in PSD performance among the bars. Each OGS bar was individually cast, wrapped, aligned, and coupled, resulting in slight variations in light collection efficiency. Minor differences in scintillation light output influence the measured waveforms and, consequently, the PSD capability for each bar. To realistically model this behavior, the simulation pipeline samples each neutron pulse independently using a binomial distribution, applying the neutron survival rate determined

by the light output and specific bar involved, in accordance with the trends shown in Figure 5.3. While this work primarily focuses on the characterization of neutron removal, it should be noted that gamma rays can also be misclassified as neutrons due to the inherent limitations of PSD. The PSD discrimination lines were designed to minimize gamma-ray misclassification, yet some level of particle misclassification remains unavoidable. For the initial development of the neutron simulation pipeline, contributions from misclassified gamma rays have been omitted, since they are assumed to be negligible, but the effects of gamma rays warrant further investigation in future work.

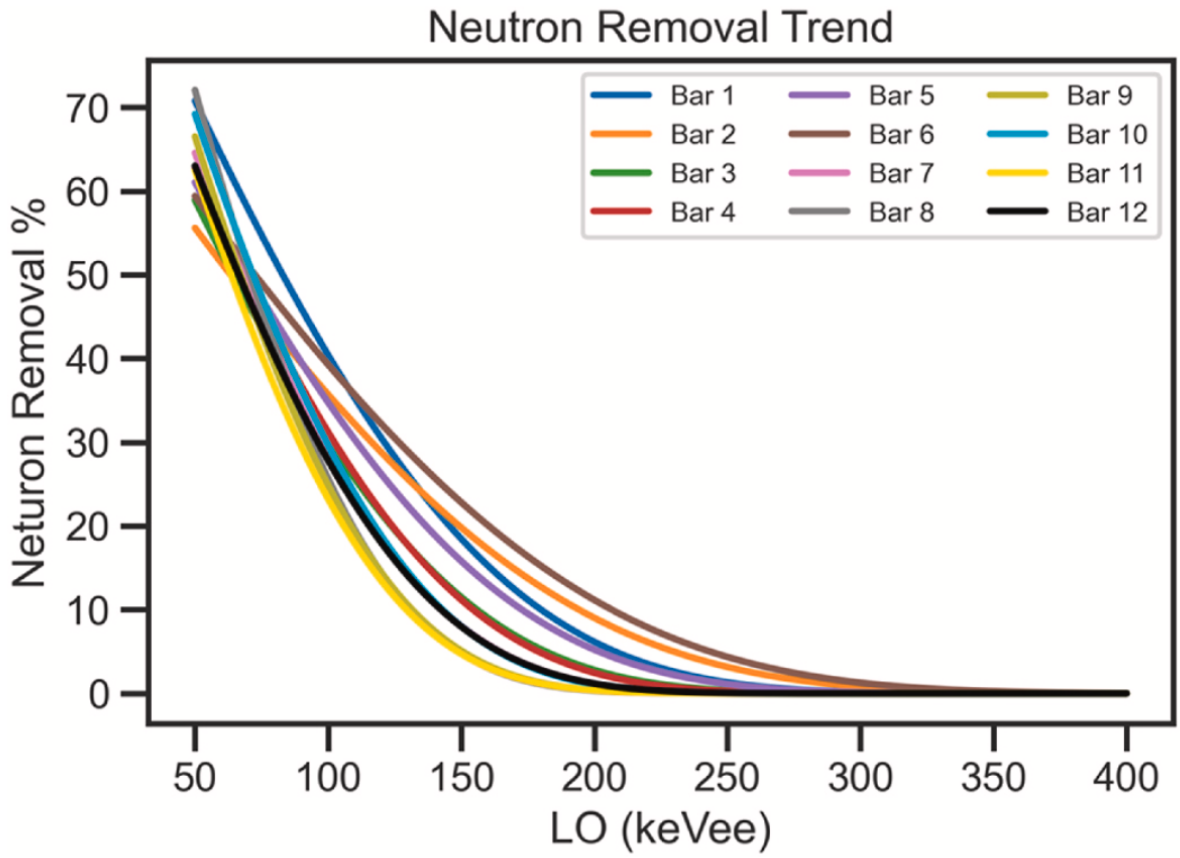

Figure 5.3: Neutron removal percentages due to PSD in the twelve OGS bars in the H2DPI as a function of light output (keVee).

5.2.3.3 Single Detector Time Resolution

The time tags in the MPPost pulse output file are reported with high precision, within an uncertainty of 0.1 ns, because they are derived from kinematic calculations in MCNPX-PoliMi. However, the actual OGS bars in the H2DPI exhibit inherent single-detector time resolution properties that influence the accuracy of the event time tags recorded during measurements. To account for this effect, MPPost allows for time broadening of pulse events based on a user-specified sigma value. In this work, the sigma is the standard deviation of a Gaussian distribution used to model single-detector time resolution. During post-processing, each pulse time tag in MPPost is randomly sampled from a Gaussian distribution centered at the corresponding exact time tag, thereby realistically reflecting the timing uncertainty present in experimental measurements.

Initial experimental characterization of the H2DPI time resolution involved using a ^{137}Cs source to determine the sigma value required for time broadening in MPPost. The coincidence time resolution (CTR) between two OGS bars in the H2DPI was measured experimentally in prior published work [33], and the single detector time resolution was subsequently calculated using the following relationship:

$$\sigma_{CTR} = \sqrt{2}\sigma_R, \tag{5.1}$$

where σ_{CTR} denotes the standard deviation of the coincidence time resolution, and σ_R denotes the single detector time resolution of the OGS bars. The relationship described in Equation 5.1 implies that both OGS bars have the same inherent timing resolution, which is assumed true for now given the same dimensions, material composition, and coupling process. In this study, a value of σ_R = 488 ps is used and is assumed to remain constant across all energies.

5.2.3.4 OGS Light Output Resolution

The final consideration addressed in this work is the incorporation of detector light output resolution into the simulated MPPost pulse output files. By default, MPPost calculates light output values directly from the exact deposited energy determined by MCNPX-PoliMi, without accounting

for uncertainty. In contrast, experimental measurements exhibit inherent light output broadening, which can be characterized and fitted using the previously discussed Equation 3.2.

Experimental characterization of the H2DPI light output resolution was conducted to determine the fitting constants for Equation 3.2. Prior published work [33] shows that measurements were performed using a ^{137}Cs source to obtain the light output response from the OGS detectors. A brute-force algorithm was employed to generate all possible combinations of α, β, and γ parameters for use in MPPost. The brute-force algorithm consisted of changing each fitting parameter from 0 - 0.2 in step sizes of 0.001. The range was chosen such that the light output did not exceed 100% at 478 keVee. The final set of fitting constants was selected by minimizing the χ^2 value between the measured and simulated light output responses. The fitting parameters utilized in this work for OGS bars in the H2DPI are: α = 0.106, β = 0.061, and γ = 0.016.

5.3 Neutron Pipeline Validation

To validate the simulation pipeline developed in this work, two measurements were conducted using the OGS H2DPI. A ^{252}Cf source, with a spontaneous fission rate of 1.04x10^6, was positioned at two distinct locations. From the perspective of the H2DPI, the first location (configuration A) corresponded to an azimuth of -20° and an altitude of 0°, with the source placed 58.4 cm from the center of the H2DPI. In configuration B, the source was positioned identically in terms of altitude and distance, but at 20° azimuth. Photographs of both experimental setups are provided in Figure 5.4. The measurement times for configurations A and B were 3369 s and 4205 s, respectively.

5.3.1 Neutron Singles Response

Figure 5.5 displays the neutron singles light output distribution comparison results for configuration A, expressed in units of absolute count rate (s^{-1}). The simulated data sets were scaled to account for both the total number of simulated particles and the activity of the ^{252}Cf source at the time of the experiment. In Figure 5.5, the "Simulated (Ideal)" distribution represents the expected

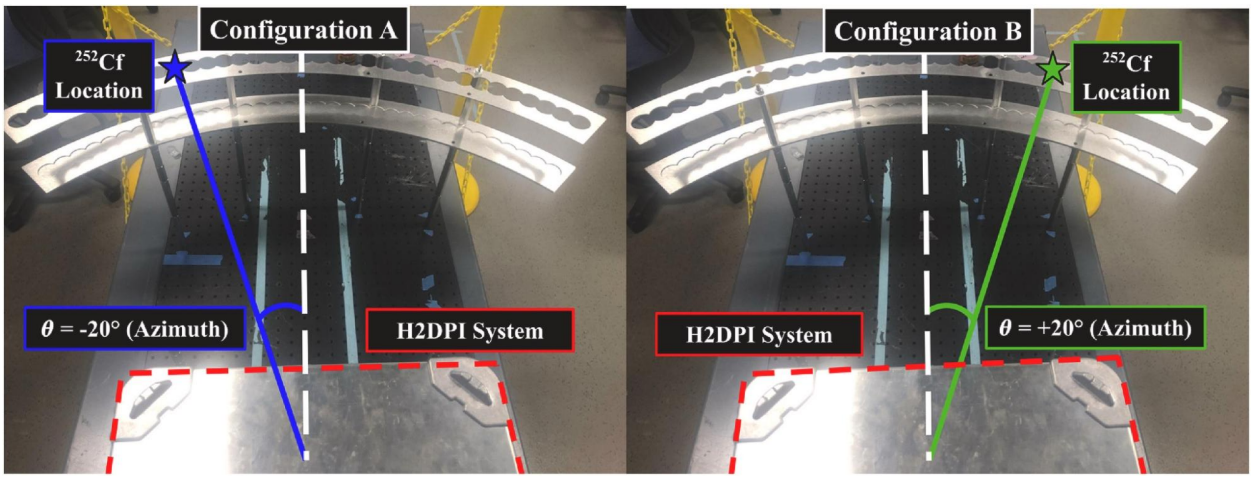

Figure 5.4: Photos of experimental setup used for validation of the simulation pipeline. The ^{252}Cf source was placed in two different locations in azimuthal space. These positions correspond to configuration A at $-20°$ (left) and configuration B at $20°$ (right).

detector response based on idealized simulation results, calculated directly by MCNPX-PoliMi. The "Simulated (Processed)" distribution reflects the simulated response after all considerations and analyses described in Section 5.2.3 have been incorporated. A comparison of the three distributions reveals a notable difference in absolute count rates between the measured and processed simulated responses at low light output values, particularly within the first two bins.

This discrepancy is attributed to the PSD analysis, which removes certain neutron events from the processed simulated data set in the low light output range. The mismatch arises primarily because the contribution from gamma rays misclassified as neutrons has not been accounted for in the current version of the simulation pipeline. Gamma-ray misclassification predominantly affects the neutron singles distribution results; however, the SBP imaging and reconstructed neutron energy analysis stages of the pipeline are largely immune to this effect, as they effectively filter out most gamma-gamma and neutron-gamma double scatter events. This filtering is accomplished by restricting accepted neutron double elastic scatter events to time differences between 0.138-10.4 ns and requiring the reconstructed neutron energy of an imageable event to have less than 50% relative uncertainty. When the first two bins in Figure 5.5 are excluded, a comparison of the integrals for the measured and processed distributions shows that the "Simulated (Processed)" count rate is

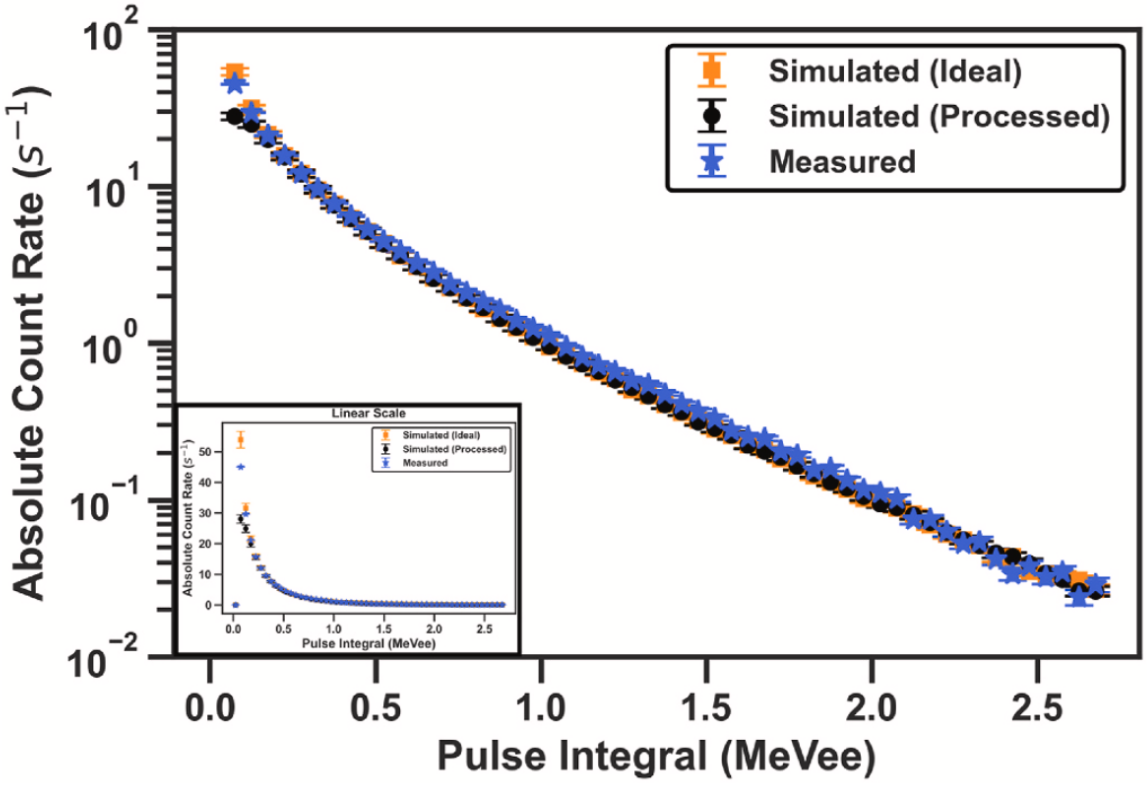

Figure 5.5: Configuration-A neutron singles pulse integral distributions of ^{252}Cf from simulated (both ideal and processed) and measured data across all bars of the H2DPI. Inset shows the same data on a linear y-axis scale.

only 6.2% lower than the measured response.

5.3.2 Neutron Spectroscopy Results

The top panel of Figure 5.6 displays the neutron spectroscopy results for configuration A, comparing various simulated data sets with the measured response. To highlight the significance of each individual analysis component, six different permutations of the simulated data are presented. In addition to the ideal and processed simulated cases, the other data sets each have only one component of the analysis enabled, corresponding to the four key considerations previously discussed in Section 5.2.3. The "Simulated (Ideal)" distribution is generated using exact X, Y, and Z coordinates from MCNPX-PoliMi, with no broadening applied and effectively zero uncertainty assigned

to all metrics during the SBP calculations. In contrast, the "Simulated (Processed)" distribution reflects the output of the simulation pipeline after all analysis components have been implemented to closely match the measured experimental response.

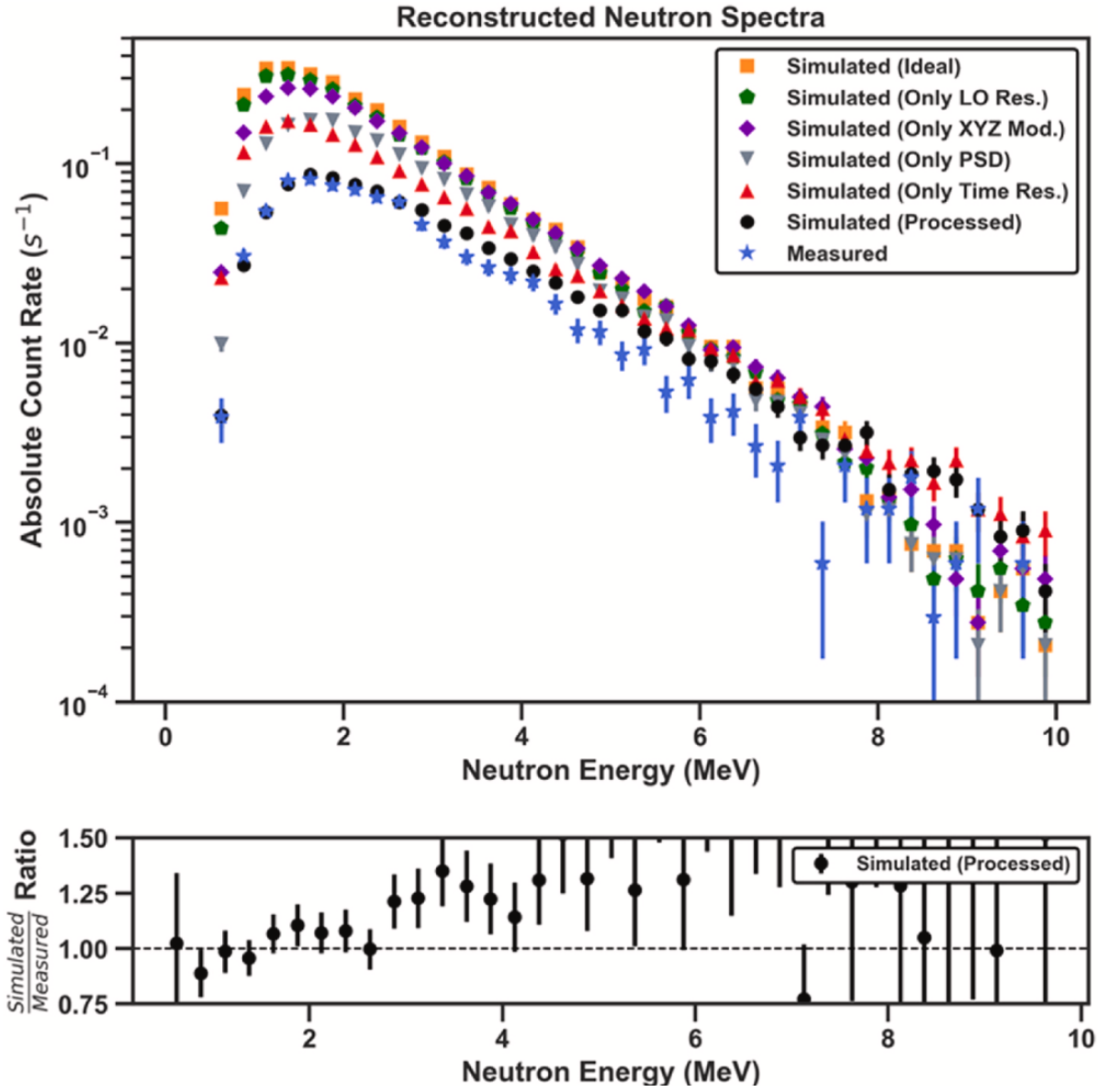

Figure 5.6: Configuration-A reconstructed neutron energy spectra comparison for various simulated data sets and the measured response (top). Ratio plot showing agreement between the processed simulated and measured spectrum (bottom).

This study aimed to quantify the significance of each component within the simulation pipeline. To assess their impact, the percent difference between the various simulated data sets and the measured response was calculated as follows:

$$Percent\ Difference\ (\%) = \frac{Simulated - Measured}{Measured} \times 100, \tag{5.2}$$

where $Simulated$ and $Measured$ refer to the integrals of the distributions presented in Figure 5.6. The percent difference values calculated for each data set, along with the propagated error, are summarized in Table 5.1. The results reveal that the pipeline components can be ordered by increasing significance as follows: detector light output resolution, X/Y/Z coordinate modification, PSD classification, and single detector time resolution. With energy resolution on the order of ten percent for events in the hundreds of keVee range, light output resolution contributes only a minor amount to the net inefficiency observed. Modifications to coordinate calculations have a greater impact, as neutron TOF energy calculations are highly sensitive to the distances measured on the timescales relevant to this work. PSD classification substantially affects the net inefficiency, since most neutron events occur at energies below 200 keVee, where PSD removes the largest fraction of neutron events. Among all factors, timing uncertainties contribute the most, again due to their significant influence on TOF calculations.

Additionally, the Simulated (Ideal) data set overestimated the measured response by 261%, while the Simulated (Processed) data showed a much smaller 14% overestimation. The percent difference calculated for the final simulated processed data set indicates that, after accounting for the imaging system detector attributes, the pipeline achieves good agreement with experimental results. The bottom panel of Figure 5.6 displays the ratio of the Simulated (Processed) to Measured distributions, where a ratio of 1 denotes perfect agreement. Notably, agreement is close to 1 below 3 MeV and approaches 1.25 below 5 MeV.

Despite the good agreement between the final simulated and measured distributions presented in Figure 5.6, some discrepancy persists at higher reconstructed energies. This difference is

Table 5.1: Summary of agreement with measured spectrometry response of configuration A for the various components of the simulation analysis.

	Percent Difference (%)
Simulated (Ideal)	$+261.0 \pm 8.7$
Simulated (Only LO Resolution)	$+228.3 \pm 7.9$
Simulated (Only XYZ Modification)	$+199.7 \pm 7.2$
Simulated (Only PSD Removal)	$+110.3 \pm 5.1$
Simulated (Only Time Resolution)	$+98.9 \pm 4.8$
Simulated (Processed)	$+14.0 \pm 2.8$

likely attributable to the assumptions made in the time resolution analysis described in subsubsection 5.2.3.3, in which a constant single detector time resolution value was applied. A more accurate approach would account for the fact that time resolution generally degrades at low light output but improves at higher energies. The choice to use a constant time broadening value affects the reconstructed neutron spectrum in two important ways.

Firstly, the use of a constant time resolution results in either under- or over-broadening of times for low- and high-energy scatters, respectively, which leads to inaccuracies in the E_{TOF} values used for incident neutron energy reconstruction. Given that the constant single detector time resolution was characterized using data predominantly from low light output events, it is expected that agreement is best in the lower energy range of the spectrum in Figure 5.6, with deviations increasing at higher energies.

Secondly, applying an inappropriate time broadening parameter may result in an incorrect number of simulated double scatters within the coincidence window defined in the code. In actual experiments, time broadening can cause some neutron events to fail to meet the timing criteria, or introduce chance coincidences that erroneously satisfy these conditions. For the simulation pipeline to more accurately reflect experimental behavior, timing resolution should be implemented as a variable parameter rather than a constant.

Another contributor to the discrepancy in the total number of events is the current pipeline's inability to fully replicate an observed phenomenon in which events are excluded from the measured data set due to the reconstructed Z coordinate falling outside the physical bounds of the OGS bars. This situation typically arises when either a low energy deposition scatter occurs or when one of the end pixels in a bar receives insufficient scintillation statistics, such as when an interaction occurs at the extreme ends of the bars. Pulse integrals may have a high degree of uncertainty and often result in a poor ratio when using Equation 3.4. The current simulation pipeline only removes scatters near the bar ends if broadening causes their reconstructed position to fall outside the boundaries. There is no method accounting for potential removal when events occur at other points along the OGS bars with low light output where one end of the bar may receive low statistics and result in a ratio that is not valid for reconstruction. If adjusting the single detector timing resolution methodology does not adequately address the disagreement in absolute count rates, future work should further characterize the Z reconstruction loss behavior to further improve pipeline accuracy.

5.3.3 Neutron Imaging Results

For the SBP imaging analysis, separate simulation runs were performed to match the expected number of spontaneous fissions that occurred during the measurement periods. The simulation for configuration A had 3.503E9 spontaneous fissions simulated while the configuration B had 4.164E9. By matching the simulated number of fission events with the amount expected to have occurred during the experiment, the imaging results enable a direct comparison of the imaging efficiencies of the H2DPI, as predicted by the simulation and as observed in the measured data.

Figure 5.7 presents the SBP images generated from ideal simulated data, processed simulated data, and measured data for configuration A. The observed numbers of imageable events (cones) were 9809 for the ideal data set, 3123 for the processed data, and 2719 for the measured data. Visually, the ideal data set yields an image that appears significantly more convergent than the others. The processed and measured images are comparable in both shape and image intensity, as indicated by the colorbar. Importantly, all three images correctly localize the ^{252}Cf source, which

was positioned at $(-20^\circ, 0^\circ)$. Applying Equation 5.2 to the number of cones obtained from the simulated datasets produces a percent difference of +260.8% for the ideal data set and +14.9% for the processed data set. These values are consistent with the percent differences reported in Table 5.1, which were derived from the reconstructed spectrum analysis. The imaging results indicate that utilizing the neutron simulation pipeline yields imaging efficiencies comparable to those observed experimentally.

Figure 5.8 displays the SBP images generated from the ideal simulated data, processed simulated data, and measured data for configuration B. The number of cones obtained were 11791 for the ideal data set, 3671 for the processed data, and 3104 for the measured data. These values are all greater than those observed for configuration A, which is expected given the longer measurement time for configuration B. Visually, the ideal data set again yields an image that appears considerably more convergent than the other two. The processed and measured images are similar in both shape and image intensity as well. All three images accurately localize the ^{252}Cf source, which was positioned at $(20^\circ, 0^\circ)$. Applying Equation 5.2 to the simulated data sets for configuration B results in percent differences of +279.9% for the ideal data and +18.3% for the processed data. These values are consistent with the trends observed for configuration A, further supporting the conclusion that developed pipeline can achieve imaging efficiencies comparable to those seen in measurements for other source configurations.

Figure 5.9 presents the azimuth and altitude profile distributions for the processed simulated and measured SBP images of configuration A. Cuts were made along the x and y axes at the anticipated source location. Azimuth and altitude values were determined using a weighted mean analysis, treating the image intensity distributions as frequency distributions. The ideal simulated data are not plotted, as their magnitude is significantly greater than the other distributions and would dominate the y-axis; however, the weighted mean values are still reported. Inspection of the profiles reveals similarities in the shape and trends. The small discrepancies observed may hint that some properties like the timing or energy resolution may also be position dependent in the real system.

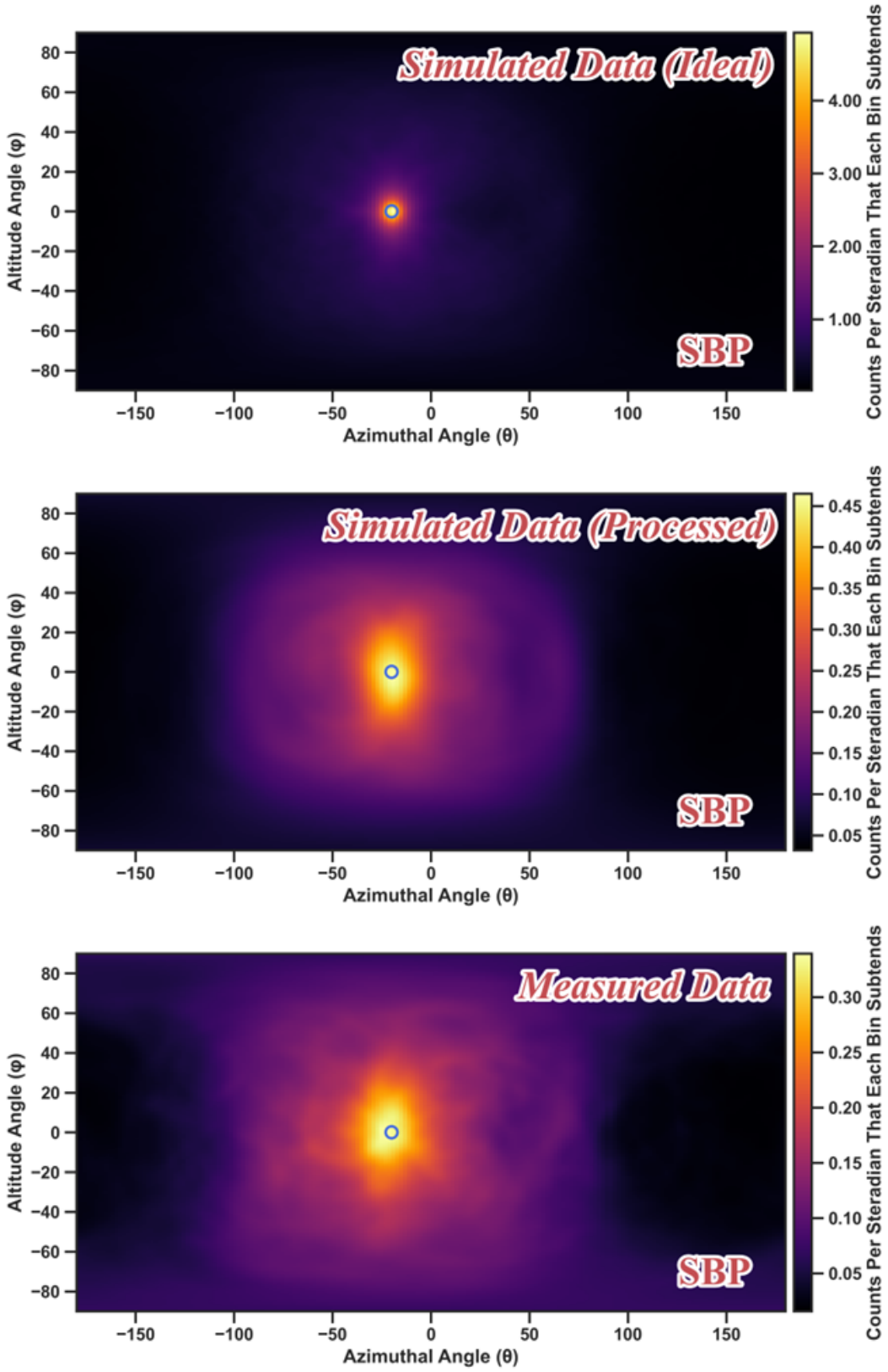

Figure 5.7: SBP neutron images from the simulated ideal (top), simulated processed (middle), and measured (bottom) data sets for configuration A. True source location is shown as a circular outline at $(-20^\circ, 0^\circ)$.

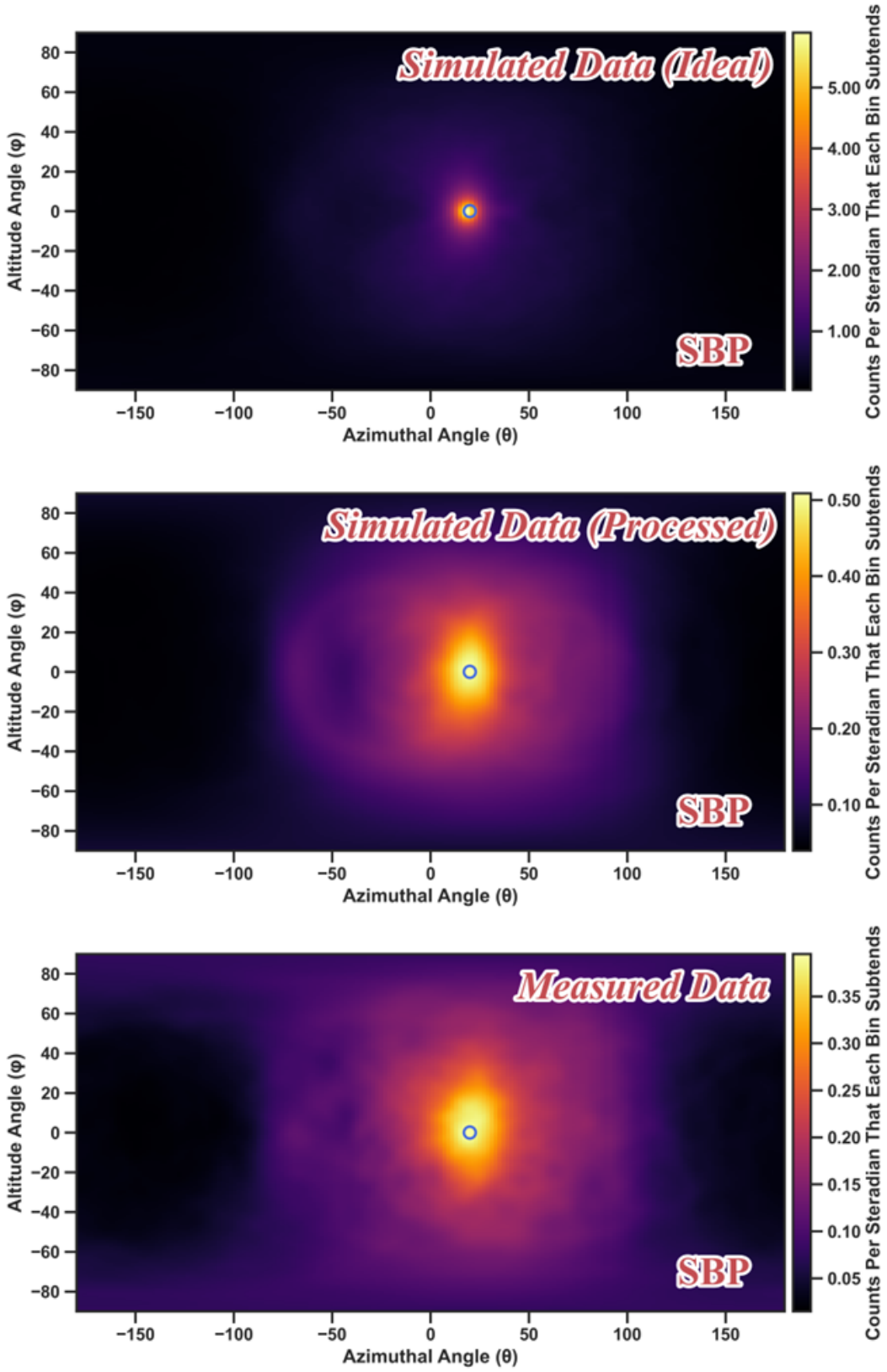

Figure 5.8: SBP neutron images from the simulated ideal (top), simulated processed (middle), and measured (bottom) data sets for configuration B. True source location is shown as a circular outline at (20°, 0°).

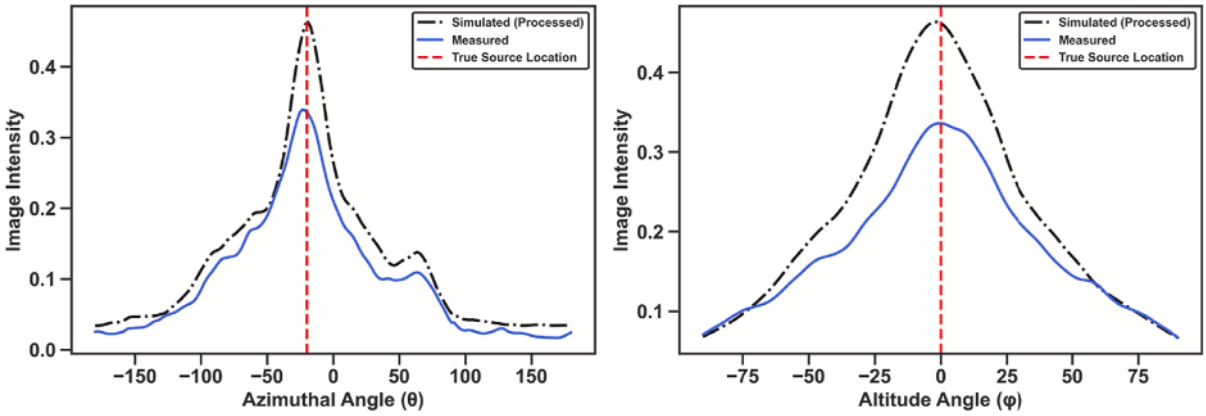

Figure 5.9: Configuration A angular distributions from SBP images for azimuth (left) and altitude (right) directions. The true source angular location is indicated by a vertical dashed line.

Table 5.2 summarizes the expected azimuth and altitude angles for the configuration A ideal simulated data, processed simulated data, and measured data. Note that the uncertainties reported are standard deviation of Gaussian fits to the distributions for data above 30% of the peak value. The results indicate that all three distributions were within 1.5° of the true azimuth angle (-20°) and within 1° of the true altitude angle (0°). For reference, at the source distance used in this experiment, a 1° angular uncertainty corresponds to approximately 1.15 cm of spatial uncertainty, while a 0.1° uncertainty equates to about 1.5 mm. These findings demonstrate that the current OGS H2DPI system, and similar scatter-based imaging systems, have limited spatial resolution capabilities but generally good accuracy.

Table 5.2: Expected angles using weighted mean of results from configuration A. Uncertainties represent the standard deviation (σ) derived from a Gaussian fit of the angular distribution.

	Azimuth Angle θ (°)	**Altitude Angle φ (°)**
Simulated (Ideal)	-19.4 ± 4.6	-0.8 ± 4.8
Simulated (Processed)	-19.2 ± 12.9	-0.9 ± 19.4
Measured	-21.3 ± 18.1	$+0.1 \pm 19.5$
True	-20	0

Figure 5.10 presents the azimuth and altitude profile distributions for the processed simulated and measured SBP images of configuration B. As with configuration A, the ideal simulated data are

not plotted due to their significantly larger magnitude. Inspection of the profiles again reveals good agreement in the shape and trends. The expected azimuth and altitude angles for the configuration B ideal simulated data, processed simulated data, and measured data are summarized in Table 5.3. The results for configuration B indicate that all three distributions were within $3.5°$ of the true azimuth angle ($20°$) and within $2°$ of the true altitude angle ($0°$).

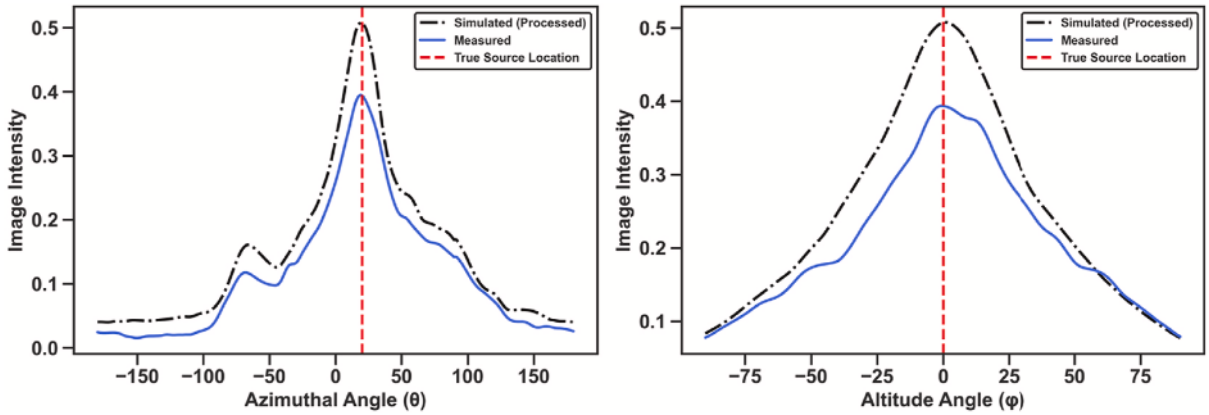

Figure 5.10: Configuration B angular distributions from SBP images for azimuth (left) and altitude (right) directions. The true source angular location is indicated by a vertical dashed line.

Table 5.3: Expected angles using weighted mean of results from configuration B. Uncertainties represent the standard deviation (σ) derived from a Gaussian fit of the angular distribution.

	Azimuth Angle θ (°)	**Altitude Angle φ (°)**
Simulated (Ideal)	$+17.9 \pm 5.1$	-0.7 ± 5.5
Simulated (Processed)	$+20.3 \pm 16.7$	-0.1 ± 22.9
Measured	$+23.4 \pm 14.3$	$+1.8 \pm 18.2$
True	$+20$	0

5.4 Characterization of Coincidence Time Resolution (CTR) as a Function of Light Output

A preliminary study utilizing coincidence measurements with Compton scattering was conducted to characterize the CTR as a function of scintillation light yield for a pair of OGS bars in the

H2DPI. Timing resolution was assessed for coincident events, each with light outputs ranging from 100 to 1100 keVee. A 2 ns time window was applied to identify coincident Compton scatter events within the dataset. The coincident data set was filtered so that the light outputs from the first and second scatters were each divided into 10 keVee intervals, producing histograms of CTR distributions spanning various light output ranges. Each subset was analyzed to determine the standard deviation of the time differences for each combination of light outputs, and these values were systematically recorded. The final result is a matrix of CTR FWHM values, with columns representing the light output of the first Compton scatter and rows representing that of the second Compton scatter. This list-mode data set was subsequently fit to the following function:

$$\sigma^2(LY_1, LY_2) = \frac{a_1}{LY_1} + \frac{a_2}{LY_2} + \frac{b_1}{LY_1^2} + \frac{b_2}{LY_2^2} + C, \tag{5.3}$$

where LY_1 and LY_2 are the light outputs, in keVee, from the first and second Compton scatters, respectively, and a_1, a_2, b_1, b_2 and C are fitting constants. Because the fit yields values in units of ps^2, the constants a_1 and a_2 have units of keVee·ps^2; b_1 and b_2 are in keVee^2·ps^2; and C is in ps^2. The fit is physics-motivated: the parameters a_1 and a_2 represent the contribution of uncertainty from timing resolution, which is typically inversely proportional to the square root of the deposited energy due to the Poisson statistics associated with scintillation photon production. The next parameters, b_1 and b_2 account for uncertainty from time jitter, which is inversely proportional to the pulse leading edge or deposited energy. The final term, C, encompasses all remaining contributions that are independent of energy. It is important to note that this function is expressed in terms of variance, hence the squared relationships for the corresponding proportionalities.

5.4.1 CTR Experimental Setup

The CTR measurement was conducted using a 30 μCi ^{60}Co gamma-ray source. The experimental setup was configured to collect coincident Compton scatters between two OGS bars positioned in alignment with the source. During the measurement, the source disk was placed within the

light-tight enclosure that houses the active volume of the H2DPI, as depicted in Figure 5.11. A source holder ensured collinear alignment of the gamma-ray source with the two OGS bars at the midpoint height of the detector array. To ensure sufficient statistics across all scattering angles and corresponding energy depositions, the source was measured for approximately 24 hours. The separation between the two OGS bars was set to 6 mm.

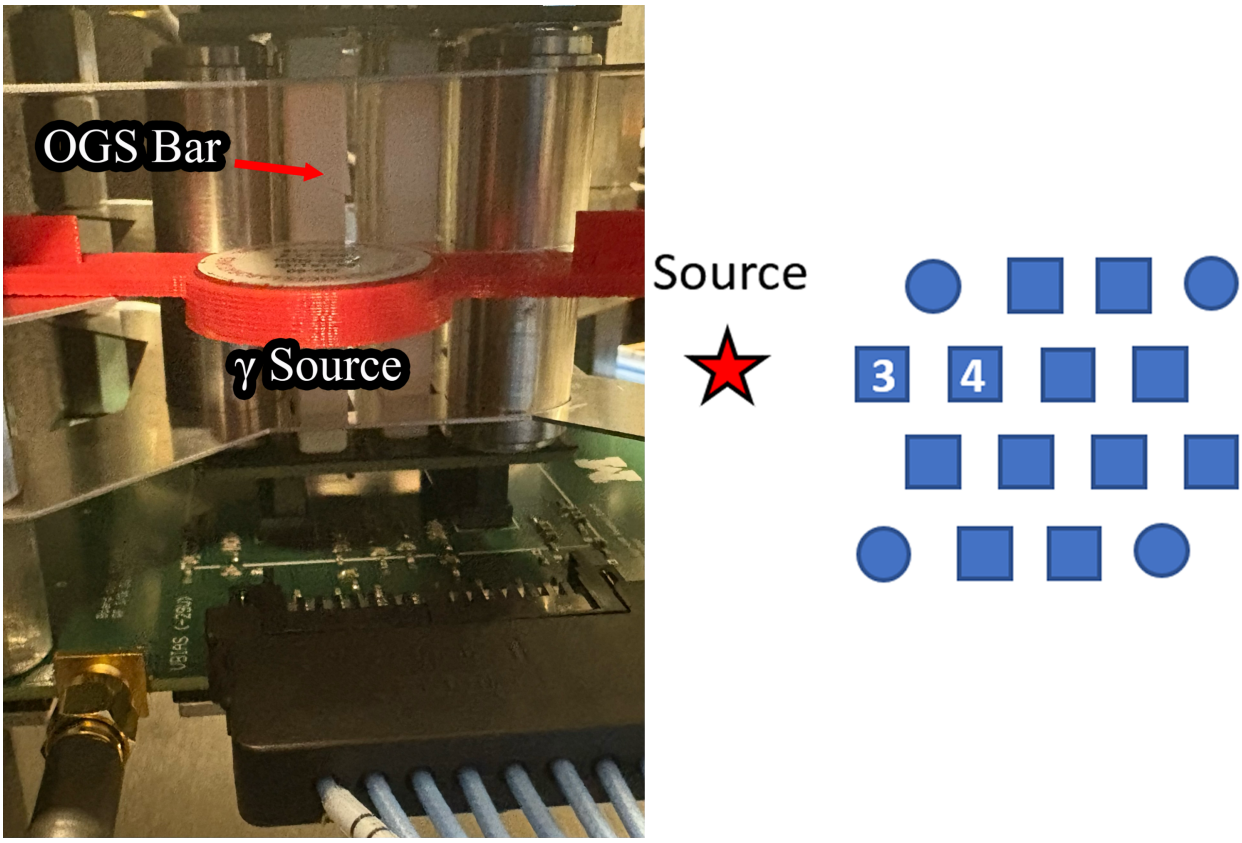

Figure 5.11: Photo of the experimental setup for CTR measurements (left). The identified OGS bar represents one of the detectors analyzed; the second bar is positioned directly behind and not visible. Top-down schematic showing OGS bars 3 and 4 relative positions (right).

5.4.2 Results of CTR Dependence on Light Output

The results from the CTR experiment are presented in Figure 5.12, which shows the FWHM values of the CTR distributions across several light outputs. Depending on the amount of scintillation light output from the events, the FWHM of the measured coincidence time resolution ranged from 653

± 16 ps for lower summed light yields around 110 keVee to 121 ± 8 ps for higher yields at 1100 keVee. The measured FWHM values were fit to Equation 5.3, with the resulting fitting coefficients summarized in Table 5.4. The residuals plot in Figure 5.12 demonstrates the quality of the fit, with most residuals falling within ± 25 ps of the measured FWHM values.

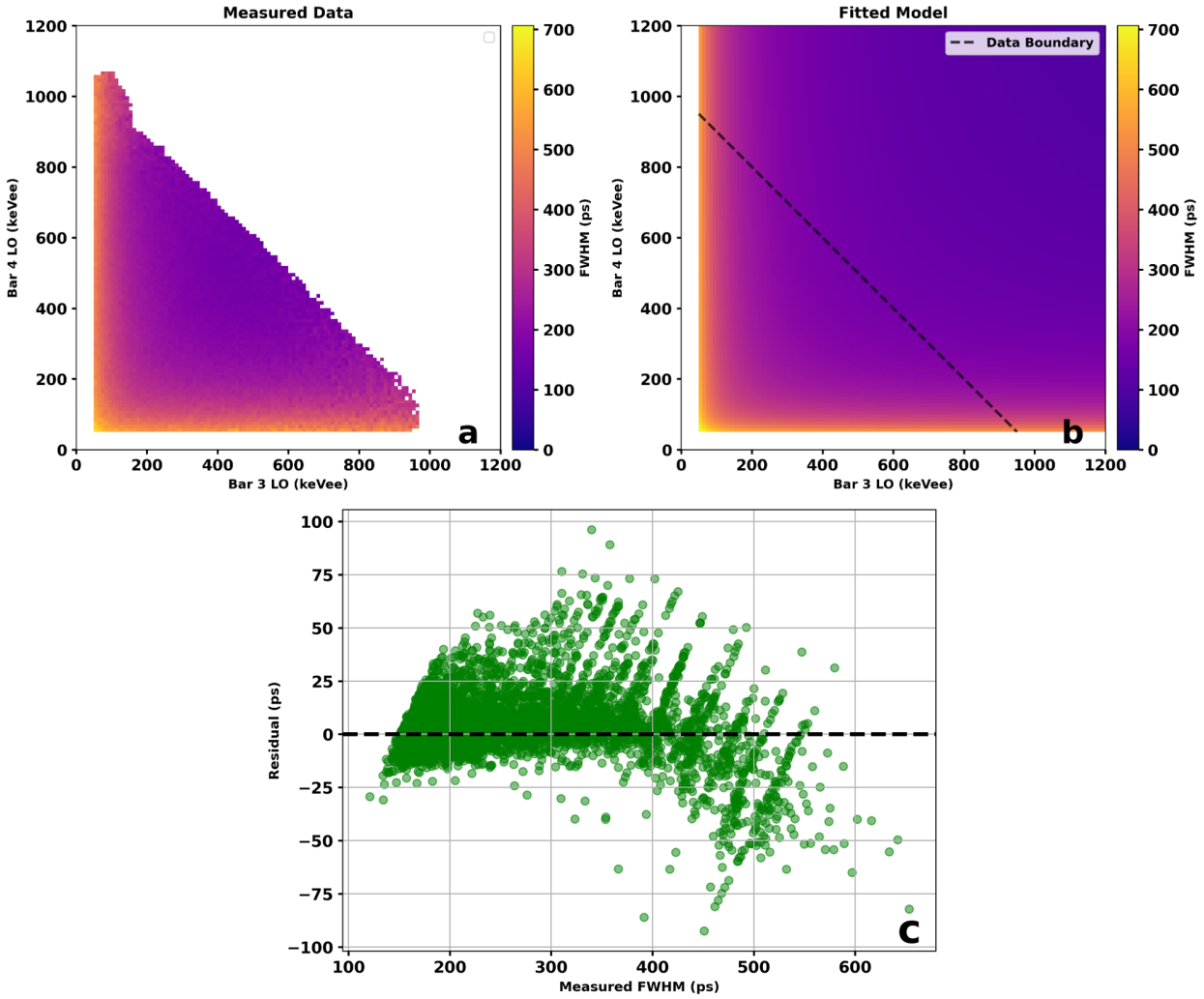

Figure 5.12: (a) ^{60}Co CTR between OGS bars 3 and 4 as a function of light output. (b) Resulting fit based on the observed data. The dashed line represents the extent of which real data is available from the measurement. (c) Residuals of the fit with respect to the measurement results.

Table 5.4: Summary of Equation 5.3 model parameters for CTR experiment.

	^{60}**Co Data Set**
a_1 **(keVee** $\cdot$ **ps**^{2}**)**	$6.8\text{E}6 \pm 1.1\text{E}5$
a_2 **(keVee** $\cdot$ **ps**^{2}**)**	$3.7\text{E}6 \pm 1.0\text{E}5$
b_1 **(keVee**^{2} $\cdot$ **ps**^{2}**)**	$5.0\text{E}8 \pm 9.1\text{E}6$
b_2 **(keVee**^{2} $\cdot$ **ps**^{2}**)**	$5.6\text{E}8 \pm 8.5\text{E}6$
C **(ps**^{2}**)**	$2.6\text{E-}13 \pm 3.8\text{E}2$

5.5 Implications

The work presented in this chapter demonstrates the development of a neutron simulation pipeline for imaging and spectroscopy using the OGS H2DPI system. This chapter highlights the extensive system characterization required to achieve good agreement between simulation results and experimental measurements. While the efforts described were specifically tailored to the H2DPI, much of the foundational work can be adapted to other scatter-based scintillation systems. Future studies should expand the scope of simulations to include neutron sources beyond ^{252}Cf, eventually incorporating SNM as well. The preliminary study described at the end of the chapter successfully characterized the dependence of CTR on scintillation light output for a pair of OGS bars in the H2DPI. Given that timing uncertainty can vary by nearly a factor of six depending on the light output, there is a strong motivation to further characterize the remaining pairs of OGS bars within the H2DPI to achieve a comprehensive system timing response. Collecting further experimental data and determining fitting parameters from Equation 5.3 for the most common bar pairings will allow variable timing uncertainty calculations to be included in both experimental and simulation pipelines, which should improve agreement between simulation results and measured data. Establishing a robust simulation model and processing pipeline will enable more accurate data analysis in future research and support verification efforts.

CHAPTER 6

Using Mixed Reality for the Real-Time Visualization of Imaging Data

6.1 Motivation

Radiation imaging and source localization are indispensable tools in routine operations, emergency response, and treaty verification scenarios involving radioactive materials. Imaging detector systems provide directional information about incoming radiation, thereby expediting searches and reducing radiation exposure risks for personnel [103]. With such systems, operators can monitor the spatial distribution, or ”hot spots”, of radiation from a safe distance, eliminating the need for close physical proximity to radioactive sources. Mixed reality (MR) is a technology that enables the interaction with both virtual and real objects, allowing complex data to be displayed in real-time as holographic overlays within the user's visual field. Over the past decade, the integration of MR and related technologies into nuclear applications has been increasingly recognized [104] and continues to evolve. Initial efforts concentrated on nuclear power plant inspections [105], but the field has since expanded to encompass general nuclear applications and explore methods for enhancing visualizations [106].

Interpreting radiation images typically requires converting two-dimensional angular information into a three-dimensional visual context. MR offers the distinct advantage of bypassing this cognitive step, enabling users to perceive radiation data directly as three-dimensional overlays onto their physical environment. This specific application of MR in redation

While this specific application of MR in radiation imaging remains largely unexplored in recent literature, parallel uses have been demonstrated in fields such as medicine and occupational safety [107]. MR technologies hold the potential to empower non-radiation professionals, including emergency responders, non-specialized armed forces, and researchers in training, to conduct routine radiation monitoring and respond effectively to accident scenarios. The objective of this work is to demonstrate a real-time MR display of both gamma ray and fast neutron images generated from data acquired with the OGS H2DPI.

6.2 Mixed Reality Implementation

6.2.1 Overview of Pipeline

An overview of the data pipeline, from detector interactions to MR display, is illustrated in Figure 6.1. Radiation events in the H2DPI are recorded following the processes described in Chapter 3. The acquired waveforms are transmitted at regular intervals via an optical connection to a data acquisition PC, where they are processed and forwarded over WiFi to a Microsoft HoloLens 2 headset using a locally hosted server. The HoloLens 2, equipped with an array of sensors for environmental mapping, projects the imaging data directly into the user's field of view. A batch list mode approach is employed to transmit data to the HoloLens, optimizing network efficiency and minimizing strain on the headset's onboard CPU. Single-event data are used to estimate total count rates for each detector (covering both neutrons and gamma rays). These average count rates serve as inputs to a pre-trained neural network, discussed in Section 6.2.3, that predicts the azimuthal direction of the source and visually indicates the direction to the user via an arrow. Double-scatter events enable reconstruction of the detected particle's incidence cone, characterized by an opening angle α. PSD is then applied to classify individual events in the OGS, facilitating the creation of distinct neutron-neutron and gamma-gamma cone datasets. A simple backprojection algorithm is used to overlay these cones, generating angular space radiation images (azimuth, altitude) for either gamma rays or fast neutrons. The resulting image is rendered as a three-dimensional projection

within the MR environment for the user's visualization.

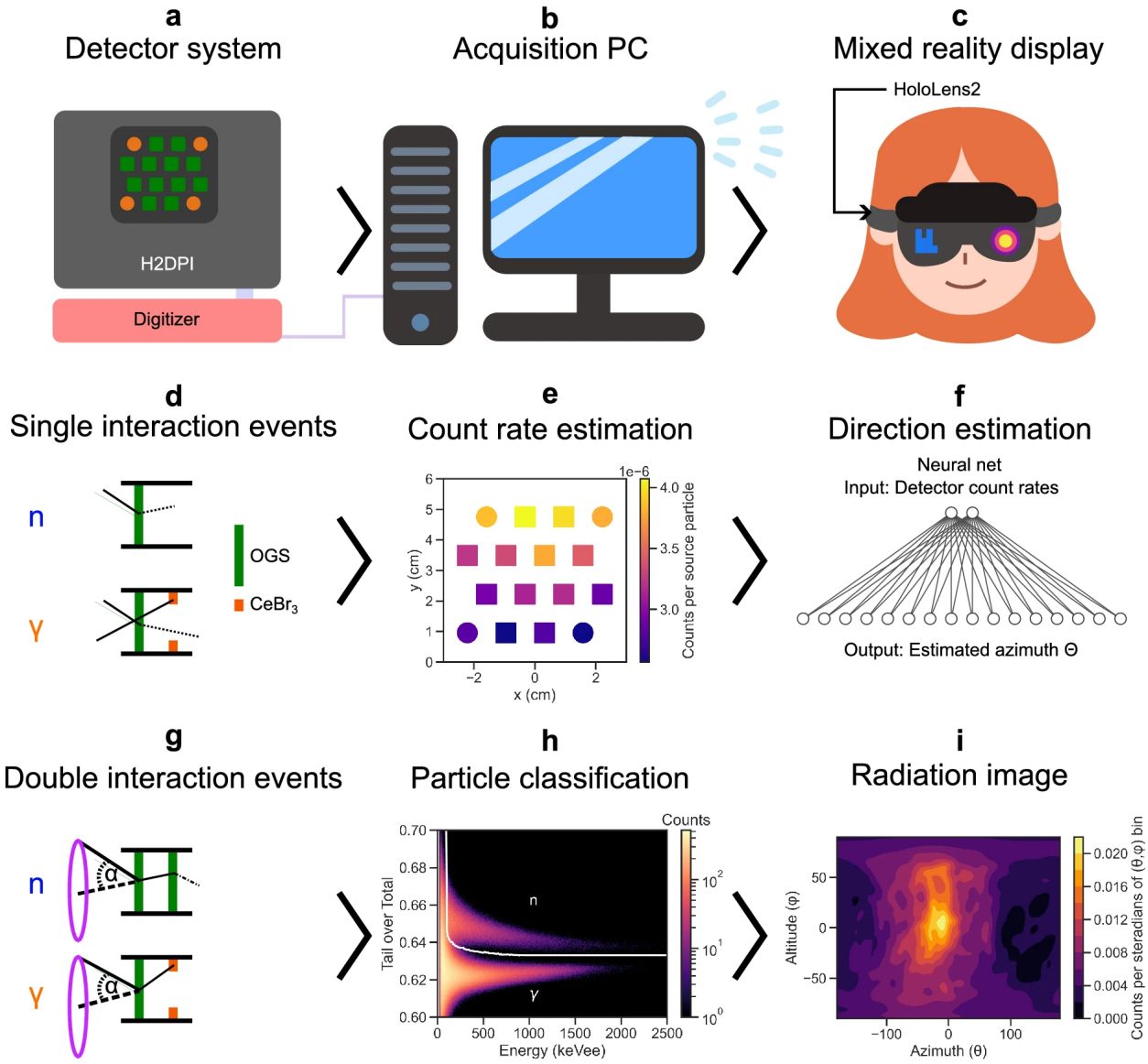

Figure 6.1: Overview of the data processing from particle interactions to MR display [35].

6.2.2 Real-Time Imaging in Mixed Reality

The MR display on the HoloLens is accomplished through a series of steps using a custom application developed in the Unity game engine [108] and deployed on the HoloLens. Three-dimensional spatial mapping is a fundamental feature of the HoloLens, and its application programming interface (API) enables the backend programmer to access and utilize the spatial map of the user's environment. Figure 6.2 presents an example of the spatial map as it would appear to the user. However, because the spatial mapping visualization is primarily useful for debugging and can significantly clutter the user's FOV, this rendering is typically toggled off during standard operation.

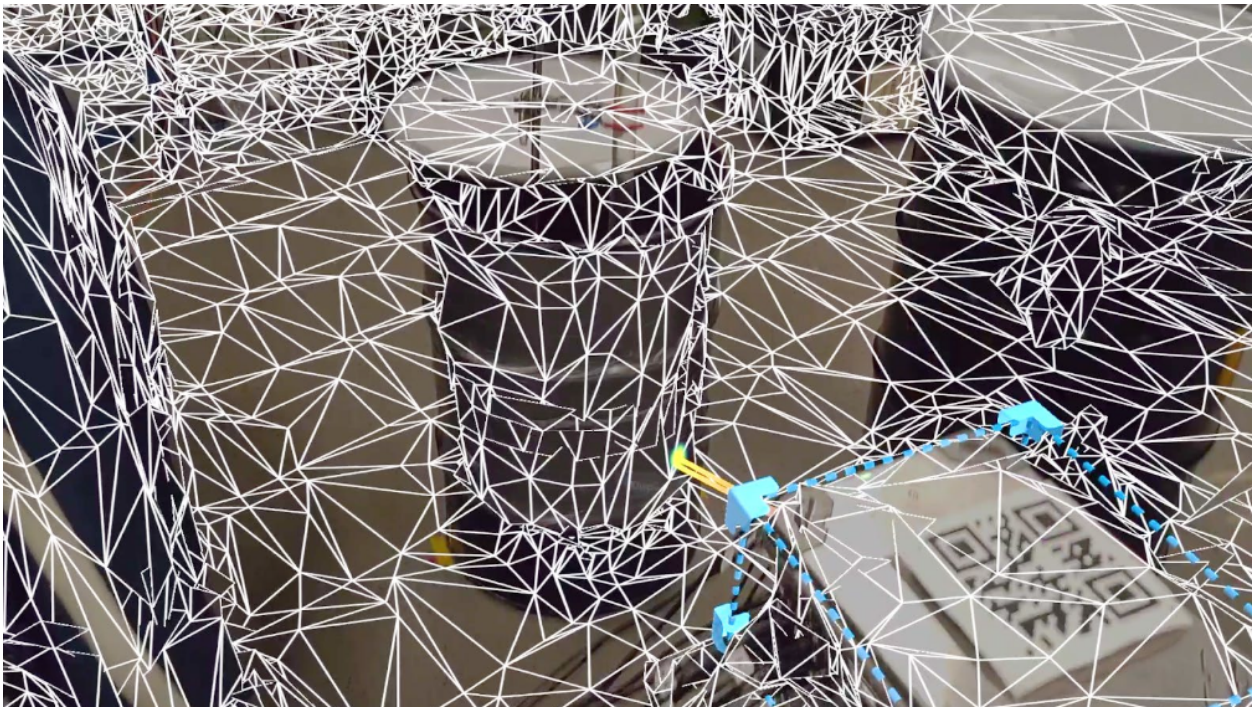

Figure 6.2: Screenshot taken on the HoloLens 2 demonstrating the native spatial mesh.

The HoloLens API also enables the scanning of QR codes within the environment to localize specific three-dimensional coordinates in the spatial map. In this application, a QR code is affixed to the surface of the H2DPI at a known position relative to the center of the detector system (as depicted in Figure 6.3), providing a reference location and establishing a frame of reference for the application. Upon receiving imaging data from the server, the visualizer executes a simple back-projection algorithm to generate a radiation image texture within H2DPI space. A pixel shader is

employed to render this image onto the spatial mesh. For each pixel in the mesh, the screen position is mapped to the reference coordinates and subsequently transformed into H2DPI spherical coordinates, which are then used to sample the corresponding value from the radiation image. A color map is applied to convey intensity, producing a colored visualization on the spatial mesh; more intense coloring corresponds to higher radiation image intensities in that spatial direction.

In addition to spatial mesh coloring, the program iterates through each pixel in the backprojected texture and projects a ray from the H2DPI to visualize the angular nature of the information contained in the image. If a ray both intersects with the spatial mesh and exceeds a specified intensity threshold, a line is drawn between the H2DPI and the point on the spatial mesh, as shown in Figure 6.3. All processing steps are typically completed in under one second, ensuring a visually smooth user experience with minimal lag. The user can select between displaying rays or spatial mesh coloring using a virtual menu located on their wrist or by using voice commands.

As an illustration of the resulting visual experience, Figure 6.3 presents screenshots captured with the HoloLens during two experimental scenarios. In the first example, a ^{137}Cs source was concealed beneath one of three caps. After approximately 30 seconds of data acquisition, the HoloLens displays either the colored spatial mesh or projected rays based on the backprojection image. Additional examples feature neutron and gamma ray images acquired using a ^{252}Cf source positioned approximately 0.5 meters in front of the detection system.

An important aspect of the colored shading used to indicate hot spots is the selection of perceptually uniform sequential colormaps [109]. The standard perceptually uniform sequential colormaps available in Matplotlib, viridis, inferno, magma, plasma, and cividis, were incorporated as selectable options in the virtual menu of the application [110]. This allows users to choose the colormap that maximizes contrast for a given background or accommodates their personal color vision abilities. For example, a colormap containing red (inferno) on a green background, such as grass, may be less effective for a user with deuteranomaly; they may choose to switch to a yellow/blue-based map (cividis) to improve visibility and interpretability.

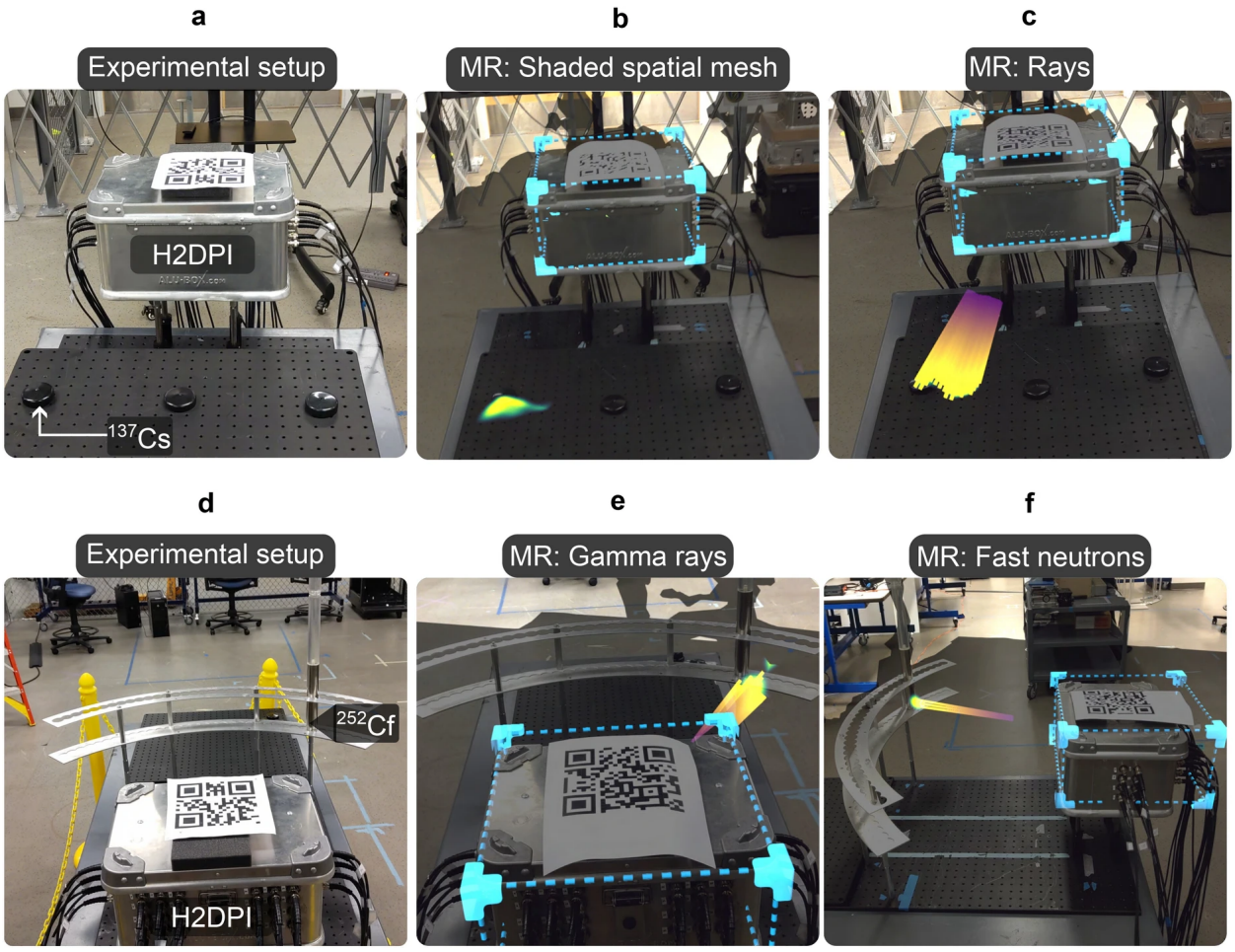

Figure 6.3: Examples of the mixed reality visuals as seen by the user wearing the HoloLens 2. (a-c) A ^{137}Cs source hidden underneath one of three caps in front of the detector system. (d-f) A ^{252}Cf source in front of the system [35].

Finally, the user also has the option to perform energy gating on the gamma-ray data similar to the implementations shown in Chapter 4. Figure 6.4 shows a screenshot of the gamma-ray coincidence spectrum collected from a measurement involving ^{137}Cs and ^{22}Na in the same FOV. Isolating the ^{22}Na would require the use of an energy gate as shown in the displayed spectrum with a gated region surrounding the 511 keV emission. Users are able to set variable energy gates at their discretion in real-time to search for specific sources if necessary.

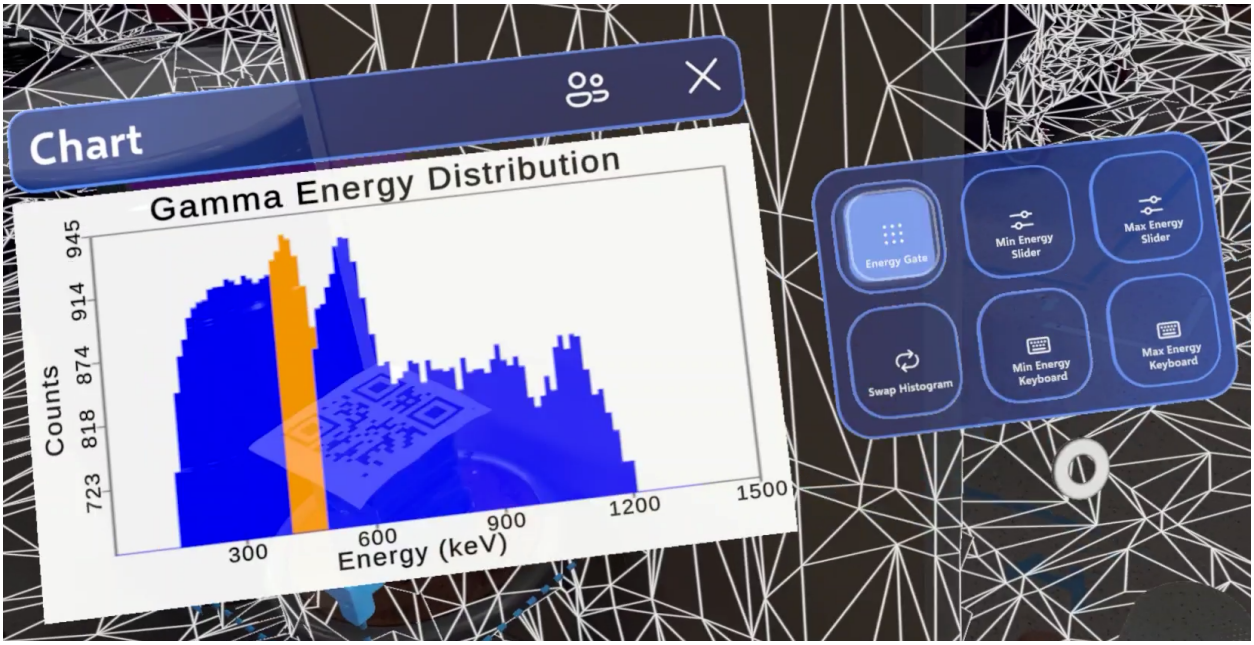

Figure 6.4: Screenshot taken on the HoloLens 2 demonstrating application of energy gate on the coincidence gamma-ray spectrum in real-time.

6.2.3 Prototype Neural Network for Fast Source Searching

Double-scatter events are significantly less frequent than single events, and in many scenarios, the measurement time may be insufficient to form a fully converged image. To address this limitation and optimally guide the detector operator in repositioning the system, single interaction count rates can be leveraged to rapidly predict the likely location of the source, as these rates can be estimated continuously throughout the measurement period. Due to the arrangement of detectors in the H2DPI, a count rate gradient is expected, detectors positioned closer to the source will record

higher count rates compared to those situated further away. This gradient enables the application of statistical learning methods to predict the angle of incidence of the radiation. Count rates per detector are calculated using a rolling average over the acquired waveforms within a set measurement interval and are then provided as input to a trained neural network, which outputs an estimated azimuthal location of the source.

The neural network was constructed using the TensorFlow 2.5 library in Python 3.8.8. Recently, the successful application of neural nets for this task was shown using arrays of NaI detectors [111, 112], or a single volume HPGe [113]. The neural network input nodes correspond to the count rates in each of the 20 detector volumes of the H2DPI. The output layer is the probability estimate for an azimuthal angle, here discretized by 1° increments into a vector of length 360. The input layer activation function was set to relu, whilst the output layer relied on softmax. Training data was produced with the Monte Carlo particle transport code MCNPX-PoliMi [114] that allows for both neutron and photon transport. An explicit model of the detector and casing was created, as shown in Figure 6.5. 360 source locations were simulated, each displaced by 1° increments at 30 cm distance to the detector, to cover the entire azimuthal range. Each angular position was simulated with 10^9 spontaneous fissions from a ^{252}Cf point source. The 20 detector volumes were tallied for neutron and photon interactions and processed into count rates per detector volume using the post-processing code MPPost [100].

The initial 360×20 data sets were augmented 100-fold by introducing Gaussian noise with zero mean and a standard deviation equal to 10% of the counted particles, resulting in a training data set of 36,000×20. It is important to note that the model's validation accuracy did not converge without the inclusion of this noisy data. Training was performed on randomly shuffled data, with a 10% validation split and using a categorical cross-entropy loss function. Figure 6.6 presents examples of the detector input data with corresponding azimuthal labels, along with plots of model accuracy and loss for both the training and validation data over the course of training epochs. Although the model was initially trained for 1000 epochs, overfitting was apparent from the increase in validation loss beyond 400 epochs; therefore, the final model was trained for 300 epochs. As shown

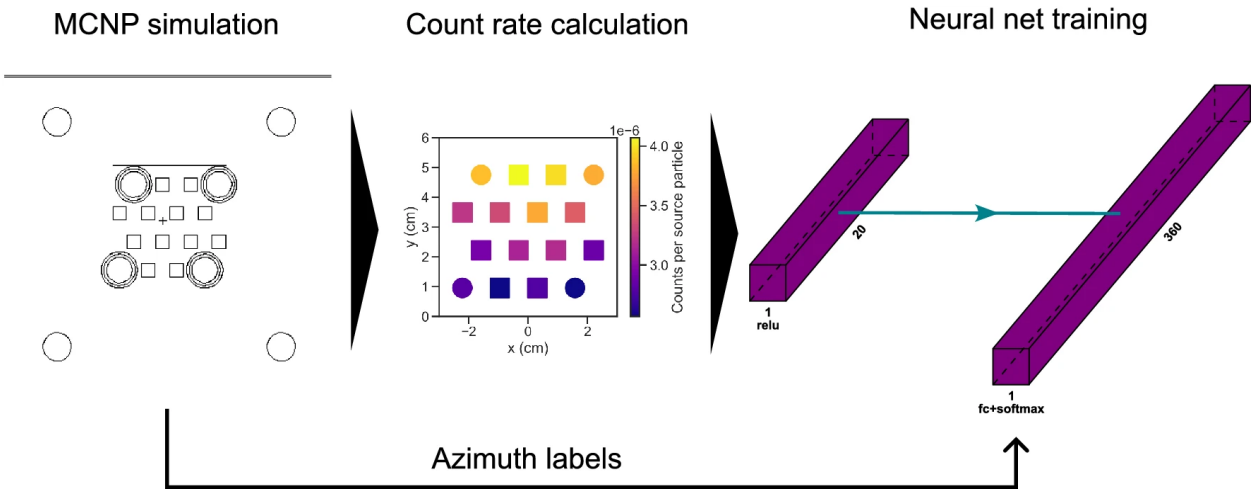

Figure 6.5: Overview of the training data generation for the source direction prediction using a neural net. Shown is the MCNP geometry model of the H2DPI (left), an example count rate response of the array (middle), and a schematic of the neural network showing the input nodes and output layer (right) [35].

in plot (b) of Figure 6.6, both the training and validation accuracies increased with the number of epochs, and no overfitting was observed. The final validation accuracy achieved was 98.8%, as reported by the training program. It was also observed that the addition of hidden layers resulted in overfitting (i.e., an oscillating validation accuracy and increasing validation loss with successive epochs [115]). This suggests regularization may be required if more complex network architectures are employed. For MR display, the directionality is determined by the neural network's output node with the highest value: for example, if node 90 is the maximal output, the MR application renders a yellow arrow indicating azimuthal direction $90°$.

Figure 6.7 presents examples of the MR visualizations for source direction estimation using both ^{137}Cs and ^{252}Cf sources. The prediction process, facilitated by the compact neural network architecture, requires only a few seconds and consistently yields reasonable results. Notably, although the neural network was trained exclusively on ^{252}Cf simulation data, it accurately predicted the source direction for both ^{252}Cf and ^{137}Cs experiments. This finding highlights the potential for future investigations to further assess and optimize neural network performance, including training on multiple source types, varying source-to-detector distances, and incorporating altitude angle estimation.

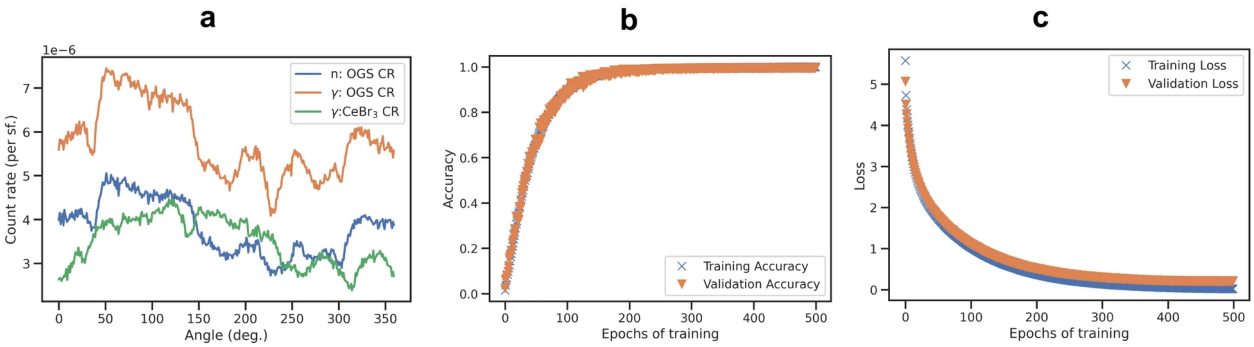

Figure 6.6: (a) Example of training data for neutron and photon interactions per spontaneous fission per source incidence angle in organic glass or $CeBr_3$ detectors. (b) Training and validation accuracy with training iterations. (c) Training and validation loss with epochs [35].

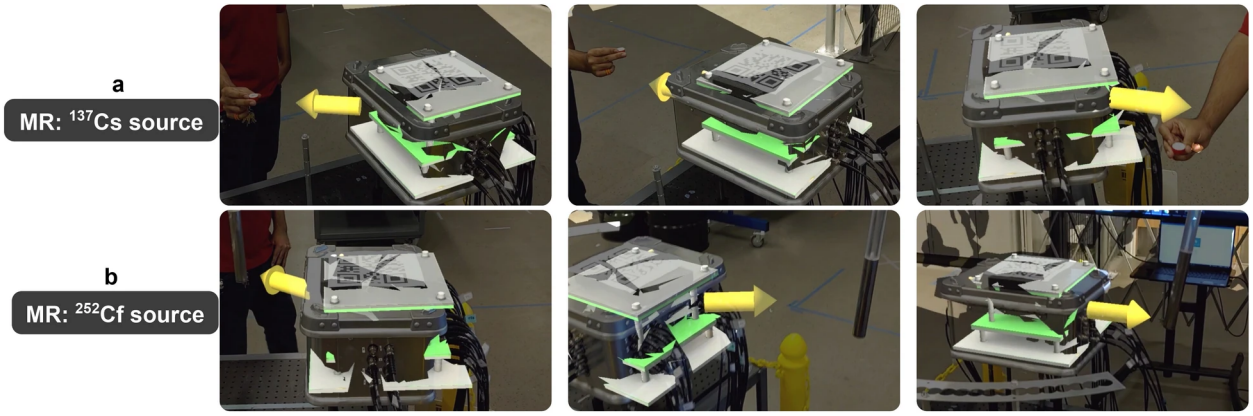

Figure 6.7: Examples of the MR visuals as seen by the user wearing the HoloLens 2 for the fast source direction estimate using a neural net. (a) A ^{137}Cs source is held in three different locations around the detector, the MR display shows a yellow arrow to represent the neural nets' guess. (b) A ^{252}Cf source is held at different locations around the detector [35].

6.3 Mock Inspection Scenario

To demonstrate the applicability of MR visualization in a field-deployable scenario, a mock inspection measurement was performed. The experimental setup consisted of three storage containers: one housing a ^{137}Cs source with an activity of 155 μCi, another containing a ^{252}Cf source with an activity of 557 μCi, and a third left empty. It is important to note that the ^{252}Cf source was shielded with lead to attenuate its gamma-ray signature, ensuring it was significantly below that of the ^{137}Cs source. The gamma source was positioned approximately 0.45 meters from the H2DPI, while the neutron source was placed at a distance of around 0.8 meters, as shown in Figure 6.8. The total

measurement time for this experiment was 100 minutes to obtain well converged visuals in the MR space. As examples in past chapters have shown, shorter measurement times can be used to obtain coarser source localization results.

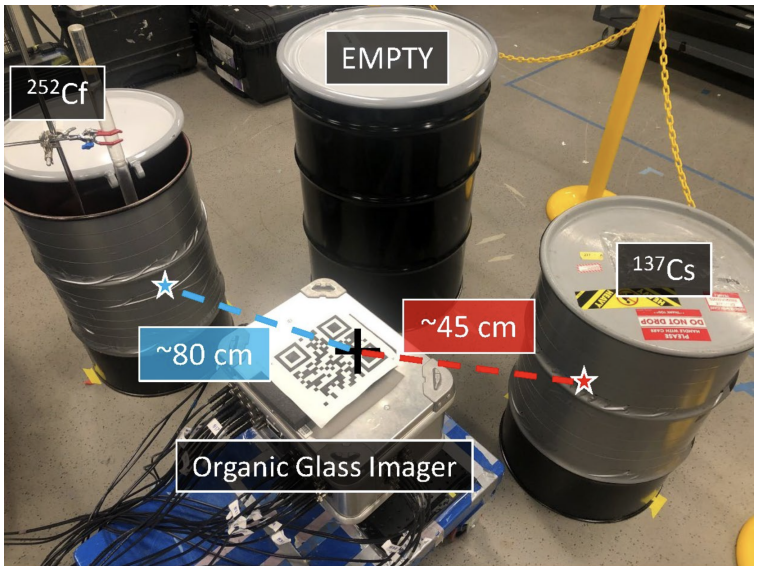

Figure 6.8: Experimental setup for the mock inspection scenario demonstration. Noted distances are with respect to the center of the H2DPI.

Screenshots in Figure 6.9 illustrate the final converged locations for both neutron and gamma-ray imaging modes within the application. In neutron mode, a distinct hotspot appears in the lower half of the leftmost barrel, while gamma-ray mode reveals a prominent hotspot on the upper half of the rightmost barrel. Importantly, the visualization also indicates that the middle barrel is empty, as no hotspots are detected in either imaging mode during the measurement. Figure 6.10 presents screenshots comparing the MR visualizations to the actual source locations in three-dimensional space. Under the experimental conditions, both imaging modes demonstrated close agreement between the visualized directions and the true source positions. Screenshots in Figure 6.11 show the spectroscopy results that the user would be able to visualize in real-time. The reconstructed neutron energy spectrum and gamma-ray coincidence spectrum shown use data from the entire measurement period. The gamma-ray coincidence spectrum clearly shows the prominent 662 keV peak associated with ^{137}Cs while the neutron spectral shape appears normal considering the more limited neutron statistics available.

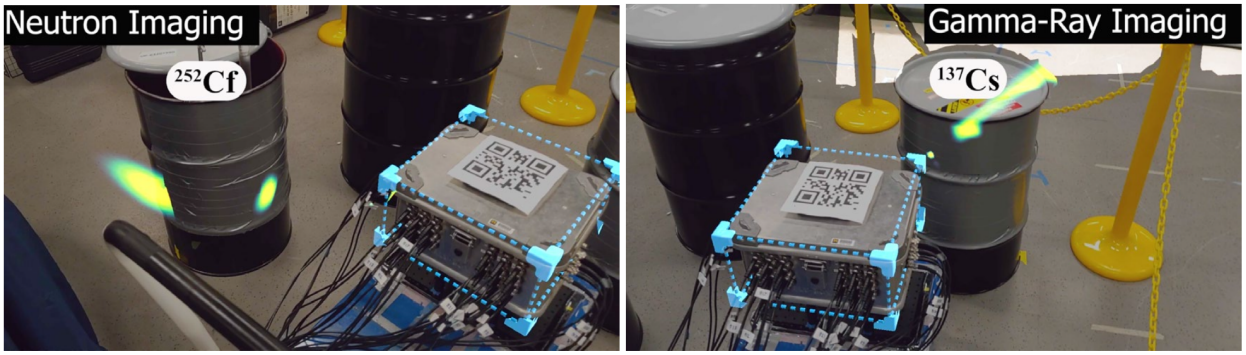

Figure 6.9: Screenshot taken on the HoloLens 2 demonstrating the final converged source locations for both imaging modes.

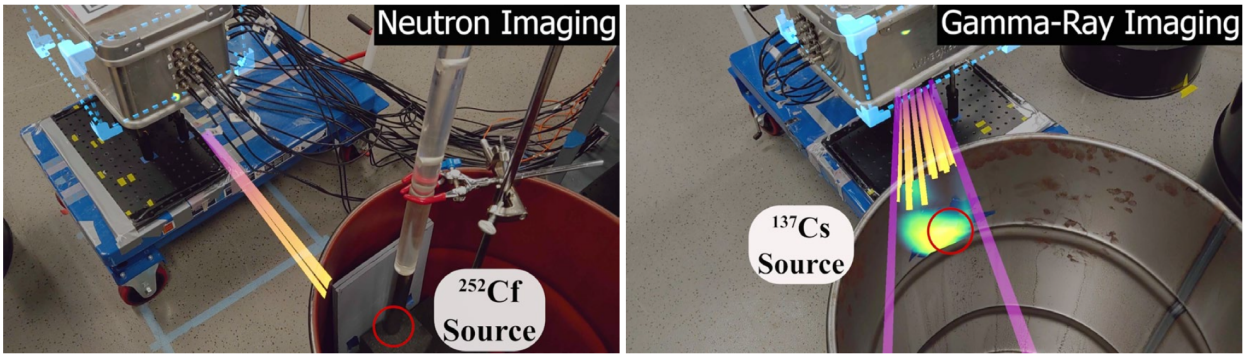

Figure 6.10: Screenshot taken on the HoloLens 2 demonstrating the agreement between the MR visuals and true source locations in physical space.

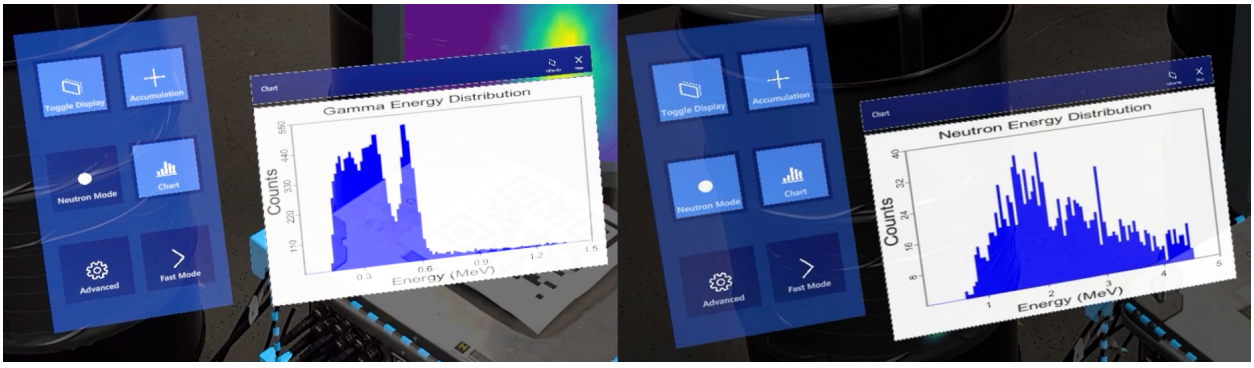

Figure 6.11: Screenshots taken on the HoloLens 2 demonstrating gamma-ray and neutron live-time spectroscopy visuals.

6.4 Implications

The primary advantage of MR visualization lies in its ability to simplify the interpretation of angular radiation images; eliminating the need for users to mentally translate two-dimensional angular hotspots into three-dimensional directions and plausible source locations. The MR implementation enables untrained individuals to interpret radiation images, reducing training requirements for general radiation measurements and increasing flexibility in task delegation during time-sensitive scenarios. MR visualization also provides a more accurate representation of the size and uncertainty associated with radiation images. When interpreting 2D radiation images, it is easy to underestimate angular uncertainty as images are projected into actual spatial source locations; images that appear converged in 2D may not be sufficient for precise source localization once viewed in MR, highlighting potential discrepancies. The implementation presented in this work is open source, facilitating its adaptation to other platforms with basic MR capabilities, such as smartphones or smart-glass devices. Nevertheless, MR remains a subjective experience. Qualitatively, laboratory demonstrations with the HoloLens 2 have yielded positive feedback, ranging from appreciation of its novelty to recognition of its utility as an intuitive tool for visualizing radiation.

CHAPTER 7

Conclusions and Future Work

7.1 Conclusions

Today, it is more important than ever to maintain robust detection and verification capabilities within the nuclear safeguards and nonproliferation regimes. Consequently, the exploration and evaluation of all available tools that can advance these objectives is imperative. Dual-particle imaging systems, with their ability to detect, localize, and spectroscopically characterize radioactive sources, have emerged as a leading technology, especially given their sensitivity to both fast neutrons and gamma rays for identifying SNM such as HEU and plutonium. This dissertation demonstrates that OGS-based imaging systems, through successful localization and spectroscopy of diverse radiation sources including SNM, are suitable for integration into modern safeguards.

This thesis systematically demonstrated that across a wide range of single- and multisource experiments, including challenging scenarios such as short measurement times, substantial shielding, and varying source strengths, the OGS H2DPI reliably localized radioactive sources within its 4π FOV. OGS achieved energy resolution values on the order of $9.2 \pm 0.2\%$, exhibited PSD capabilities superior to those of plastic scintillators but slightly below those of stilbene, and had CTR on the order of 121 ± 8 ps at light outputs around 1 MeVee. A central focus was the detection and characterization of SNM, particularly HEU and plutonium in both metallic and oxide forms. The OGS achieved successful passive gamma-ray imaging of HEU oxide and metal, leveraging the 186 keV emission. Interrogation of HEU metal with AmLi neutron sources demonstrated not only reliable

localization but also preliminary mass sensitivity through neutron singles and spectrometry analyses, adding onto the uses of the H2DPI outside of imaging. Measurements with plutonium metal and oxide further underscored the advantages of OGS as neutron singles spectroscopy allowed clear distinction between metal, oxide, and PuBe sources. Collectively, these results position the OGS H2DPI as a next-generation solution for nuclear security, providing concurrent neutron and gamma-ray imaging, sensitivity to SNM signatures, and the ability to perform energy-resolved discrimination and mass characterization, forming a solid foundation for widespread deployment in safeguards, verification, and emergency response applications. Use cases that are of particular interest for the H2DPI include deployment scenarios by IEEE inspectors during verification work, rapid source searches by personnel from parties like the U.S. Defense Treat Reduction Agency, and radiation safety training such as at nuclear power or fuel processing plants.

The presented development and validation of a neutron simulation pipeline for imaging and spectroscopy using the OGS included extensive detector characterization undertaken to achieve strong quantitative agreement between simulation and experimental responses. It is important to note that while these efforts were specifically tailored to the H2DPI, the foundational methodologies and modeling approaches developed here are broadly applicable to other scatter-based scintillation systems and support applications in nuclear research and verification scenarios.

This work showcased how utilizing MR visualization greatly simplified the interpretation of angular radiation images by seamlessly converting two-dimensional hotspots into intuitive three-dimensional spatial overlays, thereby eliminating the need for users to mentally translate complex imaging data. The MR approach can empower even untrained individuals to accurately interpret radiation images, dramatically reducing training requirements and increasing operational flexibility in time-sensitive scenarios. MR visualization provides a more realistic depiction of source size and associated uncertainty, addressing common limitations of traditional 2D image analysis, where apparent convergence may mask substantial localization ambiguity. The open-source implementation described in this work supports broad adaptation to other MR-capable platforms, such as smartphones and smart-glass devices, further extending access and utility. While MR remains a

subjective experience, laboratory demonstrations with the HoloLens 2 consistently received positive feedback, highlighting both its novelty and its value as an intuitive, user-friendly tool for real-time visualization of radiation sources.

The OGS H2DPI and dissertation work constitute a decisive advancement in portable radiation imaging, integrating novel detector materials, precise simulation modeling, and state-of-the-art MR visualization. The results presented in this dissertation establish the system's readiness for field deployment in safeguards, regulatory inspections, emergency operations, and monitoring applications. Collectively, these findings should inform the adoption and integration of OGS-based dual-particle imaging systems in nuclear security strategies, further elevating the standards for field-ready radiation detection instrumentation.

7.2 Future Work

7.2.1 OGS Material Science

This work introduces a novel scintillator material and innovative data processing pipelines, both of which offer considerable potential for future research. In particular, there are promising avenues for further refinement of the OGS material itself. Two different routes can be pursued. The first is the plasticization of OGS, which can substantially improve its structural integrity and enable the development of more robust detectors suitable for field deployment. However, plasticization may adversely impact certain detector properties, such as PSD and light output yields [47]. Careful optimization will therefore be required to balance material robustness against possible reductions in performance. The second prospective route involves doping the OGS to enhance photoelectric absorption within the material, thereby potentially eliminating the need for inorganic scintillator components. For example, tin-loaded OGS variants are already commercially available [46] and warrant further exploration. Nonetheless, comprehensive characterization will still be necessary to determine any negative effects that doping may have on imaging capabilities and other detector properties.

7.2.2 H2DPI System Design

Future work concerning the H2DPI itself includes the next logical step of constructing a fully populated array that utilizes every available pixel of the Onsemi J-Series SiPM arrays. Expanding the active volume of the system will significantly enhance detection efficiencies; however, several key engineering challenges must be addressed. For instance, current channel readout is accomplished via individual BNC cables and a separate crate of digitizer boards. A more advanced iteration of the H2DPI should incorporate application-specific integrated circuits (ASICs) or similar technologies to support greater channel densities. Adopting ASIC-based data acquisition would also enable a more compact form factor, facilitating integration within the H2DPI housing and promoting true portability. Ongoing research is examining whether PSD can be replaced by time-of-flight information alone for particle classification [116], which would further simplify data acquisition requirements. Moving toward genuine portability, future iterations should also aim to include an internal power supply, such as a rechargeable ion battery, and a temperature control system,using components such as Peltier cells [117] or automatic voltage adjusters [118], to maintain consistent SiPM gain during operation.

7.2.3 H2DPI Simulation Pipeline

Regarding the simulation pipeline for the H2DPI, a more comprehensive CTR characterization of the OGS bars should be conducted to accurately determine the imager's timing response as a function of light output. Completing this characterization will finalize the neutron component of the simulation pipeline. To achieve a fully integrated dual-particle simulation capability, the development of a complementary gamma-ray simulation pipeline is also necessary, which will require additional characterization work with the $CeBr_3$ detectors. Establishing complete neutron and gamma-ray simulation pipelines will offer valuable insights for the future redesign and optimization of the OGS H2DPI and may also benefit the broader field of scintillator scatter-based imaging systems.

7.2.4 Mixed Reality Visualization

Finally, a future volunteer study could be undertaken to assess the effectiveness of mixed-reality visualization of imaging data using the HoloLens 2.

The proposed study would comprise two groups: a subject matter expert group, including individuals with a background in nuclear engineering, and a novice user group, consisting of participants with no formal education in the field. A between groups comparison would be useful to show which user group would benefit the most from the mixed reality approach since it would make it cleaner to analyze differences. Ideally, each group would consist of at least ten individuals. During the study, participants from both groups would be tasked with localizing several sources within a designated room using two methods: the traditional approach (simple backprojection images) and the mixed-reality implementation. Users would place markers at locations where they believe sources are present; the distance from the true location would serve as a metric for accuracy. In addition, participants would complete questionnaires to gauge their reception of the system and provide feedback for further improvements. If the assumption that the mixed reality visualization is conducive for source localization by anyone, then the results may indicate that both groups' average distances from guesses to true source locations are statistically comparable to one another. Meaning that any advantages from having a formal education in the field or background knowledge of the equipment could be matched using mixed reality visuals. Findings from this study have the potential to inform enhancements to user experience and to evaluate whether the mixed-reality approach objectively improves source localization across a range of user expertise.

The mixed reality environment can also enable data collection from a mobile H2DPI and supports the integration of measurements obtained from multiple locations. Localization capabilities can be significantly improved by using this additional information in conjunction with triangulation algorithms. This advanced three-dimensional imaging approach has the potential to move beyond surface projections and achieve volumetric localization, which would greatly enhance effectiveness and usability in a wider range of scenarios.

BIBLIOGRAPHY

[1] D. D. EISENHOWER, "Atoms for Peace," Speech, United Nations General Assembly (1953). Eisenhower Presidential Library.

[2] INTERNATIONAL ATOMIC ENERGY AGENCY, *The Statute of the International Atomic Energy Agency*, IAEA, Vienna (1957).

[3] UNITED NATIONS, "Treaty on the Non-Proliferation of Nuclear Weapons," (1970). https://www.un.org/disarmament/wmd/nuclear/npt/text.

[4] UNITED NATIONS, "Comprehensive Nuclear-Test-Ban Treaty," (1996). https://www.ctbto.org/the-treaty/text-of-the-treaty/.

[5] COMPREHENSIVE NUCLEAR-TEST-BAN TREATY ORGANIZATION, "International Monitoring System (IMS)," (nd). https://www.ctbto.org/our-work/international-monitoring-system.

[6] UNITED STATES DEPARTMENT OF STATE, "Treaty between the United States of America and the Russian Federation on Measures for the Further Reduction and Limitation of Strategic Offensive Arms (New START)," (2010). https://www.state.gov/new-start/.

[7] R. PETERS, *A Nuclear Posture Review for the Next Administration: Building the Nuclear Arsenal of the 21st Century*, Heritage Foundation (2024).

[8] U.S. NUCLEAR REGULATORY COMMISSION, "Material Control and Accounting of Special Nuclear Material," (2015). 10 C.F.R. §74.4.

[9] D. ALBRIGHT and K. KRAMER, "Neptunium 237 and Americium: world inventories and proliferation concerns," *Institute for Science and International Security*, **6060**, 1 (2005).

[10] I. TECDOC, "Thorium Fuel Cycle-Potential Benefits and Challenges. IAEATECDOC-1450," *International Atomic Energy* (2005).

[11] J. S. DUSTIN and R. A. BORRELLI, "Assessment of alternative radionuclides for use in a radioisotope thermoelectric generator," *Nuclear Engineering and Design*, **385**, 111475 (2021).

[12] R. RADEV and T. D. MCLEAN, "Characterization of 244Cm neutron sources," *Applied Radiation and Isotopes*, **163**, 109225 (2020).

[13] R. T. KOUZES, J. H. ELY, L. E. ERIKSON, W. J. KERNAN, A. T. LINTEREUR, E. R. SICILIANO, D. L. STEPHENS, D. C. STROMSWOLD, R. M. VAN GINHOVEN, and M. L. WOODRING, "Neutron detection alternatives to 3He for national security applications," *Nuclear Instruments and Methods in Physics Research Section A: Accelerators, Spectrometers, Detectors and Associated Equipment*, **623**, *3*, 1035 (2010).

[14] G. GILMORE and D. JOSS, *Practical gamma-ray spectrometry*, John Wiley & Sons (2024).

[15] R. C. RUNKLE, D. L. CHICHESTER, and S. J. THOMPSON, "Rattling nucleons: New developments in active interrogation of special nuclear material," *Nuclear Instruments and Methods in Physics Research Section A: Accelerators, Spectrometers, Detectors and Associated Equipment*, **663**, *1*, 75 (2012).

[16] I. JOVANOVIC and A. S. ERICKSON, "Active Interrogation in Nuclear Security Science, Technology and Systems," *Simulation* (2020).

[17] H. AL HAMRASHDI, S. D. MONK, and D. CHENELER, "Passive gamma-ray and neutron imaging systems for national security and nuclear non-proliferation in controlled and uncontrolled detection areas: Review of past and current status," *Sensors*, **19**, *11*, 2638 (2019).

[18] J. PETROVIĆ, A. GÖÖK, and B. CEDERWALL, "Rapid imaging of special nuclear materials for nuclear nonproliferation and terrorism prevention," *Science Advances*, **7**, *21*, eabg3032 (2021).

[19] F. GAGLIARDI ET AL., "Integration of independent NDA techniques within a SLAM-based robotic system for improving safeguards standard routines: a review of the current status and possible future developments," *ESARDA Bulletin-The International Journal of Nuclear Safeguards and Non-proliferation*, **64**, 10 (2022).

[20] K. ZIOCK, "Principles and applications of gamma-ray imaging for arms control," *Nuclear Instruments and Methods in Physics Research Section A: Accelerators, Spectrometers, Detectors and Associated Equipment*, **878**, 191 (2018).

[21] T. HARVEY, A. ENQVIST, and K. BACHNER, "Applications and deployment of neutron scatter cameras in nuclear safeguards scenarios," *Journal of Nuclear Materials Management*, **48**, *2*, 4 (2020).

[22] G. F. KNOLL, *Radiation detection and measurement*, John Wiley & Sons (2010).

[23] J. K. POLACK, "A maximum-likelihood approach for localizing and characterizing special nuclear material with a dual-particle imager," PhD Thesis (2016).

[24] A. POITRASSON-RIVIÈRE, M. C. HAMEL, J. K. POLACK, M. FLASKA, S. D. CLARKE, and S. A. POZZI, "Dual-particle imaging system based on simultaneous detection of photon and neutron collision events," *Nuclear Instruments and Methods in Physics Research Section A: Accelerators, Spectrometers, Detectors and Associated Equipment*, **760**, 40 (2014).

[25] A. C. MADDEN, P. F. BLOSER, D. FOURGUETTE, L. LAROCQUE, J. S. LEGERE, M. LEWIS, M. L. MCCONNELL, M. ROUSSEAU, and J. M. RYAN, "An imaging neutron/gamma-ray spectrometer," *Chemical, biological, radiological, nuclear, and explosives (CBRNE) sensing XIV*, vol. 8710, 405–416, SPIE (2013).

[26] W. STEINBERGER, "A handheld dual particle imager for imaging and characterizing special nuclear material," PhD Thesis, University of Michigan (2021).

[27] H. AL HAMRASHDI, D. CHENELER, and S. D. MONK, "A fast and portable imager for neutron and gamma emitting radionuclides," *Nuclear Instruments and Methods in Physics Research Section A: Accelerators, Spectrometers, Detectors and Associated Equipment*, **953**, 163253 (2020).

[28] R. LOPEZ, W. STEINBERGER, N. GIHA, P. MARLEAU, S. CLARKE, and S. POZZI, "Neutron and gamma imaging using an organic glass scintillator handheld dual particle imager," *Nuclear Instruments and Methods in Physics Research Section A: Accelerators, Spectrometers, Detectors and Associated Equipment*, **1042**, 167407 (2022).

[29] R. LOPEZ, W. M. STEINBERGER, N. GIHA, S. D. CLARKE, and S. A. POZZI, "Uranium imaging using a novel organic glass-based dual-particle imager," *Proc. 63rd Virtual INMM Annu. Meeting*, vol. 1, 1561–1569 (2022).

[30] R. LOPEZ, S. D. CLARKE, and S. A. POZZI, "HEU neutron imaging with organic glass using AmLi interrogation," *Proceedings of the 66th INMM Annual Meeting* (2025).

[31] R. LOPEZ, O. PAKARI, S. CLARKE, and S. POZZI, "Multiparticle Imaging of Weapons-Grade Plutonium Metal Using an Organic Glass-Based System," *Proceedings of the INMM & ESARDA Joint Annual Meeting, Vienna, Austria*, 22–26 (2023).

[32] R. LOPEZ, V. MOZIN, P. KERR, S. CLARKE, and S. POZZI, "Simultaneous Imaging of Plutonium and Thorium with Organic Glass System," *2024 IEEE Nuclear Science Symposium (NSS), Medical Imaging Conference (MIC) and Room Temperature Semiconductor Detector Conference (RTSD)*, 1–1, IEEE (2024).

[33] R. LOPEZ, O. PAKARI, C. BALLARD, S. CLARKE, and S. POZZI, "A simulation pipeline for fast neutron imaging and spectroscopy using quantified detector attributes," *Radiation Measurements*, **184**, 107440 (2025).

[34] R. LOPEZ, O. PAKARI, D. BREITENMOSER, S. D. CLARKE, and S. A. POZZI, "Impact of Light Output on the Timing Resolution of Organic Glass Scintillator Bars in a Dual-Ended Readout Configuration," (2025)Manuscript in preparation.

[35] O. PAKARI, R. LOPEZ, I. DRUCKMAN, E. MENG, E. ZHOU, Z. WANG, S. D. CLARKE, and S. A. POZZI, "Real-time mixed reality display of dual particle radiation detector data," *Scientific Reports*, **13**, *1*, 362 (2023).

[36] R. LOPEZ, O. PAKARI, S. CLARKE, and S. POZZI, "Neutron and Gamma Organic Glass Imager with Visualization using Augmented Reality," *Journal of Physics: Conference Series*, vol. 3130, 012004, IOP Publishing (2025).

[37] P. L. FENG, N. R. MYLLENBECK, and J. S. CARLSON, "Organic glass scintillators," *Plastic Scintillators: Chemistry and Applications*, 243–283, Springer.

[38] W. KLÖPFFER and M. HEPP, "Triplet-triplet annihilation in dilute, solid solutions of aromatic polymers," *Monatshefte für Chemie/Chemical Monthly*, **125**, *1*, 25 (1994).

[39] Y.-C. M. WU, M. F. MOLAIRE, D. S. WEISS, F. A. ANGEL, C. R. DEBLASE, and B. P. FORS, "Synthesis of amorphous monomeric glass mixtures for organic electronic applications," *The Journal of organic chemistry*, **80**, *24*, 12740 (2015).

[40] J. S. CARLSON, P. MARLEAU, R. A. ZARKESH, and P. L. FENG, "Taking advantage of disorder: Small-molecule organic glasses for radiation detection and particle discrimination," *Journal of the American Chemical Society*, **139**, *28*, 9621 (2017).

[41] C. BHUGRA and M. J. PIKAL, "Role of thermodynamic, molecular, and kinetic factors in crystallization from the amorphous state," *Journal of pharmaceutical sciences*, **97**, *4*, 1329 (2008).

[42] I. AUJARD, J.-P. BALTAZE, J.-B. BAUDIN, E. COGNE, F. FERRAGE, L. JULLIEN, É. PEREZ, V. PREVOST, L. M. QIAN, and O. RUEL, "Tetrahedral onsager crosses for solubility improvement and crystallization bypass," *Journal of the American Chemical Society*, **123**, *34*, 8177 (2001).

[43] D. M. WALTERS, L. ANTONY, J. J. DE PABLO, and M. EDIGER, "Influence of molecular shape on the thermal stability and molecular orientation of vapor-deposited organic semiconductors," *The Journal of Physical Chemistry Letters*, **8**, *14*, 3380 (2017).

[44] J. DOWNS and F. SMITH, "Organic-glass scintillators," *Nucleonics*, **16**, *3* (1958).

[45] BLUESHIFT OPTICS, "blueshiftoptics.com," (nd). https://blueshiftoptics.com (accessed May 18, 2024).

[46] RADIATION MONITORING DEVICES, INC., "Organic Glass Scintillator," (nd). https://www.rmdinc.com/product-category/products/organic-glass-scintillator/ (accessed May 18, 2024).

[47] L. Q. NGUYEN, H. M. TRAN, A. I. BENIN, J. S. CARLSON, P. MARLEAU, M. SWEANY, and P. L. FENG, "Organic glass scintillator formulations and mold development towards scalable and cast-in-place pixelated fabrications," *Nuclear Instruments and Methods in Physics Research Section A: Accelerators, Spectrometers, Detectors and Associated Equipment*, **1036**, 166835 (2022).

[48] J. B. BIRKS, *The theory and practice of scintillation counting: International series of monographs in electronics and instrumentation*, vol. 27, Elsevier (2013).

[49] P. L. FENG, "Molecular design considerations for different classes of organic scintillators," *Plastic Scintillators: Chemistry and Applications*, 223–242, Springer.

[50] J. R. LAKOWICZ, *Principles of fluorescence spectroscopy*, Springer (2006).

[51] D. L. DEXTER, "A theory of sensitized luminescence in solids," *The journal of chemical physics*, **21**, *5*, 836 (1953).

[52] T. H. SHIN, P. L. FENG, J. S. CARLSON, S. D. CLARKE, and S. A. POZZI, "Measured neutron light-output response for trans-stilbene and small-molecule organic glass scintillators," *Nuclear Instruments and Methods in Physics Research Section A: Accelerators, Spectrometers, Detectors and Associated Equipment*, **939**, 36 (2019).

[53] T. LAPLACE, B. GOLDBLUM, J. BEVINS, D. BLEUEL, E. BOURRET, J. BROWN, E. CALLAGHAN, J. CARLSON, P. FENG, G. GABELLA ET AL., "Comparative scintillation performance of EJ-309, EJ-276, and a novel organic glass," *Journal of Instrumentation*, **15**, *11*, P11020 (2020).

[54] W. K. WARBURTON, J. S. CARLSON, and P. L. FENG, "Organic glass scintillator (OGS) property comparisons to Stilbene, EJ-276 and BC-404," *Nuclear Instruments and Methods in Physics Research Section A: Accelerators, Spectrometers, Detectors and Associated Equipment*, **1018**, 165778 (2021).

[55] T. WU, Y. SUN, N. LI, M. M. DE VILLIERS, and L. YU, "Inhibiting surface crystallization of amorphous indomethacin by nanocoating," *Langmuir*, **23**, *9*, 5148 (2007).

[56] W. M. STEINBERGER, N. P. GIHA, P. MARLEAU, S. D. CLARKE, and S. A. POZZI, "Optimizing the position of inorganic scintillators in a handheld dual particle imager," *2020 IEEE Nuclear Science Symposium and Medical Imaging Conference (NSS/MIC)*, 1–5, IEEE (2020).

[57] *MICROJ-series: Silicon Photomultipliers (SiPM), High PDE and Timing Resolution Sensors in a TSV Package* (2021)Publication No. MICROJ-SERIES/D.

[58] N. P. GIHA, M. L. RUCH, A. DI FULVIO, W. M. STEINBERGER, and S. A. POZZI, "Readout electronics of a handheld dual particle imager," *2017 IEEE Nuclear Science Symposium and Medical Imaging Conference (NSS/MIC)*, 1–3, IEEE (2017).

[59] CAEN S.P.A., *User Manual UM2792: V1730/VX1730 & V1725/VX1725 Digitizers*, CAEN S.p.A. (2016)Available at https://www.caen.it/products/v1730/.

[60] KEYSIGHT TECHNOLOGIES, *User's Guide: E364xA Dual Output DC Power Supplies*, 12th ed. (2019)Part No. E3646-90001. Available at https://www.keysight.com/us/en/assets/9018-01166/user-manuals/9018-01166.pdf.

[61] *UM5960 - CoMPASS User Manual (Rev. 20)* (2022). https://www.caen.it/products/compass/.

[62] M. A. NORSWORTHY, A. POITRASSON-RIVIÈRE, M. L. RUCH, S. D. CLARKE, and S. A. POZZI, "Evaluation of neutron light output response functions in EJ-309 organic scintillators," *Nuclear Instruments and Methods in Physics Research Section A: Accelerators, Spectrometers, Detectors and Associated Equipment*, **842**, 20 (2017).

[63] G. DIETZE and H. KLEIN, "Gamma-calibration of NE 213 scintillation counters," *Nuclear Instruments and Methods in Physics Research*, **193**, *3*, 549 (1982).

[64] W. STEINBERGER, N. GIHA, M. HUA, S. CLARKE, and S. POZZI, "Anisotropic neutron response of trans-stilbene and impact on a handheld dual particle imager," *Nuclear Instruments and Methods in Physics Research Section A: Accelerators, Spectrometers, Detectors and Associated Equipment*, **1003**, 165266 (2021).

[65] H. KNOX and T. MILLER, "A technique for determining bias settings for organic scintillators," *Nuclear Instruments and Methods*, **101**, *3*, 519 (1972).

[66] S. POZZI, M. BOURNE, and S. CLARKE, "Pulse shape discrimination in the plastic scintillator EJ-299-33," *Nuclear Instruments and Methods in Physics Research Section A: Accelerators, Spectrometers, Detectors and Associated Equipment*, **723**, 19 (2013).

[67] J. POLACK, M. FLASKA, A. ENQVIST, C. SOSA, C. LAWRENCE, and S. POZZI, "An algorithm for charge-integration, pulse-shape discrimination and estimation of neutron/photon misclassification in organic scintillators," *Nuclear Instruments and Methods in Physics Research Section A: Accelerators, Spectrometers, Detectors and Associated Equipment*, **795**, 253 (2015).

[68] J. F. ZIEGLER and J. P. BIERSACK, "The stopping and range of ions in matter," *Treatise on heavy-ion science: volume 6: astrophysics, chemistry, and condensed matter*, 93–129, Springer.

[69] N. P. GIHA, W. M. STEINBERGER, L. Q. NGUYEN, J. S. CARLSON, P. L. FENG, S. D. CLARKE, and S. A. POZZI, "Organic glass scintillator bars with dual-ended readout," *Nuclear Instruments and Methods in Physics Research Section A: Accelerators, Spectrometers, Detectors and Associated Equipment*, **1014**, 165676 (2021).

[70] M. L. RUCH, "Silicon Photomultipliers for Compact Neutron Scatter Cameras," *Ph. D. Thesis* (2017).

[71] S. J. WILDERMAN, J. A. FESSLER, N. H. CLINTHORNE, J. LEBLANC, and W. L. ROGERS, "Improved modeling of system response in list mode EM reconstruction of Compton scatter camera images," *IEEE Transactions on Nuclear Science*, **48**, *1*, 111 (2001).

[72] D. GOODMAN, "Passive Characterization of Unknown Spaces Using Large-Volume, Pixelated CdZnTe," PhD Thesis (2019).

[73] H. H. BARRETT, T. WHITE, and L. C. PARRA, "List-mode likelihood," *Journal of the Optical Society of America A*, **14**, *11*, 2914 (1997).

[74] L. A. SHEPP and Y. VARDI, "Maximum likelihood reconstruction for emission tomography," *IEEE transactions on medical imaging*, **1**, *2*, 113 (2007).

[75] L. PARRA and H. H. BARRETT, "List-mode likelihood: EM algorithm and image quality estimation demonstrated on 2-D PET," *IEEE transactions on medical imaging*, **17**, *2*, 228 (1998).

[76] Z. WANG, A. C. BOVIK, H. R. SHEIKH, and E. P. SIMONCELLI, "Image quality assessment: from error visibility to structural similarity," *IEEE transactions on image processing*, **13**, *4*, 600 (2004).

[77] R. LOPEZ, O. PAKARI, S. D. CLARKE, and S. A. POZZI, "Shielded Californium-252 Measurements Using an Organic Glass Dual Particle Imager," *2022 IEEE Nuclear Science Symposium and Medical Imaging Conference (NSS/MIC)*, 1–4, IEEE (2022).

[78] A. I. TOPUZ and I. A. REYHANCAN, "Neutronic Analysis of a Nuclear-Chicago NH3 Neutron Howitzer," *arXiv preprint arXiv:1806.05255* (2018).

[79] J. VALENTIN, *Nuclear decay data for dosimetric calculations*, Elsevier (2009).

[80] H3D, INC., "H420 Gamma-Ray Spectrometer Specifications," (nd). https://h3dgamma.com/H420Specs.pdf.

[81] PHDS CO., "GeGI - Germanium Gamma-Ray Imaging HPGe Spectrometer," (2024). https://phdsco.com/wp-content/uploads/2024/05/20240514-GeGI-Front-and-Back-MK-DIGITAL-BEST.pdf.

[82] G. CHOPPIN, J. LILJENZIN, and J. RYDBERG, "The transuranium elements," *Radiochem. Nucl. Chem.*, 415–439, Butterworth-Heinemann Woburn.

[83] D. LOAIZA, R. BREWER, R. SANCHEZ, and Y. ROZHIKHIN, "Neptunium-237 sphere surrounded by hemispherical shells of highly enriched uranium," *Los Alamos National Laboratory* (2009).

[84] I. CHALLENGES, "TECDOC-1450," *IAEA, Vienna* (2005).

[85] I. CROSSLAND, *Nuclear fuel cycle science and engineering*, Elsevier (2012).

[86] R. ROTHE, "Extrapolated experimental critical parameters of unreflected and steel-reflected massive enriched uranium metal spherical and hemispherical assemblies," , Lockheed Idaho Technologies Co., Idaho National Engineering and ... (1997).

[87] D. REILLY, N. ENSSLIN, H. SMITH JR, and S. KREINER, "Passive nondestructive assay of nuclear materials," , US Nuclear Regulatory Commission (NRC), Washington, DC (United States ... (1991).

[88] N. KLEEDTKE, M. HUA, and S. POZZI, "Genetic algorithm optimization of tin–copper graded shielding for improved plutonium safeguards measurements," *Nuclear Instruments and Methods in Physics Research Section A: Accelerators, Spectrometers, Detectors and Associated Equipment*, **988**, 164877 (2021).

[89] M. E. MOORE, A. V. MOZHAYEV, R. S. WITTMAN, and E. K. MACE, "Configuration and impurity quantification of AmLi sources using radiography and gamma spectroscopy," *Nuclear Instruments and Methods in Physics Research Section A: Accelerators, Spectrometers, Detectors and Associated Equipment*, **990**, 164987 (2021).

[90] S. CLARKE, R. LOPEZ, V. MOZIN, P. KERR, J. HUTCHINSON, P. MARLEAU, and S. POZZI, "Neutron spectroscopy of plutonium using a handheld detection system," *Scientific Reports*, **14**, *1*, 17192 (2024).

[91] S. POZZI, S. D. CLARKE, W. WALSH, E. MILLER, J. DOLAN, M. FLASKA, B. WIEGER, A. ENQVIST, E. PADOVANI, J. MATTINGLY ET AL., "MCNPX-PoliMi for nuclear nonproliferation applications," *Nuclear Instruments and Methods in Physics Research Section A: Accelerators, Spectrometers, Detectors and Associated Equipment*, **694**, 119 (2012).

[92] B. HUISMAN, E. MUÑOZ, D. DAUVERGNE, J. M. LÉTANG, D. SARRUT, and E. TESTA, "Analytical modeling and Monte Carlo simulations of multi-parallel slit and knife-edge slit prompt gamma cameras," *Physics in Medicine & Biology*, **68**, *11*, 115009 (2023).

[93] B. CHENG, Y. XU, S. LI, Q. REN, X. PEI, K. MEN, J. DAI, and X. G. XU, "Development and clinical application of a GPU-based Monte Carlo dose verification module and software for 1.5 T MR-LINAC," *Medical Physics*, **50**, *5*, 3172 (2023).

[94] I. MERIC, E. ALAGOZ, L. B. HYSING, T. KÖGLER, D. LATHOUWERS, W. R. LIONHEART, J. MATTINGLY, J. OBHODAS, G. PAUSCH, H. E. PETTERSEN ET AL., "A hybrid multi-particle approach to range assessment-based treatment verification in particle therapy," *Scientific reports*, **13**, *1*, 6709 (2023).

[95] M. Y. HUA, B. GODDARD, C. LLOYD, E. C. LEPPINK, S. A. ABRAHAM, J. D. NOEY, S. D. CLARKE, and S. A. POZZI, "Simulation of the nondestructive assay of 237Np using active neutron multiplicity counting," *Nuclear Science and Engineering*, **194**, *2*, 154 (2020).

[96] T. BILY, O. HUML, and B. BELKO, "Delayed neutron counting of uranium pins using moderated neutrons from portable DD neutron generator in high frequency mode," *Applied Radiation and Isotopes*, **191**, 110527 (2023).

[97] S. NAEEM, S. CLARKE, and S. POZZI, "Validation of Geant4 and MCNPX-PoliMi simulations of fast neutron detection with the EJ-309 liquid scintillator," *Nuclear Instruments and Methods in Physics Research Section A: Accelerators, Spectrometers, Detectors and Associated Equipment*, **714**, 98 (2013).

[98] M. B. CHADWICK, M. HERMAN, P. OBLOŽINSKÝ, M. E. DUNN, Y. DANON, A. KAHLER, D. L. SMITH, B. PRITYCHENKO, G. ARBANAS, R. ARCILLA ET AL., "ENDF/B-VII. 1 nuclear data for science and technology: cross sections, covariances, fission product yields and decay data," *Nuclear data sheets*, **112**, *12*, 2887 (2011).

[99] S. OHNISHI, "Gxsview: Geometry and cross section viewer for calculating radiation transport," *SoftwareX*, **14**, 100681 (2021).

[100] E. C. MILLER, S. D. CLARKE, M. FLASKA, S. PRASAD, S. A. POZZI, and E. PADOVANI, "MCNPX-PoliMi post-processing algorithm for detector response simulations," *Journal of Nuclear Materials Management*, **40**, *2*, 34 (2012).

[101] A. ENQVIST, C. C. LAWRENCE, B. M. WIEGER, S. A. POZZI, and T. N. MASSEY, "Neutron light output response and resolution functions in EJ-309 liquid scintillation detectors," *Nuclear Instruments and Methods in Physics Research Section A: Accelerators, Spectrometers, Detectors and Associated Equipment*, **715**, 79 (2013).

[102] R. BATCHELOR, W. GILBOY, J. PARKER, and J. TOWLE, "The response of organic scintillators to fast neutrons," *Nuclear Instruments and Methods*, **13**, 70 (1961).

[103] L. MARQUES, A. VALE, and P. VAZ, "State-of-the-art mobile radiation detection systems for different scenarios," *Sensors*, **21**, *4*, 1051 (2021).

[104] H. ISHII, "Augmented reality. Fundamentals and nuclear related applications," *International Electronic Journal of Nuclear safety and simulation*, **1** (2010).

[105] O. POPOV, A. IATSYSHYN, D. SOKOLOV, M. DEMENT, I. NEKLONSKYI, and A. YELIZAROV, "Application of virtual and augmented reality at nuclear power plants," *Systems, decision and control in energy II*, 243–260, Springer.

[106] F. MCGEE, R. MCCALL, and J. BAIXAULI, "Comparison of spatial visualization techniques for radiation in augmented reality," *Proceedings of the 2024 CHI Conference on Human Factors in Computing Systems*, 1–15 (2024).

[107] S. WU, L. HOU, G. K. ZHANG, and H. CHEN, "Real-time mixed reality-based visual warning for construction workforce safety," *Automation in Construction*, **139**, 104252 (2022).

[108] J. K. HAAS, "A history of the unity game engine," (2014).

[109] G. HATTAB, T.-M. RHYNE, and D. HEIDER, "Ten simple rules to colorize biological data visualization," (2020).

[110] J. HUNTER, "Matplotlib: A 2D graphics environment Computing In Science Engineering 9 3 90–95 Matplotlib is a 2D graphics package used for Python for application development interactive scripting and publication-quality image generation across user interfaces and operating systems," *IEEE COMPUTER SOC10. 1109/MCSE. 2007.55*.

[111] M. DURBIN, C. BALBIER, and A. LINTEREUR, "Development of a fully connected residual neural network for directional gamma ray detection," *International Journal of Modern Physics: Conference Series*, vol. 50, 2060010, World Scientific (2020).

[112] D. FOBAR, W. VANDERLIP, W. KOCH, and P. CHAPMAN, "A machine learning approach to a multidetector array response function for nuclear search," *IEEE Transactions on Nuclear Science*, **69**, *8*, 1939 (2022).

[113] R. GLADEN, T. HARVEY, S. CHIRAYATH, A. FAIRCHILD, A. KOYMEN, A. WEISS, and V. CHIRAYATH, "Implementation of a machine learning technique for estimating gamma direction using a coaxial high purity germanium detector," *Nuclear Instruments and Methods in Physics Research Section A: Accelerators, Spectrometers, Detectors and Associated Equipment*, **1039**, 167067 (2022).

[114] S. A. POZZI, E. PADOVANI, and M. MARSEGUERRA, "MCNP-PoliMi: a Monte-Carlo code for correlation measurements," *Nuclear Instruments and Methods in Physics Research Section A: Accelerators, Spectrometers, Detectors and Associated Equipment*, **513**, *3*, 550 (2003).

[115] I. GOODFELLOW, "Deep learning," (2016).

[116] W. HERIOT, D. BREITENMOSER, R. LOPEZ, S. D. CLARKE, and S. A. POZZI, "IDual Particle Imaging Using Time-of-Flight Neutron Classification," (2026)Manuscript in preparation.

[117] E. FOSCHI, G. LEVI, L. QUADRANI, C. SBARRA, C. GUANDALINI, M. ZUFFA ET AL., "Study of a silicon photodetector thermal stabilization using a Peltier cell," , Comsol France, 38-Grenoble (France) (2007).

[118] F. LICCIULLI and C. MARZOCCA, "An active compensation system for the temperature dependence of SiPM gain," *IEEE Transactions on Nuclear Science*, **62**, *1*, 228 (2015).